UNIVERSITÀ DEGLI STUDI DI ROMA "LA SAPIENZA"
Dottorato di Ricerca in Fisica - XIV Ciclo

Measurements of Branching Ratios and *CP* violating asymmetries in $B \to \pi^+\pi^-$ and $B \to K^\pm\pi^\mp$ decays with the *BABAR* experiment

Tesi presentata da
Gianluca Cavoto
per il conseguimento del titolo di
Dottore di Ricerca

Direttore della Ricerca:

Chiar.mo Prof.
Fernando Ferroni

Coordinatore del
Dottorato di Ricerca:

Chiar.mo Prof.
Guido Martinelli

Anno Accademico 2000-2001

A cate,
per aver sopportato tutto questo.
Almeno per un po'.

Obsessions, of course, can never be shared.
J.Coe, *The House of Sleep.*

Contents

Introduction

The study of neutral and charged B mesons decays to final states with pion and kaons (*charmless twobody B decays*) is a crucial a test of *CP* violation and flavor physics in the Standard Model. Measurements of Branching Ratios ($\mathcal{B}$) for these decays, as well as asymmetries in the decay rates, can be compared with models derived within the Standard Model. An important new kind of measurement, a time-dependent *CP* asymmetry analysis, can now be performed at B-factory experiments as *BABAR* at SLAC and BELLE at KEK.

In this thesis, data collected by the *BABAR* experiment are analyzed: results based on year 2000 data (published in [1]) are presented for measurements of $\mathcal{B}$ for the charged channels $B^0 \to h'^+h^-$ (with $h', h = \pi, K$) and asymmetry in the decay rates ($\mathcal{A}_{K\pi}$) for $B^0 \to K^\pm\pi^\mp$ channel.

Data collected until June 2001 are included in a time-dependent *CP* asymmetry analysis for the $B \to \pi^+\pi^-$ channel. These results have to be considered still preliminary. Nevertheless they represent the first measurement of this kind ever attempted ([2]).

The first Chapter describes the main motivation leading to this analysis. Many theoretical efforts have been spent in the last few years to understand the dynamics of these low energy processes ([3],[4]): popular phenomenogical models based on *factorization* have been able to make prediction of rates and to establish relations with Standard Model parameterization of *CP* violation in B physics, commonly given in the form of *angle* α and γ of the *Unitarity Triangle*. New and precise measurements of rates with high statistics are necessary to improve the results from CLEO experiment ([5]), to discriminate between theoretical models, and to yield a measurement of α and γ angles.

In the second Chapter a description of *BABAR* detector installed at the B-factory PEP-II is given. Special attention is devoted to the sub-detectors and the experimental tools relevant for this analysis (particle identification, tracking efficiency study, B-counting technique). Kaon identification at relatively high momenta is the key point to separate the three channels in $B^0 \to h'^+h^-$ decay topology and therefore a detailed study has been performed.

Since $B^0 \to h'^+h^-$ decays have a small $\mathcal{B}$ ($\approx 10^{-5}$) and given the two body decay topology, continuum $q\bar{q}$ production provides a huge background to those channels. A multivariate analysis technique (a *Fisher discriminant*) is used to combine information from the event decay topology. This is described in the third Chapter along with the preselection that leads to the final dataset. The final fit to extract signal yields is performed with a global likelihood technique that combines all the relevant information to separate the three signal channels from background. $\mathcal{B}$ are then extracted. In the fourth Chapter an extension of the $\mathcal{B}$ analysis is described to include flavor tagging and Δt information in the global fit. This allows a time-dependent CP asymmetry analysis of $B \to \pi^+\pi^-$ mode. In the fifth Chapter a comparison of the experimental results with the model prediction is performed.

Chapter 1

Charmless Twobody B decays into Pions and Kaons

1.1 Introduction

After more than 30 years from a first discovery of its violation in the K^0 system ([6]), *CP* symmetry is a still one of the open problems in particle physics. Standard Model with three quark generation predicts *CP* violation, but more experimental tests are needed to have a clear picture of the phenomenon. In this Chapter a brief introduction to *CP* violation in quantum field theory is given in Section 1.2. In Section 1.3 the common formalism to describe neutral B meson system is introduced. Mixing and time evolution of neutral B mesons are described, emphasizing the properties of a coherent $B^0\overline{B}^0$ state at the $\Upsilon(4S)$ resonance. *CP* violation can be produced in the B system through different mechanisms leading to measurements of *CP* violation *in decay* and *in the interference between decays with and without mixing* : in these cases time-integrated and time-dependent *CP* asymmetries are observable quantities accessible at a B-factory. In Section 1.4 the CKM picture of *CP* violation in Standard model is given: unitarity of the CKM matrix is translated in the now usual Unitarity triangle parameters. In Section 1.5 some of the several theoretical models developed in the last few years to understand the dynamics of charmless hadronic B decays are briefly introduced. Strong interactions make challenging the extraction of CKM parameters from experimental observables: it is therefore necessary to have good models able to parametrize the strong interaction contribution to *CP* violating observables to disentagle the weak interaction componentes we would like to finally measure.

1.2 *CP* violation

This Section introduces the basic concepts of the description of *CP* symmetry breaking in a context of a quantum field theory. The fundamental point is that *CP* symmetry is broken in any theory that has complex coupling constants in the Lagrangian which cannot be removed by any choice of phase redefinition of the fields in the theory.

Three discrete operations are potential symmetries of a field theory Lagrangian. Two of them, *parity* and *time reversal* are spacetime symmetries and constitute part of the Poincaré group. Parity, denoted by P, sends $(t, \mathbf{x}) \to (t, -\mathbf{x})$, reversing the handedness of space. Time reversal, denoted by T, sends $(t, \mathbf{x}) \to (-t, \mathbf{x})$, interchanging the forward and backward light-cones. A third (non-spacetime) discrete operation is *charge conjugation*, denoted by C. This operation interchanges particles and antiparticles. The combination CP replaces a particle by its antiparticle and reverses momentum and helicity. The combination CPT is an exact symmetry in any local Lagrangian field theory.

There is no experimental evidence that electromagnetic and strong interactions violate P, C or T symmetry . The weak interactions do violate C and P separately, but preserve CP and T to a good approximation. Rare processes, involving neutral K mesons, have been observed to exhibit CP violation ([6]). Very recently CP violation has been observed in the B physics sector too ([7],[8],[9],[10]). All observations to date are consistent with exact CPT symmetry.

To understand whether a given theory can accommodate CP violation, one needs to know the transformation properties of the fields under the various discrete symmetries. In particular for a Dirac spinor:

$$P\psi(t,\mathbf{x})P = \gamma^0\psi(t,-\mathbf{x}), \tag{1.1}$$

$$T\psi(t,\mathbf{x})T = -\gamma^1\gamma^3\psi(-t,\mathbf{x}), \tag{1.2}$$

$$C\psi(t,\mathbf{x})C = -i(\bar{\psi}(t,\mathbf{x})\gamma^0\gamma^2)^T. \tag{1.3}$$

Similarly, the CP transformation properties of scalar (H), pseudoscalar (A) and vector boson (W) fields, and also of the derivative operator are given by

$$\begin{array}{ccccc} \text{term} & H & A & W^{\pm\mu} & \partial_\mu \\ CP\text{−transformed term} & H & -A & -(-1)^\mu W^{\mp\mu} & (-1)^\mu\partial_\mu \end{array} \tag{1.4}$$
$$.$$

Taking into account the Lorentz invariance and hermiticity of the Lagrangian, the above CP transformation rules imply that each of the combinations of fields and derivatives that appear in the Lagrangian transforms under CP to its hermitian conjugate. However, there are coefficients in front of these expressions which represent either coupling constants or particle masses and which do not transform under CP. If any of these quantities are complex, then the coefficients in front of CP-related terms are complex conjugates of each other. In such a case, CP is not necessarily a good symmetry of the Lagrangian.

Note, however, that not all Lagrangian phases are physically meaningful quantities.

Consider for example a typical Yukawa-type term,

$$y_{ij} H \bar{\psi}_i \psi_j + \text{hermitian conjugate.} \tag{1.5}$$

The phase of y_{ij} can be changed by redefining the phase of any one of the three fields H, ψ_i, ψ_j that enter this term. In general such redefinitions will also change the phase of any other terms in the Lagrangian that involve these same fields, unless the complex conjugate field appears with the same power in the same term.

If any non-zero phases for couplings remain after all possible field redefinitions have been used to eliminate as many of them as possible, then there is *CP* violation.

However, there is, in general, convention-dependence as to where the complex phases appear. One can choose to make certain terms real and leave others complex, but a different choice, related to the first by field redefinitions, has the same physical consequences. Only those differences between pairs of phases that are unchanged by such redefinitions are physically meaningful.

In order to introduce how such phase differences manifest themselves as *CP*-violating effects, namely rate differences between pairs of *CP* conjugate processes, some conventions and notation for neutral B mesons need to be established.

1.3 $B^0\bar{B}^0$ system

This Section treats the quantum mechanics of the two state system of neutral B mesons, thus it is completely model independent([11]).

The systems of interest are neutral self-conjugate pairs of mesons. There are two such systems involving b quarks: B_d mesons, made of one b type quark or antiquark and one d type; and B_s mesons made of one b and one s. A description of this system can be given in terms of different neutral states. There are two flavor eigenstates, which have definite quark content and are most useful to understand particle production and particle decay processes; and there are eigenstates of the Hamiltonian, namely states of definite mass and lifetime, which propagate through space in a definite fashion. If *CP* were a good symmetry, the mass eigenstates would also be *CP* eigenstates. But since *CP* is not a good symmetry, the mass eigenstates can be different from *CP* eigenstates. In any case the mass eigenstates are not flavor eigenstates, and therefore the flavor eigenstates are mixed up as they propagate in space and time. The flavor eigenstates for B_d are $B^0 = \bar{b}d$

and $\bar{B}^0 = \bar{d}b$[1]. The following general discussion applies to both B systems, and a similar notation can be used also for K^0 or D^0 mesons.

An arbitrary linear combination of the neutral B-meson flavor eigenstates ,

$$a|B^0\rangle + b|\bar{B}^0\rangle, \tag{1.6}$$

is governed by a time-dependent Schrödinger equation

$$i\frac{d}{dt}\begin{pmatrix} a \\ b \end{pmatrix} = H\begin{pmatrix} a \\ b \end{pmatrix} \equiv (M - \frac{i}{2}\Gamma)\begin{pmatrix} a \\ b \end{pmatrix} \tag{1.7}$$

where M and Γ are 2×2 Hermitian matrices. CPT invariance guarantees $H_{11} = H_{22}$.

A perturbative expression for H_{ij} matrix elements ([12]) :

$$\begin{aligned} M_{ij} &= m_B\delta_{ij} + \langle i|H_W^{\Delta B=2}|j\rangle + \mathcal{P}\sum_n \frac{1}{m_B - E_n}\langle i|H_W^{\Delta B=1}|n\rangle\langle n|H_W^{\Delta B=1}|j\rangle \\ \Gamma_{ij} &= 2\pi\sum_n \delta(E_n - m_B)\langle i|H_W^{\Delta B=1}|n\rangle\langle n|H_W^{\Delta B=1}|i\rangle \end{aligned} \tag{1.8}$$

where $\mathcal{P}$ is the principal part, m_B the B^0 mass, and E_n the energy of the intermediate state $|n\rangle$.

Since virtual (off-shell) and real (on-shell) intermediate states contribute respectively to M and Γ, the off-diagonal terms in these matrices, M_{12} and Γ_{12} are the dispersive and absorptive parts respectively of the transition amplitude from B^0 to $\bar{B}^0$. They are therefore particularly important in discussing CP violation phenomenology.

The light B_L and heavy B_H mass eigenstates are given by

$$|B_L\rangle = p|B^0\rangle + q|\bar{B}^0\rangle, \tag{1.9}$$

$$|B_H\rangle = p|B^0\rangle - q|\bar{B}^0\rangle. \tag{1.10}$$

The complex coefficients p and q obey the normalization condition

$$|q|^2 + |p|^2 = 1. \tag{1.11}$$

Note that $\arg(q/p^*)$ is just an overall common phase for $|B_L\rangle$ and $|B_H\rangle$ and has no physical significance.

The mass difference Δm_d and width difference $\Delta\Gamma_B$ between the neutral B mesons are defined as follows:

$$\Delta m_d \equiv M_H - M_L, \quad \Delta\Gamma_B \equiv \Gamma_H - \Gamma_L, \tag{1.12}$$

---

[1] The convention is that B^0 is the isospin partner of B^+; therefore it contains the $\bar{b}$ quark. This is similar to the K mesons, where K^0, the isospin partner of K^+, contains the $\bar{s}$ quark.

so that Δm_d is positive by definition. Finding the eigenvalues of (1.7), one gets

$$(\Delta m_d)^2 - \frac{1}{4}(\Delta\Gamma_B)^2 = 4(|M_{12}|^2 - \frac{1}{4}|\Gamma_{12}|^2), \tag{1.13}$$

$$\Delta m_d \Delta\Gamma_B = 4\mathcal{R}e(M_{12}\Gamma_{12}^*). \tag{1.14}$$

The ratio q/p is given by

$$\frac{q}{p} = -\frac{\Delta m_d - \frac{i}{2}\Delta\Gamma_B}{2(M_{12} - \frac{i}{2}\Gamma_{12})} = -\frac{2(M_{12}^* - \frac{i}{2}\Gamma_{12}^*)}{\Delta m_d - \frac{i}{2}\Delta\Gamma_B}, \tag{1.15}$$

The states B^0 and $\bar{B}^0$ are related through *CP* transformation:

$$CP|B^0\rangle = e^{2i\xi_B}|\bar{B}^0\rangle, \quad CP|\bar{B}^0\rangle = e^{-2i\xi_B}|B^0\rangle. \tag{1.16}$$

The phase ξ_B is *arbitrary*. The freedom in defining it comes from the fact that flavor conservation (in particular b-flavor) is a symmetry of the strong interactions. This is true for any possible final state f and its *CP* conjugate $e^{2i\xi_f}\bar{f}$.

1.3.1 Time Evolution of Neutral B_d Mesons

The two neutral B_d mesons are expected to have a negligible difference in lifetime,

$$\Delta\Gamma_{B_d}/\Gamma_{B_d} = O(10^{-2}). \tag{1.17}$$

Note that $\Delta\Gamma_{B_d}$ has not yet been measured. The difference in width is produced by decay channels common to B^0 and $\bar{B}^0$. The branching ratios for such channels are of order 10^{-3} or less. As various channels contribute with opposite signs, one expects that their sum does not exceed the individual level, hence $\Delta\Gamma_{B_d} \ll \Gamma_{B_d}$ is a rather safe and model independent assumption [13]. On the other hand, Δm_d has been measured [14],

$$x_d \equiv \Delta m_d/\Gamma_{B_d} = 0.730 \pm 0.029. \tag{1.18}$$

From (1.17) and (1.18) one learns that, independently from the model,

$$\Delta\Gamma_B \ll \Delta m_d. \tag{1.19}$$

Equations (1.17) and (1.19) imply that, to $O(10^{-2})$ accuracy, Eqs. 1.13, 1.14 and 1.15 simplify into

$$\Delta m_d = 2|M_{12}|, \quad \Delta\Gamma_B = 2\mathcal{R}e(M_{12}\Gamma_{12}^*)/|M_{12}|, \tag{1.20}$$

$$q/p = -|M_{12}|/M_{12}. \tag{1.21}$$

Any B state can then be written as an admixture of the states B_H and B_L, whose amplitudes evolve in time

$$a_H(t) = a_H(0)e^{-iM_H t}e^{-\frac{1}{2}\Gamma_H t}, \quad a_L(t) = a_L(0)e^{-iM_L t}e^{-\frac{1}{2}\Gamma_L t}. \tag{1.22}$$

A state which is created at time $t = 0$ as initially pure B^0, denoted as $|B^0_{\rm phys}\rangle$, has $a_L(0) = a_H(0) = 1/(2p)$. Similarly an initially pure $\bar{B}^0$, $|\bar{B}^0_{\rm phys}\rangle$, has $a_L(0) = -a_H(0) = 1/(2q)$. The time evolution is thus given by

$$|B^0_{\rm phys}(t)\rangle = g_+(t)|B^0\rangle + (q/p)g_-(t)|\bar{B}^0\rangle, \tag{1.23}$$

$$|\bar{B}^0_{\rm phys}(t)\rangle = (p/q)g_-(t)|B^0\rangle + g_+(t)|\bar{B}^0\rangle, \tag{1.24}$$

where

$$g_+(t) = e^{-iMt}e^{-\Gamma t/2}\cos(\Delta m_d\ t/2), \tag{1.25}$$

$$g_-(t) = e^{-iMt}e^{-\Gamma t/2} i\sin(\Delta m_d\ t/2), \tag{1.26}$$

$M = \frac{1}{2}(M_H + M_L)$ and $\Gamma = \frac{1}{2}(\Gamma_H + \Gamma_L)$. We define *average lifetime* $\tau = \frac{1}{\Gamma}$

From Eq.1.26 it is straightforward to compute the probability that a B meson *produced as* a B^0 decays after a time t *as a* $\bar{B}^0$. The appearance of a $\bar{B}^0$ (B^0) from a B^0 ($\bar{B}^0$) pure initial state is commonly defined as $B^0\bar{B}^0$ *mixing* or *beauty oscillation* since the *beauty* content of an initial pure B^0 ($\bar{B}^0$) state evolves as

$$f = e^{-\Gamma t}(1 + cos(\Delta m_d t))$$

Δm_d is therefore the *mixing frequency* of the $B^0\bar{B}^0$ system.

At a B factory, that is an e^+e^- collider operating at the $\Upsilon(4S)$ resonance, the B^0 and $\bar{B}^0$ mesons are produced in the decay of the Υ. In this environment the simplest way to determine the *beauty* quantum number of the decaying B is to use leptons (l) as *tagging* particles (Section 4.2.1). By counting the number of "same-sign"(ss) events, (($l^+\,l^+$) or ($l^-\,l^-$)), and "opposite-sign" (os) events, ($l^+\,l^-$), a measurement of Δm_d can be extracted from a simultaneous fit of their decay time distribution.

In Fig.1.1 the quantity

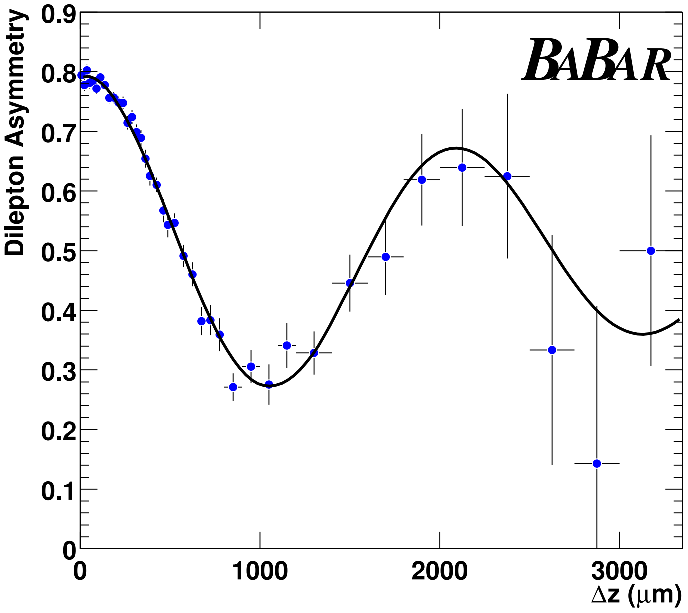

Figure 1.1: Year 2000 *BABAR* data: $A_{\text{mixing}}(t)$ with superimposed fit: the *beauty oscillation* pattern is clearly visible.

$$A_{\text{mixing}}(t) = \frac{N_{\text{os}}(t) - N_{\text{ss}}(t)}{N_{\text{os}}(t) + N_{\text{ss}}(t)} \tag{1.27}$$

is displayed for *BABAR* data, clearly showing the pattern of the oscillation.

At $\Upsilon(4S)$ B^0 and $\bar{B}^0$ mesons are in a *coherent* $L = 1$ state. The coherence can be illustrated in this way. Each of the two particles evolve in time as described above for a single B. Since they evolve in phase, at any time, until one particle decays, there is always exactly one B^0 and one $\bar{B}^0$ present. This is yet one more particle physics case of the classic Einstein-Podolsky-Rosen paradox. However, once one of the particles decays, the other continues to evolve, and thus there are possible events with two B or two $\bar{B}$ decays, whose probability is governed by the time between the two decays. The two particles from the Υ decay are identified by the angle θ that they make with the e^- beam direction in the Υ rest frame. Then the two-B state

$$\begin{aligned} S(t_f, t_b) \quad &= \tfrac{1}{\sqrt{2}}\{B^0_{\text{phys}}(t_f, \theta, \phi)\bar{B}^0_{\text{phys}}(t_b, \pi - \theta, \phi + \pi) \\ &-\bar{B}^0_{\text{phys}}(t_f, \theta, \phi)B^0_{\text{phys}}(t_b, \pi - \theta, \phi + \pi)\}\sin(\theta) \end{aligned} \tag{1.28}$$

can be written as

$$\begin{aligned} S(t_f,t_b) \ &= \tfrac{1}{\sqrt{2}} e^{-(\Gamma/2+iM)(t_f+t_b)}\{\cos[\Delta m_d(t_f-t_b)/2](B^0_f\bar{B}^0_b-\bar{B}^0_f B^0_b) \\ &\quad -i\sin[\Delta m_d(t_f-t_b)/2](\tfrac{p}{q}B^0_f B^0_b-\tfrac{q}{p}\bar{B}^0_f\bar{B}^0_b)\}\sin(\theta_f), \end{aligned} \tag{1.29}$$

where t_f is the proper time of the B_f, the B particle in the forward half-space at angle $(\theta_f<\pi/2,\phi_f)$ and t_b is the proper time for the backward-moving B_b, at $(\pi-\theta_f,\phi_f+\pi)$. Since the B's have equal, back-to-back momenta in this frame, until the time when one of these particles decays, $t_f=t_b$ and Eq.1.29 contains one B^0 and one $\bar{B}^0$. However decay stops the clock for the decayed particle, thus the terms that depend on $\sin[\Delta m_d(t_f-t_b)/2]$ begin to play a role.

From Eq.1.29 one can derive the amplitude for decays where one of the two B's decays to any state f_1 at time t_1 and the other decays to f_2 at time t_2. One obtains[2]

$$\begin{aligned} A(t_1,t_2) \ &= \tfrac{1}{\sqrt{2}} e^{-(\Gamma/2+iM)(t_1+t_2)}\zeta(t_1,t_2)\{\cos[\Delta m_d(t_1-t_2)/2](A_1\bar{A}_2-\bar{A}_1A_2) \\ &\quad -i\sin[\Delta m_d(t_1-t_2)/2](\tfrac{p}{q}A_1A_2-\tfrac{q}{p}\bar{A}_1\bar{A}_2)\}\sin(\theta_1), \end{aligned} \tag{1.30}$$

where A_i is the amplitude for a B^0 to decay to the state f_i, $\bar{A}_i$ is the amplitude for a $\bar{B}^0$ to decay to the *same* state f_i. Any state that identifies the flavor of the parent B (*tagging decay*) has either A_f or $\bar{A}_f=0$. We will use the term *flavor tagging* or simply *tagging* to indicate any algorithm able to identify those decays (Section 4.2.1). In Eq.1.30 to keep signs consistent with Eq.1.29

$$\zeta(t_1,t_2)=\begin{cases}+1 & t_1=t_f,\ t_2=t_b,\\ -1 & t_1=t_b,\ t_2=t_f\end{cases} \tag{1.31}$$

is introduced, but this overall sign factor will disappear in the rate.

It is now straightforward to calculate the time dependent rate for producing the combined final states f_1,f_2. One finds

$$\begin{aligned} R(t_1,t_2) \ &= Ce^{-\Gamma(t_1+t_2)}\{(|A_1|^2+|\bar{A}_1|^2)(|A_2|^2+|\bar{A}_2|^2)-4\mathcal{R}e(\tfrac{q}{p}A_1^*\bar{A}_1)\mathcal{R}e(\tfrac{q}{p}A_2^*\bar{A}_2) \\ &\qquad -\cos(\Delta m_d(t_1-t_2)) \\ &\qquad [(|A_1|^2-|\bar{A}_1|^2)(|A_2|^2-|\bar{A}_2|^2)+4\mathcal{I}m(\tfrac{q}{p}A_1^*\bar{A}_1)\mathcal{I}m(\tfrac{q}{p}A_2^*\bar{A}_2)] \\ &\qquad +2\sin(\Delta m_d(t_1-t_2)) \\ &\qquad [\mathcal{I}m(\tfrac{q}{p}A_1^*\bar{A}_1)(|A_2|^2-|\bar{A}_2|^2)-(|A_1|^2-|\bar{A}_1|^2)\mathcal{I}m(\tfrac{q}{p}A_2^*\bar{A}_2)]\}. \end{aligned} \tag{1.32}$$

---

[2] The fact that $\sin(2\pi-\theta)$ = -$\sin(\theta)$ is used to write Eq.1.30 with θ_1 running over angles $(0,\pi)$.

Here an integral over all directions for both B has been performed, so the angular dependence has been dropped from the expressions, and an overall normalization factor C has appeared. The approximation $|q/p| = 1$ has also been used.

To measure *CP* asymmetries one looks for events where one B decays to a final *CP* eigenstate f_{CP} at time t_f, while the second decays to a tagging mode at time $t_{\rm tag}$. For example, take a tagging mode with $A_2 = 0$, $\bar{A}_2 = \bar{A}_{\rm tag}$. This then identifies the *other* B-particle as a B^0 at time $t_2 = t_{\rm tag}$ at which the tag decay occurs. Note that this is true even when the tag decay occurs after the *CP* eigenstate decay. In this case the state of the other B at any time $t_f < t_{\rm tag}$ must be just that mixture that, if had it not decayed, would have evolved to become a B^0 at time $t_f = t_{\rm tag}$. The double time expression reduces to the form

$$\begin{aligned} R(t_{\rm tag}, t_{f_{CP}}) \quad &= Ce^{-\Gamma(t_{\rm tag}+t_{f_{CP}})}|\bar{A}_{\rm tag}|^2|A_{f_{CP}}|^2 \\ &\{1 + |\lambda_{f_{CP}}|^2 + \cos[\Delta m_d(t_{f_{CP}} - t_{\rm tag})](1 - |\lambda_{f_{CP}}|^2) \\ &-2\sin[\Delta m_d(t_{f_{CP}} - t_{\rm tag})]\mathcal{I}m(\lambda_{f_{CP}})\} \end{aligned} \tag{1.33}$$

where

$$\lambda_{f_{CP}} \equiv \frac{q}{p}\frac{\bar{A}_{f_{CP}}}{A_{f_{CP}}} = \eta_{f_{CP}}\frac{q}{p}\frac{\bar{A}_{\bar{f}_{CP}}}{A_{f_{CP}}}. \tag{1.34}$$

The second form for $\lambda_{f_{CP}}$ here uses the property

$$\bar{A}_{f_{CP}} = \eta_{f_{CP}}\bar{A}_{\bar{f}_{CP}}, \tag{1.35}$$

where $\eta_{f_{CP}}$ is the *CP* eigenvalue of the state f_{CP}. The amplitudes $A_{f_{CP}}$ and $\bar{A}_{\bar{f}_{CP}}$ are related by *CP* and differ only in the signs of the weak phases, while $\eta_{f_{CP}} = \pm 1$, so the second form is useful in calculating the expected asymmetries.

For the case where the tag final state has $\bar{A}_2 = 0$, $A_2 = A_{\rm tag}$, which identifies the second particle as a $\bar{B}$ at time $t_{\rm tag}$, an expression similar to Eq.1.33 applies, except that the signs of both the cosine and the sine terms are reversed. Thus the difference of the rates divided by their sum, which measures the time-dependent *CP* asymmetry, is given by

$$a_{f_{CP}}(\Delta t) = \frac{(1 - |\lambda_{f_{CP}}|^2)\cos(\Delta m_d \Delta t) - 2\mathcal{I}m\lambda_{f_{CP}}\sin(\Delta m_d \Delta t)}{1 + |\lambda_{f_{CP}}|^2}, \tag{1.36}$$

where

$$\Delta t = t_{f_{CP}} - t_{\rm tag}. \tag{1.37}$$

It is useful to note that the above expressions can be integrated over the variable (t_1+t_2), which for $t_1 \geq 0$ and $t_2 \geq 0$ can take values between $|t_1 - t_2|$ and infinity. Thus one can fit the dependence on the variable $t_1 - t_2$ without having to measure the Υ decay time. The fact that the variable $t_1 - t_2$ can be related to the distance between the locations of the two decays is of course the prime reason for building an energy-asymmetric collider for a B factory. If one had to integrate over this variable as well, all information on the coefficient of $\sin(\Delta m_d(t_1-t_2))$ would be lost in the above expressions, and the experiment would be sensitive only to those *CP*-violating effects that give[3] $|\lambda_{f_{CP}}| \neq 1$. From Eq.1.36 the decay rate distribution f_+ (f_-) for $B \to f_{CP}$ when B_{tag} is a B^0 ($\overline{B}^0$) is given by

$$f_{\pm}(\Delta t) = \frac{e^{-|\Delta t|/\tau}}{4\tau}\left[1 \pm S_{f_{CP}} \sin(\Delta m_d \Delta t) \mp C_{f_{CP}} \cos(\Delta m_d \Delta t)\right], \tag{1.38}$$

where

$$S_{f_{CP}} = \frac{2\mathcal{I}m\lambda_{f_{CP}}}{1+|\lambda_{f_{CP}}|^2} \text{ and } C_{f_{CP}} = \frac{1-|\lambda_{f_{CP}}|^2}{1+|\lambda_{f_{CP}}|^2}. \tag{1.39}$$

Those are the basic distributions which enter the fit to data, in particular $C_{f_{CP}}$ and $S_{f_{CP}}$ are the parameters we want to extract from the experiment.

1.3.2 Types of *CP* violation in *B* Decays

The type of *CP* violation introduced at the end of the previous Section is usually called *CP violation in the interference between decays with and without mixing*; sometimes this is abbreviated as "interference between mixing and decay". It's common use to refer to the observable *CP* asymmetries generated in this case as *time-dependent CP asymmetries* . Experimentally, for the neutral B system, *CP* violation in the interference between decays with and without mixing can be observed by comparing decays into final *CP* eigenstates of a time-evolving neutral B state that begins at time zero as B^0 to those of the state that begins as a $\bar{B}^0$:

$$a_{f_{CP}}(\Delta t) = \frac{\Gamma(B^0_{\mathrm{phys}}(\Delta t) \to f_{CP}) - \Gamma(\bar{B}^0_{\mathrm{phys}}(\Delta t) \to f_{CP})}{\Gamma(B^0_{\mathrm{phys}}(\Delta t) \to f_{CP}) + \Gamma(\bar{B}^0_{\mathrm{phys}}(\Delta t) \to f_{CP})}. \tag{1.40}$$

The observable quantity defined in Eq.1.40 is the experimental counterpart of Eq.1.36: in this way this type of *CP* violation can be related to Langrangian parameter through

---

[3] Note that this is a consequence of the coherent production of the two B states, in a hadronic environment, where the B's are produced incoherently, time-integrated rates are always integrals from $t = 0$ to infinity and hence retain information about the $\sin(\Delta m_d t)$ behavior.

$C_{f_{CP}}$ and $S_{f_{CP}}$. However the relation linking $C_{f_{CP}}$ and $S_{f_{CP}}$ to the fundamental theory parameters is, in general, not trivial and can require other measurements or the assumption of some phenomenological model as we will see in Section 1.5.

Another possible manifestation of *CP* violation is usually known as *CP* violation *in decay*, which can occour not only in neutral B meson decays but in charged B meson decays too. It happens when the amplitude (A_f) for a decay and its *CP* conjugate process amplitude ($\bar{A}_{\bar{f}}$) have different magnitudes. This is due to the presence of two types of non-trivial phases in A_f and $\bar{A}_{\bar{f}}$, usually referred to in literature as "weak" and "strong" phases.

Complex parameters in any Lagrangian term that contributes to the amplitude will appear in complex conjugate form in the *CP* conjugate amplitude. Thus their phases appear in A_f and $\bar{A}_{\bar{f}}$ with opposite signs. In the Standard Model these phases occur only in the CKM matrix which is part of the electroweak sector of the theory, hence these are often called "weak phases". As usual only the difference between the weak phases in two different terms in A_f is convention independent.

A second type of phase can appear in scattering or decay amplitudes even when the Lagrangian is real. Such phases do not violate *CP*, therefore they appear in A_f and $\bar{A}_{\bar{f}}$ with the same sign. Their origin is the possible contribution from intermediate on-shell states to the decay process, that is an absorptive part of an amplitude that has contributions from coupled channels. Usually the dominant rescattering is due to strong interactions, hence the designation "strong phases" for the phase shifts so induced. Again only the relative strong phases of different terms in a scattering amplitude have physical meaning.

Thus it is useful to write each contribution to A in three parts: its magnitude A_i; its weak phase term $e^{i\phi_i}$; and its strong phase term $e^{i\delta_i}$. Then, if several amplitudes contribute to $B^0 \to f$, the amplitude A_f and the *CP* conjugate amplitude $\bar{A}_{\bar{f}}$ are given by:

$$A_f = \sum_i A_i e^{i(\delta_i+\phi_i)}, \quad \bar{A}_{\bar{f}} = e^{2i(\xi_f-\xi_B)} \sum_i A_i e^{i(\delta_i-\phi_i)}, \tag{1.41}$$

where ξ_f and ξ_B are defined in Section 1.2 (If f is a CP eigenstate then $e^{2i\xi_f} = \pm 1$ is its CP eigenvalue.) The convention-independent quantity is then

$$\left|\frac{\bar{A}_{\bar{f}}}{A_f}\right| = \left|\frac{\sum_i A_i e^{i(\delta_i-\phi_i)}}{\sum_i A_i e^{i(\delta_i+\phi_i)}}\right|. \tag{1.42}$$

When *CP* is conserved, the weak phases ϕ_i are all equal. Therefore, from Eq.1.42 one sees that

$$|\bar{A}_{\bar{f}}/A_f| \neq 1 \quad \Longrightarrow \quad CP \text{ violation.} \tag{1.43}$$

This type of *CP* violation is here called *CP violation in decay.* It is often also called *direct CP violation.* It results from the *CP*-violating interference among various terms in the decay amplitude. From Eq.1.42 it can be seen that a *CP* violation of this type will not occur unless at least two terms that have different weak phases acquire different strong phases, since:

$$|A|^2 - |\bar{A}|^2 = -2\sum_{i,j} A_i A_j \sin(\phi_i - \phi_j)\sin(\delta_i - \delta_j). \tag{1.44}$$

Any *CP* asymmetries in charged B decays,

$$\mathcal{A}_f = \frac{\Gamma(B^+ \to f) - \Gamma(B^- \to \bar{f})}{\Gamma(B^+ \to f) + \Gamma(B^- \to \bar{f})}, \tag{1.45}$$

are due to *CP* violation in decay.

More generally Eq.1.45 defines *CP* violation in decay for neutral meson too, when the decay is *self-tagging* . This happens when a B^0 can only decay to the final state f and $\overline{B}^0$ to the final state $\bar{f}$: an example is $B^0 \to K^+\pi^-$ decay where the $B^0 \to K^-\pi^+$ is strongly suppressed. We usually refer to this kind of measurement as *time-independent CP asymmetry* or *charge asymmetry.*

In terms of the decay amplitudes we can express

$$\mathcal{A}_f = \frac{1 - |\bar{A}/A|^2}{1 + |\bar{A}/A|^2}. \tag{1.46}$$

Comparing this equation to definition in Eq.1.39, it's clear why a non-null $C_{f_{CP}}$ is a sign of direct *CP* violation too.

The magnitude and strong phase of any amplitude involve long distance strong interaction physics, and cannot be calculated from first principles. In many cases one can only relate experiment to Standard Model parameters through model dependent calculations (Section 1.5). Nevertheless in B physics it is commonly believed that in many channels direct *CP* asymmetry can show up.

Another quantity that is independent of phase conventions and physically meaningful is

$$\left|\frac{q}{p}\right|^2 = \left|\frac{M_{12}^* - \frac{i}{2}\Gamma_{12}^*}{M_{12} - \frac{i}{2}\Gamma_{12}}\right|. \tag{1.47}$$

When *CP* is conserved, the mass eigenstates must be *CP* eigenstates. In that case the relative phase between M_{12} and Γ_{12} vanishes. Therefore, Eq.1.47 implies

$$|q/p| \neq 1 \quad \Longrightarrow \quad CP \text{ violation.} \tag{1.48}$$

This type of *CP* violation is here called *CP violation in mixing*; it is often referred to as *indirect CP violation*. It results from the mass eigenstates being different from the *CP* eigenstates. So far *CP* violation in mixing has been observed unambiguously in the neutral kaon system only.

For the neutral B system, this effect could be observed through the asymmetries in semileptonic decays:

$$a_{\text{sl}} = \frac{\Gamma(\bar{B}^0_{\text{phys}}(t) \to \ell^+\nu X) - \Gamma(B^0_{\text{phys}}(t) \to \ell^-\nu X)}{\Gamma(\bar{B}^0_{\text{phys}}(t) \to \ell^+\nu X) + \Gamma(B^0_{\text{phys}}(t) \to \ell^-\nu X)}. \tag{1.49}$$

In terms of $|q/p|$,

$$a_{\text{sl}} = \frac{1 - |q/p|^4}{1 + |q/p|^4}, \tag{1.50}$$

which follows from

$$\langle \ell^-\nu X|H|B^0_{\text{phys}}(t)\rangle = (q/p)g_-(t)A^*, \quad \langle \ell^+\nu X|H|\bar{B}^0_{\text{phys}}(t)\rangle = (p/q)g_-(t)A. \tag{1.51}$$

Effects of *CP* violation in mixing in neutral B_d decays are expected to be small, $O(10^{-2})$ and generally hard to be related to CKM parameters.

1.4 *CP* violation in the Standard Model

We now move to describe the Standard Model's picture of *CP* violation through the CKM mechanism. At the end of this Section some Standard Model phenomenological parameters relevant to B physics (Unitarity Triangle angles, α,β, and γ) will be introduced. The main challenge of this analysis is to connect the phenomenological parameters introduced in the previous Section ($C_{f_{CP}}$,$S_{f_{CP}}$,and $\mathcal{A}_f$) to the CKM parameters in the specific context of charmless hadronic B decays.

1.4.1 The CKM Picture of *CP* Violation

In the Standard Model (SM) [15] of $SU(3)_C \times SU(2)_L \times U(1)_Y$ gauge symmetry with three fermion generations, *CP* violation arises from a single phase in the mixing matrix for quarks [17]. Each quark generation consists of three multiplets:

$$Q_L^I = \begin{pmatrix} U_L^I \\ D_L^I \end{pmatrix} = (3,2)_{+1/6}, \quad u_R^I = (3,1)_{+2/3}, \quad d_R^I = (3,1)_{-1/3}, \tag{1.52}$$

where $(3,2)_{+1/6}$ denotes a triplet of $SU(3)_C$, doublet of $SU(2)_L$ with hypercharge $Y = Q - T_3 = +1/6$, and similarly for the other representations. The interactions of quarks with the $SU(2)_L$ gauge bosons are given by

$$\mathcal{L}_W = -\frac{1}{2} g \overline{Q_{Li}^I} \gamma^\mu \tau^a \mathbf{1}_{ij} Q_{Lj}^I W_\mu^a, \tag{1.53}$$

where γ^μ operates in Lorentz space, τ^a operates in $SU(2)_L$ space and $\mathbf{1}$ is the unit matrix operating in generation space. The interactions of quarks with the single Higgs scalar doublet $\phi(1,2)_{+1/2}$ of the Standard Model are given by

$$\mathcal{L}_Y = -G_{ij} \overline{Q_{Li}^I} \phi d_{Rj}^I - F_{ij} \overline{Q_{Li}^I} \tilde{\phi} u_{Rj}^I + \text{hermitian conjugate}, \tag{1.54}$$

where G and F are general *complex* 3×3 matrices. Their complex nature is the source of CP violation in the Standard Model. With the spontaneous symmetry breaking, $SU(2)_L \times U(1)_Y \to U(1)_{\text{EM}}$ due to a non null Higgs field expectation value ($\langle \phi \rangle \neq 0$), the two components of the quark doublet become distinguishable, as are the three members of the W^μ triplet. The charged current interaction in (1.53) is given by

$$\mathcal{L}_W = -\sqrt{\frac{1}{2}} g \overline{u_{Li}^I} \gamma^\mu \mathbf{1}_{ij} d_{Lj}^I W_\mu^+ + \text{h.c.}. \tag{1.55}$$

The mass terms that arise from the replacement $\mathcal{R}e(\phi^0) \to \sqrt{\frac{1}{2}}(v + H^0)$ in (1.54) are given by

$$\mathcal{L}_M = -\sqrt{\frac{1}{2}} v G_{ij} \overline{d_{Li}^I} d_{Rj}^I - \sqrt{\frac{1}{2}} v F_{ij} \overline{u_{Li}^I} u_{Rj}^I + \text{hermitian conjugate}, \tag{1.56}$$

namely

$$M_d = Gv/\sqrt{2}, \qquad M_u = Fv/\sqrt{2}. \tag{1.57}$$

The phase information is now contained in these mass matrices. To transform to the mass eigenbasis, one defines four unitary matrices such that

$$V_{dL} M_d V_{dR}^\dagger = M_d^{\text{diag}}, \qquad V_{uL} M_u V_{uR}^\dagger = M_u^{\text{diag}}, \tag{1.58}$$

where M_q^{diag} are diagonal and real, while V_{qL} and V_{qR} are complex. The charged current interactions (1.55) are given in the mass eigenbasis by

$$\mathcal{L}_W = -\sqrt{\frac{1}{2}} g \overline{u_{Li}} \gamma^\mu \bar{V}_{ij} d_{Lj} W_\mu^+ + \text{h.c.}. \tag{1.59}$$

(Quark fields with no superscript denote mass eigenbasis.) The matrix $\bar{V} = V_{uL}V_{dL}^{\dagger}$ is the (unitary) mixing matrix for three quark generations. As such, it generally depends on nine parameters: three can be chosen as real angles (like the Cabibbo angle) and six are phases. However, one may reduce the number of phases in $\bar{V}$ by a transformation

$$\bar{V} \quad \Longrightarrow \quad V = P_u \bar{V} P_d^*, \tag{1.60}$$

where P_u and P_d are diagonal phase matrices. This is a legitimate transformation because it amounts to redefining the phases of the quark-mass-eigenstate fields:

$$q_{Li} \to (P_q)_{ii} q_{Li}, \quad q_{Ri} \to (P_q)_{ii} q_{Ri}, \tag{1.61}$$

which does not change the real diagonal mass matrix M_q^{diag}. The five phase differences among the elements of P_u and P_d can be chosen so that the transformation (1.60) eliminates five of the six independent phases from $\bar{V}$; thus V has one irremovable phase. This phase is called the Kobayashi-Maskawa phase [17], δ_{KM}, and the mixing matrix is called the *Cabibbo-Kobayashi-Maskawa* (CKM) matrix [16]. It is interesting to note that the same procedure applied to a two-generation Standard Model Lagrangian with a single Higgs field would remove all *CP*-violating phases—that theory could not accommodate *CP* violation without the addition of extra fields.

The irremovable phase in the CKM matrix allows *CP* violation. To see this, let's recall the *CP* transformation laws (1.4),

$$\bar{\psi}_i \psi_j \to \bar{\psi}_j \psi_i, \quad \bar{\psi}_i \gamma^\mu W_\mu (1-\gamma_5) \psi_j \to \bar{\psi}_j \gamma^\mu W_\mu (1-\gamma_5) \psi_i. \tag{1.62}$$

Thus the mass terms and gauge interactions are obviously *CP*-invariant if all the masses and couplings are real. In particular, consider the coupling of $W^\pm$ to quarks. It has the form

$$g V_{ij} \bar{u}_i \gamma_\mu W^{+\mu} (1-\gamma_5) d_j + g V_{ij}^* \bar{d}_j \gamma_\mu W^{-\mu} (1-\gamma_5) u_i. \tag{1.63}$$

The *CP* operation interchanges the two terms except that V_{ij} and V_{ij}^* are not interchanged. Therefore, *CP* is a good symmetry only if there is a mass basis and choice of phase convention where all couplings and masses are real.

The fact that the three generation Standard Model with a single Higgs multiplet contains only a single independent *CP*-violating phase makes the possible *CP*-violating effects in this theory all very closely related. This makes the pattern of *CP* violations in B decays strongly constrained in this model. The goal of the B factory is to test whether this pattern occurs.

1.4.2 The Unitarity Triangle

The unitarity of the CKM matrix is manifest using an explicit parameterization. There are various useful ways to parameterize it, but the standard choice is the following:

$$V = \begin{pmatrix} c_{12}c_{13} & s_{12}c_{13} & s_{13}e^{-i\delta} \\ -s_{12}c_{23} - c_{12}s_{23}s_{13}e^{i\delta} & c_{12}c_{23} - s_{12}s_{23}s_{13}e^{i\delta} & s_{23}c_{13} \\ s_{12}s_{23} - c_{12}c_{23}s_{13}e^{i\delta} & -c_{12}s_{23} - s_{12}c_{23}s_{13}e^{i\delta} & c_{23}c_{13} \end{pmatrix}, \tag{1.64}$$

where $c_{ij} \equiv \cos\theta_{ij}$ and $s_{ij} \equiv \sin\theta_{ij}$.

The unitarity of the CKM matrix implies various relations among its elements. Three of them are very useful for understanding the Standard Model predictions for *CP* violation:

$$V_{ud}V_{us}^* + V_{cd}V_{cs}^* + V_{td}V_{ts}^* = 0, \tag{1.65}$$

$$V_{us}V_{ub}^* + V_{cs}V_{cb}^* + V_{ts}V_{tb}^* = 0, \tag{1.66}$$

$$V_{ud}V_{ub}^* + V_{cd}V_{cb}^* + V_{td}V_{tb}^* = 0. \tag{1.67}$$

Each of these three relations requires the sum of three complex quantities to vanish and so can be geometrically represented in the complex plane as a triangle. These are "the unitarity triangles"; note that the term *Unitarity Triangle* is usually reserved for the relation (1.67) only.

The rescaled Unitarity Triangle (Fig. 1.2) is derived from (1.67) by (a) choosing a phase convention such that $(V_{cd}V_{cb}^*)$ is real, and (b) dividing the lengths of all sides by $|V_{cd}V_{cb}^*|$. The shape of the triangle is unchanged. Two vertices of the rescaled Unitarity Triangle are thus fixed at (0,0) and (1,0). The coordinates of the remaining vertex are denoted by (ρ, η). It is customary these days to express the CKM matrix in terms of four Wolfenstein parameters (λ, A, ρ, η) with $\lambda = |V_{us}| = 0.22$ playing the role of an expansion parameter and η representing the *CP*-violating phase [18]:

$$V = \begin{pmatrix} 1-\frac{\lambda^2}{2} & \lambda & A\lambda^3(\rho - i\eta) \\ -\lambda & 1-\frac{\lambda^2}{2} & A\lambda^2 \\ A\lambda^3(1-\rho-i\eta) & -A\lambda^2 & 1 \end{pmatrix} + O(\lambda^4). \tag{1.68}$$

λ is small, and for each element in V, the expansion parameter is actually λ^2. Hence it is sufficient to keep only the first few terms in this expansion. The relation between the parameters of (1.64) and (1.68) is given by

$$s_{12} \equiv \lambda, \quad s_{23} \equiv A\lambda^2, \quad s_{13}e^{-i\delta} \equiv A\lambda^3(\rho - i\eta). \tag{1.69}$$

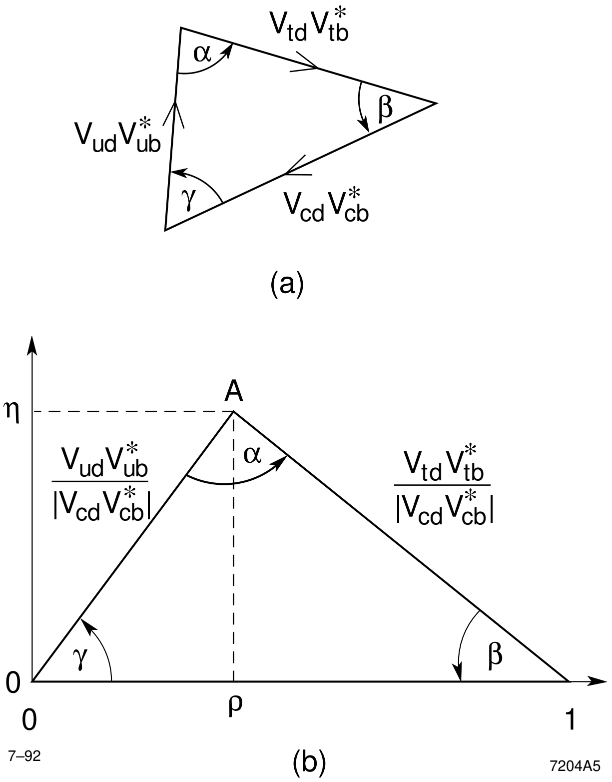

Figure 1.2: The Unitarity Triangle (a), rescaled (b) with all sides divided by $|V_{cb}^{*}V_{cd}|$

This specifies the higher order terms in (1.68). The definition of (λ, A, ρ, η) given in (1.69) allows an elegant improvement of the accuracy of the original Wolfenstein parameterization. In particular, defining

$$V_{us} = \lambda, \quad V_{cb} = A\lambda^2, \quad V_{ub} = A\lambda^3(\rho - i\eta), \tag{1.70}$$

one can then write

$$V_{td} = A\lambda^3(1 - \bar{\rho} - i\bar{\eta}), \tag{1.71}$$

$$\mathcal{I}m V_{cd} = -A^2\lambda^5\eta, \quad \mathcal{I}m V_{ts} = -A\lambda^4\eta, \tag{1.72}$$

where

$$\bar{\rho} = \rho(1 - \lambda^2/2), \quad \bar{\eta} = \eta(1 - \lambda^2/2), \tag{1.73}$$

turns out to be excellent approximations to the exact expressions [19]. Depicting the rescaled Unitarity Triangle in the $(\bar{\rho}, \bar{\eta})$ plane, the lengths of the two complex sides are

$$R_b \equiv \sqrt{\bar{\rho}^2 + \bar{\eta}^2} = \frac{1 - \lambda^2/2}{\lambda}\left|\frac{V_{ub}}{V_{cb}}\right|, \quad R_t \equiv \sqrt{(1 - \bar{\rho})^2 + \bar{\eta}^2} = \frac{1}{\lambda}\left|\frac{V_{td}}{V_{cb}}\right|. \tag{1.74}$$

The three angles of the Unitarity Triangle are denoted by α, β and γ:

$$\alpha \equiv \arg\left[-\frac{V_{td}V_{tb}^*}{V_{ud}V_{ub}^*}\right], \quad \beta \equiv \arg\left[-\frac{V_{cd}V_{cb}^*}{V_{td}V_{tb}^*}\right], \tag{1.75}$$

The third angle is then

$$\gamma \equiv \arg\left[-\frac{V_{ud}V_{ub}^*}{V_{cd}V_{cb}^*}\right] \equiv \pi - \alpha - \beta. \tag{1.76}$$

These are physical quantities and, as discussed below, can be extracted by *CP* asymmetries in various B decays. The consistency of the various measurements provides independent tests of the Standard Model.

The angle β gives, to a good approximation, the Standard Model phase between the neutral B mixing amplitude and its leading decay amplitudes.

It is straightforward to express the angles of the triangle in terms of $\bar\rho$ and $\bar\eta$. For example, the following two relations are useful:

$$\sin 2\alpha = \frac{2\bar\eta[\bar\eta^2 + \bar\rho(\bar\rho - 1)]}{[\bar\eta^2 + (1-\bar\rho)^2][\bar\eta^2 + \bar\rho^2]}, \quad \sin 2\beta = \frac{2\bar\eta(1-\bar\rho)}{\bar\eta^2 + (1-\bar\rho)^2}. \tag{1.77}$$

If this Unitarity Triangle Standard Model picture holds, it is possible to constrain $(\bar\rho, \bar\eta)$ and therefore α, β, and γ from several, *indirect* measurements which depend on the value of $\bar\rho$ e $\bar\eta$ [20].

- the ratio $\frac{|V_{ub}|}{|V_{cb}|}$ can be represented by a circle centered at (0,0) in the complex plane $(\bar\rho, \bar\eta)$.

$$\left|\frac{V_{ub}}{V_{cb}}\right| = \frac{\lambda}{1 - \frac{\lambda^2}{2}} \sqrt{\overline{\rho}^2 + \overline{\eta}^2}\,. \tag{1.78}$$

- Δm_d can be represented by a circle centered at (1,0)

$$\Delta m_d = \frac{G_F^2}{6\pi^2} m_W^2\ \eta_c S(x_t)\ A^2\lambda^6\ [(1-\overline{\rho})^2 + \overline{\eta}^2]\ m_{B_d}\ f_{B_d}^2 \hat{B}_{B_d}\ , \tag{1.79}$$

  where $S(x_t)$ is the Inami-Lim function [21] and $x_t = m_t^2/M_W^2$ (with m_t being the t quark mass in the regularization scheme $\overline{MS}$, $m_t^{\overline{MS}}(m_t^{\overline{MS}})$, and m_W the W boson mass). η_c is the short distance correction now calculated at *next-to-leading* order in perturbative QCD. $f_{B_d}^2 \hat{B}_{B_d}$ is a factor hiding all the non-perturbative effects that contribute to Δm_d. It can be provided by lattice QCD methods.

- Δm_s (mixing frequency for B_s mesons) is again a circle. When compared to Δm_d the following relation holds:

$$\frac{\Delta m_d}{\Delta m_s} = \frac{m_{B_d} f_{B_d}^2 \hat{B}_{B_d}}{m_{B_s} f_{B_s}^2 \hat{B}_{B_s}} \left(\frac{\lambda}{1 - \frac{\lambda^2}{2}}\right)^2 [(1-\overline{\rho})^2 + \overline{\eta}^2]\,. \tag{1.80}$$

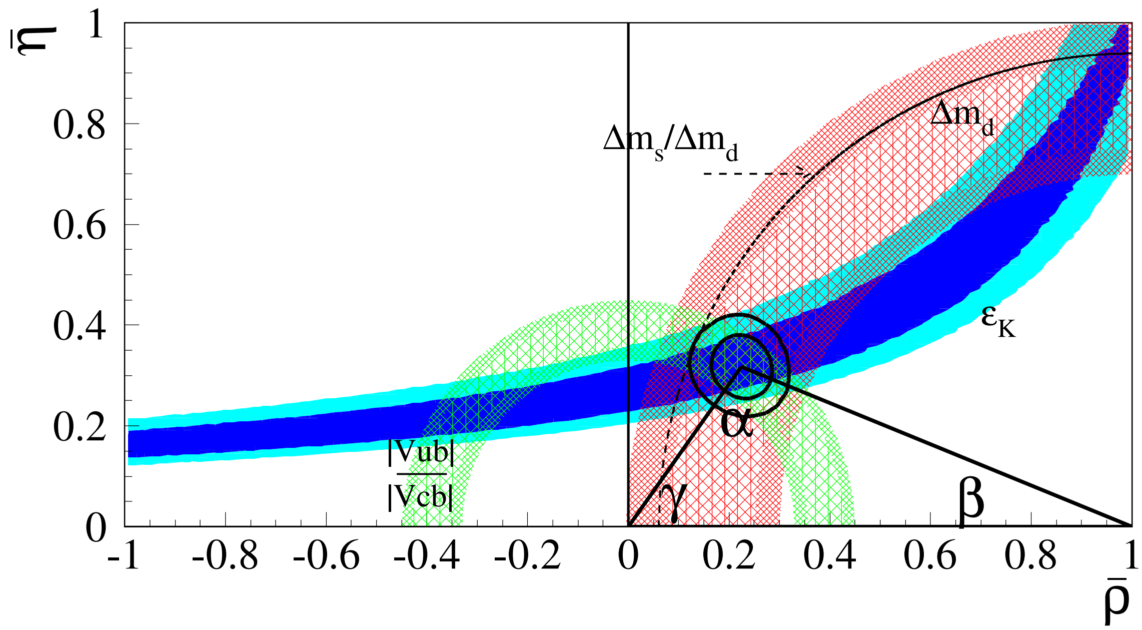

Figure 1.3: Limits on $(\bar{\rho}, \overline{\eta})$ from indirect measurements. Every band represents the total uncertainty on the relative quantity.

- ϵ_K, phenomenological parameter describing "indirect" *CP* violation in the $K^0\bar{K}^0$ system. It constrains $\overline{\rho}$ and $\overline{\eta}$ via the following relation

$$|\varepsilon_K| \; = C_\varepsilon \; A^2\lambda^6 \; \overline{\eta} \left[-\eta_1 S(x_c) + \eta_2 S(x_t) \left(A^2\lambda^4 \left(1-\overline{\rho}\right)\right) + \eta_3 S(x_c, x_t)\right] \; \hat{B}_K \; , \quad (1.81)$$

where

$$C_\varepsilon = \frac{G_F^2 f_K^2 m_K m_W^2}{6\sqrt{2}\pi^2 \Delta m_K} \; . \quad (1.82)$$

$S(x_i)$ and $S(x_i, x_j)$ again are the Inami-Lim functions [21], being $x_q = m_q^2/m_W^2$ and including NLO correction [22, 23, 24].f_K is the kaon decay constant and Δm_K the neutral kaon system mixing frequency.

Those four curves should cross in one single point in order to determine $\bar{\rho}$–$\bar{\eta}$. Experimental and theoretical uncertainties have to be folded in to find a region of allowed values with some given confidence level. Different analyses are found in literature ([20],[25],[26]). They usually differ in the way of treatment of the uncertainties on the theoretical parameters. In Fig. 1.3 the various quantities are represented as bands to show the total uncertainty on them. Following the *bayesian* approach proposed in [20], the values shown in Tab.1.1 are obtained for $\overline{\rho}$, $\overline{\eta}$, $\sin(2\beta)$, $\sin(2\alpha)$,and γ.

Parameter	value
$\overline{\rho}$	0.224 ± 0.038
$\overline{\eta}$	0.317 ± 0.040
$\sin(2\beta)$	0.698 ± 0.066
$\sin(2\alpha)$	-0.42 ± 0.23
γ	$(54.8 \pm 6.2)^\circ$

Table 1.1: Results from the Unitarity Triangle analysis in [20]

.

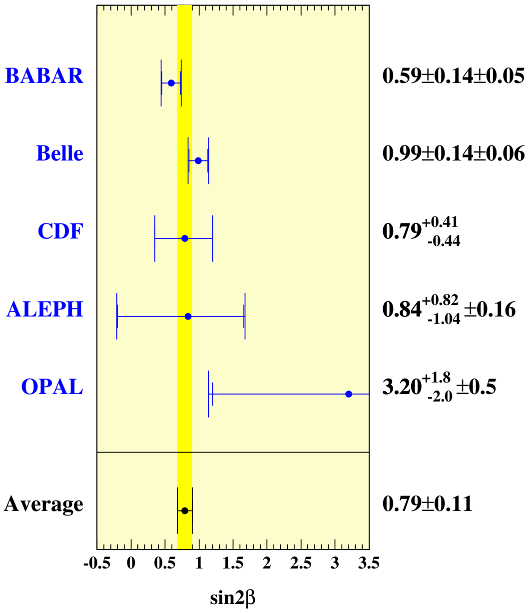

Figure 1.4: $\sin2\beta$ experimental values

It is possible to compare the value of $\sin(2\beta)$ found in this Unitarity Triangle analysis, with the results recently published by *BABAR* and *Belle* collaboration ([9],[10]) and with the older *LEP* and *CDF* collaboration results. Experimental values and world average are given in Fig.1.4. Agreement between the Unitarity Triangle analysis prediction and the newest, more accurate, experimental measurements is already impressive, with no indication of new physics beyond the Standard Model yet.

1.5 Phenomenological models

Standard Model Lagrangian describes fundamental interactions in terms of quarks, which, unfortunately, are bound by strong dynamics into color neutral hadrons. Those bound states are non-pertubative in nature and this makes problematic the extraction of precise information about physics at higher energies. To explore new physics effects the main theoretical challenge is therefore to untangle higher energy weak interaction effects from those low energy nonperturbative QCD process. *Effective field theories* provide the common theoretical formalism. The basic idea of effective theory is that in a given process, only certain degrees of freedom may be important for understanding the physics of that process. In particular, it is often the case that kinematical considerations which restrict the momenta of external particles, effectively restrict the momenta of virtual particles as well. Thus it is sensible to remove from the theory intermediate states of high virtuality. Their absence may be compensated by introducing new "effective" interactions between the degrees of freedom which remain. Effective field theories are often constructed using the technique of the operator product expansion (**OPE**), which provides an elegant and general conceptual framework.

As an example, let's consider the weak decay of a b quark, $b \to c\overline{u}d$, which is mediated by the decay of a virtual W boson. In the *fundamental theory* we start from (in this case the Standard Model), the decay amplitude involves an explicit W propagator and is proportional to

$$\overline{c}\gamma^{\mu}(1-\gamma^5)b\,\overline{d}\gamma_{\mu}(1-\gamma^5)u \times \frac{(ig_W)^2/4}{p^2 - M_W^2}\,, \tag{1.83}$$

where g_W is the Standard Model weak interaction coupling constant and p^{μ} is the momentum of the virtual W. Since $m_b \ll M_W$, the kinematics constrains $p^2 \ll M_W^2$, so the virtuality of the W is of order M_W. In this low momentum limit, the process $b \to c\overline{u}d$ appears to be a local interaction, with four fermions interacting via a potential which is a δ function where the four particles coincide, generating the four-fermion Fermi interaction lagrangian.

This can be seen by making a Taylor expansion of the amplitude in powers of p^2/M_W^2,

$$\overline{c}\gamma^{\mu}(1-\gamma^5)b\,\overline{d}\gamma_{\mu}(1-\gamma^5)u \times \frac{g_W^2}{8M_W^2}\left[1 + \frac{p^2}{M_W^2} + \frac{p^4}{M_W^4} + \ldots\right]. \tag{1.84}$$

The coefficient of the first term is just the usual Fermi constant, $G_F/\sqrt{2}$. This expansion is valid in the limit $p^2 \ll M_W^2$. In this regime, one may consider a nonrenormalizable *effective field theory,* with interactions of dimension six and beyond: this theory has in fact an explicit ultraviolet cutoff in the mass of the particle which has been removed from the theory and, until processes kinematically well below the cutoff are considered, the theory is well-defined and predictive. When the effective theory is constructed simply by removing out the W boson, a so-called tree level theory is generated. However, radiative corrections in the fundamental theory have to be included, where off-shell gluons and light quarks play a role. As a consequence, there is potentially a radiative correction of order $\alpha_s \ln(M_W/m_b)$, that has to be resummed with the *renormalization group equation* tecnique. This implies that, in the effective theory, operators such as

$$O_I = \overline{c}_i \gamma^\mu (1-\gamma^5) b^i \, \overline{d}_j \gamma_\mu (1-\gamma^5) u^j \tag{1.85}$$

receive radiative corrections and must be subtracted and renormalized (here the color indices i and j are explicit). They therefore acquire a dependence on the renormalization scale μ, which has to be cancelled out in any physical quantity. In this renormalization procedure, operators with different color structure arise such as

$$O_{II} = \overline{c}_i \gamma^\mu (1-\gamma^5) b^j \, \overline{d}_j \gamma_\mu (1-\gamma^5) u^i \, , \tag{1.86}$$

The interaction Hamiltonian of the effective theory has therefore the following *Wilson expansion*

$$\mathcal{H}_{\text{eff}} = C_I(\mu) O_I(\mu) + C_{II}(\mu) O_{II}(\mu) \, , \tag{1.87}$$

By computing the dependence on μ of the operators $O_i(\mu)$, one can deduce the μ-dependence of the *Wilson coefficients* $C_i(\mu)$.

For $\mu = m_b$, the Wilson coefficients resum the potentially large (in the limit of $M_W \to \infty$) logarithms: in this sense they contain the contribution of short-distance (or high energy) physics. They act as new *effective* coupling constant at low energy and in this way they implement the separation of scales we want.

As soon as same-order in g_W diagrams are considered in the fundamental theory (such as *penguin diagram*, Fig.1.5) several new operators arise: they are especially interesting in B physics since they lead to flavor-changing interactions at low energies which are suppressed in Standard Model at tree level.

However, in order to have a complete prediction for a real process rate, physical hadrons, not quarks, have to be considered. This opens the problem of the computation of hadronic matrix elements, involving non-perturbative QCD.

Within this theoretical framework it is possible to write down the effective weak Hamiltonian for charmless hadronic B decays. In this thesis we focus on twobody hadronic B decays with a pion or a kaon in the final state. In particular we are here interested only

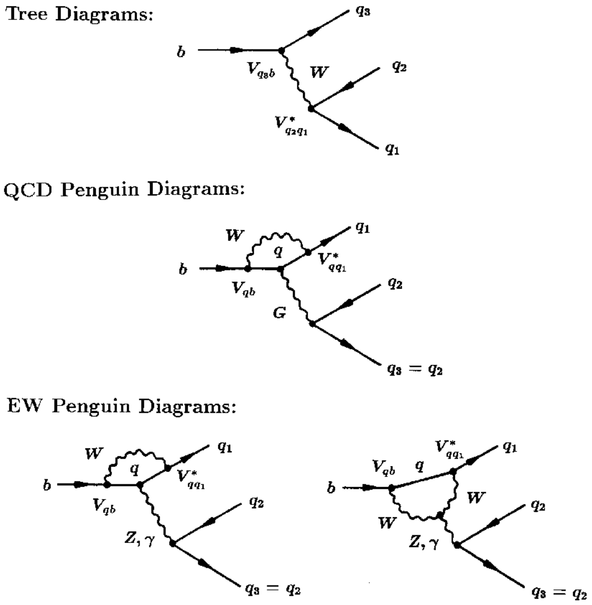

Figure 1.5: Quark diagrams contributing to b decays.

into charged final states (h'^+h^-, with $h', h = \pi, K$). Such a weak Hamiltonian consists of a sum of local operators Q_i multiplied by the Wilson coefficients C_i and products of elements of the quark mixing matrix, $\lambda_p = V_{pb}V^*_{ps}$ or $\lambda'_p = V_{pb}V^*_{pd}$ (with $p = u, c$). Using the unitarity relation $-\lambda_t = \lambda_u + \lambda_c$, we write

$$\mathcal{H}_{\text{eff}} = \frac{G_F}{\sqrt{2}} \sum_{p=u,c} \lambda'_p \Big(C_1\, Q_1^p + C_2\, Q_2^p + \sum_{i=3,\ldots,10} C_i\, Q_i + C_{7\gamma}\, Q_{7\gamma} + C_{8g}\, Q_{8g} \Big) + \text{h.c.}\,, \qquad (1.88)$$

where $Q^p_{1,2}$ are the left-handed current–current operators arising from W-boson exchange, $Q_{3,\ldots,6}$ and $Q_{7,\ldots,10}$ are *QCD* and *electroweak* penguin operators, and $Q_{7\gamma}$ and Q_{8g} are the *electromagnetic* and *chromomagnetic dipole* operators. For channels like $B \to \pi\pi$, they are given by

$$\begin{aligned}
Q_1^p &= (\bar{p}b)_{V-A}(\bar{d}p)_{V-A}\,, & Q_2^p &= (\bar{p}_i b_j)_{V-A}(\bar{d}_j p_i)_{V-A}\,, \\
Q_3 &= (\bar{d}b)_{V-A} \textstyle\sum_q (\bar{q}q)_{V-A}\,, & Q_4 &= (\bar{d}_i b_j)_{V-A} \textstyle\sum_q (\bar{q}_j q_i)_{V-A}\,, \\
Q_5 &= (\bar{d}b)_{V-A} \textstyle\sum_q (\bar{q}q)_{V+A}\,, & Q_6 &= (\bar{d}_i b_j)_{V-A} \textstyle\sum_q (\bar{q}_j q_i)_{V+A}\,, \\
Q_7 &= (\bar{d}b)_{V-A} \textstyle\sum_q \frac{3}{2} e_q (\bar{q}q)_{V+A}\,, & Q_8 &= (\bar{d}_i b_j)_{V-A} \textstyle\sum_q \frac{3}{2} e_q (\bar{q}_j q_i)_{V+A}\,, \\
Q_9 &= (\bar{d}b)_{V-A} \textstyle\sum_q \frac{3}{2} e_q (\bar{q}q)_{V-A}\,, & Q_{10} &= (\bar{d}_i b_j)_{V-A} \textstyle\sum_q \frac{3}{2} e_q (\bar{q}_j q_i)_{V-A}\,, \\
Q_{7\gamma} &= \frac{-e}{8\pi^2}\, m_b\, \bar{d}\sigma_{\mu\nu}(1+\gamma_5)F^{\mu\nu}b\,, & Q_{8g} &= \frac{-g_s}{8\pi^2}\, m_b\, \bar{d}\sigma_{\mu\nu}(1+\gamma_5)G^{\mu\nu}b\,, \qquad (1.89)
\end{aligned}$$

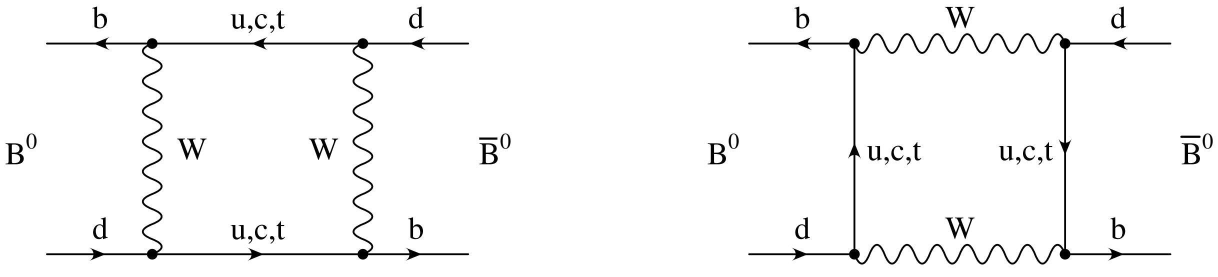

Figure 1.6: *Box diagram* inducing $B^0\bar{B}^0$ mixing in Standard Model.

where $(\bar{q}_1 q_2)_{V\pm A} = \bar{q}_1\gamma_\mu(1\pm\gamma_5)q_2$, i, j are colour indices, e_q are the electric charges of the quarks in units of $|e|$, and a summation over $q = u, d, s, c, b$ is implied. A corresponding formula, with obvious substitutions, holds for other decays such as $B \to K\pi$.

In the case of time-dependent *CP* asymmetry, the physical quantity $\lambda_{f_{CP}}$ (see Eq.1.34)

$$\lambda_{f_{CP}} = \eta_{f_{CP}} \frac{q}{p} \frac{\bar{A}_{\bar{f}_{CP}}}{A_{f_{CP}}}. \tag{1.90}$$

encapsulates all the *CP* violation effects.

Let's consider now the decay $B^0 \to \pi^+\pi^-$.

For this final state $\eta_{f_{CP}} = \eta_{\pi\pi} = +1$. Moreover, within the Standard Model, to a very good approximation (neglecting *CP* violation in the mixing), the box diagram (Fig.1.6) provides an estimate of $\frac{q}{p}$

$$\frac{q}{p} = -\frac{M_{12}^*}{|M_{12}|} = \frac{V_{tb}^* V_{td}}{V_{tb} V_{td}^*} e^{2i\xi_B}. \tag{1.91}$$

Finally, considering the weak Hamiltonian Eq.1.88, one can select the operators with the quark quantum numbers required for the decay $B^0 \to \pi^+\pi^-$. If this decay were dominated by the W-mediated tree diagram, one would find

$$\frac{\bar{A}_{\pi\pi}}{A_{\pi\pi}} = \eta_{\pi\pi} \frac{V_{ub} V_{ud}^*}{V_{ub}^* V_{ud}} e^{-2i\xi_B}. \tag{1.92}$$

Combining Eq.1.91 and Eq.1.92, gives

$$\lambda_{\pi\pi} = \left(\frac{V_{tb}^* V_{td}}{V_{tb} V_{td}^*}\right)\left(\frac{V_{ud}^* V_{ub}}{V_{ud} V_{ub}^*}\right) \implies \mathcal{I}m\lambda_{\pi\pi} = \sin(2\alpha). \tag{1.93}$$

The pure penguin term in Eq.1.88 has a weak phase, $\arg(V_{td}^* V_{tb})$, different from the term with the tree contribution, so it modifies both $\mathcal{I}m\lambda_{\pi\pi}$ and (if there are non-trivial strong phases) $|\lambda_{\pi\pi}|$. The total decay amplitude can be written as

$$A_{\pi\pi} = Te^{i\gamma}e^{i\delta_T} + Pe^{-i\beta}e^{i\delta_P},\ \bar{A}_{\pi\pi} = Te^{-i\gamma}e^{i\delta_T} + Pe^{i\beta}e^{i\delta_P}, \tag{1.94}$$

where T and P are the (real) tree and penguin amplitudes, respectively, and $\delta_{T(P)}$ are the corresponding strong phases. Defining $r = P/T$ and $\delta = \delta_P - \delta_T$, the expression for $\lambda_{\pi\pi}$ becomes ([27])

$$\lambda_{\pi\pi} = e^{-2i\beta}\frac{e^{-i\gamma} + re^{i\beta}e^{i\delta}}{e^{i\gamma} + re^{-i\beta}e^{i\delta}} = e^{2i\alpha}\frac{1 - re^{i(\delta-\alpha)}}{1 - re^{i(\delta+\alpha)}} \equiv |\lambda_{\pi\pi}|\, e^{2i\alpha_{\mathrm{eff}}}, \tag{1.95}$$

which reduces to Eq.1.93 in the limit $r \to 0$. It is clear that $r,\ \delta \neq 0$ implies $|\lambda_{f_{CP}}| \neq 1$ and $2\alpha_{\mathrm{eff}} \neq 2\alpha$. If the strong phase difference vanishes (no observable direct CP violation), then $|\lambda_{f_{CP}}| = 1$, but the penguin-induced shift in α remains as long as r is significant. It is possible to extract α in the presence of penguins with little or no theoretical error using an isospin analysis [28] (see [29] and [30] for caveats to this statement). In addition to $S_{\pi\pi}$ and $C_{\pi\pi}$, this analysis requires measurements of the separate branching fractions for $B^0 \to \pi^0\pi^0$ and $\overline{B}^0 \to \pi^0\pi^0$, as well as the charge-averaged branching fraction for $B^\pm \to \pi^\pm\pi^0$. However, unless the $\pi^0\pi^0$ rate is surprisingly large, it will be several years before such an analysis would be possible. Alternatively, it has been shown [31] that a general bound exists for the penguin-induced shift in α,

$$\sin^2\Delta < \frac{\langle\mathcal{B}(B^0 \to \pi^0\pi^0)\rangle}{\mathcal{B}(B^+ \to \pi^+\pi^0)}, \tag{1.96}$$

where $\Delta \equiv \alpha_{\mathrm{eff}} - \alpha$ and $\langle\mathcal{B}(B^0 \to \pi^0\pi^0)\rangle$ is the charge-averaged decay rate. To be useful, this bound obviously requires an upper limit on $B^0 \to \pi^0\pi^0$ less than the measured rate for $\pi^+\pi^0$ ($\sim 5 \times 10^{-6}$), but this should be possible in the near future [32]. This approach has been extended, under various assumptions, to include bounds derived from ratios of branching fractions involving $\pi^0\pi^0$, $\pi^+\pi^0$, $\pi^+\pi^-$, $K^+\pi^-$, and $K^0\overline{K}^0$ decays [33], or by assuming the isospin triangles for $B \to \pi\pi$ and $\bar{B} \to \pi\pi$ close [34].

Finally, it is possible to calculate the shift in α using the *factorization* model ([35]). In fact, the rather ambitious program of factorization is a model-independent calculation of the strong phases difference δ and r. To understand the physical picture behind factorization let's consider the two-body decays $B \to M_1M_2$, where the "emission particle" M_2 (the meson not obtaining the spectator quark from the B meson) is a light meson.

A simple example is $B \to D\pi$, which is mediated by the quark transition $b \to c\bar{u}d$. Immediately after the weak decay, the quarks typically find themselves with a large momentum and in the middle of a medium of gluons and light quark-antiquark pairs, with which they subsequently interact strongly. However, if the $\overline{u}d$ pair has a small invariant mass, $m(\overline{u}d) \approx m_\pi$, then these two quarks will remain close together as they move through the colored medium. If, in addition, they are initially in a color singlet state, then they will interact with the medium not individually but as a single color dipole. Since the distance between the $\overline{u}$ and the d grows slowly, it is possible that the pair will have left the colored environment completely before its dipole moment is large enough for its interactions to be significant. In this case, the pair will hadronize as a single π. This phenomenon is known as "color transparency".

If, by contrast, the $\overline{u}d$ pair has a large invariant mass, then the quarks will interact strongly with the medium. In this case, their reassembly into a single π is extremely unlikely. As a result, it is reasonable to hypothesize that the decay $B \to D\pi$ is dominated by the former scenario, and that the matrix element actually *factorizes*, so that we can write

$$\langle D\pi|\, \overline{c}\gamma^\mu(1-\gamma^5)b\, \overline{d}\gamma_\mu(1-\gamma^5)u\, |\overline{B}\rangle = \langle D|\, \overline{c}\gamma^\mu(1-\gamma^5)b\, |\overline{B}\rangle \times \langle \pi|\, \overline{d}\gamma_\mu(1-\gamma^5)u\, |0\rangle\,. \quad (1.97)$$

The result is even simpler: $\langle \pi|\, \overline{d}\gamma_\mu(1-\gamma^5)u\, |0\rangle$ is related to f_π, (pion decay constant) and $\langle D|\, \overline{c}\gamma^\mu(1-\gamma^5)b\, |\overline{B}\rangle$ may be extracted from semileptonic B decays. Eq.1.97 is a rigorous formula in the so called heavy-quark limit[4] $m_b \gg \Lambda_{\rm QCD}$. Recently, this idea has been thouroghly studied and extended ([36],[3]) to charmless nonleptonic B decays, in the framework of a theory known as *QCD factorization*. However, concerns have been raised about the consistency of such a theory, since corrections of order $\frac{\Lambda_{\rm QCD}}{m_b}$ systematically neglected in the factorization approach, can be relevant to reproduce experiment ([4]).

Applying the QCD factorization formula and neglecting power-suppressed effects, the matrix elements of the effective weak Hamiltonian can be written in the form ([3],[36])

$$\langle \pi K|\mathcal{H}_{\rm eff}|\bar{B}\rangle = \frac{G_F}{\sqrt{2}} \sum_{p=u,c} \lambda_p\, \langle \pi K|\mathcal{T}_p + \mathcal{T}_p^{\rm ann}|\bar{B}\rangle\,, \quad (1.98)$$

---

[4] $\Lambda_{\rm QCD}$ is the energy scale where hadronization takes place and non perturbative effects become dominant.

where

$$\begin{aligned}
\mathcal{T}_p &= a_1(\pi K)\,\delta_{pu}\,(\bar{u}b)_{V-A}\otimes(\bar{d}u)_{V-A}\\
&+ a_2(\pi K)\,\delta_{pu}\,(\bar{d}b)_{V-A}\otimes(\bar{u}u)_{V-A}\\
&+ a_3(\pi K)\sum\nolimits_q(\bar{d}b)_{V-A}\otimes(\bar{q}q)_{V-A}\\
&+ a_4^p(\pi K)\sum\nolimits_q(\bar{q}b)_{V-A}\otimes(\bar{d}q)_{V-A}\\
&+ a_5(\pi K)\sum\nolimits_q(\bar{d}b)_{V-A}\otimes(\bar{q}q)_{V+A}\\
&+ a_6^p(\pi K)\sum\nolimits_q(-2)(\bar{q}b)_{S-P}\otimes(\bar{d}q)_{S+P}\\
&+ a_7(\pi K)\sum\nolimits_q(\bar{d}b)_{V-A}\otimes\tfrac{3}{2}e_q(\bar{q}q)_{V+A}\\
&+ a_8^p(\pi K)\sum\nolimits_q(-2)(\bar{q}b)_{S-P}\otimes\tfrac{3}{2}e_q(\bar{d}q)_{S+P}\\
&+ a_9(\pi K)\sum\nolimits_q(\bar{d}b)_{V-A}\otimes\tfrac{3}{2}e_q(\bar{q}q)_{V-A}\\
&+ a_{10}^p(\pi K)\sum\nolimits_q(\bar{q}b)_{V-A}\otimes\tfrac{3}{2}e_q(\bar{d}q)_{V-A}\,. \qquad (1.99)
\end{aligned}$$

Here $(\bar{q}_1q_2)_{S\pm P}=\bar{q}_1(1\pm\gamma_5)q_2$, and a summation over $q=u,d$ is implied. The symbol $\otimes$ indicates that the matrix elements of the operators in $\mathcal{T}_p$ are to be evaluated in the factorized form $\langle\pi K|j_1\otimes j_2|\bar{B}\rangle\equiv\langle\pi|j_1|\bar{B}\rangle\,\langle K|j_2|0\rangle$ or $\langle K|j_1|\bar{B}\rangle\,\langle\pi|j_2|0\rangle$, as appropriate. “Nonfactorizable” corrections are, by definition, included in the coefficients a_i. The matrix elements for B mesons (i.e., mesons containing a $\bar{b}$-antiquark) are obtained from (1.98) by CP conjugation. The term $\mathcal{T}_p^{\rm ann}$ in (1.98) arises from further contributions and introduces a set of coefficients $b_i(\pi K)$, similar to $a_i(\pi K)$. Just to give the reader a feeling of how the factorization prediction proceeds, in terms of the parameters a_i, we write the $\bar{B}^0\to\pi^+K^-$ decay amplitude without $b_i(\pi K)$ contributions

$$-A(\bar{B}^0\to\pi^+K^-) \;=\; \left[\lambda_u\,a_1+\lambda_p\,(a_4^p+a_{10}^p)+\lambda_p\,r_\chi^K\,(a_6^p+a_8^p)\right]A_{\pi K}^{fact}\,,. \qquad (1.100)$$

where a summation over $p=u,c$ is understood and r_χ^K is a parameter depending on quark masses. $A_{\pi K}^{fact}$ is one of the factorized matrix elements

$$A_{\pi K}^{fact} \;=\; i\frac{G_F}{\sqrt{2}}\,(m_B^2-m_\pi^2)\,F_0^{B\to\pi}(m_K^2)\,f_K\,. \qquad (1.101)$$

where $F_0^{B\to\pi}(q^2)$ is a semileptonic form factors. From this formula, just counting the Cabibbo angle powers, it is evident as this amplitude is dominated by the penguin contribution, being $\lambda_u\sim\lambda^4$ (which multiply the tree term a_1) and $-(\lambda_u\lambda_c)=\lambda_t\sim\lambda^2$.

The $B^0\to\pi^+\pi^-$ decay amplitude is given by

$$-\bar{A}_{\pi\pi} \;=\; \left[\lambda'_u\,a_1+\lambda'_p\,(a_4^p+a_{10}^p)+\lambda'_p\,r_\chi^\pi\,(a_6^p+a_8^p)\right]A_{\pi\pi}^{fact}\,, \qquad (1.102)$$

Mode	No. Events	Sig.	effic.	$\mathcal{B} \times 10^6$
$\pi^+\pi^-$	$20.0^{+7.6}_{-6.5}$	4.2σ	0.48	$4.3^{+1.6}_{-1.4} \pm 0.5$
$\pi^+\pi^0$	$21.3^{+9.7}_{-8.5}$	3.2σ	0.39	< 12.7
$K^+\pi^-$	$80.2^{+11.8}_{-11.0}$	11.7σ	0.48	$17.2^{+2.5}_{-2.4} \pm 1.2$
$K^+\pi^0$	$42.1^{+10.9}_{-9.9}$	6.1σ	0.38	$11.6^{+3.0+1.4}_{-2.7-1.3}$
$K^0\pi^+$	$25.2^{+6.4}_{-5.6}$	7.6σ	0.14	$18.2^{+4.6}_{-4.0} \pm 1.6$
$K^0\pi^0$	$16.1^{+5.9}_{-5.0}$	4.9σ	0.11	$14.6^{+5.9+2.4}_{-5.1-3.3}$
K^+K^-	$0.7^{+3.4}_{-0.7}$	0.0σ	0.48	< 1.9
$K^+\overline{K}^0$	$1.4^{+2.4}_{-1.3}$	1.1σ	0.14	< 5.1

Table 1.2: Summary of CLEO $\mathcal{B}$ results from a sample of $9.13\,\mathrm{fb}^{-1}$ ([5]).

Mode	$\mathcal{A}_f$
$K^+\pi^-$	$-0.04 \pm 0.16 \pm 0.02$
$K^+\pi^0$	$-0.29 \pm 0.23 \pm 0.02$
$K^0\pi^+$	$+0.18 \pm 0.24 \pm 0.02$

Table 1.3: Summary of CLEO $\mathcal{A}$ results from a sample of $9.13\,\mathrm{fb}^{-1}$ ([37]).

where now $\lambda'_p = V_{pb}V^*_{pd}$, $a_i \equiv a_i(\pi\pi)$, and

$$A^{fact}_{\pi\pi} = i\frac{G_F}{\sqrt{2}}\left(m_B^2 - m_\pi^2\right) F_0^{B\to\pi}(m_\pi^2)\, f_\pi\,. \tag{1.103}$$

In the case of $\pi\pi$ final states the tree term multiplies $\lambda'_u \sim \lambda^3$, while the penguin terms $-(\lambda'_u + \lambda'_c) = \lambda'_t \sim \lambda^3$. It is clear that in this case there is no relative Cabibbo suppression of either tree or penguin term with respect to the other, and if penguin terms are not dinamically suppressed in the matrix element, both the weak phases of the tree and penguin terms have to contribute to the total weak phase of $\bar{A}_{\pi\pi}$. Using the same effective Hamiltonians and therefore the same $a_i(K\pi)(a_i(\pi\pi))$ coefficient and $A^{fact}_{\pi K}(A^{fact}_{\pi\pi})$ it is possible to calculate formulae similar to Eq.1.100(Eq.1.102) for the other $K\pi(\pi\pi)$ channels. Measuring all the Branching Ratios for those channels and comparing with QCD factorization prediction is therefore a very stringent test. Moreover, Eq.1.102 contains, in fact, a prediction for the strong phase δ and penguin-to-tree ratio r. A fit to experimental data can therefore allow for an extraction of γ and, in presence of a measurement of time-dependent CP asymmetry, α value can be disentangled.

Before the advent of B-Factories in year 2000, Branching Ratio and charge asymmetry measurements for twobody charmless B decays were reported by CLEO collaboration only ([5],[37]) on a data sample of $9.13\,\mathrm{fb}^{-1}$. In Tab.1.2 the most recent CLEO results are given for all the twobody channels. It is important to notice that in the experimental literature it is common to define charge asymmetry as

$$\mathcal{A}_f = \frac{n_{\bar{f}} - n_f}{n_{\bar{f}} + n_f} \tag{1.104}$$

where n_f ($n_{\bar{f}}$) is the number of $B(\bar{B})$ meson (containing a $\bar{b}$ (b) quark therefore) decaying to the final state $f(\bar{f})$. There is therefore a sign difference in this definition with respect to Eq.1.45 and Eq.1.46. In this analysis the experimental definition Eq.1.104 is adopted.

After illustrating in the next Chapters the experimental analyses which lead to the measurement of Branching Ratios (inspired by the CLEO analysis) and *CP* asymmetries, in Chapter 5 we will compare QCD factorization prediction with experimental results, trying to put further contraints on CKM parameters.

Chapter 2

The *BABAR* experiment at PEP-II

2.1 Introduction

The design of the *BABAR* detector ([38]) at PEP-II B Factory is optimized for *CP* violation studies, but it is also well suited for searches of rare B decays. The PEP-II B Factory is an asymmetric e^+e^- collider designed to operate at a luminosity of 3×10^{33} $\mathrm{cm}^{-2}\mathrm{s}^{-1}$ and above, at a center-of-mass energy of 10.58 GeV, the mass of the $\Upsilon(4S)$ resonance. In PEP-II, the electron beam of 9.0 GeV collides head-on with the positron beam of 3.1 GeV resulting in a Lorentz boost to the $\Upsilon(4S)$ resonance of $\beta\gamma = 0.56$. This boost makes it possible to reconstruct the decay vertices of the two B mesons, to determine their relative decay times Δt, and thus to measure the time dependence of their decay rates. This requires events in which one B meson decays to a *CP* eigenstate that is fully reconstructed and the other B meson is tagged as B^0 or a $\overline{B}^0$ by its decay products: a charged lepton, a charged kaon, or other flavor sensitive features such as a low momentum charged pion from a D^* decay. The very small branching ratios of B mesons to *CP* eigenstates, typically 10^{-4}, the need for full reconstruction of final states, plus the need to tag the second neutral B, place stringent requirements on the detector, which must have excellent reconstruction efficiency for charged particles and very good momentum resolution to separate small signals from background. Very good vertex resolution, both transverse and parallel to the beam direction is required with an efficient electron and muon identification, with low misidentification probablities for hadrons. This feature is crucial for tagging the B flavor. Efficient and accurate identification of hadrons over a wide range of momenta is critical for B flavor-tagging and for the reconstruction of exclusive states, such as $B^0 \to K^\pm\pi^\mp$ or $B^0 \to \pi^+\pi^-$themselves.

Fig. 2.1 shows a longitudinal section through the detector center. The detector is installed at the PEP-II interaction region. To maximize the geometric acceptance for the boosted $\Upsilon(4S)$ decays, the whole detector is offset relative to the beam-beam interaction point (IP) by 0.37 m in the direction of the lower energy beam.

The inner detector consists of a silicon vertex tracker, a drift chamber, a ring-imaging Čerenkov detector, and a CsI calorimeter. These detector systems are surrounded by a superconducting solenoid that generates a field of 1.5 T. The steel flux return is instrumented for muon and neutral hadron detection. The polar angle coverage extends to 350 mrad in the forward direction and 400 mrad in the backward direction, defined relative to the high energy beam. The right handed coordinate system is anchored on the main

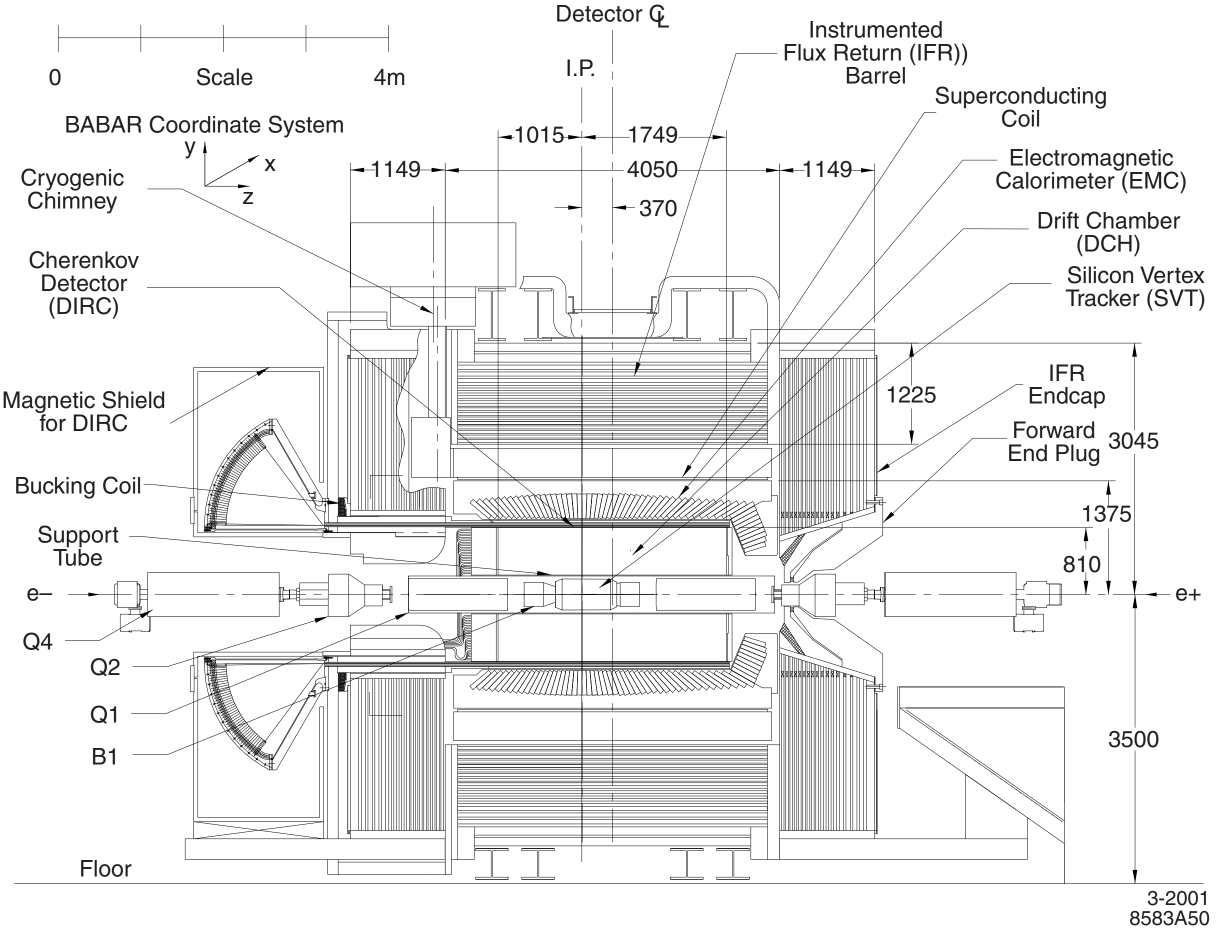

Figure 2.1: *BABAR* detector longitudinal section.

tracking system, the drift chamber, with the z-axis coinciding with its principal axis. The positive y-axis points upward and the positive x-axis points away from the center of the PEP-II storage rings.

A trigger system is used to enhance interesting collision events with respect to background from, for instance, interactions of beams with residual gas. A first level (*L1 trigger*) is implemented in hardware and is designed to provide a maximal output rate of 2 kHz. Another level, *Level 3* (L3), is realized in software and its output rate is limited to 120 Hz by the downstream storage and processing capacity.

Simulation of *BABAR* detector response is realized with a GEANT3-based [39] application. Particle production and decays are simulated in an event *generator* program interfaced to LUND/JETSET [40]. We refer to simulated events sample as *full Monte Carlo* (or simply *Monte Carlo*) events.

2.2 The B-factory PEP-II

PEP-II is an e^+e^- storage ring system designed to operate at a center of mass (CMS) energy of 10.58 GeV, corresponding to the mass of the $\Upsilon(4S)$ resonance. The parameters of these energy asymmetric storage rings are presented in Tab. 2.1. PEP-II has surpassed its design goals, both in terms of the instantaneous and the integrated daily luminosity, with significantly fewer bunches than anticipated.

Table 2.1: PEP-II beam parameters. Values are given both for the design and for typical colliding beam operation in the first year. HER and LER refer to the high energy e^- and low energy e^+ ring, respectively. σ_{Lx}, σ_{Ly}, and σ_{Lz} refer to the horizontal, vertical, and longitudinal r.m.s. size of the luminous region. More recently PEP-II has reached the record peak luminosity of 4.1 $10^{33}\,\mathrm{cm}^{-2}\mathrm{s}^{-1}$ with a record daily integrated luminosity of 270 pb^{-1}

Parameters	Design	Typical
Energy HER/LER (GeV)	9.0/3.1	9.0/3.1
Current HER/LER (A)	0.75/2.15	0.7/1.3
# of bunches	1658	553-829
Bunch spacing (ns)	4.2	6.3-10.5
σ_{Lx} (μm)	110	120
σ_{Ly} (μm)	3.3	5.6
σ_{Lz} (μm)	9000	9000
Luminosity ($10^{33}\,\mathrm{cm}^{-2}\mathrm{s}^{-1}$)	3	2.5
Daily int. luminosity (pb^{-1}/d)	135	120

Most of the data are recorded at the peak of the $\Upsilon(4S)$ resonance: they are referred to as *on-resonance data*. In Tab.2.2 the main processes active at the $\Upsilon(4S)$ resonance are summarized with their cross sections: the production of light quark pairs (u, d, s) and *charm* quark pairs is usually referred to as *continuum* production. In order to allow for studies of this non-resonant continuum about 12% of data are taken at a CMS energy 40 MeV below the $\Upsilon(4S)$. They are commonly referred to as *off-resonance data*.

The bunches collide head-on and are separated magnetically in the horizontal plane by a pair of dipole magnets (*B1* in Fig.2.1), followed by a series of offset quadrupoles: they are permanent magnets made of samarium-cobalt placed inside the field of the *BABAR* solenoid. The collision axis is off-set from the z-axis of the *BABAR* detector by about 20 mrad in the horizontal plane to minimize the perturbation of the beams by the solenoid field.

Table 2.2: Production cross-sections at $\sqrt{s} = M_{\Upsilon(4S)}$. The *Bhabha* cross-section into e^+e^- is the effective cross-section, expected within the experimental acceptance.

$e^+e^- \to$	Cross-section (nb)
$b\bar{b}$	1.05
$c\bar{c}$	1.30
$s\bar{s}$	0.35
$u\bar{u}$	1.39
$d\bar{d}$	0.35
$\tau^+\tau^-$	0.94
$\mu^+\mu^-$	1.16
e^+e^-	~ 40

The beam parameters that are most critical for the *BABAR* performance are the luminosity, the energies of the two beams, and the position, angles, and size of the luminous region (*beamspot*). While PEP-II measures radiative Bhabha scattering to provide a fast monitor of the relative luminosity for operations, *BABAR* derives the absolute luminosity offline from other QED processes, primarily e^+e^- and $\mu^+\mu^-$ production. During operation, the mean energies of the two beams are calculated from the total magnetic bending strength and the average deviations of the accelerating frequencies from their central values. While the systematic uncertainty in the PEP-II calculation of the absolute beam energies is estimated to be 5–10 MeV, the relative energy setting for each beam is accurate and stable to about 1 MeV. The r.m.s. energy spreads of the LER and HER beams are 2.3 MeV and 5.5 MeV, respectively.

The direction of the beams relative to *BABAR* is measured iteratively run-by-run using $e^+e^- \to e^+e^-$ and $e^+e^- \to \mu^+\mu^-$ events.

The size and position of the luminous region are critical parameters for the decay-time-dependent analyses and their values are monitored continuously online and offline. The design values for the size of the luminous region are presented in Tab. 2.1. The vertical size is too small to be measured directly. It is inferred from the measured luminosity, the horizontal size, and the beam currents; it varies typically by 1–2 μm.

The transverse position, size, and angles of the luminous region relative to the *BABAR* coordinate system are determined by analyzing the distribution of the distance of closest approach to the z-axis of the tracks in well measured two-track events as a function of the azimuth ϕ. The longitudinal parameters are derived from the longitudinal vertex distribution of the two tracks. The uncertainties in the average beam position are of the order of a few μm in the transverse plane and 100 μm along the collision axis. Run-by-run variations in the beam position are comparable to these measurement uncertainties, indicating that the beams are stable over the period of a typical run. These measurements are also checked offline by measuring the primary vertices in multi-hadron events[1]. The measured horizontal and longitudinal beam sizes, corrected for tracking resolution, are consistent with those measured by PEP-II.

In Fig.2.2 the integrated luminosity delivered by PEP-II and recorded by *BABAR* is shown up to the beginning of September 2001. We refer to data recorded during year 2000 as Run 1 data. Run 2 started at the beginning of 2001 and is still going on. In this analysis Run 2 data recorded and processed up to the end of June 2001 are considered.

2.2.1 B counting

Measurements of Branching Ratios require a precise knowledge of integrated luminosity and total $B\bar{B}$ cross section at the $\Upsilon(4S)$ peak. This is equivalent to count directly $\Upsilon(4S)$ decays on a stastical basis in the same data set that is used for the Branching Ratio analysis. This is realized applying *hadronic* event selection criteria to both on-resonance and off-resonance data sets, with the assumption that the increase in the ratio of hadronic events to muon pairs between on and off resonance running is due to $\Upsilon(4S)$ production. The number of $\Upsilon(4S)$ mesons satisfying the criteria (N_{Υ}) is given by:

$$N_{\Upsilon} = N_{\mathrm{MH}} - N_{\mu\mu} \cdot R_{\mathrm{off}} \cdot \kappa, \tag{2.1}$$

where

- N_{MH} = hadronic events satisfying the selection criteria in the on-resonance sample;
- $N_{\mu\mu}$ = muon pairs selected in the on-resonance sample;
- $R_{\mathrm{off}} = N^{\mathrm{off}}_{\mathrm{MH}}/N^{\mathrm{off}}_{\mu\mu}$, the ratio of hadronic events to muon pairs in the appropriate off-resonance sample;
- κ = a factor, close to 1, that takes into account the dependence of cross-section on the center of mass energy and also possible variations of efficiencies.

---

[1] By vertexing all the reconstructed tracks in the event it is possible to have an estimate of the position of the *primary vertex*, that is of the $\Upsilon(4S)$ decay point. Because of the boost along z inducing a relative displacement of the two B mesons the resolution of this method is rather poor and it is worsened by the presence of long-lived particles in the transverse plane.

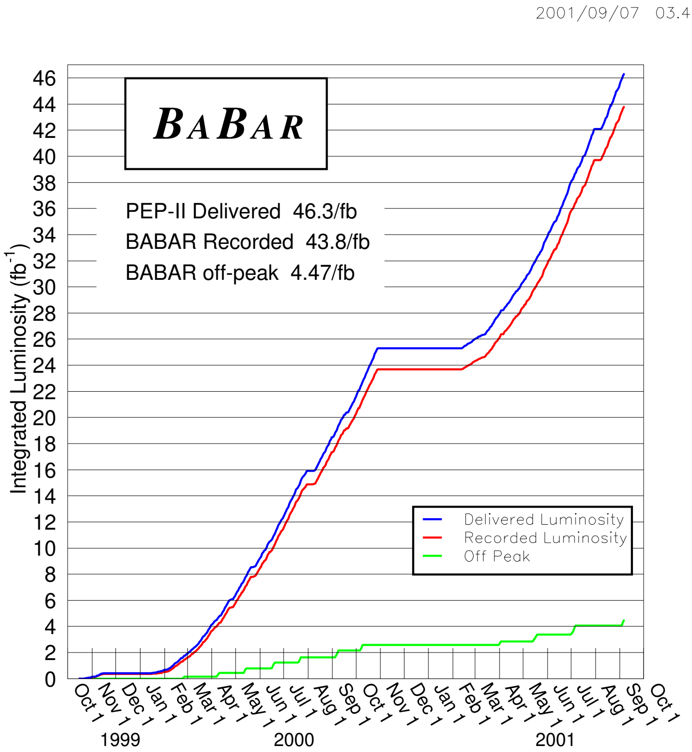

Figure 2.2: PEP-II delivered and recorded luminosity from the beginning of data taking

The hadronic selection is based on requirements on the number of good-quality tracks and on event primary vertex: this rejects low multiplicity final states (*Bhabha*, radiative *Bhabha*, $\gamma\gamma$ interaction events) and beam-gas interaction events. Moreover, a cut on second Fox-Wolfram moment R_2 (see Section3.2) enhances $B\overline{B}$ events relatively to $non-\Upsilon(4S)$ hadronic decays. A requirement on total detected energy in the event is also used.

In a data set the total number of *produced* $\Upsilon(4S)$ is:

$$N^0_{\Upsilon} = N_{\Upsilon}/\epsilon_{B\overline{B}}, \tag{2.2}$$

where $\epsilon_{B\overline{B}}$ is the efficiency for $B\overline{B}$ events to satisfy the selection criteria.

$\epsilon_{B\overline{B}}$ is evaluated with Monte Carlo simulation after a careful validation confirming that the variables shapes used in the hadronic selection are well reproduced.

Assuming the $B\overline{B}$ production saturates $\Upsilon(4S)$ decays and $\mathcal{B}(\Upsilon(4S) \to B^0\bar{B}^0)$ is equal to $\mathcal{B}(\Upsilon(4S) \to B^+B^-)$, N^0_Υ is the number of $B\overline{B}$ pairs, $N_{B\overline{B}}$, in the data set. In Run 1 data[2] we measure

$$N_{B\overline{B}} = (22.57 \pm 0.36)\, 10^6$$

The error is dominated by systematic uncertainty on $\epsilon_{B\overline{B}}$, mainly due to the uncertainty on the number of good-quality tracks.

2.3 *BABAR* tracking system

The charged particle tracking system is made of two components, the silicon vertex tracker (SVT) and the drift chamber (DCH).

The SVT has been designed to measure angles and positions of charged particles just outside the beam pipe. It consists of five layers of double-sided silicon strip detectors (Fig. 2.3) that are assembled from modules with readout at each end, thus reducing the amount of inactive material in the acceptance volume. The inner three layers primarily provide position and angle information for the measurement of the vertex position. They are mounted as close to the water-cooled beryllium beam pipe as practical (at a radius $r = 3.2\,cm$), thus minimizing the impact of multiple scattering in the beam pipe on the extrapolation to the vertex. The outer two layers are located at a much larger radius ($r = 9.1\,cm$) in order to provide the coordinate and angle measurements needed for linking SVT and DCH tracks.

The principal purpose of the DCH is momentum measurement for charged particles. It also supplies information for the charged particle trigger and a measurement of $\mathrm{d}E/\mathrm{d}x$ for particle identification. The DCH is of compact design, with 40 layers of small, approximately hexagonal cells (Fig. 2.4). Longitudinal information is derived from wires placed at small angles (*stereo layers*) to the principal axis. Wires in the *axial layers* are parallel to the principal axis and both axial and stereo layers provide curvature measurement of tracks. By choosing low-mass wires, and a helium-based gas mixture the multiple scattering inside the DCH is kept to a minimum. At normal incidence the DCH is $1.08\,10^{-2}$ radiation length long. The readout electronics is mounted on the backward endplate of the chamber, minimizing the amount of material in front of the calorimeter endcap. Each of the 7,104 small drift cell consists of one sense wire surrounded by six field wires, as

---

[2] Run 2 data result is not available to this date

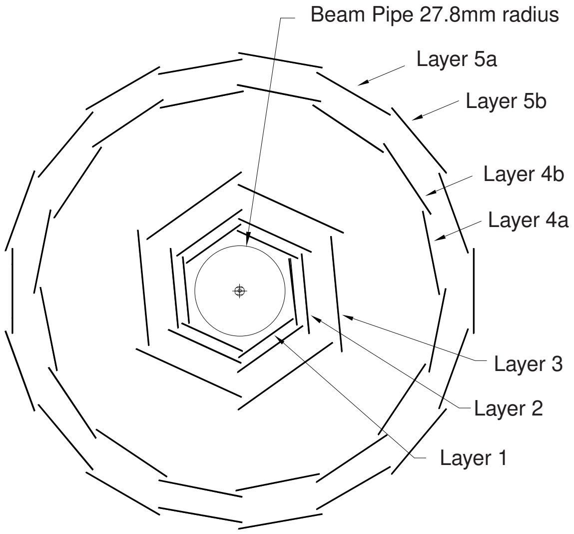

Figure 2.3: Schematic view of SVT: tranverse section.

shown in Fig. 2.5. While the field wires are at ground potential, a positive high voltage is applied to the sense wires. An avalanche gain of approximately 5×10^4 is obtained at a typical operating voltage of 1960 V and with a 80:20 helium:isobutane gas mixture. During part of year 2000 the operating voltage was lowered to 1900 V to preserve some damaged section of the DCH. The main effect was a reduced hit efficiency and, consequently, a reduced tracking efficiency and a worse momentum resolution with some impact on the final data analysis. During year 2001 data-taking the operating voltage was set to 1930 V .

The global coordinate system is defined by the DCH position: because of seismic activity the SVT moves with respect to the DCH so it must be periodically aligned as a whole in the DCH system. Moreover, the SVT is not a perfect rigid body and the relative position of its 340 modules must be determined too. The alignement procedure is performed using tracks from $e^+e^- \to \mu^+\mu^-$ events and cosmic rays. It consists of two steps. A *global alignement* procedure, updated on a run-by-run basis, able to detemine the six global alignment parameters, three translations and three rotations, by minimizing the difference between the track parameters obtained with the SVT-only and the DCH-only fits. A *SVT local alignement* procedure that is more complex, but, since the local internal positions are relatively stable, is performed only when needed, typically after magnet quenches or detector access. The *SVT local alignement* can represent a source of system-

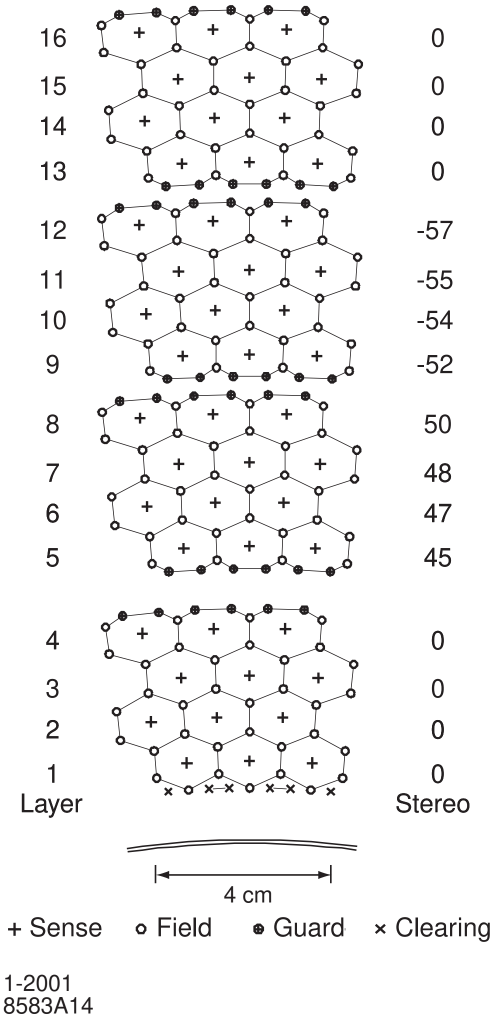

Figure 2.4: Schematic layout of drift cells for the four innermost superlayers. Lines between field wires aid in visualization of the cell boundaries. The numbers on the right side give the stereo angles (mrad) of sense wires in each layer. The 1 mm-thick beryllium inner wall is shown inside of the first layer.

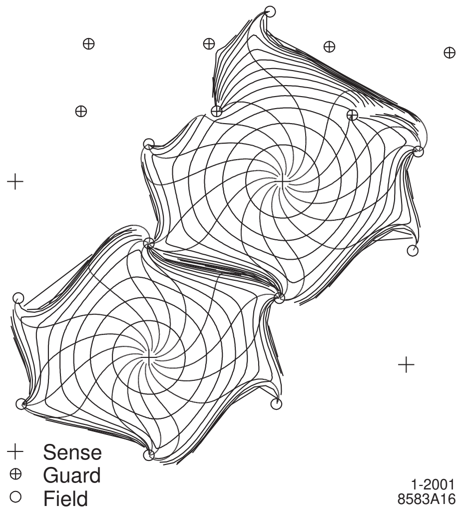

Figure 2.5: Drift cell isochrones (contours of equal drift times of ions) in cells of layers 3 and 4 of an axial superlayer. The isochrones are spaced by 100 ns. They are circular near the sense wires, but become irregular near the field wires, and extend into the gap between superlayers.

atic bias or distortion in the measure of Δz and therefore it must be accounted for in the CP asymmetry analysis.

The reconstruction of charged particle tracks relies on information from both tracking systems, the SVT and the DCH. Charged tracks are defined by five parameters $(d_0, \phi_0, \omega, z_0, \tan\lambda)$ and their associated error matrix. These parameters are measured at the point of closest approach to the z-axis; d_0 and z_0 are the distances of this point from the origin of the coordinate system in the x–y plane and along the z-axis, respectively. The angle ϕ_0 is the azimuth of the track, λ its dip angle relative to the transverse plane, and $\omega = 1/p_t$ is its curvature. d_0 and ω are signed variables; their sign depends on the charge of the track. The track finding and the fitting procedures make use of Kalman filter algorithm [41] that takes into account the detailed distribution of material in the detector and the full map of the magnetic field. Charged particle tracking has been studied with large samples of cosmic ray muons, e^+e^-, $\mu^+\mu^-$, and $\tau^+\tau^-$ events, as well as multi-hadrons.

For measurement of Branching Ratios for final states containing charged particles only, it is relevant to know the tracking efficiency in order to correctly normalize the yields. These studies are based on data, but they are aimed to eventually validate the detector Monte Carlo simulation. At the same time a good knowledge of basic quantities such as track fit parameters is relevant to understand detector performance: this is described in the next Subsections.

2.3.1 Tracking efficiency

Track reconstruction uses information from the SVT, the DCH and the L3 trigger. The absolute event timing information (the event start time t_0) is determined iteratively by the track finding algorithms along with the five helix parameters.

In L3 trigger there is an algorithm that performs track *pattern recongnition* in the DCH and, subsequently, a rough track fitting with an estimate of t_0. This track *pattern recongnition* is based on the L1 *track segment* finder modules[3]. In the subsequent reconstruction steps, tracks are selected by performing helix fits to the hits used by the L3 track finding algorithm. A search for additional hits in the DCH that may belong on these tracks is performed, while t_0 is further improved by using only hits associated with tracks. Two more sophisticated tracking procedures are applied which are designed to find tracks that either do not pass through the entire DCH or do not originate from the IP. These algorithms primarily use track segments that have not already been assigned to other tracks, and thus benefit from a progressively cleaner tracking environment with a constantly improving t_0. At the end of this process, tracks are again fit using a Kalman filter method. The resulting tracks are then extrapolated into the SVT and SVT track segments are added, provided they are consistent with the expected error in the extrapolation through the intervening material and inhomogeneous magnetic field. Among the possible SVT segments, those with the smallest residuals and the largest number of SVT layers are retained and a Kalman fit is performed to the full set of DCH and SVT hits. Any remaining SVT hits are then passed to two complementary standalone track finding algorithms. Finally, an attempt is made to combine tracks that are only found by one of the two tracking systems and thus recover tracks scattered in the material of the support tube.

The efficiency for reconstructing tracks in the DCH has been measured as a function of transverse momentum, polar and azimuthal angles in multi-track events. These measurements rely on specific final states and exploit the fact that the track reconstruction

---

[3] These L1 modules identify in each DCH superlayers structures of four contiguous *hits*, called *track segments*.

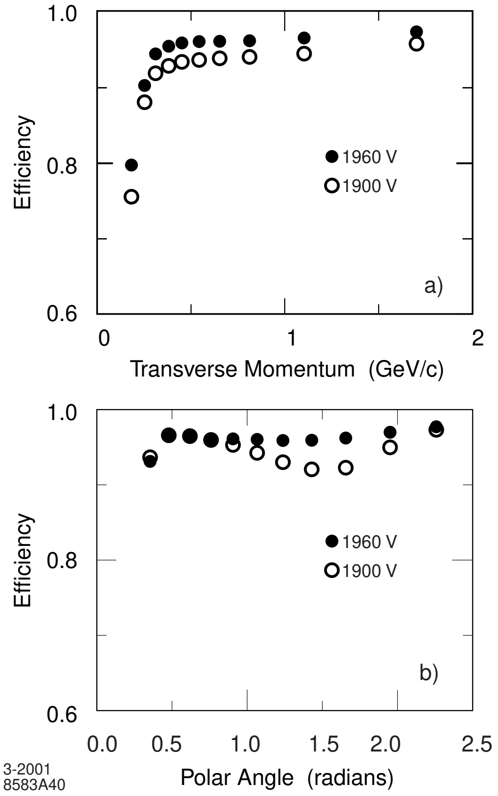

Figure 2.6: The track reconstruction efficiency in the DCH at operating voltages of 1900 V and 1960 V, as a function of a) transverse momentum, and b) polar angle. The efficiency is measured in multi-hadron events as the fraction of all tracks detected in the SVT for which the DCH portion is also reconstructed.

can be performed independently in the SVT and the DCH.

The absolute DCH tracking efficiency ([42]) is determined as the ratio of the number of reconstructed DCH tracks to the number of tracks detected in the SVT, with the requirement that they fall within the acceptance of the DCH.

Such studies have been performed using different samples of multi-hadron events. Fig. 2.6 shows the result of one of these studies for the two voltage settings in Run 1. The presence of additional SVT hits originated from machine background produces “fake” tracks. The DCH tracking efficiency errors are dominated by the uncertainty in the correction for these fake tracks. At the design voltage of 1960 V, the per-track efficiency averages $(98 \pm 1)\%$ for $p_t > 200\,\mathrm{MeV}/c$ and polar angles $\theta > 500\,\mathrm{mrad}$. The data recorded at 1900 V show a reduction in efficiency by about 5% for tracks at close to normal incidence, indicating that the cells are not fully efficient at this voltage. Data analysis usually discards badly-fitted tracks, tracks not coming from the interaction point or pointing out of a fiducial volume. Different level of track *quality* can be set, for instance *good* tracks with *very loose*, *loose* or *tight* requirements. In this analysis we use only tracks such that

- $N(\text{DCH hits}) \geq 12$
- $d_0 < 1.5\,\mathrm{cm}$
- $z_0 < 10\,\mathrm{cm}$
- $p_t > 100\,\mathrm{MeV}/c$
- $0.410 < \theta < 2.540\,\mathrm{radians}$

$N(\text{DCH hits})$ is the number of DCH hits associated to the track fit: 12 hits is the minimum number of hits required to have a good track fit, since this is equivalent to having 4 hits per superlayer in 3 different superlayers. d_0 and z_0 are the transverse and longitudinal distances of closest approach to the geometrical origin of *BABAR* and are used to reject tracks not pointing to IP. Fake tracks in the DCH have low transverse momentum, so a cut on p_t is used to suppress them. The requirement on the polar angle θ defines the fiducial volume where we have a reliable tracking efficiency estimate. We will refer to these criteria as `GoodTracksAccLoose` criteria.

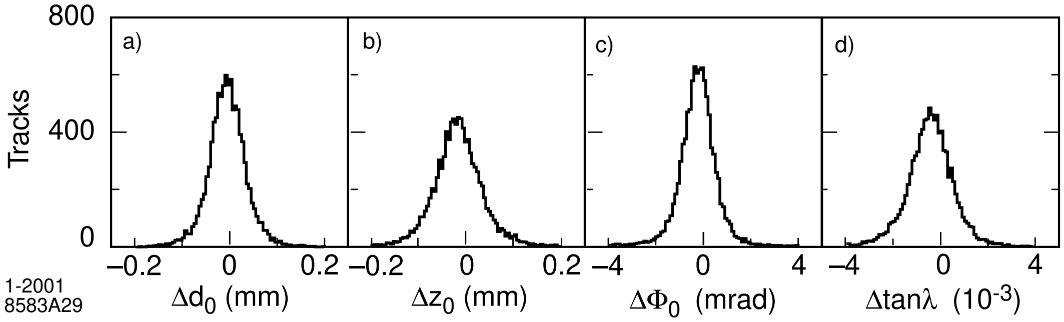

Figure 2.7: Measurements of the differences between the fitted track parameters of the two halves of cosmic ray muons, with transverse momenta above 3 GeV/c, a) Δd_0, b) Δz_0, c) $\Delta\phi_0$, and d) $\Delta\tan\lambda$.

2.3.2 Track Parameter Resolutions

The resolution in the five track parameters is monitored using e^+e^- and $\mu^+\mu^-$ events. It is further investigated offline for tracks in multi-hadron events and cosmic ray muons.

Cosmic rays that are recorded during normal data-taking offer a simple way of studying the track parameter resolution. The upper and lower halves of the cosmic ray tracks traversing the DCH and the SVT are fit as two separate tracks, and the resolution is derived from the difference of the measured parameters for the two track halves. To assure that the tracks pass close to the IP, cuts are applied on the d_0, z_0, and $\tan\lambda$. The results of this comparison for the coordinates of the point of closest approach and the angles are shown in Fig. 2.7 for tracks with momenta above p_t of 3 GeV/c. The distributions are symmetric; the non-Gaussian tails are small. The distributions for the differences in z_0 and $\tan\lambda$ show a clear offset, attributed to residual problems with the internal alignment of the SVT. Based on the full width at half maximum of these distributions the resolutions for single tracks can be stated as

$$\sigma_{d_0} = 23\mu m \qquad \sigma_{\phi_0} = 0.43\,\mathrm{mrad}$$

$$\sigma_{z_0} = 29\mu m \qquad \sigma_{\tan\lambda} = 0.53 \cdot 10^{-3}$$

The dependence of the resolution in d_0 and z_0 on the transverse momentum p_t is presented in Fig. 2.8. The measurement is based on tracks in multi-hadron events. The resolution is determined from the width of the distribution of the difference between the measured parameters, d_0 and z_0, and the coordinates of the vertex reconstructed from the remaining tracks in the event. These distributions peak at zero, but have a tail for positive values due to the effect of particle decays. Consequently, only the negative part of the distributions reflects the measurement error and is used to extract the resolution. Event shape cuts and a cut on the χ^2 of the vertex fit are applied to reduce the effect of weak decays on this measurement. The contribution from the vertex errors are subtracted in quadrature from the measured resolutions. The d_0 and z_0 resolutions so measured are about $25\,\mu$m and $40\,\mu$m respectively at $p_t = 3\,\mathrm{GeV}/c$. These values agree well with expectations, and are also in reasonable agreement with the results obtained from cosmic rays.

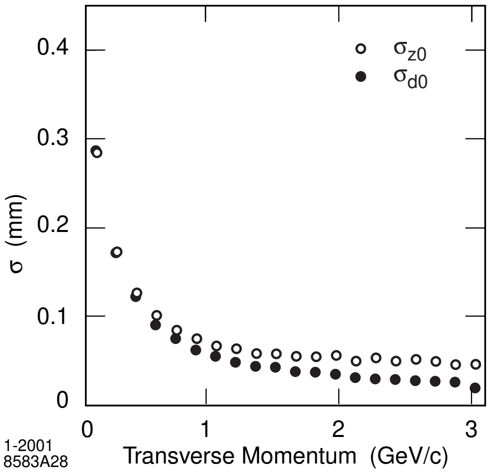

Figure 2.8: Resolution in the parameters d_0 and z_0 for tracks in multi-hadron events as a function of the transverse momentum. The data are corrected for the effects of particle decays and vertexing errors.

Fig. 2.9 shows the estimated error in the measurement of the difference along the z-axis between the vertices of the two neutral B mesons. One of the B's is fully reconstructed, the other serves as a flavor tag (see Chapter 4). The r.m.s. of $190\,\mu$m is dominated by the reconstruction of the tagging B, the r.m.s. resolution for the fully reconstructed B meson is $70\,\mu$m.

While the position and angle measurements near the IP are dominated by the SVT, the DCH contributes primarily to the p_t measurement. Fig. 2.10 shows the resolution in the transverse momentum derived from cosmic muons. The data are well represented by a linear function,

$$\sigma_{p_t}/p_t = (0.13 \pm 0.01)\% \cdot p_t + (0.45 \pm 0.03)\%,$$

where the transverse momentum p_t is measured in GeV/c. These values for the resolution parameters are very close to the initial estimates and can be well reproduced by Monte Carlo simulations.

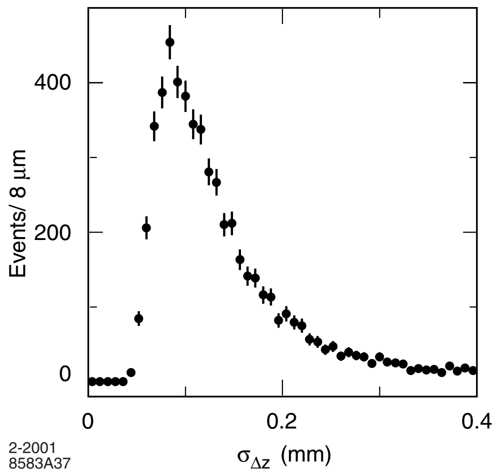

Figure 2.9: Estimated error in the difference Δz between the B meson vertices for a sample of events in which one B^0 is fully reconstructed.

2.4 Particle Identification

The study of *CP*-violation using hadronic final states of the $B\overline{B}$ meson system requires the ability to identify the b-quark charge of one of the B mesons via the cascade decay $b \to c \to s$, while fully reconstructing the final state of the other over a large region of solid angle and momentum. The momenta of the kaons used for flavor tagging extend up to about 2 GeV/c, with most of them below 1 GeV/c, since they come from the secondary decays of *charm* mesons. *Particle Identification* (PID) below 700 MeV/c exploits primarily the dE/dx measurements in the DCH and SVT. In Fig.2.12 dE/dx in the DCH as a function of track momenta is shown for different control samples of particles.

On the other hand, pions from the rare two-body decays $B^0 \to \pi^+\pi^-$and $B^0 \to K^+\pi^-$ must be well-separated from kaons. They have momenta between 1.7 and 4.2 GeV/c with a strong momentum-polar angle correlation between the tracks: higher momenta occur at the more forward angles because of the center-of-mass system boost (Fig.2.11). The momenta of the two daughter tracks in these decays are in a region where the mean DCH dE/dx for kaons and pions differ by only about 1σ. Moreover, given the momentum and therefore mass resolution at high momenta, from kinematics alone, one is not able to adequately distinguish the two decays.

BABAR has therefore a dedicated PID subdetector. It is a new kind of ring-imaging Čerenkov detector called the DIRC [43] (*Detector of Internally Reflected Čerenkov* light). It was designed to be able to provide π/K separation of $\sim 4\ \sigma$ or greater, for all tracks

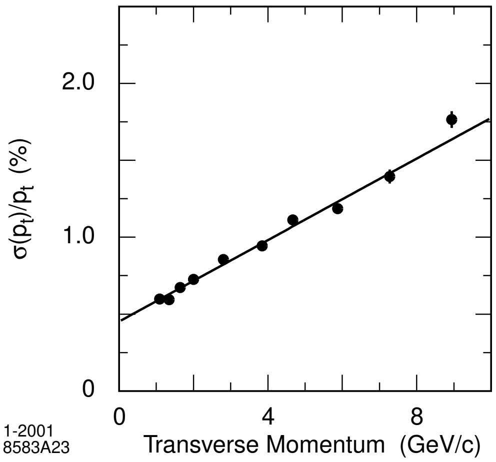

Figure 2.10: Resolution in the transverse momentum p_t determined from cosmic ray muons traversing both the DCH and the SVT.

from B-meson decays from the pion Čerenkov threshold up to 4.2 GeV/c.

The DIRC is placed before the calorimeter and therefore it should be thin and uniform in terms of radiation lengths (to minimize degradation of the calorimeter energy resolution) and small in the radial dimension to reduce the volume, hence, the cost of the calorimeter. Finally, for operation at high luminosity, it needs fast signal response, and should be able to tolerate high backgrounds.

Fig. 2.13 shows a schematic of the DIRC geometry that illustrates the principles of light production, transport, and imaging. The radiator material of the DIRC is synthetic, fused silica in the form of long, thin bars with rectangular cross section. These bars serve both as radiators and as light pipes for the portion of the light trapped in the radiator by total internal reflection. Fused, synthetic silica is chosen because of its resistance to ionizing radiation, its long attenuation length, large index of refraction, low chromatic dispersion within the wavelength acceptance of the DIRC, and because it allows an excellent optical finish on the surfaces of the bars.

In the following, the variable θ_c is used to designate the Čerenkov angle, ϕ_c denotes the azimuthal angle of a Čerenkov photon around the track direction, and n represents the mean index of refraction of fused silica ($n = 1.473$), with the familiar relation

$$\cos\theta_c = 1/n\beta \tag{2.3}$$

($\beta = v/c$, $v =$ velocity of the particle, $c =$ velocity of light).

For particles with $\beta \approx 1$, some photons will always lie within the total internal re-

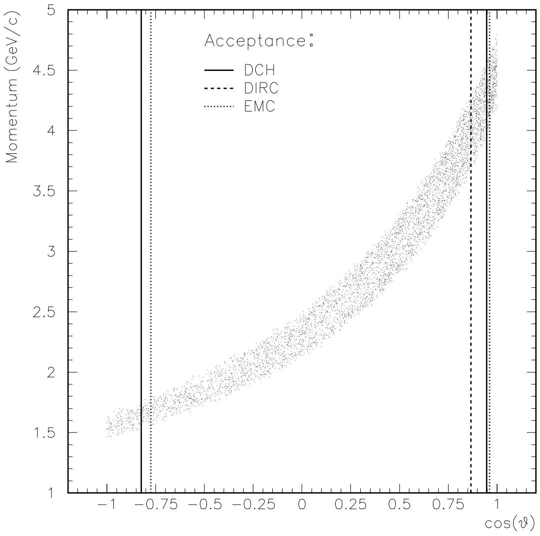

Figure 2.11: Lab momentum vs. cosine of the polar angle for two-body decay products. Vertical lines mark the boundaries of DCH (solid), DIRC (dashed), and EMC (dot) detectors.

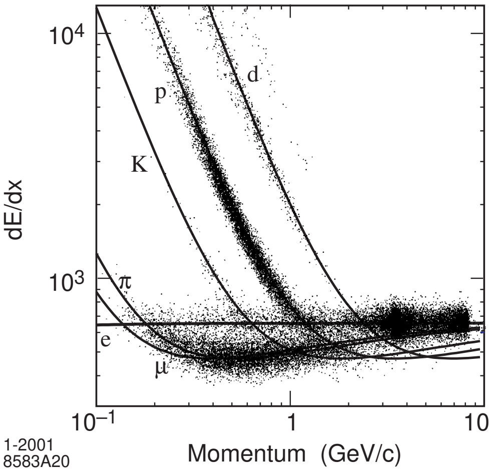

Figure 2.12: Measurement of dE/dx in the DCH as a function of track momenta. The data include large samples of beam background triggers, as evident from the high rate of protons. The curves show the Bethe-Bloch predictions derived from selected control samples of particles of different masses. is clear that dE/dx in the DCH is able to separate pion from kaon at relatively low momenta

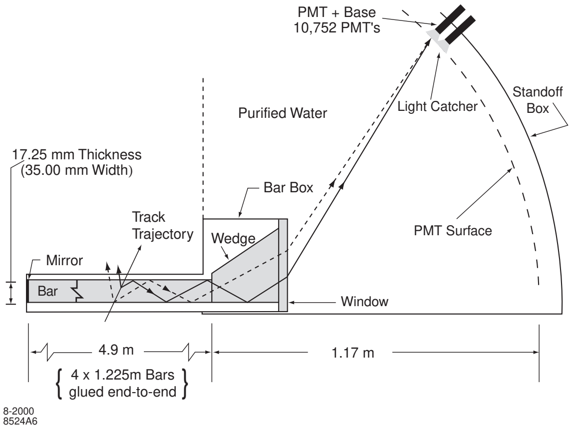

Figure 2.13: Schematics of the DIRC fused silica radiator bar and imaging region. Not shown is a 6 mradangle on the bottom surface of the wedge.

flection limit, and will be transported to either one or both ends of the bar, depending on the particle incident angle. To avoid instrumenting both ends of the bar with photon detectors, a mirror is placed at the forward end, perpendicular to the bar axis, to reflect incident photons to the backward, instrumented end.

Once photons arrive at the instrumented end, most of them emerge into a water-filled expansion region, called the *standoff box*. A fused silica *wedge* at the exit of the bar reflects photons at large angles relative to the bar axis. It thereby reduces the size of the required detection surface and recovers those photons that would otherwise be lost due to internal reflection at the fused silica/water interface. The photons are detected by an array of densely packed photomultiplier tubes (PMTs), each surrounded by reflecting *light catcher* cones to capture light which would otherwise miss the active area of the PMT. The PMTs are placed at a distance of about 1.2 m from the bar end. The expected Čerenkov light pattern at this surface is essentially a conic section, where the cone opening-angle is the Čerenkov production angle modified by refraction at the exit from the fused silica window.

The DIRC is intrinsically a three-dimensional imaging device. Photons are focused onto the phototube detection surface via a *pinhole* defined by the exit aperture of the bar, so that the photon propagation angles can be measured. Imaging in the DIRC occurs in three dimensions, by recording the time of the PMT signal. As the track position and angles are known from the tracking system, the two angles (θ_c, ϕ_c) can be determined. This over-constraint on the angles is particularly useful in dealing with ambiguities and

Cut
$\lvert\Delta M - 0.1454\,\mathrm{GeV}/c^2\rvert < 3\sigma_{\Delta M}$
$\lvert M(K\pi) - m(D^0)\rvert < 3\sigma_{D^0}\lvert$
$p^*(D^0) > 2.5\,\mathrm{GeV}/c$
$\cos\theta^*_K < 0.8$
$1.75 < p(\pi) < 4.25\,\mathrm{GeV}/c$ or $1.75 < p(K) < 4.25\,\mathrm{GeV}/c$

Table 2.3: Cuts used to select a control sample of $D^{*+} \to K^-\pi^+\pi^+$ decays.

high background rates.

2.4.1 Pion-Kaon separation

In order to assess and parameterize the performance of DIRC, without relying on Monte Carlo simulation, one must identify a source of pions and kaons, the selection of which does not utilize particle ID from the DIRC. An ideal control sample consists of the daughter tracks from $D^0 \to K^-\pi^+$ decays in the reaction $D^{*+} \to D^0\pi^+ \to (K^-\pi^+)\pi^+$. The $\pi(K)$ track is always the one with the same(opposite) charge as the D^* and cutting on the small $D^{*+} - D^0$ mass difference ensures that there is virtually no contamination from incorrectly reconstructed D^0 candidates (i.e. a true $D^0 \to K^-\pi^+$ reconstructed as a $\bar{D}^0 \to \pi^-K^+$ candidate and then combined with a random track to form a D^{*-} candidate). Candidates in the D^0 mass sideband regions are used for background subtraction. The resulting sample can be used to provide a parameterization of the θ_c distributions for pions and kaons. A simple set of cuts were used to select a very clean sample of D^{*+} decays in which either the K or π track from the D^0 decay has a momentum in the range $1.75 - 4.25\,\mathrm{GeV}/c$, covering 90% of the momentum range of the daughters of $B \to h'^+h^-$ decays. The cuts are summarized in Tab.2.3. Loose requirements on tracks quality are used. ΔM is the measured mass difference between the D^{*+} candidate and the D^0 candidate, $\sigma_{\Delta M}$ is the measured resolution on this quantity, $M(K\pi)$ is the reconstructed D^0 mass and σ_{D^0} is the resolution on $M(K\pi)$. The mass resolutions are measured to be $0.6\,\mathrm{MeV}/c^2$ for $\sigma_{\Delta M}$ and $9\,\mathrm{MeV}/c^2$ for σ_{D^0}. The quantity $\cos\theta^*_K$ is the cosine of the angle of the kaon track with respect to the D^0 flight direction, measured in the D^0 center of mass system. For signal decays this distribution is flat, whereas the combinatorial background is peaked in the forward and backward directions.

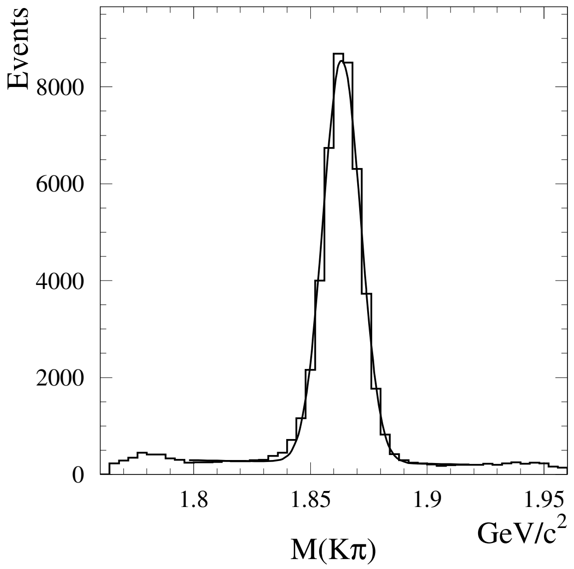

Figure 2.14: The $K^-\pi^+$ invariant mass distributions for D^0 candidates in data using the cuts described in the text.

Fig. 2.14 shows the $M(K^-\pi^+)$ distribution with all cuts applied except that on $M(K^-\pi^+)$ itself. The fitted number of D^0 candidates is 41900 ± 210 and the purity is 94%.

The same set of cuts is used to select a sample of D^{*+} in the Monte Carlo data. This sample is also used to check that the Monte Carlo accurately reproduces the efficiency of the PID cuts (Tab. 3.2). This is demonstrated in Fig.2.15 and Fig.2.16 which display the efficiencies of the PID cuts used in the $B \to h'^+h^-$ analysis for kaons and pions, respectively, for both the data and Monte Carlo control samples. There is good agreement between the two samples. Fig.2.17 and Fig.2.18 compare the efficiencies obtained from the Monte Carlo D^{*+} control sample to those obtained directly from Monte Carlo $B \to h'^+h^-$ decays.

Pion and kaon θ_c

We define θ_c' as the expected Čerenkov angle for a given particle hypothesis (according to Eq.2.3). The θ_c parameterizations are therefore determined by forming the $\theta_c - \theta_c'$ distributions for the kaon and pion tracks of the D^0 decays in the D^{*+} control sample. These distributions are obtained in $\cos\theta$ slices in the range $-1.0 \to 1.0$, where θ is the polar angle of the track and are fitted to single Gaussians. The widths (σ_{θ_c}) and offsets from zero of the means are tabulated. Fig. 2.19 displays the offsets and widths of the

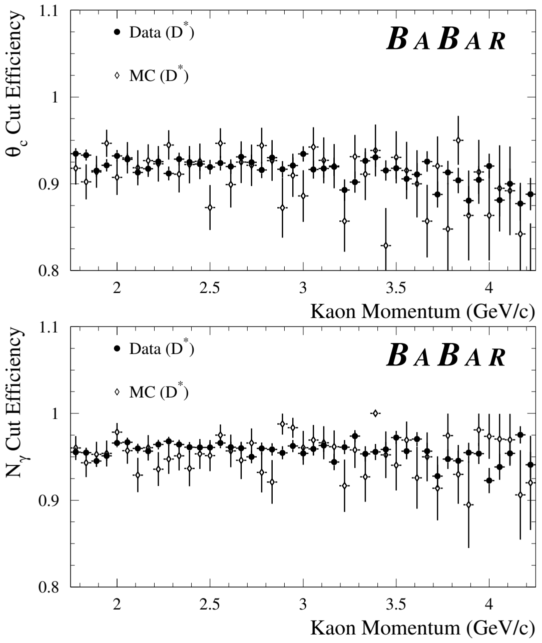

Figure 2.15: The efficiency versus momentum of the $\theta_c > 0$ cut (top) and the $N_\gamma > 5$ cut (bottom) for kaons in the D^{*+} control sample in data (filled circles) and Monte Carlo simulation (open diamonds).

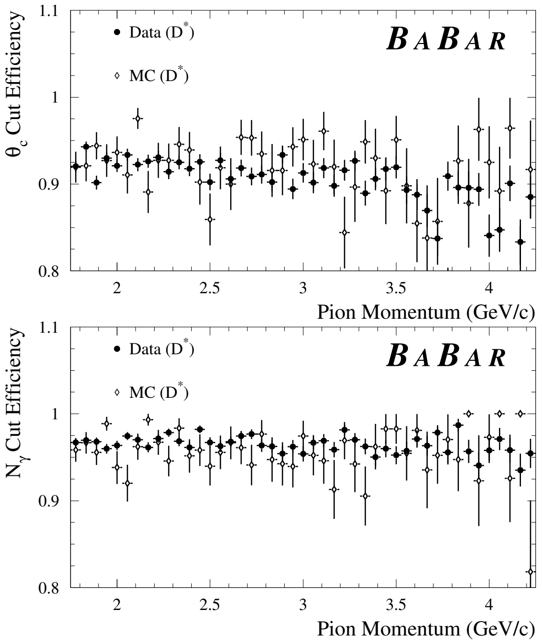

Figure 2.16: The efficiency versus momentum of the $\theta_c > 0$ cut (top) and the $N_\gamma > 5$ cut (bottom) for pions in the D^{*+} control sample in data (filled circles) and Monte Carlo simulation (open diamonds).

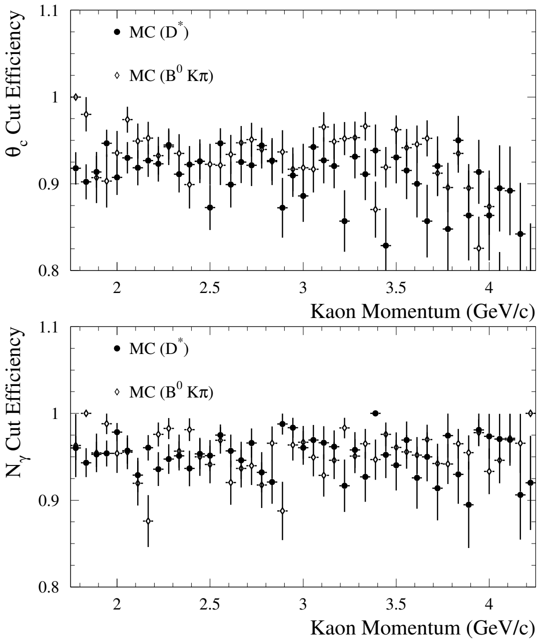

Figure 2.17: The efficiency versus momentum of the $\theta_c > 0$ cut (top) and the $N_\gamma > 5$ cut (bottom) for kaons in the Monte Carlo D^{*+} control sample (filled circles) and Monte Carlo simulated $B \to h'^{+}h^{-}$ decays (open diamonds).

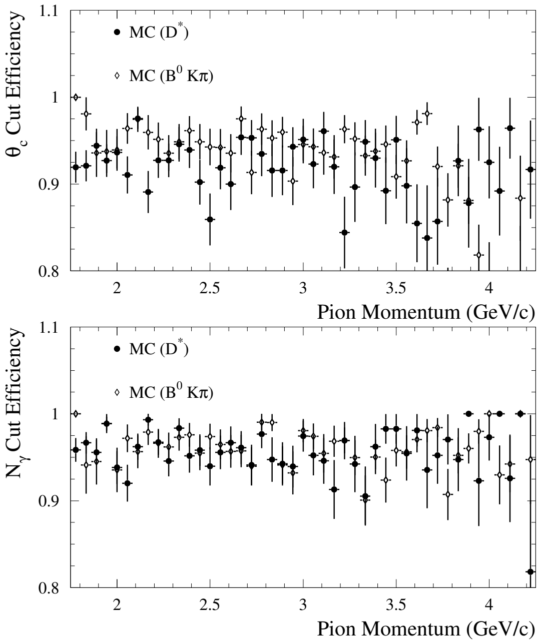

Figure 2.18: The efficiency versus momentum of the $\theta_c > 0$ cut (top) and the $N_\gamma > 5$ cut (bottom) for pions in the Monte Carlo D^{*+} control sample (filled circles) and Monte Carlo simulated $B \to h'^{+}h^{-}$ decays (open diamonds).

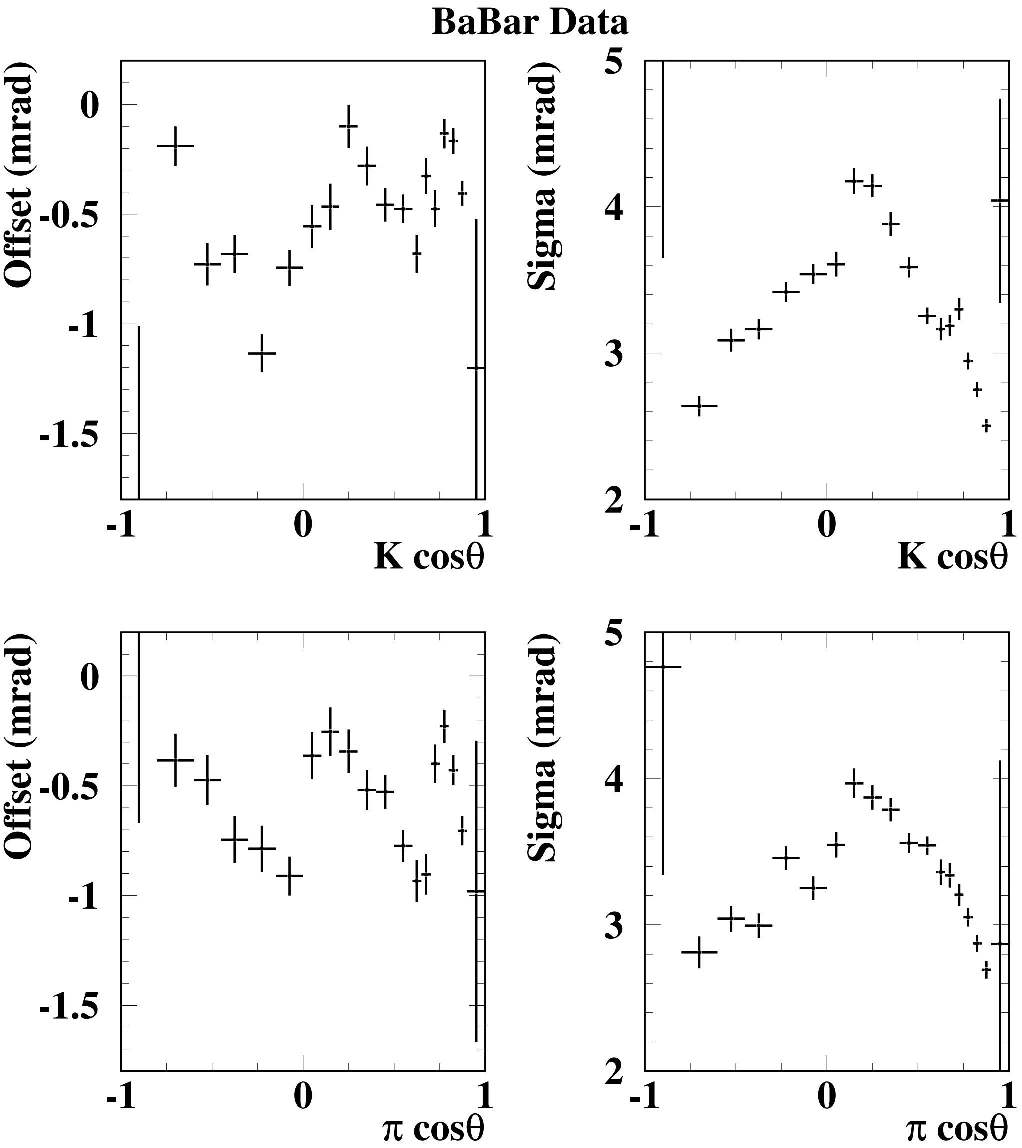

Figure 2.19: The offsets (left) of the measured mean θ_c from the expected value, and resolutions on θ_c (right) for kaons (top) and pions (bottom).

Gaussian fits.

The distributions of θ_c versus track momentum and measured K–π separation are given in Fig. 2.20. The K–π separation is defined as $(\langle\theta_c(\pi)\rangle - \langle\theta_c(K)\rangle)/\langle\sigma_{\theta_c}\rangle$. The separation is greater than 2.5σ throughout the momentum range.

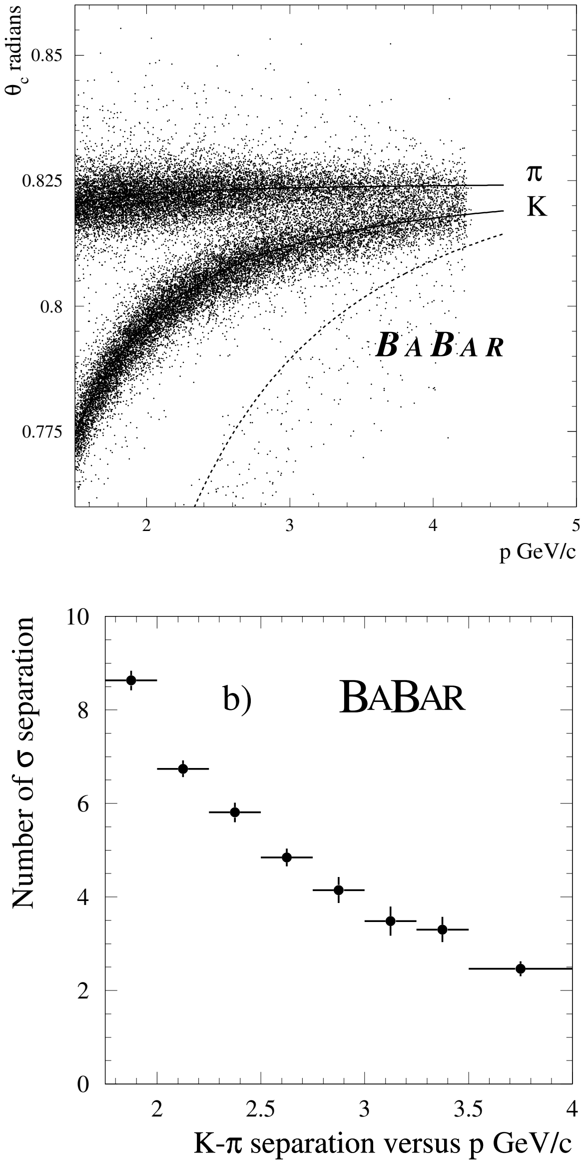

Figure 2.20: The Čerenkov angle (upper plot) and K–π separation (lower plot) as functions of momentum for tracks in the D^0 control sample. Both tracks must be in the same momentum bin to achieve a given θ_c separation. Tracks below the dashed line in upper plot are rejected as proton candidates.

There are a few cases where a true kaon(pion) is assigned a θ_c measurement consistent with a pion(kaon). This effect is due to biases in the θ_c reconstruction algorithm and *not* to poorly reconstructed θ_c measurements which would lead to long, non-Gaussian tails. Moreover, the decay amplitude for $D^0 \to K^+\pi^-$ is suppressed twice by Cabibbo angle and the D^0 mass resolution is 4 times worse when a daughter track is assigned the wrong mass. The presence of this decay, therefore, cannot explain the size of the effect. We in fact observe a "satellite" peak centered at the expected θ_c difference for pions and kaons by plotting $\theta_c - \theta_c'$ in bins of momentum. To good approximation, the satellite peak constitutes 3%(2%) of the total number of selected kaon(pion) tracks and has a width three times that of the primary peak. Fig.2.21 displays the quantity $\theta_c - \theta_c'$ for kaon tracks in four representative momentum bins. Overlayed on the distributions are the results of the double Gaussian fits to both the primary and the satellite peaks. No significant momentum or $\cos\theta$ dependence is observed. The effect is present in Monte Carlo simulated decays at a somewhat smaller level ($\sim 1\%$).

The satellite peak is included in the θ_c parameterization as a second Gaussian with width and relative area fixed to the values described above, and centered at the opposite particle hypothesis.

Fig. 2.22 shows the distribution of the quantity $(\theta_c - \theta_c')/\sigma_{\theta_c}$, along with Gaussian fits, as a function of track momentum for kaons in the D^{*+} control sample. The distributions for pions are similar. The distributions are centered at zero and have widths close to one. The clusters of events to the right of the each peak are the satellite events referred to above.

The θ_c measurements for pions and kaons in Monte Carlo simulated $B \to h'^+h^-$ decays is compared with those derived from the Monte Carlo D^{*+} control sample and a good agreement is found. This validates the use of the D^{*+} decays in the data as a means of parameterizing the θ_c resolutions and offsets for the signal sample.

Since data collected in year 2001 profit of a better detector alignment and of a better tuned reconstruction algorithm, the θ_c parameterization is expected to be different for Run 2 data. Fig.2.23 shows the offset and resolution parameterization for Run 2 data. The global features are similar to Run 1 data (compare with Fig.2.19) but with smaller offsets and a somewhat better resolution. We therefore use separate parameterizations for the different datasets. Fig.2.24 shows example pull distributions for Run 2. The "satellite" peaks observed in Run 1 is not present in Run 2.

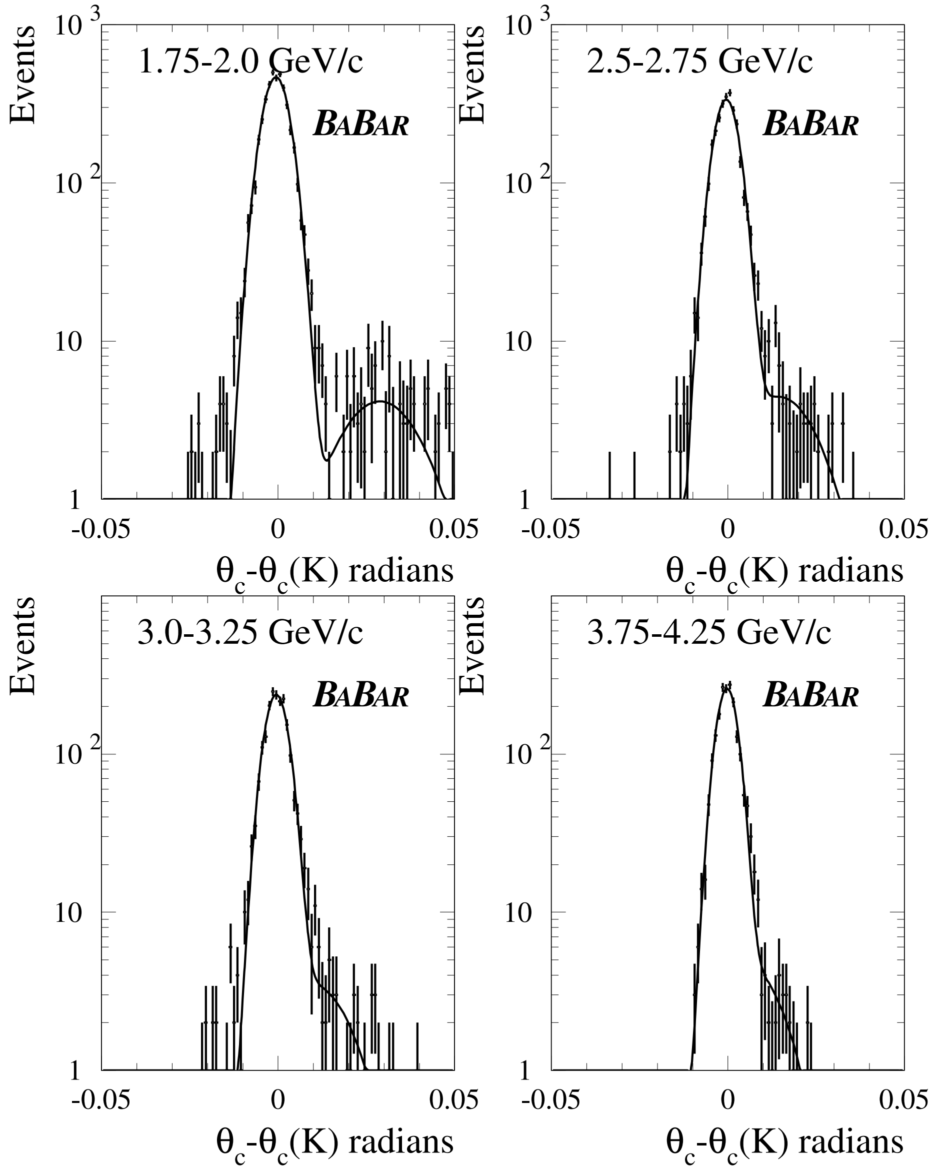

Figure 2.21: The distributions of $\theta_c - \theta'_c$ for kaon tracks selected from the D^{*+} control sample in selected bins of momentum.

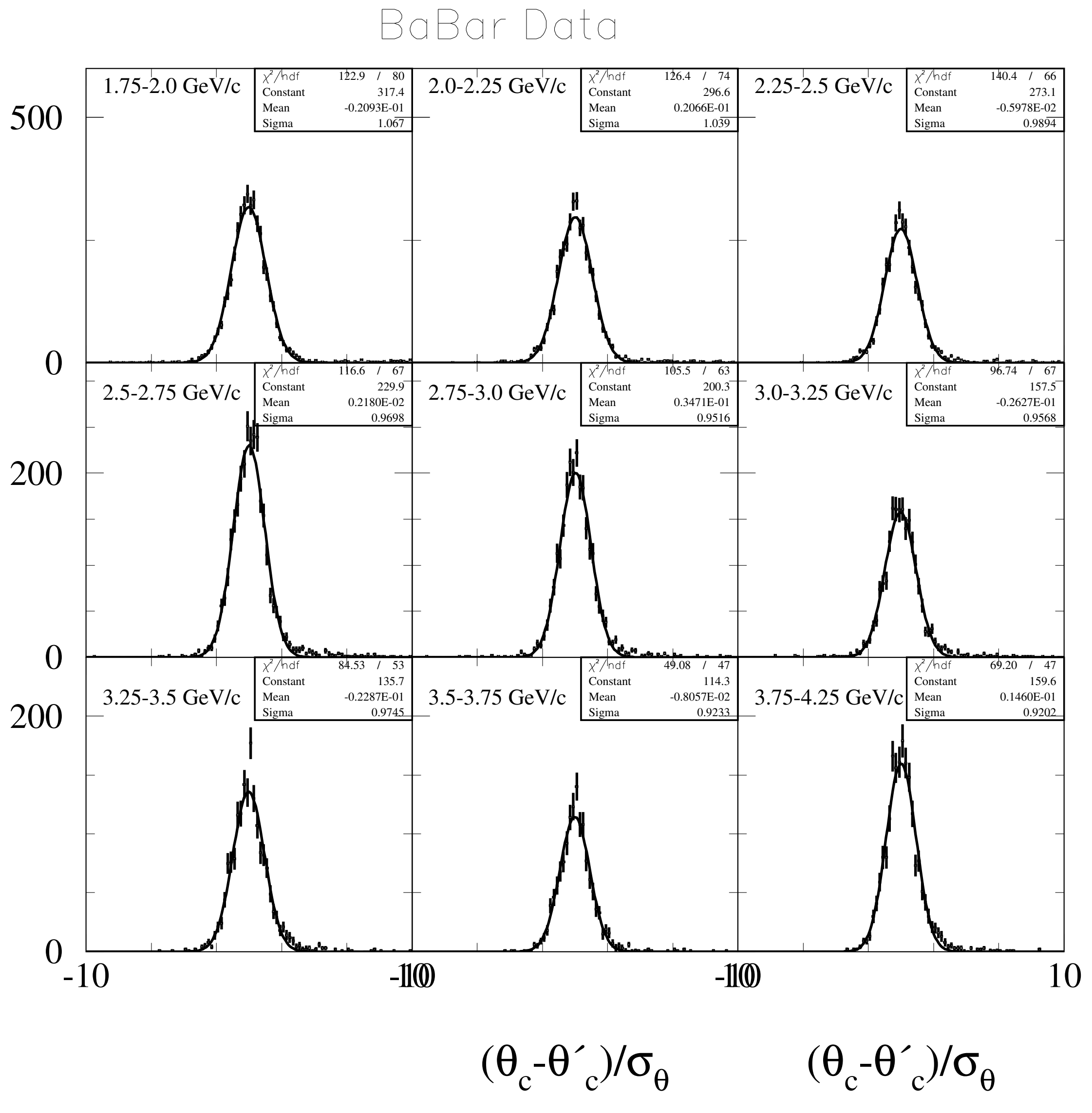

Figure 2.22: The distributions of $(\theta_c - \theta'_c)/\sigma_{\theta_c}$ for kaon tracks selected from the D^{*+} control sample in bins of 250 MeV/c, except for the last bin which spans the range $3.75 < p(K) < 4.25$ GeV/c.

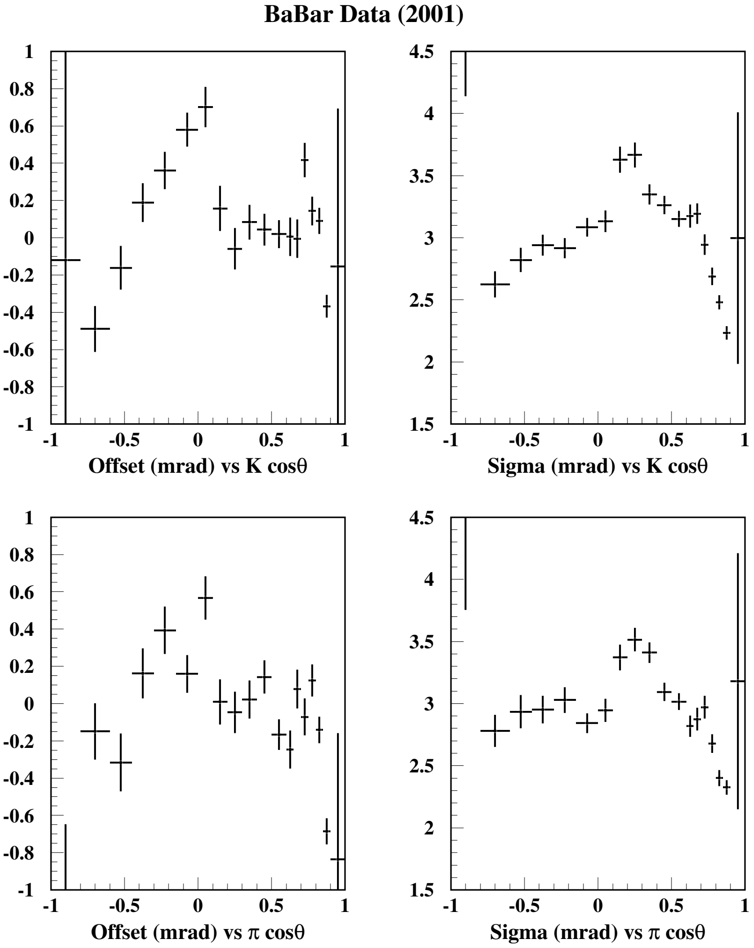

Figure 2.23: Distributions of θ_c offsets (left) and resolutions (right) in the Run 2 D^0 control sample as functions of track polar angle. Top plots are for kaons, bottom plots are for pions.

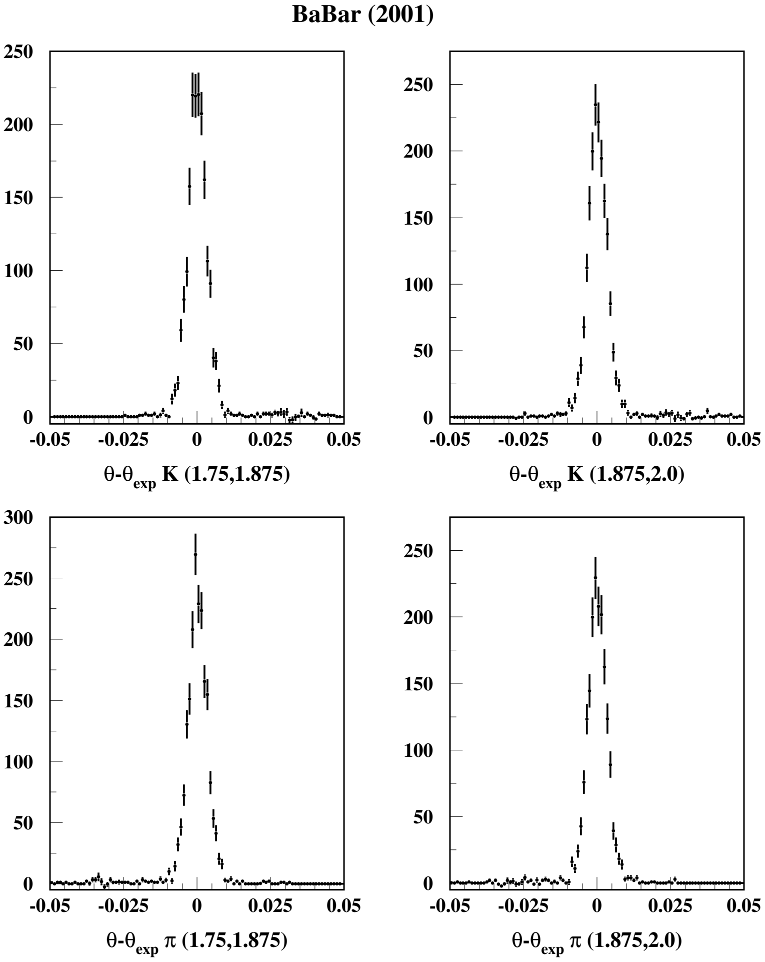

Figure 2.24: Distributions of $\theta_c - \theta_c(\mathrm{exp})$ + offset for kaons (top) and pions (bottom) in the Run 2 D^0 control sample. The left (right) plots correspond to the momentum bin 1.75–1.875 GeV/c (1.875–2.0 GeV/c).

2.5 Electromagnetic Calorimeter and Instrumented Flux Return

2.5.1 Electromagnetic Calorimeter

The electromagnetic calorimeter (EMC) is designed to detect electromagnetic showers with excellent energy and angular resolution over the energy range from 20 MeV to 4 GeV. This coverage allows the detection of low energy π^0s and η^0s from B decays and higher energy photons and electrons from electromagnetic, weak, and radiative processes. The EMC is a finely segmented array of projective geometry made of thallium doped cesium iodide (CsI(Tl)) crystals. The crystals are arranged in modules that are supported individually from an external support structure. This structure is built in two sections, a barrel and a forward endcap. To obtain the desired resolution, the amount of material in front of and in-between the crystals is minimized. The individual crystals are read out by pairs of silicon PIN diodes. Low noise analog circuits and frequent, precise calibration of the electronics and energy response over the full dynamic range are crucial for maintaining the desired performance.

Neutral particles (photons, π^0, neutral hadrons) are detected in the EMC as clusters of close crystals where energy has been deposited They are required to be not matched to any charged track estrapolated from tracking volume to EMC inner surface. Quality requirements applied to those clusters allow to reject fakes or particles (especially low energy photons) not coming from the collision events. In this analysis `GoodNeutralLooseAcc` photon quality criteria are imposed on EMC clusters. They basically tend to reject background photons accepting showers with $E > 30$ MeV in the EMC fiducial volume and $LAT < 0.8$. A lateral energy distribution variable, LAT, is defined as

$$LAT = \frac{\sum_{i=3}^{n} E_i r_i^2}{\sum_{i=3}^{n} E_i r_i^2 + E_1 r_0^2 + E_2 r_0^2} \quad E_1 \geq E_2 \geq ... \geq E_n \tag{2.4}$$

where n is the number of crystals in the cluster,r_0 the average distance between two crystal front faces ($\sim$ 5 cm), E_i is the energy deposited in the i^{th} crystal, and r_i is the distance between the i^{th} crystal and the cluster center (the center of gravity). This variable is able to discriminate between electromagnetic and hadronic showers since electromagnetic showers have a narrower, Gaussian distribution around the center of gravity.

EMC is also crucial for electron identification. Different criteria are established to select electron with different level of purity. Electrons are separated from charged hadrons primarily on the basis of the ratio of the energy E deposited in the EMC to the track momentum p ($\frac{E}{p}$) and of LAT. In addition, the $\mathrm{d}E/\mathrm{d}x$ energy loss in the DCH and the DIRC Cherenkov angle are required to be consistent with an electron. The most important variable for the discrimination of hadrons is the ratio of the shower energy to the track momentum (E/p). Fig. 2.25 shows the efficiency for electron identification and the pion[4] mis-identification probability as a function of momentum for two sets of selection criteria.

The electron efficiency is measured using radiative Bhabhas and $e^+e^- \to e^+e^-e^+e^-$ events. The pion misidentification probability is measured for selected charged pions from K^0_S decays and three-prong τ decays. A tight (very tight) selection results in an efficiency plateau at 94.8% (88.1%) in the momentum range $0.5\,\mathrm{GeV}/c < p < 2\,\mathrm{GeV}/c$. The pion misidentification probability is of order 0.3% (0.15%) for the tight (very tight) selection criteria. In this analysis we adopt the very tight selection (`VeryTightElectronSelection`).

2.5.2 Instrumented Flux Return

The instrumented flux return (IFR) is designed to identify muons and to detect neutral hadrons. For this purpose, the magnet flux return steel in the barrel and the two end doors are segmented into layers, increasing in thickness from 2 cm on the inside to 10 cm at the outside. Between these steel absorbers, single gap resistive plate chambers (RPCs) are inserted which detect streamers from ionizing particles via external capacitive readout strips: the signals are read out on both sides of the gap by external electrodes made of aluminum strips. There are 19 layers of RPCs in the barrel sectors and 18 layers in the end doors. The total thickness of steel at normal incidence is 65 cm in the barrel region, 60 cm in the endcaps. Two additional cylindrical layers of RPCs with four readout planes are placed just in front of the magnet cryostat to detect particles exiting the EMC.

Muons are identified by measuring the number of traversed interaction lenghts in the entire detector and comparing it with the number of expected interaction lenghts for a muon of a given momentum. Moreover, the projected intersections of a track with the RPC planes are computed and, for each readout plane, all strips clusters detected within a predefined distance from the predicted intersection are associated with the track: the average number and the r.m.s. of the distribution of RPC strips per layer gives additional

---

[4] Pion contamination is an important figure of merit since pions in hadronic decays at $\Upsilon(4S)$ are the most abundant particle species: there are on average 7 pions per lepton.

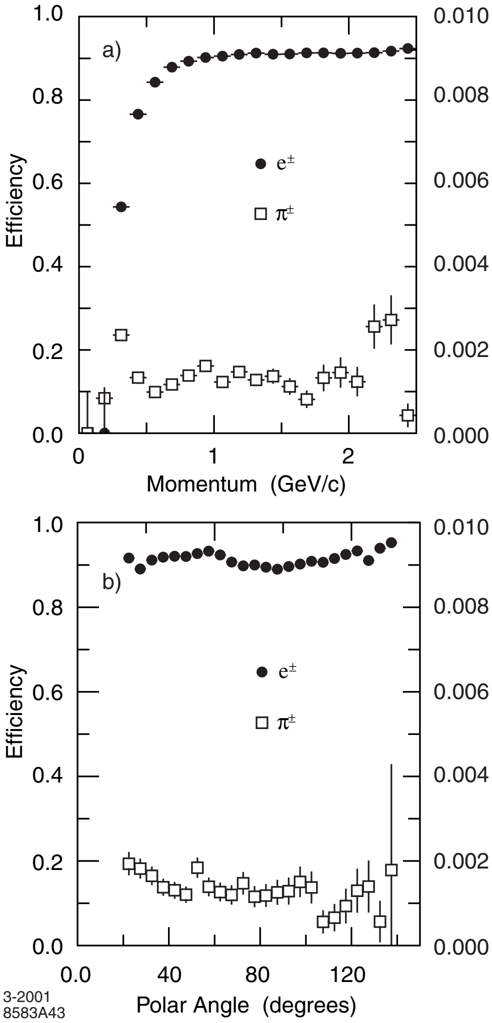

Figure 2.25: The electron efficiency (left scale) and pion mis-identification probability (right scale) as a function of a) the particle momentum and b) the polar angle, measured in the laboratory system.

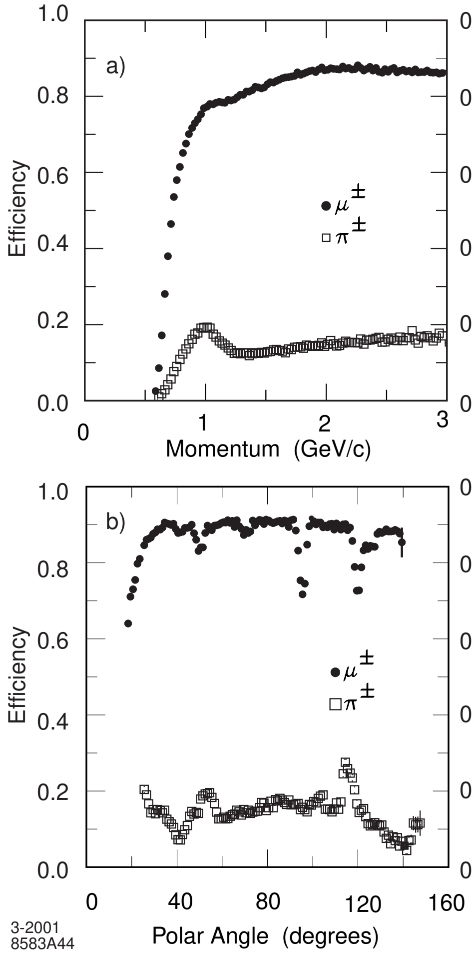

Figure 2.26: Muon efficiency (left scale) and pion misidentification probability (right scale) as a function of a) the laboratory track momentum, and b) the polar angle (for $1.5 < p < 3.0\,\mathrm{GeV}/c$ momentum), obtained with loose selection criteria.

μ/π discriminating power. We expect in fact the average number of strips per layer to be larger for pions producing an hadronic interaction than for muons. Other variables exploiting clusters distribution shapes are constructed. Selection criteria based on all these variables are applied to select muons. The performance of the muon selection has been tested on samples of kinematically identified muons from $\mu\mu ee$ and $\mu\mu\gamma$ final states and pions from three-prong τ decays and $K_S \to \pi^+\pi^-$ decays. As illustrated in Fig. 2.26, a muon detection efficiency of $\sim$ 90% has been achieved in the momentum range of $1.5 < p < 3.0\,\mathrm{GeV}/c$ with a pion misidentification probability of about 6–8%. Decays in flight contribute about 2% to this probability. The fake rate can be reduced by a factor of about two by applying a tighter selection criteria which lower the muon detection efficiency to about 80%.

Chapter 3

Measurement of Branching Ratios

3.1 Introduction

As described in Chapter 1, the study of charmless hadronic B decays plays an important role in understanding the mechanism of *CP* violation. In this Chapter a description of the search for charmless twobody $B^0 \to h'^+h^-$ decays with $h', h = \pi, K$ in *BABAR* data collected during the year 2000 (*Run 1 data*) is given. Final results on this data set have been already published in [1]. Background suppression and particle identification are the two most critical issues for this analysis. The dominant background comes from continuum $e^+e^- \to q\bar{q}$ production. Since the charmless two-body B decays Branching Ratios are small compared to $q\bar{q}$ cross section, an analysis with high efficiency on signal able to separate on statistical basis signal from background is preferred to a high-purity low-size sample analysis. Most of this separation is achieved by using kinematic and topological variables. In Section 3.2, all relevant variables are introduced. The CLEO approach of using a *Fisher discriminant* technique based on event topology is also adopted in this analysis. In Section 3.3 the event selection defining the final analysis data sample is described and its efficiency discussed. Particle Identification is clearly vital to measure decay mode containing pions and kaons and, since in these decays the particles have 1.7-4.2 GeV momentum (Fig.3.1), the Čerenkov angle θ_c is the only measurement which provides good K-π discrimination. A detailed study has been reported in Section 2.4. In Section 3.4 the maximum likelihood fit used to extract the number of $B \to \pi^+\pi^-$,$B \to K^+\pi^-$ and $B \to K^+K^-$ decays (*yields*) in the data sample is described. The fit incorporates the Fisher output and kinematic variables of the B candidate, which are used to separate signal and background, as well as the Čerenkov angle, which is used to distinguish between the three types of signal. Finally systematics effects are evaluated and Branching Ratios are determined. Charge asymmetry in the self-tagging channel $K^\pm\pi^\mp$

$$\mathcal{A}_{K\pi} = \frac{N_{K^-\pi^+} - N_{K^+\pi^-}}{N_{K^-\pi^+} + N_{K^+\pi^-}}; \tag{3.1}$$

is also measured. In Section 3.5 final results are summarized.

3.2 Discriminant Variables

Kinematic variables

Kinematic constraint of $\Upsilon(4S)$ decay into a $B\bar{B}$ pair can be exploited to define a pair of variables, *beam energy-substituted mass* m_{ES} and *energy difference* ΔE.

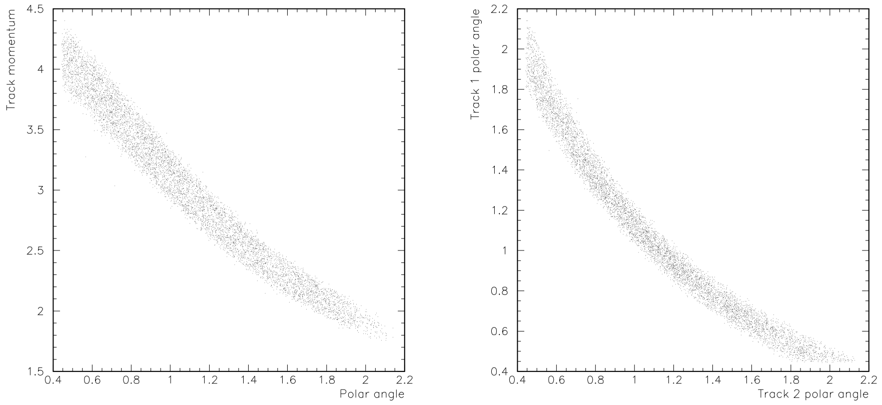

Figure 3.1: Correlation plots of track momentum vs. polar angle (left) and between the polar angles of the two tracks (right) in signal $\pi\pi$ Monte Carlo.

We define the *beam energy-substituted mass* [44] as:

$$m_{\rm ES} = \sqrt{(\frac{1}{2}s + \mathbf{p_0} \cdot \mathbf{p_B})^2/E_0^2 - p_B^2}\,, \tag{3.2}$$

where $\sqrt{s}$ and E_0 are the total energies of the e^+e^- system in the Center of Mass (CM) and laboratory (LAB) frames, respectively; $\mathbf{p_0}$ and $\mathbf{p_B}$ are the momentum vectors in the LAB frame of the e^+e^- system and the B candidate, respectively; and p_B is the magnitude of the B candidate momentum in the LAB frame. An equivalent definition of this variable (see for example [5]) is given by

$$m_{\rm ES} = \sqrt{(\sqrt{s}/2)^2 - p_B^{*2}}\,, \tag{3.3}$$

where p^* is the B candidate momentum in the CM frame. In this form it is clear that, since $p_B^{*2} \ll (\sqrt{s}/2)^2$, the experimental resolution on $m_{\rm ES}$ is dominated by beam energy fluctuations.

The advantage of using the definition in Eq.3.2 is that there are no differences between the distributions for $B \to \pi^+\pi^-$, $B \to K^+\pi^-$ and $B \to K^+K^-$ decays. To an excellent approximation, the shapes of the $m_{\rm ES}$ distributions for all fully-reconstructed B decays to final states with charged tracks only are Gaussian and practically identical. Plots of the distribution for signal and background events are given in Section 3.4.1.

The *energy difference* ΔE is defined as

$$\Delta E = E_B^* - \sqrt{s}/2\,, \tag{3.4}$$

where E_B^* is the B candidate energy in the CM frame. Signal events are Gaussian distributed in ΔE. Detector momentum resolution is the main component of this experimental smearing. For this analysis, since the pion mass is assigned to all tracks, the $B \to K^+\pi^-$ and K^+K^- decays have ΔE shifted from zero by an amount depending on the momenta of the tracks. From Monte Carlo simulation we find average shifts of -45 and $-91\,\mathrm{MeV}$ for the $K^+\pi^-$ and K^+K^- decays, respectively. This is shown Section 3.4.1.

It is important to notice that m_{ES} and ΔE are dependent variables by their definition; but, since the sources of experimental smearing are uncorrelated (beams energy for m_{ES} and detector momentum resolution for ΔE), m_{ES} and ΔE also are practically uncorrelated.

Topological variables

A powerful method to discriminate signal events from $q\overline{q}$ background events exploits the differences in their characteristic topologies. In a true signal event, the primary e^+e^- pair produces a $B\overline{B}$ pair via the $\Upsilon(4S)$ resonance. In the $\Upsilon(4S)$ rest frame, the B mesons have low momenta ($\sim 340\,\mathrm{MeV}/c$), so that the decay of each B meson is nearly isotropic. An additional feature of a signal event is that there is no correlation between the directions of the decay products coming from the two B mesons.

In a light-quark (u, d, s) continuum event and $c\overline{c}$ event, on the contrary, the event shape has a pronounced two-jet structure, so there is a strongly preferred direction characterizing the whole event. Fake B candidates from such an event will therefore tend to have less isotropic decay shapes in the $\Upsilon(4S)$ rest frame, and there will also be correlations between the directions of the decay products of the two B meson candidates, since they will tend to lie within the two jets.

A set of discriminating variables used for continuum identification and suppression can be chosen. There are many of them, but at some level they are all correlated, since they are exploiting the same physical information. In the following we give an incomplete list and we choose few of them among those more powerful in separating background from signal. The choice of reference frame can affect the discriminating power of the variables in use. For global event variables, it is appropriate to use the $\Upsilon(4S)$ rest frame, while for variables using properties of the B decay products, the B rest frame is used. In practice, this distinction does not make very much difference, as the two frames are very similar, owing to the small momentum of the B in the $\Upsilon(4S)$ rest frame.

Another consideration when using each of these variables is the choice of the subset of the event to which it should be applied. For some variables, only the charged tracks in the event are used, for others all charged and neutral candidates are included. For discrimination purposes, a variable may be applied globally to the event, or just to the decay products of the signal B candidate or of the other B in the event (the latter is hereafter referred to as the 'rest of the event').

- **Thrust**

  The thrust axis of an event, $\hat{T}$, is defined to be the direction which maximizes the sum of the longitudinal momenta of the particles. Thrust, T, is related to this direction [45] by

  $$T = \frac{\sum_i |\hat{T} \cdot \mathbf{p}_i|}{\sum_i |\mathbf{p}_i|}. \tag{3.5}$$

  The allowed range of T is (0.5, 1), where $T \sim 1$ corresponds to a highly directional event, and $T = 0.5$ corresponds to an isotropic event.

  In a typical background event for a two-body decay, the decay particles of the B candidate lie in one of the two jets, having therefore opposite directions. Thus the decay axis of the B candidate is roughly collinear with the thrust axis for the rest of the event. For a true signal event, the B decay axis is uncorrelated with the thrust axis of the rest of the event, which in that case comes from the decay of the other B meson.

  For background discrimination, the cosine of the angle between the thrust axis of the rest of the event is usually taken with each of the following: the B direction; each B decay product direction; the thrust axis of the signal B decay products.

- **Sphericity**

  As with thrust, sphericity provides good separation of $q\overline{q}$ continuum events and signal again due to the jet structure of $q\overline{q}$ events. Sphericity is a measure of the sum of the squares of transverse momenta for each track with respect to the event axis. Defined over the interval (0,1), with highly directional events having low sphericity, and isotropic events corresponding to sphericity = 1.

  Sphericity is defined [46] as,

  $$S = \frac{3}{2}(\lambda_2 + \lambda_3)\,, \tag{3.6}$$

where λ_2 and λ_3 are the two larger eigenvalues of the diagonalized sphericity tensor

$$S^{\alpha\beta} = \frac{\sum_i p_i^\alpha p_i^\beta}{\sum_i \mathbf{p}_i^2}\,, \tag{3.7}$$

where $\alpha, \beta = 1{,}2{,}3$ correspond to the x, y, z components. Sphericity distributions for typical signal and continuum background Monte Carlo events are shown in Fig. 3.2.

The Sphericity Axis of the system is determined by the direction of the eigenvector corresponding to the largest eigenvalue. The sphericity axis of the rest of the event is used in an analogous way to the thrust axis of the rest of the event. The cosine of the angle between the sphericity axis of the rest of the event taken with the sphericity axis of the signal B decay products is indicated as $\cos\theta_S$ (Fig. 3.3).

- **Aplanarity**

  Aplanarity is a measure of the transverse component of momentum out of the event plane. It is related to the smallest eigenvalue of the sphericity tensor [46] by

$$A = \frac{3}{2}\lambda_3\,. \tag{3.8}$$

In the case of a totally planar event, $\lambda_3 = 0$, so the Aplanarity is zero. In an isotropic event the three eigenvalues are of equal magnitude ($\frac{1}{3}$), and the Aplanarity takes a maximum value of $\frac{1}{2}$.

- **Fox-Wolfram Moments**

The Fox-Wolfram moments, H_l, are defined [47] as,

$$H_l = \sum_{i,j} \frac{|\mathbf{p}_i|.|\mathbf{p}_j|}{E_{\text{vis}}^2} P_l(cos\theta_{ij}) \tag{3.9}$$

where P_l are the Legendre polynomials, $\mathbf{p}_i$,$\mathbf{p}_j$ are the particle momenta, θ_{ij} is the opening angle between particles i and j, and E_{vis} is the total detected energy of the event.

Neglecting the particle masses, energy-momentum conservation requires that $H_0 = 1$. For 2-jet events, $H_1 = 0$ and $H_l \sim 1$ for l even, and $H_l \sim 0$ for l odd. For this application the ratio of Fox-Wolfram 2nd to 0th moments is used as the discriminating variable, and it is indicated as R_2 in the following (Fig.3.4).

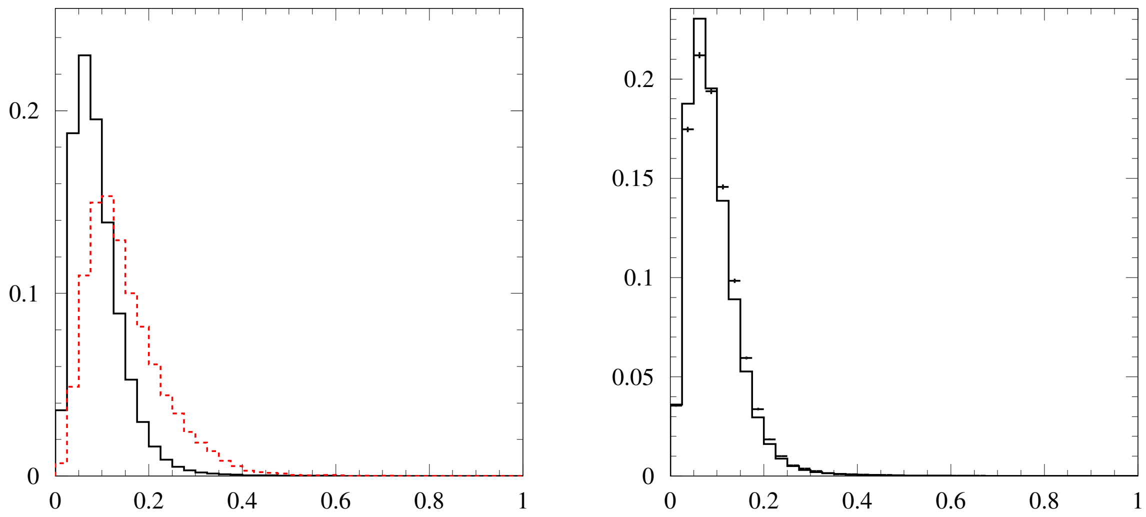

Figure 3.2: Left: sphericity distribution for signal $B \to \pi^+\pi^-$ Monte Carlo (dashed line) and background $q\bar{q}$ Monte Carlo (solid line) events. Right: comparison between off-resonance data (dots) and background $q\bar{q}$ Monte Carlo (solid line) events. Normalization is to area.

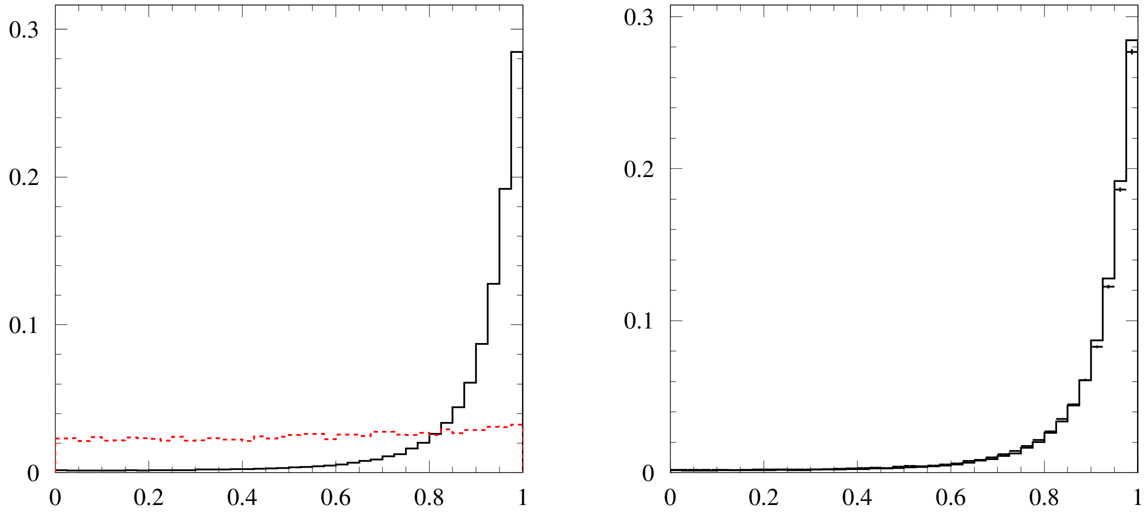

Figure 3.3: Left: $cos\theta_S$ distribution for signal $B \to \pi^+\pi^-$ Monte Carlo (dashed line) and background $q\bar{q}$ Monte Carlo (solid line) events. Right: comparison between off-resonance data (dots) and background $q\bar{q}$ Monte Carlo (solid line) events. Normalization is to area.

Continuum Monte Carlo events are compared with off-resonance data. The shapes of the distributions (Fig.3.2, Fig.3.3, Fig.3.4) well agree and this gives confidence that Monte Carlo is able to reproduce topological variables distributions.

3.2.1 Fisher discriminant

A Fisher discriminant technique is also used to separate signal from background ([5]). The Fisher discriminant $\mathcal{F}$ is a linear combination of N discriminating variables x_i,

$$\mathcal{F} = \sum_{i=1}^{N} \alpha_i x_i, \tag{3.10}$$

where the coefficients α_i are chosen to maximize the statistical separation between the two classes of events, signal and background. The discrimination task consists of determining an axis in the R^N space of the discriminating variables such that the two classes c are maximally separated. In order to apply this method, one needs only the mean values of each variable over the full sample, $(\bar{\mathbf{x}})$, the means over each class, $(\bar{\mathbf{x}}_1,\ \bar{\mathbf{x}}_2)$, and the total covariance matrix, $T_{\mu\nu}$. This matrix may be separated into two components: $T_{\mu\nu} = W_{\mu\nu} + B_{\mu\nu}$ where $W_{\mu\nu}$ and $B_{\mu\nu}$ are the *Within-* and *Between-* class matrices respectively.

$$\begin{aligned} T_{\mu\nu} &= \tfrac{1}{n} \textstyle\sum_i (x_{i\mu} - \bar{x}_\mu)(x_{i\nu} - \bar{x}_\nu) \\ W_{\mu\nu} &= \tfrac{1}{n} \textstyle\sum_{c=1}^{2} \sum_{i=1}^{n_c} (x_{i\mu} - \bar{x}_{c\mu})(x_{i\nu} - \bar{x}_{c\nu}) \\ B_{\mu\nu} &= \textstyle\sum_{c=1}^{2} \tfrac{n_c}{n} (\bar{x}_{c\mu} - \bar{x}_\mu)(\bar{x}_{c\nu} - \bar{x}_\nu) \end{aligned} \tag{3.11}$$

where $n = \sum_{c=1}^{2} n_c$. W reflects the dispersion of the events relative from the center of gravity of their own class $(\bar{x}_{c\mu})$, and B represents the distance of a class to the total center of gravity $(\bar{x}_\mu)$.

The distance between the projected points will naturally be maximum along the direction defined by the line between $\mathbf{x}_1$ and $\mathbf{x}_2$. Then the segment $(\bar{\mathbf{x}}_1, \bar{\mathbf{x}}_2)$ is the projection axis. In his original work [48], Fisher proposed to normalize the projected distance by the quadratic sum of the projected dispersion of each class. Mathematically, discriminating an event means comparing the value of a discriminating function (the projection) for the event $(\mathbf{x})$, given by

$$\mathcal{F} = \frac{\sqrt{n_1 n_2}}{n} (\bar{\mathbf{x}}_1 - \bar{\mathbf{x}}_2)^T W^{-1} \mathbf{x} \tag{3.12}$$

with some threshold value. Here, the threshold is

$$\theta_0 = \frac{\sqrt{n_1 n_2}}{n} \left(\bar{\mathbf{x}}_1 - \bar{\mathbf{x}}_2\right)^T W^{-1} \left(\bar{\mathbf{x}}_1 + \bar{\mathbf{x}}_2\right)/2 \tag{3.13}$$

where n_1, n_2 are the number of events in each sample and n is the total number of events. It is often preferred to compare to 0, in which case the discriminating function is simply redefined by $\mathcal{F} - \theta_0$.

We use nine discriminating variables: they are constructed from the scalar sum of the momenta of all charged and neutral particles, as defined by the `GoodTracksAccLoose` and `GoodNeutraleAccLoose` lists, (excluding the signal B decay products) flowing into nine concentric cones centered on the B candidate thrust axis in the CM frame. Each cone subtends an angle of 10° and is folded to combine the forward and backward intervals (Fig.3.5). More energy will be found in the cones nearer the candidate thrust axis in jet-like continuum background events than in the more isotropic $B\overline{B}$ events. A variety of discriminating variables have been considered in addition to the cones, but detailed comparisons show no significant gain. This is the same cone definition used in the CLEO analysis ([5]).

No cuts are applied to the Fisher discriminant. Instead, signal-background discrimination is achieved by using $\mathcal{F}$ in the maximum likelihood fit. The comparison of $\mathcal{F}$ for signal and background events is described in detail in Section 3.4.1.

3.3 Data samples and event selection

Run 1 data were used in this analysis. This sample amounts to $19.4\,\mathrm{fb}^{-1}$ of on-resonance data, which corresponds to $(22.57 \pm 0.36) \times 10^6$ $B\overline{B}$ pairs. Background studies utilized the entire Run 1 off-resonance sample of $2.67\,\mathrm{fb}^{-1}$. All cuts were tuned using Monte Carlo simulation and off-resonance data samples and were defined before analyzing the dataset. The initial data sample is defined by the combination of two very loose selection imposed to the full *BABAR* dataset.

- A very general requirement based on the presence of at least three *good* tracks in the event (called `BGFMultiHadron`). This is meant to select with maximal efficiency generic hadronic events among the events logged by the online data acquisition chain: many detector triggers in fact are not due to e^+e^- collision events, but to beam-gas or beam-wall interactions.

- A dedicated kinematic selection (called `twobody`) that selects charmless two-body *exclusive* B decay topologies[1] very efficiently. In the case of $h'^{+}h^{-}$ topology, an event is flagged as `twobody` when the B candidate formed pairing two reconstructed tracks has a CMS momentum p^{*}_{B} less than 1.5 GeV and the two final state particles with an invariant mass M_B (using the pion hypothesis) such that $|M_B - M_B^{PDG}| < 0.6$ GeV.

Those two requirements reduces the data sample to few percents of the full *BABAR* dataset. Nevertheless, it remains primarily background.

Further selection criteria are employed to greatly reduce the background while maintaining a high efficiency for signal events. Additional cuts are used to ensure that the PID information for each of the candidates is of sufficient quality to be used in the analysis. These criteria and their associated efficiencies are described below.

3.3.1 Preselection

Most of the background can be eliminated by simple kinematic cuts which make use of the differences between $B\overline{B}$ and continuum events, which is the primary source of background. First, the following selection is applied:

- $R_2 < 0.95$
- Sphericity > 0.01

where the first cut removes the majority of two-prong events and the second removes additional τ background. The R_2 and sphericity variables are computed using all the charged tracks and neutral clusters.

After applying the cuts described above, candidate B mesons are reconstructed by forming all pairs of oppositely charged tracks, passing the `GoodTracksAccLoose` criteria. The momentum vectors of the daughter particles are recalculated using the estimated B candidate decay vertex as their production vertex. Simple four-vector addition, assuming the pion mass for both of the charged tracks, is then used to form the $B \to h'^{+}h^{-}$ candidate four-vector.

Continuum background suppression is achieved by requiring

$$|\cos\theta_{\mathrm{S}}| < 0.9\,, \tag{3.14}$$

---

[1] It is designed to look separately for $h'^{+}h^{-}$, $h^{+}K^0_S$, $h^{+}\pi^0$, $\pi^0\pi^0$, $\pi^0K^0_S$, and $K^0_SK^0_S$, with $K^0_S \to \pi^+\pi^-$ and $\pi^0 \to \gamma\gamma$.

where θ_S is the angle between the sphericity axes of the B candidate and the rest of the event (using all `GoodTracksAccLoose` charged tracks and `GoodNeutralLooseAcc` neutral particle candidates which are not used for the B candidate).

The signal region in the m_{ES} -ΔE plane is defined as:

$$\begin{aligned} 5.2 < m_{ES} < 5.3\,\mathrm{GeV}/c^2 \\ -0.15 < \Delta E < 0.15\,\mathrm{GeV}\,. \end{aligned} \tag{3.15}$$

The total number of events in the signal region that satisfy the preselection criteria is 26404.

3.3.2 PID selection

A cut on the number of signal photons observed in the DIRC is used to improve the θ_c resolution and reduce the size of non-Gaussian tails. The cut $N_{sig}(\gamma) > 5$ is used, where $N_{sig}(\gamma)$ is the number of observed signal photons for the track. Protons are explicitly removed with the cut $\theta_c - \theta_c(p) > 10\,\mathrm{mrad}$, where $\theta_c(p)$ is the expected mean value of θ_c for a proton of a given momentum. Electrons are removed by rejecting tracks which pass the `VeryTightElectronSelection` criteria (Section 2.5).

The performance of the PID cuts are studied in data using a pure sample of kaons and pions obtained from a control sample of $D^{*+} \to D^0\pi^+$, with $D^0 \to K^-\pi^+$. These studies are described in Section 2.4. Good agreement is observed between the efficiency of the PID cuts in Monte Carlo simulated events and that obtained from this control sample. Thus, the PID efficiencies obtained from Monte Carlo simulated $B \to h'^+h^-$ decays are used without any corrections.

The number of events in the signal region surviving both the preselection and PID criteria is 16032.

3.3.3 Efficiencies

The efficiencies for the preselection and PID criteria are summarized in Tab. 3.1 and Tab.3.2, and are obtained from samples of Monte Carlo simulated $B \to h'^+h^-$ decays. The PID efficiencies are relative to the preselection efficiency and the $\theta_c > 0$ cut includes the DIRC geometrical acceptance.

The difference in track reconstruction efficiency between data and Monte Carlo simulated events is taken into account by using lookup tables to scale the reconstruction

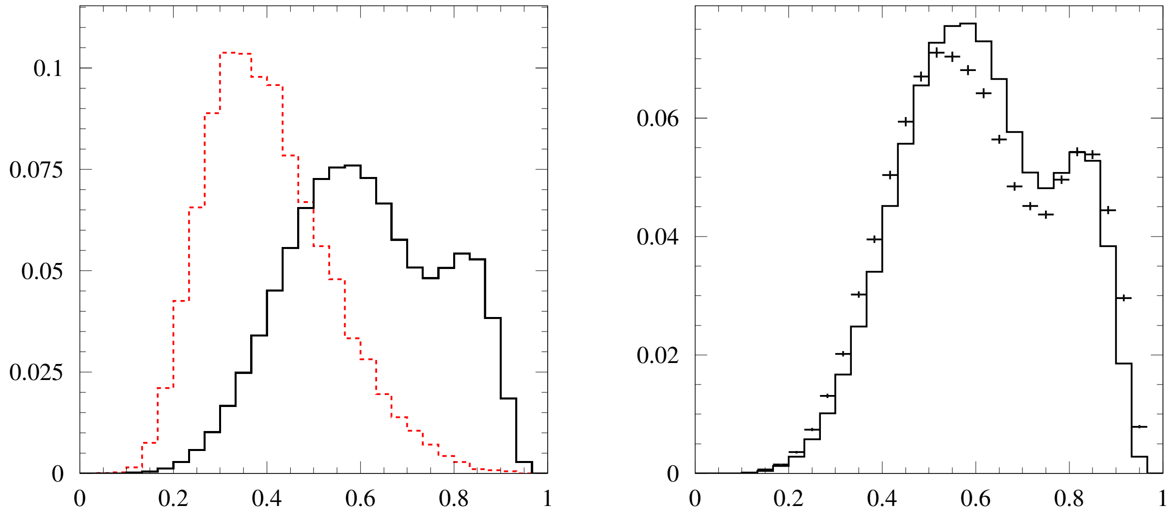

Figure 3.4: Left: R_2 distribution for signal $B \to \pi^+\pi^-$ Monte Carlo (dashed line) and background $q\bar{q}$ Monte Carlo (solid line) events. Right: comparison between off-resonance data (dots) and background $q\bar{q}$ Monte Carlo (solid line) events. Normalization is to area.

	Effic. (%)		
Cut	$\pi^+\pi^-$	$K^+\pi^-$	K^+K^-
Tag bits + `BGFMultiHadron`	70.09 ± 0.36	68.10 ± 0.34	66.79 ± 0.34
R_2 + *Sphericity* + $\lvert\cos\theta_S\rvert < 0.9$	87.72 ± 0.31	88.41 ± 0.28	88.10 ± 0.29
Preselection	61.48 ± 0.38	60.21 ± 0.36	58.85 ± 0.36

Table 3.1: Summary of efficiencies for the preselection in the decay mode $B \to h'^+h^-$. The m_{ES} and ΔE cuts are 100% efficient on signal. The quoted uncertainties are from Monte Carlo sample statistics only.

	Effic. (%)		
Cut	$\pi^+\pi^-$	$K^+\pi^-$	K^+K^-
$\theta_c > 0$	81.54 ± 0.39	83.18 ± 0.35	82.42 ± 0.36
$N_{sig}(\gamma) > 5$	93.73 ± 0.27	93.81 ± 0.25	92.97 ± 0.27
Proton + electron rejection	97.86 ± 0.17	97.64 ± 0.16	97.51 ± 0.17
PID Selection	74.79 ± 0.44	76.19 ± 0.40	74.71 ± 0.41

Table 3.2: Efficiency of PID cuts, as estimated with Monte Carlo simulated $B \to h'^+h^-$ decays. The quoted efficiencies in each row are those obtained after having applied all the cuts in the preceeding rows, as well as the preselection cuts. The quoted uncertainties are from Monte Carlo sample statistics only.

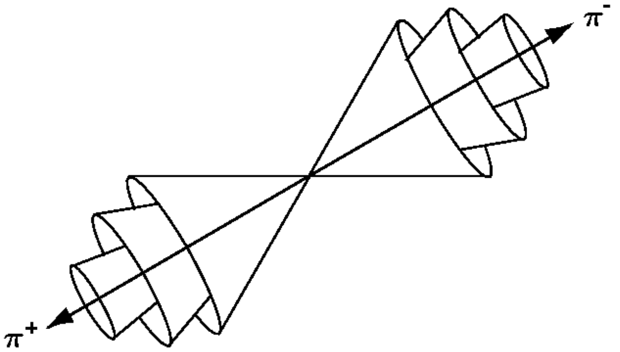

Figure 3.5: Picture of the first three cones coaxial to the B candidate thrust axis used to define the Fisher discriminant's variables

efficiency for each track in the Monte Carlo sample. The scale factors are functions of p_T, polar and azimuthal angles of the track, as well as the track multiplicity of the event (see Section 2.3). The overall correction factor to the efficiency is estimated to be 0.975 and is not included in Tab. 3.1.

The total efficiencies (including the tracking efficiency correction) for all cuts in the selection are:

$$\epsilon(\pi^+\pi^-) = (44.83 \pm 0.38)\% \quad \epsilon(K^+\pi^-) = (44.73 \pm 0.35)\% \quad \epsilon(K^+K^-) = (42.87 \pm 0.35)\% \,. \tag{3.16}$$

3.4 Analysis of $B \to h'^+h^-$

In this Section we present the analysis used to determine the h'^+h^- yields in the signal sample defined by the aforementioned selection criteria. An unbinned maximum likelihood fit is employed to determine a total of eight parameters from the data:

- $N_{\pi\pi}$, the number of $B \to \pi^+\pi^-$ decays;
- $N_{K\pi}$, the number of $B \to K^+\pi^-$ decays;

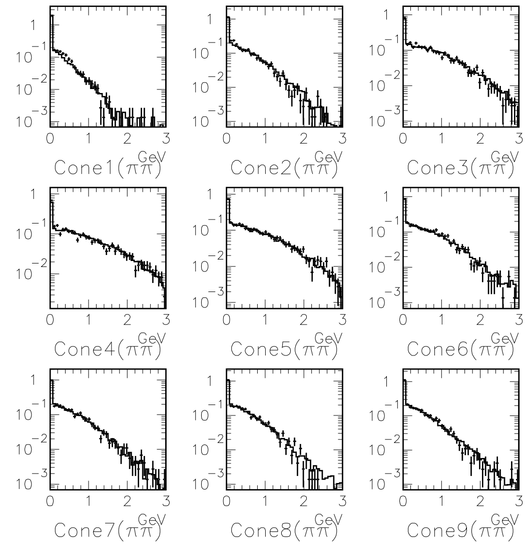

Figure 3.6: Comparison of CLEO cones in off-resonance data (dots) and Monte Carlo sample (histo) used to train the Fisher discriminant.

- $\mathcal{A}_{K\pi}$, the observed asymmetry between $B \to K^-\pi^+$ and $B \to K^+\pi^-$ decays,

$$\frac{N_{K^-\pi^+} - N_{K^+\pi^-}}{N_{K^-\pi^+} + N_{K^+\pi^-}}; \tag{3.17}$$

- N_{KK}, the number of $B \to K^+K^-$ decays;
- $N_{b\pi\pi}$, the number of background $\pi^+\pi^-$ candidates;
- $N_{bK\pi}$, the number of background $K^\pm\pi^\mp$ candidates;
- $\mathcal{A}_{bK\pi}$, the observed asymmetry between the number of background $K^-\pi^+$ and $K^+\pi^-$candidates;
- N_{bKK}, the number of background K^+K^- candidates.

Five quantities from each h'^+h^- candidate are used as inputs to the fit: $m_{\rm ES}$, ΔE, $\mathcal{F}$ and θ_+ and θ_-, the measured θ_c values for the h'^+ and h^- track, respectively.

The signal yields are divided by the efficiency estimates detailed in Section 3.3.3 and multiplied by the number of neutral B mesons produced in the dataset in order to obtain Branching Ratio measurements.

The distributions for $m_{\rm ES}$, ΔE and $\mathcal{F}$ provide good discrimination between signal and background, while the use of the Čerenkov angles, θ_+ and θ_-, allows the fitter to measure the particle ID content of the $h'^{+}h^{-}$ candidates: $\pi^{+}\pi^{-}$, $K^{+}\pi^{-}$ and $K^{+}K^{-}$. The quantity ΔE provides additional separation power for the three signal modes since the $B \to \pi^{+}\pi^{-}$, $B \to K^{+}\pi^{-}$ and $B \to K^{+}K^{-}$ distributions are shifted with respect to each other.

The likelihood, L, for the selected sample is given by the product of the *probability distribution functions* (PDFs) for each individual candidate and a Poisson factor which will be described shortly. The quantity $-2\log L$ is minimized, which is equivalent to maximing L itself, with respect to the eight fit parameters. The PDF for a given event i is the sum of signal and background terms:

$$\begin{aligned} \mathcal{P}_i\left(m_{\mathrm{ES},i}, \Delta E_i, \mathcal{F}_i, \theta_{+,i}, \theta_{-,i}\right) &= \frac{N_{\pi\pi}}{N'}\mathcal{P}_i^{\pi\pi} + \frac{N_{b\pi\pi}}{N'}\mathcal{P}_i^{b\pi\pi} \\ &+ \frac{N_{KK}}{N'}\mathcal{P}_i^{KK} + \frac{N_{bKK}}{N'}\mathcal{P}_i^{bKK} \\ &+ \frac{N_{K\pi}}{2N'}\left(1-\mathcal{A}_{K\pi}\right)\mathcal{P}_i^{K^{+}\pi^{-}} + \frac{N_{bK\pi}}{2N'}\left(1-\mathcal{A}_{bK\pi}\right)\mathcal{P}_i^{bK^{+}\pi^{-}} \\ &+ \frac{N_{K\pi}}{2N'}\left(1+\mathcal{A}_{K\pi}\right)\mathcal{P}_i^{K^{-}\pi^{+}} + \frac{N_{bK\pi}}{2N'}\left(1+\mathcal{A}_{bK\pi}\right)\mathcal{P}_i^{bK^{-}\pi^{+}}, \end{aligned} \tag{3.18}$$

where $N' \equiv \sum_k N_k$. The PDF for each component, in turn, is the product of the PDFs for each of the fit input variables:

$$\mathcal{P}^k = \mathcal{P}^k_{m_{\mathrm{ES}}}\mathcal{P}^k_{\Delta E}\mathcal{P}^k_{\mathcal{F}}\mathcal{P}^k_{\theta_+}\mathcal{P}^k_{\theta_-}\,. \tag{3.19}$$

The Poisson factor is the probability of observing N total events (the number of events used in the fit) when N' are expected. The likelihood is thus:

$$L = e^{-N'}\left(N'\right)^N \prod_{i=1}^{N}\mathcal{P}_i\,. \tag{3.20}$$

Note that the factor $(N')^N$ in the above equation cancels an identical factor in the denominator that arises from Eq.3.18.

In the following Section, descriptions of the PDFs, as well as the samples used to estimate them, are presented. This is followed by a section detailing the result of the maximum likelihood fit and the Branching Ratio estimates.

3.4.1 Sample definitions

The functional forms of the PDFs introduced in the previous Section are derived from data samples that are independent of the sample used in the fit. These samples include:

off-resonance data, on-resonance data in the ΔE sidebands, control samples of fully reconstructed $B^- \to D^0\pi^-$ decays, control samples of $c\overline{c} \to D^{*+}X$ decays and Monte Carlo simulated events. The definitions of the samples used in this analysis are described below, followed by descriptions of how the PDFs used in the fit are derived from these samples.

- **Monte Carlo simulated events:** As mentioned in Section 3.3.3, a large sample of Monte Carlo simulated events is used to study both background and signal distributions and selection efficiencies. The samples used consist of: ~ 16000 of each type of $B \to h'^+h^-$ signal; $15,803,300$ continuum $e^+e^- \to q\overline{q}$ events (corresponding to $\sim 4.66\,\text{fb}^{-1}$); $4,032,400$ $e^+e^- \to \tau^+\tau^-$ events; and $936,100$ *charmless* $B\overline{B}$ decays (this corresponds to an effective luminosity of $\sim 18\,\text{fb}^{-1}$)[2].

- **ΔE sideband data:** h'^+h^- candidates are selected in the following range: $5.2 < m_{\text{ES}} < 5.3\,\text{GeV}/c^2$ and $|\Delta E| < 0.42\,\text{GeV}$. The ΔE variable is used to subdivide the data into two samples:

$$0.15 < |\Delta E| < 0.42\,\text{GeV} \qquad \text{(Sideband)} \tag{3.21}$$

$$-0.15 < \Delta E < 0.15\,\text{GeV} \qquad \text{(Signal)} \tag{3.22}$$

  The ΔE signal range defines the region in which 100% of the signal lies. The sideband region is used to study characteristics of the background. The lower sideband contains a small amount of feed-down from higher multiplicity charmless B decays. In Fig.3.7 we show the correlation plot of ΔE versus m_{ES} for charmless Monte Carlo events. We estimate that ~ 12 events/ fb^{-1} are present in the lower sideband; this background is found to be negligible in the signal region.

- **m_{ES} sideband data:** The m_{ES} sideband sample includes all candidates which are in the *signal* ΔE region, given above, and have $5.2 < m_{\text{ES}} < 5.26\,\text{GeV}/c^2$. The charmless $B\overline{B}$ Monte Carlo sample is used to estimate the amount of feed-down from other charmless B decays. It is found to be negligible in the ΔE signal region.

- **Off-resonance data:** Data taken below the $\Upsilon(4S)$ resonance, which amounts to $2.67\,\text{fb}^{-1}$, is used to study continuum $e^+e^- \to q\overline{q}$ background, free from any $B\overline{B}$ contamination.

---

[2] *charmless* Monte Carlo events are generic $B\overline{B}$ decays with at least one B meson forced to decay to a final state with no *charmed* meson nor charmonia

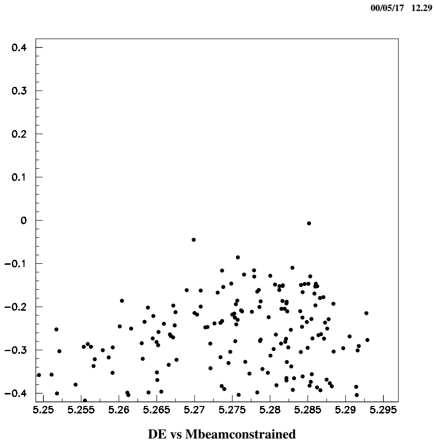

Figure 3.7: ΔE vs m_{ES} distribution for $B^0 \to \rho^+\pi^-$ Monte Carlo events

- $B^- \to D^0\pi^-$ **control sample:** The resolution of m_{ES} and ΔE for $B \to h'^+h^-$ decays can be studied using a sample of fully reconstructed $B^- \to D^0\pi^-$ decays, where $D^0 \to K^-\pi^+$. We consider this decay since its final state multiplicity is close to h'^+h^-. The m_{ES} resolution is dominated by the spread in the beam energies for B decays involving only charged tracks in the final state. Hence, the relatively large statistics of the $B^- \to D^0\pi^-$ signal can be used to accurately measure both the mean and resolution of m_{ES} for the $B \to h'^+h^-$ signal. The ΔE resolution, on the other hand, is dominated by the track momentum resolution, and differs between the control sample and the signal, due to the on-average softer momenta of the tracks in the control sample. We know that Monte Carlo simulation is presently unable to reproduce adequately ΔE. An amount of additional momentum smearing should therefore be applied to Monte Carlo simulated $B \to h'^+h^-$ decays in order to accurately represent what is expected in the data. A comparison of the ΔE resolutions obtained in data and Monte Carlo simulated $B^- \to D^0\pi^-$ decays can be used to estimate that amount. This control sample is selected with requirements on the D^0 mass and on θ_c angle of its negatively charged daughter track to be consistent with the kaon hypothesis. For consistency with the signal data sample the same topological preselection is applied (cut on $\cos\theta_S$).

- $c\bar{c} \to D^{*+}X$ **control sample:** A very pure sample of kaon and pion tracks is derived from reconstructed $D^{*+} \to D^0\pi^+ \to (K^-\pi^+)\pi^+$ decays, the selection of which is described in Section 2.4. The $\pi(K)$ track is always the one with the same(opposite)

Fit Variable	Shape	Samples Used
Signal m_{ES}	Gaussian	$D^0\pi^-$ (MC h'^+h^-)
Bkgd. m_{ES}	ARGUS	Sideband (Off-res, MC $q\overline{q}$)
Signal ΔE	Gaussian	$D^0\pi^-$ (MC h'^+h^-)
Bkgd. ΔE	Quadratic	Sideband (Off-res, MC $q\overline{q}$)
Signal Fisher	Double Gaussian	MC h'^+h^- ($D^0\pi^-$)
Bkgd. Fisher	Double Gaussian	Sideband (Off-res, MC $q\overline{q}$)
Kaon θ_c	Gaussian	D^{*+} (MC D^{*+}, MC h'^+h^-)
Pion θ_c	Gaussian	D^{*+} (MC D^{*+}, MC h'^+h^-)

Table 3.3: Summary of functional forms of PDFs used in the fit and the samples used to obtain them. The samples in parentheses represent additional samples which were used as consistency checks and provide alternative parameterizations that can be used for studies of systematics.

charge as the D^*. The control sample used is limited to those decays for which one of the D^0 daughter tracks is in the momentum range relevant for $B \to h'^+h^-$ decays: 1.75–4.25 GeV/c. This sample is used to obtain parameterizations of the Čerenkov θ_c measurement for high momentum tracks.

Tab. 3.3 summarizes the functional forms used for the PDFs and the samples from which they are extracted. Details of the PDFs are given in the following subsections. In all cases, reliance on Monte Carlo events only was avoided as much as possible.

Beam energy-substituted mass m_{ES}

The background shape in m_{ES} is parameterized using the ARGUS function [49]:

$$\frac{dN}{dm_{\mathrm{ES}}} = N \cdot m_{\mathrm{ES}} \cdot \sqrt{1-x^2} \cdot \exp\left(-\xi \cdot (1-x^2)\right) , \tag{3.23}$$

where $x = m_{\mathrm{ES}}/m_{\mathrm{max}}$ and the parameter ξ is determined from a fit[3]. A fit (Fig. 3.8) to the on-resonance sideband region after applying the selection cuts gives $\xi = 22.0 \pm 0.5$ with $m_{\mathrm{max}} = 5.2895\,\mathrm{GeV}/c^2$.

The off-resonance (Fig.3.9) and Monte Carlo simulated $q\overline{q}$ data samples are used to demonstrate that the m_{ES} distribution obtained from the on-resonance sideband sample accurately represents the shape of the background in the on-resonance signal region.

---

[3] The endpoint of the ARGUS curve, m_{max}, is not directly floated in this fit to m_{ES}. Several fits are done with m_{max} held fixed. We choose the value of m_{max} corresponding to the fit with the minimum χ^2.

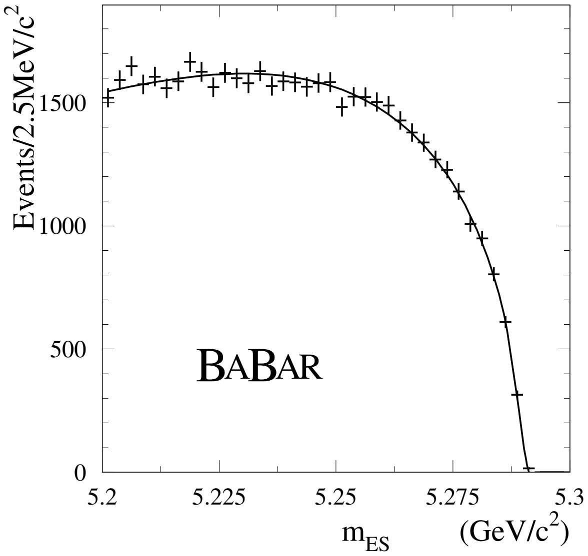

Figure 3.8: The $m_{\rm ES}$ distribution for candidates in the on-resonance sideband region. The distribution is fitted with an ARGUS function, described in the text. The χ^2/dof for the fit is 1.0.

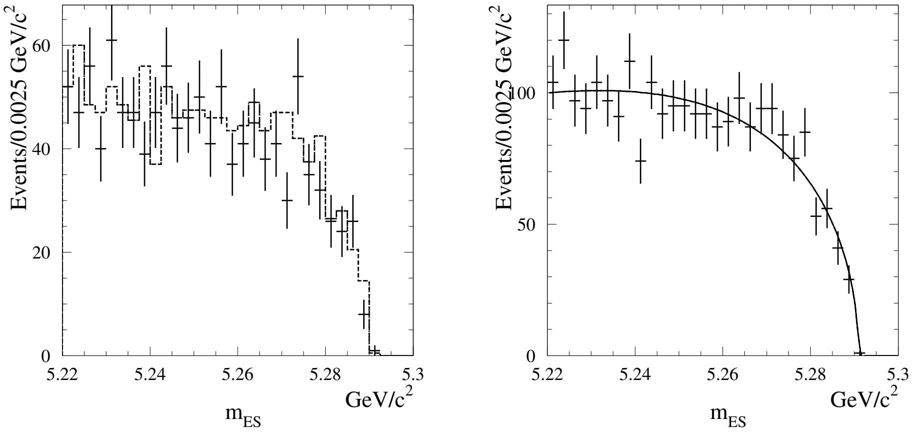

Figure 3.9: $m_{\rm ES}$ distributions. Left: Comparison of off-resonance sideband (histogram) and signal (error bars) regions. Right: Comparison of the ARGUS fit to on-resonance sideband with the off-resonance sideband region. $\chi^2/N_{\rm dof} = 26.0/28$

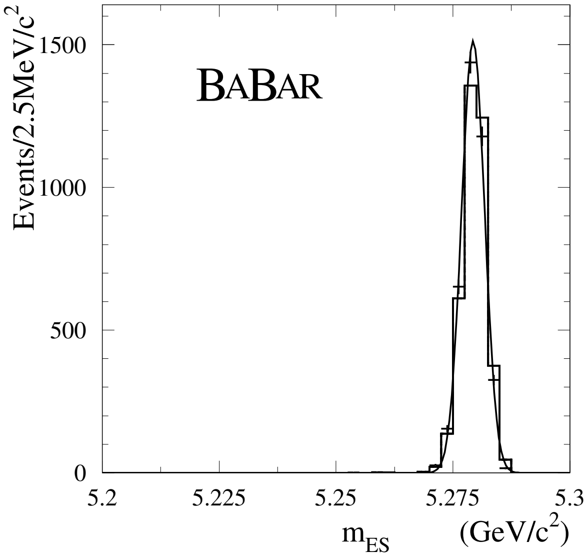

Figure 3.10: The $m_{\rm ES}$ distribution for fully reconstructed $B^- \to D^0\pi^-$ ($D^0 \to K^-\pi^+$) decays (points) and for $B \to h'^+h^-$ decays (histogram) in Monte Carlo simulated events.

As discussed above, the shape of the $m_{\rm ES}$ distribution for $B \to h'^+h^-$ decays can very reliably be taken directly from the $m_{\rm ES}$ distribution of fully reconstructed $B^- \to D^0\pi^-$ decays. This is demonstrated in Fig. 3.10, which displays the $m_{\rm ES}$ distribution for Monte Carlo simulated $B \to \pi^+\pi^-$ and $B^- \to D^0\pi^-$ decays. Since there is good agreement between the two modes, we use the $m_{\rm ES}$ distribution for $B^- \to D^0\pi^-$ decays in data, displayed in Fig. 3.11, to parameterize the $m_{\rm ES}$ PDFs. The distribution is fitted to a Gaussian for the signal and an ARGUS function for the background. The fit gives $\langle m_{\rm ES}\rangle = 5.280\,{\rm GeV}/c^2$ and $\sigma(m_{\rm ES}) = 2.6\,{\rm MeV}/c^2$.

Energy difference ΔE

Similarly to $m_{\rm ES}$, the on-resonance sideband data is used to determine the shape of ΔE for background in the signal region. As it is demonstrated in Fig. 3.12, a second order polynomial is found to give the best fit results. Also shown are the distributions of ΔE for off-resonance data and Monte Carlo simulated continuum events. There is good agreement between the shapes of all three samples.

The $B^- \to D^0\pi^-$ control sample is used to understand the ΔE resolution for $B \to h'^+h^-$ events. The ΔE distributions for $B^- \to D^0\pi^-$ decays in data and Monte Carlo simulated events are shown in Fig. 3.13. The Monte Carlo distribution is best fit by the sum of two Gaussians, but the statistics are not large enough in the data sample

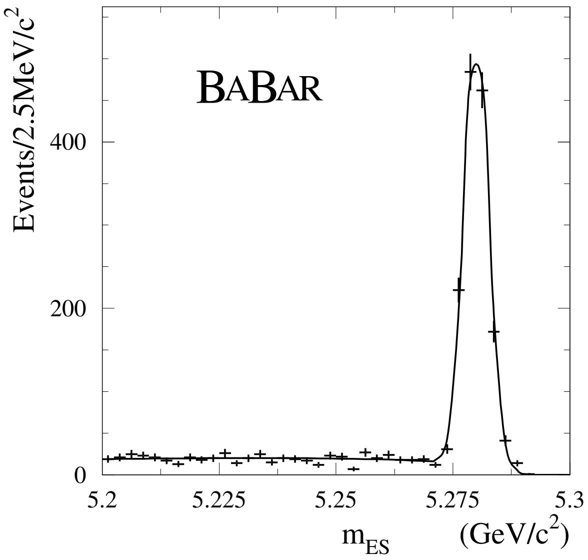

Figure 3.11: The $m_{\rm ES}$ distribution for fully reconstructed $B^- \to D^0\pi^-$ ($D^0 \to K^-\pi^+$) decays. The fit function is described in the text.

to perform a reliable double Gaussian fit. Thus, in fitting the data ΔE distribution we assume rather arbitrarily that the relative area of the wider Gaussian and its width are fixed to the values obtained from the Monte Carlo. The combinatorial background in the data ΔE distribution was subtracted off using $m_{\rm ES}$ sideband data. What remains is the $B^- \to D^0\pi^-$ signal as well as a large "shoulder" to the left of the signal, which is due primarily to fake B decays.

The widths of the narrower Gaussians are $15.35 \pm 0.25\,\mathrm{MeV}$ and $19.13 \pm 0.75\,\mathrm{MeV}$ for Monte Carlo simulated decays and for Run 1 data, respectively. From this comparison, one estimates a 25% degradation of the ΔE resolution for data, with respect to the Monte Carlo simulation. In addition, the data ΔE distribution is found to be offset from zero by $-5.4 \pm 0.9\,\mathrm{MeV}$. Offsets of the order -2 to $-5\,\mathrm{MeV}$ are observed in other fully reconstructed B decays as well, so we assume that the reconstructed ΔE for $B \to h'^+h^-$ decays is shifted downward by $5\,\mathrm{MeV}$.

The ΔE distribution for Monte Carlo simulated $B \to \pi^+\pi^-$ decays is shown in Fig. 3.14. A single Gaussian of width $21\,\mathrm{MeV}$ accurately describes this distribution. The assumption is made that the resolution in data is 25% worse (the factor described above), or $26\,\mathrm{MeV}$. Because of such a considerable correction factor, a large range of possible ΔE resolutions is used in computing the associated systematic uncertainty: $23.5\,\mathrm{MeV}$ (the lower bound from using twice the uncertainty on the correction factor) to $31\,\mathrm{MeV}$ (a

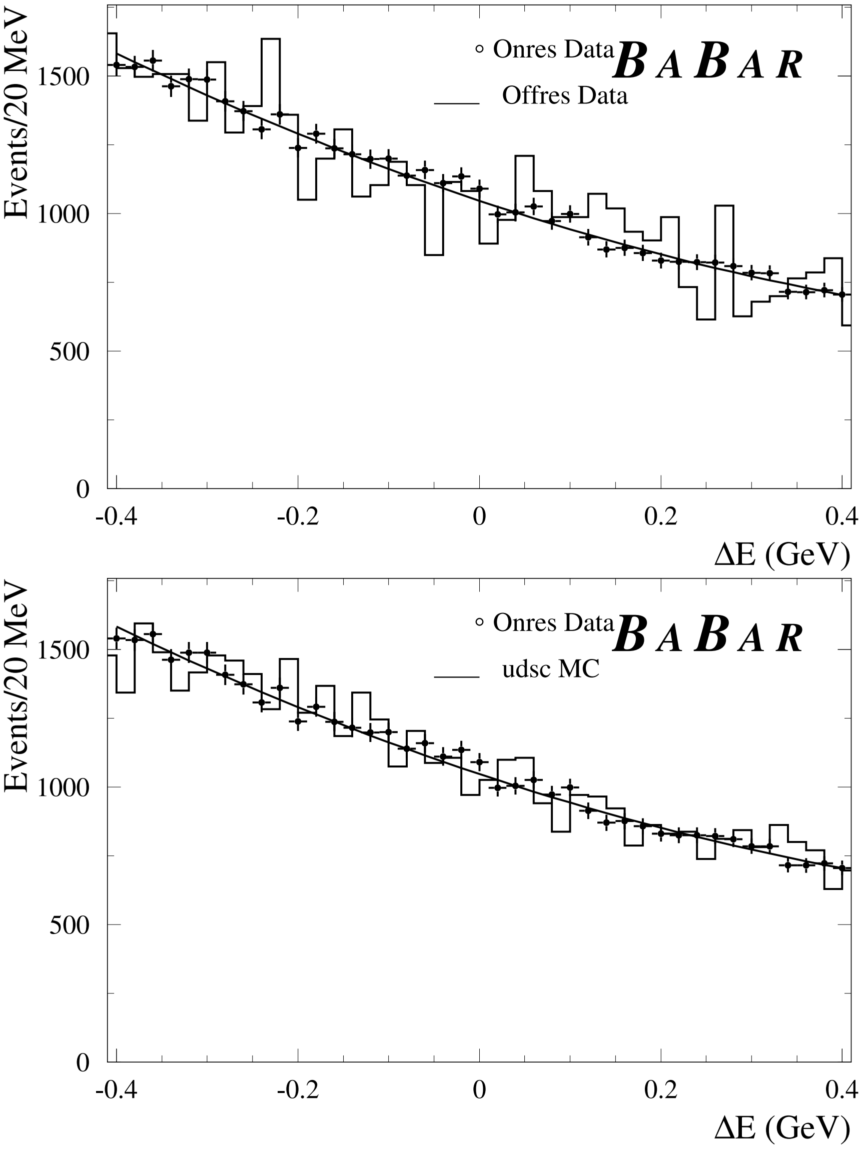

Figure 3.12: The distribution of ΔE for the entire region of on-resonance data, sideband and signal, is given by the points with error bars in both plots. The solid curve represents a fit of a second order polynomial to the sideband regions only ($|\Delta E| > 0.15$). The histogram in the upper plot is off-resonance data and the histogram in the lower plot is continuum Monte Carlo (both normalized to the same area as the on-resonance distribution).

conservative estimate of the upper bound).

The assumption that the $B \to h'^+h^-$ ΔE resolution is expected to be about 26 MeV is tested by introducing a 1.25 *smearing* factor to the reconstructed curvature parameters of charged tracks in both Monte Carlo simulated $B^- \to D^0\pi^-$ and $B \to h'^+h^-$ decays. The ΔE resolution for the $D^0\pi^-$ sample is found to be about 19 MeV (width of the narrower, core Gaussian), in good agreement with the observed ΔE resolution in data. The ΔE resolution for the Monte Carlo simulated $B \to h'^+h^-$ decays becomes 26 MeV, which is consistent with the nominal value we are assuming.

As was described in Section 3.3.1, the pion mass is assigned to both charged tracks when forming a B candidate and calculating ΔE. Thus, $B \to K^+\pi^-$ and $B \to K^+K^-$ decays will have a ΔE value which is not centered at zero, but is shifted to negative values by a quantity which depends on the momenta of the kaon track(s). This is due to the fact that the candidate energies are calculated in the CM system and the boost to that frame depends on the mass hypotheses of the h'^+ and h^- tracks. Therefore the ΔE PDF for $B \to K^+\pi^-$ decays consists of a Gaussian with a mean given by the following analytical form:

$$\langle \Delta E \rangle = -\gamma_{\text{boost}} \times \left(\sqrt{M_K^2 + p^2} - \sqrt{M_\pi^2 + p^2} \right) , \tag{3.24}$$

where γ_{boost} is the Lorentz factor of $\Upsilon(4S)$ in the lab and p is the lab momentum of the assumed kaon track. A similar expression is used for the $B \to K^+K^-$ PDF. Fig.3.15 shows the correlation between ΔE and momentum p for $\pi\pi$ and $K\pi$ Monte Carlo events. The variation due to this boost effect is of the order $\sim \pm 15$ MeV. On average, the mean ΔE value for $B \to K^+\pi^-(B \to K^+K^-)$ decays is $-45(-91)$ MeV. Fig 3.15 shows the reconstructed ΔE distributions in Monte Carlo events, for all three signal modes.

Fisher output $\mathcal{F}$

The distribution for $\mathcal{F}$ for the background is determined from events in the m_{ES} sideband region of the on-resonance sample since the statistics are large and the sample is almost free from contamination from $B\overline{B}$ events (a small amount of which is present in the lower ΔE sideband sample). The distribution is parameterized by the sum of two Gaussians, as shown in Figs. 3.16 and 3.17. The points are the m_{ES} sideband data and the overlayed histograms are the distributions obtained from off-resonance and Monte Carlo simulated continuum events, using the full m_{ES} region (5.2-5.3 GeV/c^2). These parameterizations

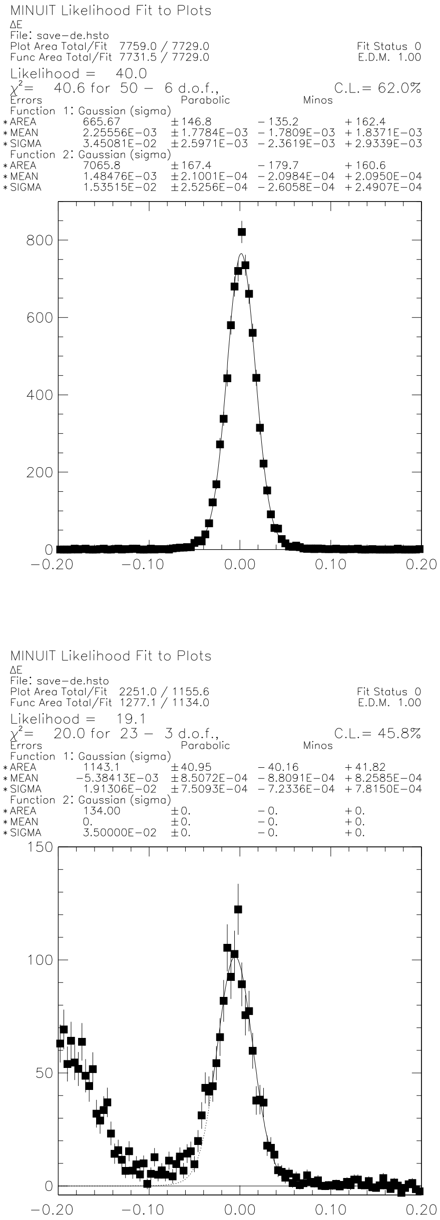

Figure 3.13: The ΔE distributions for fully reconstructed $B^- \to D^0\pi^-$ ($D^0 \to K^-\pi^+$) decays in (top) Monte Carlo simulated events, and (bottom) Run 1 data. The fits are described in the text.

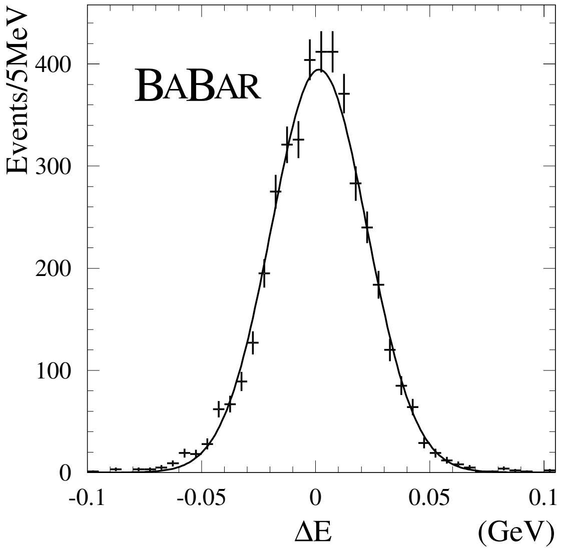

Figure 3.14: The ΔE distribution for reconstructed $B \to \pi^+\pi^-$ decays in Monte Carlo simulated data. The distribution is fitted with a Gaussian.

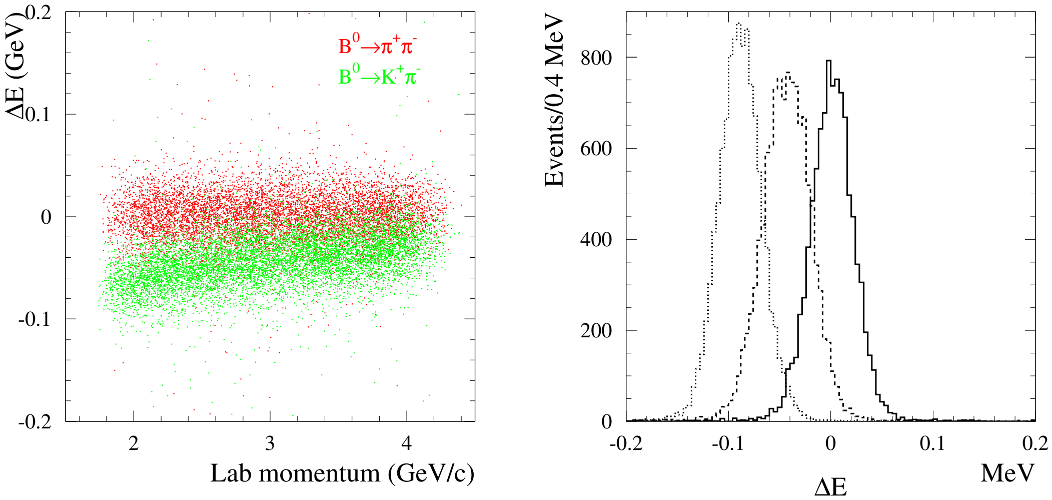

Figure 3.15: Left: correlation plot between ΔE and momentum for $\pi\pi$ (upper band) and $K\pi$ (lower band) decays. The shift in $K\pi$ is momentum dependent due to the boost. Right: the reconstructed ΔE distributions for Monte Carlo simulated $B \to \pi^+\pi^-$ (solid), $B \to K^+\pi^-$ (dashed) and $B \to K^+K^-$ (dotted) decays. As noted in the text, the $K^+\pi^-$ and K^+K^- distributions are centered at negative values (-45 and $-91\,\text{MeV}$, respectively) because the charged tracks are assigned the pion mass in calculating the B candidate energy.

derived from off-resonance data and Monte Carlo continuum events are used in computing systematic uncertainties due to the $\mathcal{F}$ parameterization.

The distribution of $\mathcal{F}$ is the same for all three signal modes, as well as for $B^- \to D^0\pi^-$ events, and is found to be well-modelled by the Monte Carlo simulation. For signal two Gaussians are used to describe the distribution too. Hence, Monte Carlo simulated $B \to h'^+h^-$ decays are used to describe the Fisher PDF for signal. Fig. 3.18 displays $\mathcal{F}$ for Monte Carlo simulated $B \to h'^+h^-$ decays (histogram centered below zero), $B^- \to D^0\pi^-$ decays in the data (filled dots), Monte Carlo simulated continuum background (histogram centered above zero) and on-resonance $m_{\rm ES}$ sideband data (open dots).

Čerenkov **angle** θ_C

PDF for θ_c are derived as descibed in Section 2.4 from D^*/D^0 control sample.

Correlations between PDFs

The PDFs described in the previous Sections are assumed to be uncorrelated in the maximum likelihood fit. To check this assumption we have calculated the linear correlation coefficient c_{jk} between the PDFs for variables j and k. The definition of c_{jk} is

$$c_{jk} = \frac{s_{jk}^2}{s_j s_k}, \tag{3.25}$$

where

$$s_{jk}^2 \equiv \frac{1}{N-1}\sum_i \left[\left(x_j^{(i)} - \bar{x_j}\right)\left(x_k^{(i)} - \bar{x_k}\right)\right], \tag{3.26}$$

where $x_j^{(i)}$ is the value of the j variable in the i^{th} event of the sample. We define $s_j \equiv s_{jj}$. Tab. 3.4 summarizes the correlation coefficients obtained from Monte Carlo simulated $B \to h'^+h^-$ decays.

3.4.2 Maximum likelihood fit

The unbinned maximum likelihood fit and the parameterizations of the PDFs have been described in detail at the beginning of this Section. The fit is performed using all events which pass the preselection and the PID cuts described in Section 3.3. The sample consists of 16032 candidates. The results from the fit are given in Tab. 3.5. The correlation matrix is given in Tab.3.6.

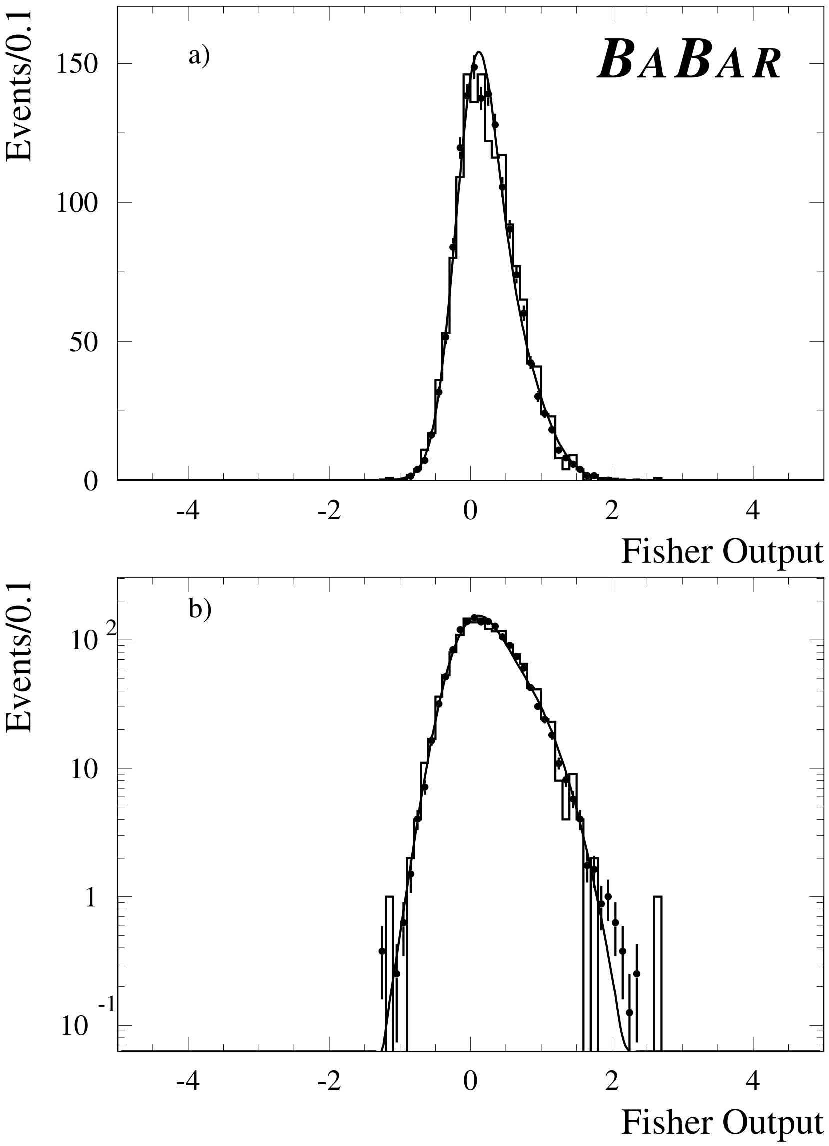

Figure 3.16: The $\mathcal{F}$ distribution for on-resonance m_{ES} sideband data (points) and off-resonance data (histogram). The two distributions are normalized to the same, arbitrary, area. The curve represents a double Gaussian fit to the on-resonance m_{ES} sideband distribution. The bottom plot shows the same quantities, but with a log scale on the y-axis.

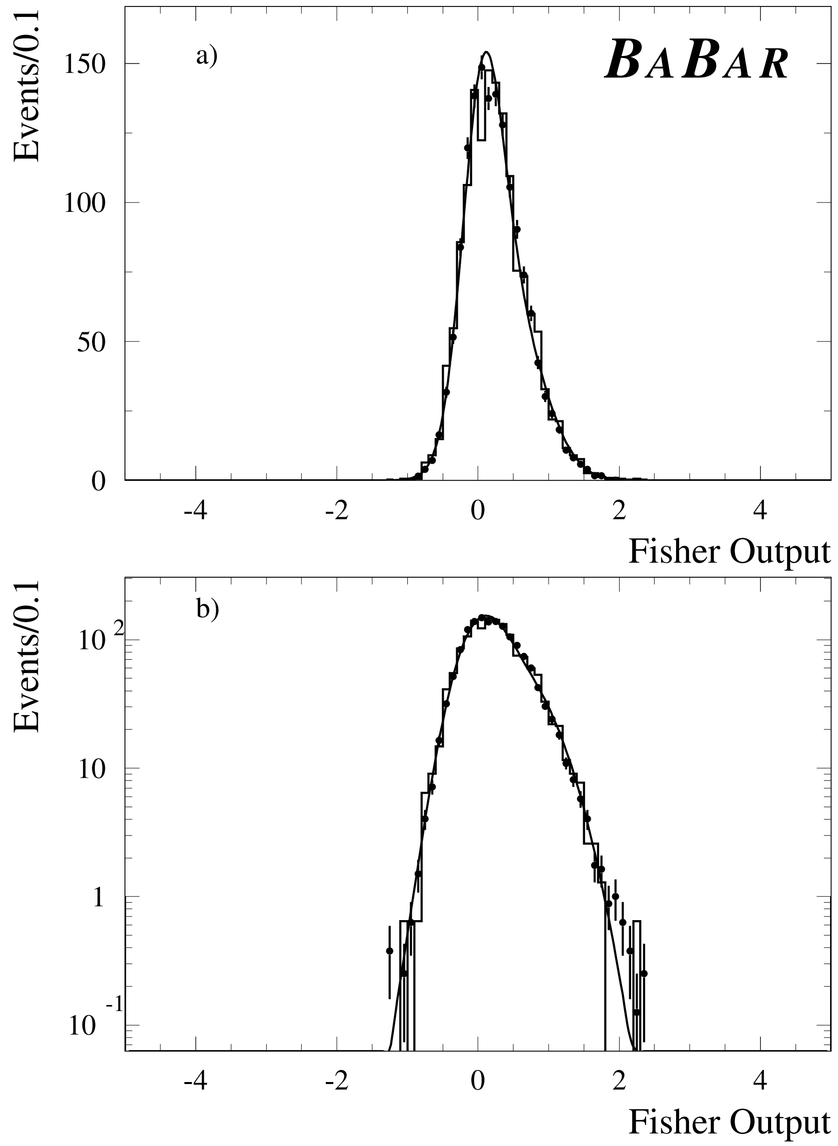

Figure 3.17: The $\mathcal{F}$ distribution for on-resonance m_{ES} sideband data (points) and Monte Carlo simulated continuum events (histogram). The two distributions are normalized to the same, arbitrary, area. The curve represents a double Gaussian fit to the on-resonance m_{ES} sideband distribution. The bottom plot shows the same quantities, but with a log scale on the y-axis.

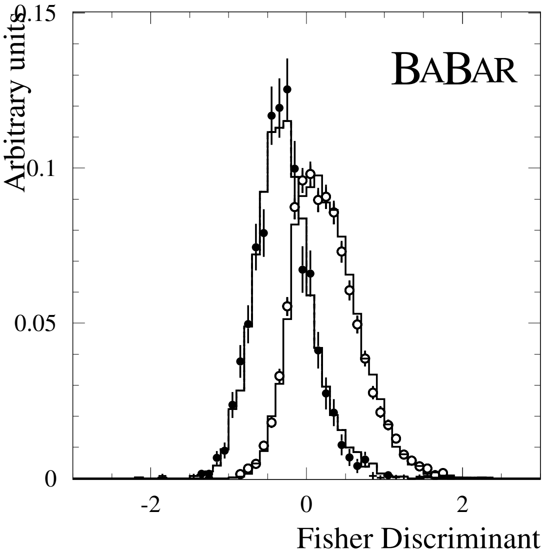

Figure 3.18: The $\mathcal{F}$ distribution for Monte Carlo simulated $B \to h'^+h^-$ decays (histogram centered below zero), $B^- \to D^0\pi^-$ decays in the data (filled dots), Monte Carlo simulated continuum background (histogram centered above zero) and on-resonance $m_{\rm ES}$ sideband data (open dots).

Variables	correlation
$m_{\rm ES}$, ΔE	-0.143
$m_{\rm ES}$, $\mathcal{F}$	-0.021
$m_{\rm ES}$, θ_+	-0.017
$m_{\rm ES}$, θ_-	-0.002
ΔE, $\mathcal{F}$	0.032
ΔE, θ_+	-0.017
ΔE, θ_-	0.005
$\mathcal{F}$, θ_+	0.005
$\mathcal{F}$, θ_-	0.031
θ_+, θ_-	-0.032

Table 3.4: Linear correlation coefficients between variables used in the maximum likelihood fit. Results are obtained from Monte Carlo simulated $B \to h'^+h^-$ decays.

Table 3.5: Results from the maximum likelihood fit.

Parameter	Fit Result
$N_{\pi\pi}$	41 ± 10
$N_{K\pi}$	169 ± 17
$\mathcal{A}_{K\pi}$	-0.19 ± 0.10
N_{KK}	$8.2^{+7.8}_{-6.4}$
$N_{b\pi\pi}$	8152 ± 95
$N_{bK\pi}$	4844 ± 81
$\mathcal{A}_{bK\pi}$	0.011 ± 0.017
N_{bKK}	2817 ± 58

Param.	$N_{\pi\pi}$	$N_{K\pi}$	$\mathcal{A}_{K\pi}$	N_{KK}	$N_{b\pi\pi}$	$N_{bK\pi}$	$\mathcal{A}_{bK\pi}$	N_{bKK}
$N_{\pi\pi}$	1.000	−0.074	−0.136	−0.153	−0.108	−0.108	0.009	0.115
$N_{K\pi}$	−0.074	1.000	0.066	0.143	−0.001	−0.043	0.009	−0.007
$\mathcal{A}_{K\pi}$	−0.136	0.066	1.000	0.147	0.135	−0.018	−0.016	−0.120
N_{KK}	−0.153	0.143	0.147	1.000	0.006	−0.132	−0.025	0.235
$N_{b\pi\pi}$	−0.108	−0.001	0.135	0.006	1.000	−0.190	−0.018	0.031
$N_{bK\pi}$	−0.180	−0.043	−0.018	−0.132	−0.190	1.000	−0.009	−0.110
$\mathcal{A}_{bK\pi}$	0.009	0.009	−0.016	−0.025	−0.018	−0.009	1.000	0.020
N_{bKK}	0.115	−0.007	−0.120	0.235	0.031	−0.110	0.020	1.000

Table 3.6: Parameter correlation coefficients from the fit.

The statistical significances of the signals are determined to be 4.7σ for $\pi^+\pi^-$, 15.8σ for $K^+\pi^-$ and 1.3σ for K^+K^-. The statistical significance for a given mode is determined by fixing its yield to zero and performing the fit with all other parameters allowed to float. The change in $-2\ln L$ from its value in the nominal fit is the square of the statistical significance for that mode.

Distributions of $m_{\rm ES}$ and ΔE

The $m_{\rm ES}$ and ΔE distributions of all selected $B \to h'^+h^-$ candidates are shown in Fig. 3.19. Overlayed on the distributions are the projections from the fit. Since the signal to background ratio in the final sample is still very small, we enhance the number of signal events by cutting on likelihood ratios only for display's purpose. For any given event, the "likelihood" for any of the 8 possible hypotheses, L_j, is given by the product of the fitted yield for the hypothesis of interest, N_j, and its PDF, $\mathcal{P}^j$. The quantities

$$\begin{aligned}
R_{\rm sig} &= \frac{L_{\pi\pi} + L_{K^+\pi^-} + L_{K^-\pi^+} + L_{KK}}{L_{\pi\pi} + L_{K^+\pi^-} + L_{K^-\pi^+} + L_{KK} + L_{b\pi\pi} + L_{bK^+\pi^-} + L_{bK^-\pi^+} + L_{bKK}} \qquad (3.27)\\
R_{\pi\pi} &= \frac{L_{\pi\pi}}{L_{\pi\pi} + L_{K^+\pi^-} + L_{K^-\pi^+} + L_{KK}}\\
R_{K\pi} &= \frac{L_{K^+\pi^-} + L_{K^-\pi^+}}{L_{\pi\pi} + L_{K^+\pi^-} + L_{K^-\pi^+} + L_{KK}}
\end{aligned}$$

give the relative likelihoods for any event to be signal, $B \to \pi^+\pi^-$ and $B \to K^+\pi^-$, respectively. The $m_{\rm ES}$ and ΔE distributions for events enriched in $B \to \pi^+\pi^-$ or $B \to K^+\pi^-$ decays are displayed in Fig. 3.20. In making the plots, the likelihoods described above are defined using the PDFs for all variables *except* the one being plotted. For the $m_{\rm ES}$ (ΔE) plots the $R_{\rm sig}$ cut used is $R_{\rm sig} > 0.1\,(0.2)$, and for the $B \to \pi^+\pi^-$ ($K^+\pi^-$) plots $R_{\pi\pi}$ ($R_{K\pi}$) is required to be greater than 0.5 (0.75).

Because the Monte Carlo simulation does not accurately describe the ΔE or θ_c resolutions of signal decays, simulated "toy" Monte Carlo events are used to determine the efficiencies of these cuts on signal. For background events, the efficiencies are estimated using $m_{\rm ES}$ and ΔE sideband data. The curves in Fig. 3.20 represent the projections of the maximum likelihood fit in the $m_{\rm ES}$ and ΔE planes, with signal and background normalizations given by the yields from the nominal fit, scaled by the efficiencies of the likelihood ratio cuts.

"Toy" Monte Carlo studies

The performance of the fit has been studied using "toy" Monte Carlo simulation in which hundreds, or thousands, of "toy" experiments are generated with statistics similar to those observed in the fit to the Run 1 data. In each "toy" experiment, the fit variables ($m_{\rm ES}$, ΔE, $\mathcal{F}$, θ_+ and θ_-) are generated according to the probability distributions (PDFs) actually used in the maximum likelihood fit. The numbers of signal and background events in each experiment are given by Poissonian distributions with means given by the nominal Run 1 fit results.

The track momenta are generated according to 2-body B decay kinematics, including the P-wave decay of $\Upsilon(4S) \to B\overline{B}$, in the CMS, and then boosted to the laboratory frame (using an average boost). This ensures that one obtains the proper momentum-polar angle

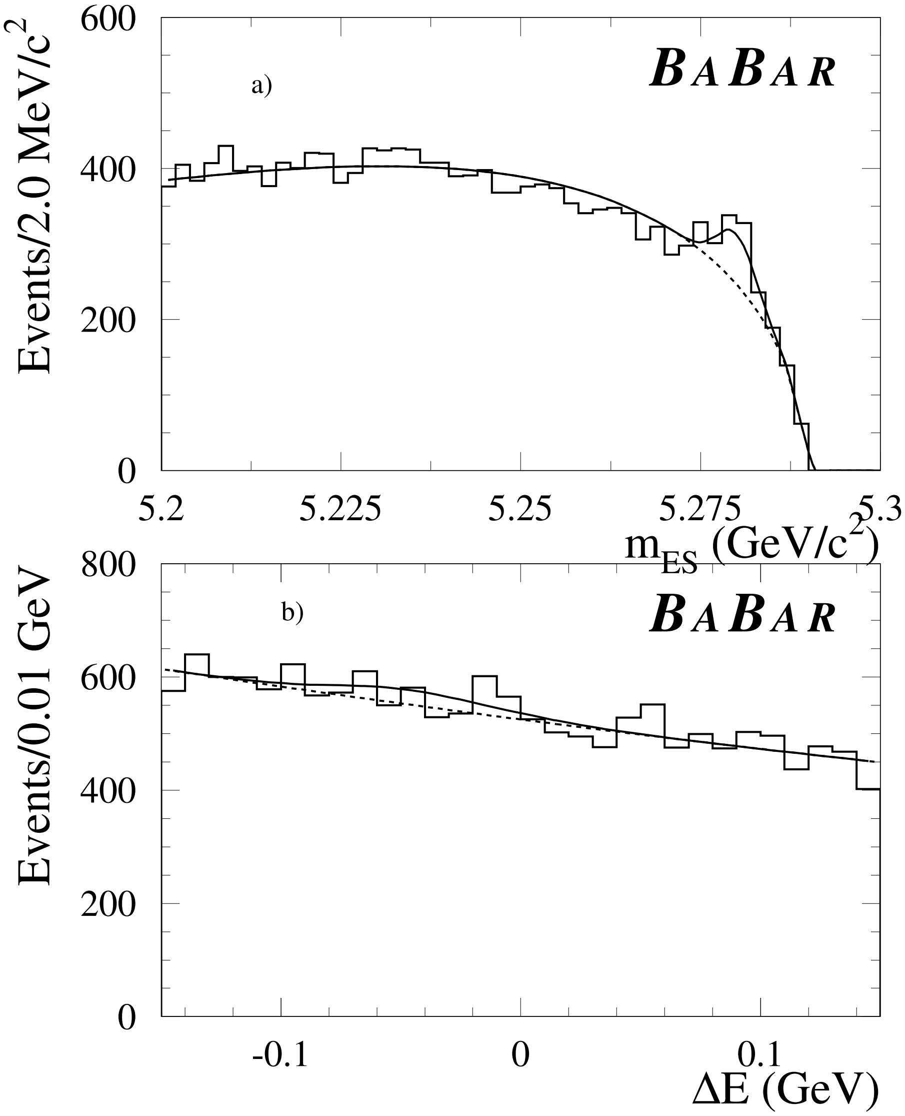

Figure 3.19: The m_{ES} (a) and ΔE (b) distributions for all selected $B \to h'^{+}h^{-}$ candidates. The solid curves represent the fit predictions and the dashed curves represent the predicted background contributions.

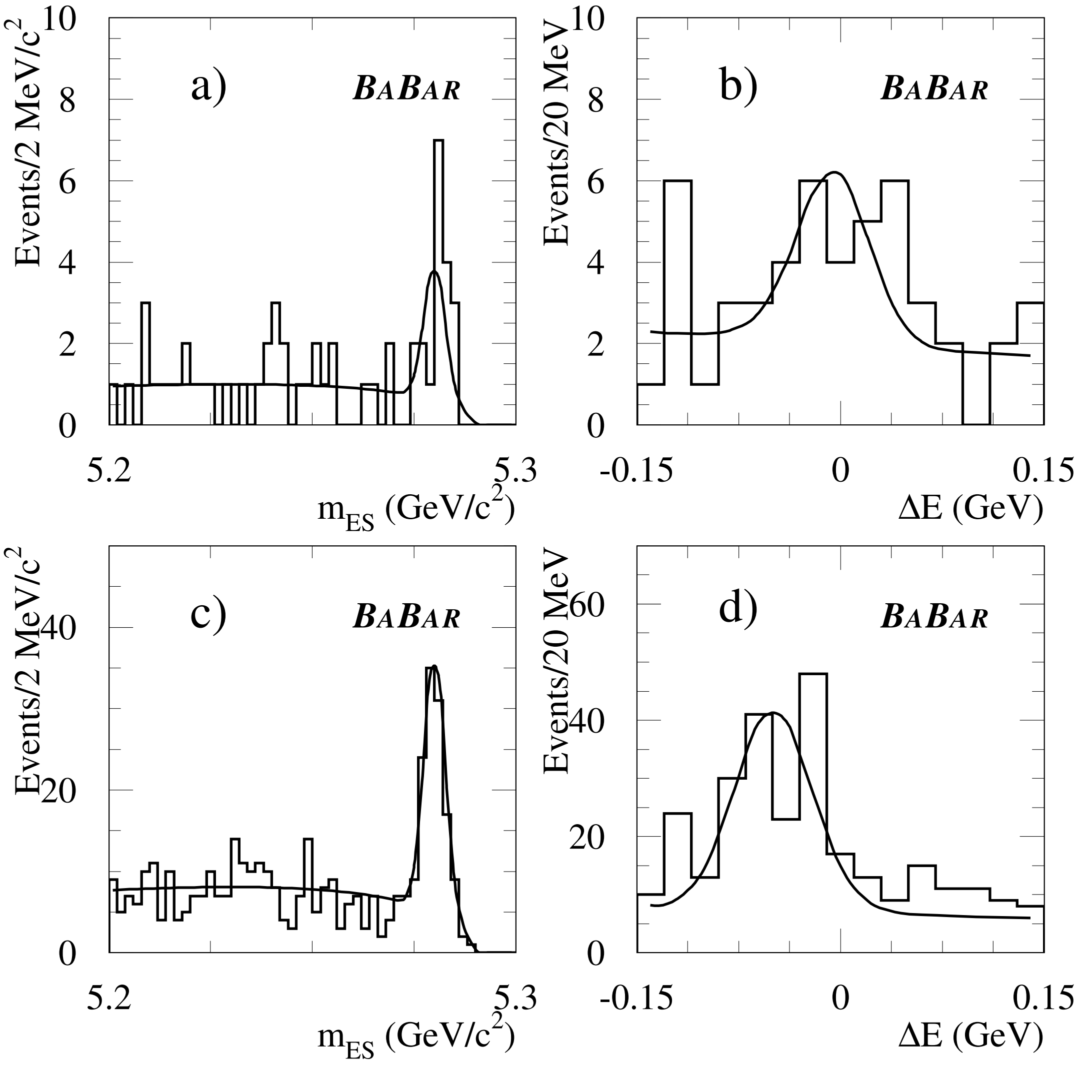

Figure 3.20: The $m_{\rm ES}$ and ΔE distributions for events enriched in $B \to \pi^+\pi^-$ decays, (a) and (b), and $B \to K^+\pi^-$ decays, (c) and (d). The likelihood ratio cuts used to make the plots are described in the text. The solid curves represent the fit predictions and are also described in the text.

(Fig.2.11) correlation for each track as well as the proper momentum-momentum correlation for pairs of tracks forming $B \to h'^{+}h^{-}$ candidates. The DIRC θ_c measurements are simulated for each track based upon its momentum and $\cos\theta$. The θ_c offsets, resolutions and satellite peak features are all included in the simulation.

A total of 1000 such "toy" experiments were generated and fitted. The distributions of parameter pulls, defined as $(N_j^{\rm fit} - N_j^{\rm gen})/\sigma_j$, where $N_j^{\rm fit}$ and $N_j^{\rm gen}$ are the fitted and generated values for fit parameter j, and σ_j is the error on N_j returned by the fit, are given in Figs. 3.21 and 3.22. The distributions of the errors returned by the fit, σ_j, are given in Figs. 3.23 and 3.24. To very good approximation, the pulls are all centered at zero and have unit width, as to be expected. In addition, the measured errors on the parameters in the data fit are very close to the mean values obtained from the "toy" Monte Carlo experiments. This indicates that the data fit results are "typical."

Finally, the distribution of the minimum values of $-2\log L$ from the "toy" Monte Carlo experiments is displayed in Fig. 3.25. The arrow indicates the value obtained from the fit to the data. Approximately 4% of the "toy" experiments have a value larger than that of the data fit. This suggests a "goodness-of-fit" of only 4%. This untypical value can be due to different several reason. We know, in fact, that there remain features in the data which are not completely modelled in the "toy" Monte Carlo experiments, for instance fit variable correlations and kinematical differences between signal and background. Moreover, we found the presence of few "outlier" events that can easily pull the $-2\log L$ of our experiment far from the average value. We checked that if these events are taken out from the fit, the fitted parameters do not change. In future improvements of the analysis we will change the event selection to eliminate outliers.

3.4.3 Systematic uncertainties

The systematic uncertainties in the unbinned likelihood analysis come primarily from the imperfect knowledge of the correct parameterizations for each of the variables. Systematic uncertainties resulting from the choice of cut values in the sample selection are small in comparison. The systematic uncertainty associated with each PDF may be estimated in two ways:

- Each parameter, in each PDF, can be varied within a conservative range which covers any potential systematic uncertainties in the parameterization, such as possible

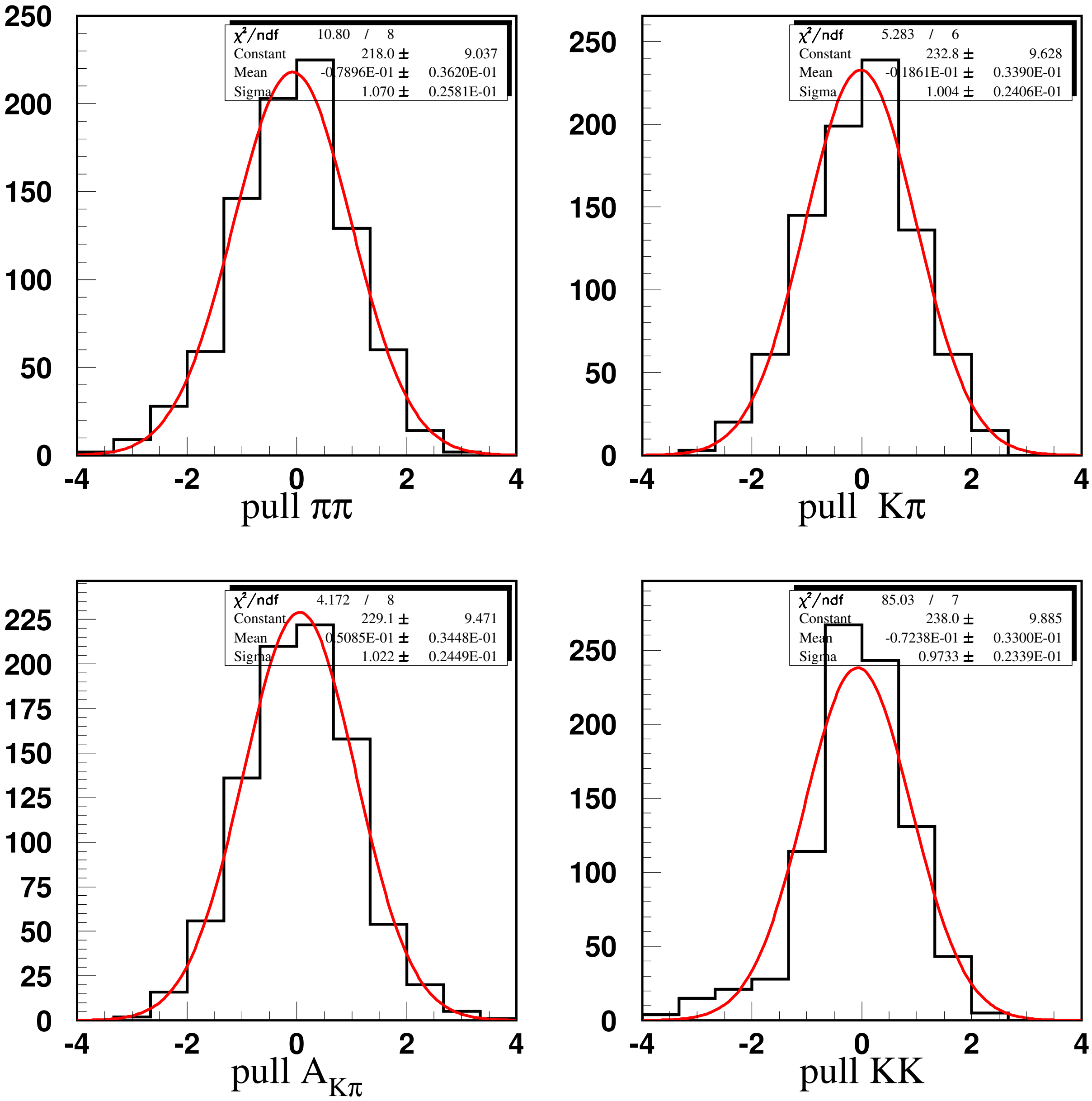

Figure 3.21: The distributions of pulls of signal fit parameters ($N_{\pi\pi}$, $N_{K\pi}$, $\mathcal{A}_{K\pi}$, N_{KK}), obtained from 1000 "toy" Monte Carlo experiments. This test reveals the presence of no significant bias or bad error estimates for the fitted parameters.

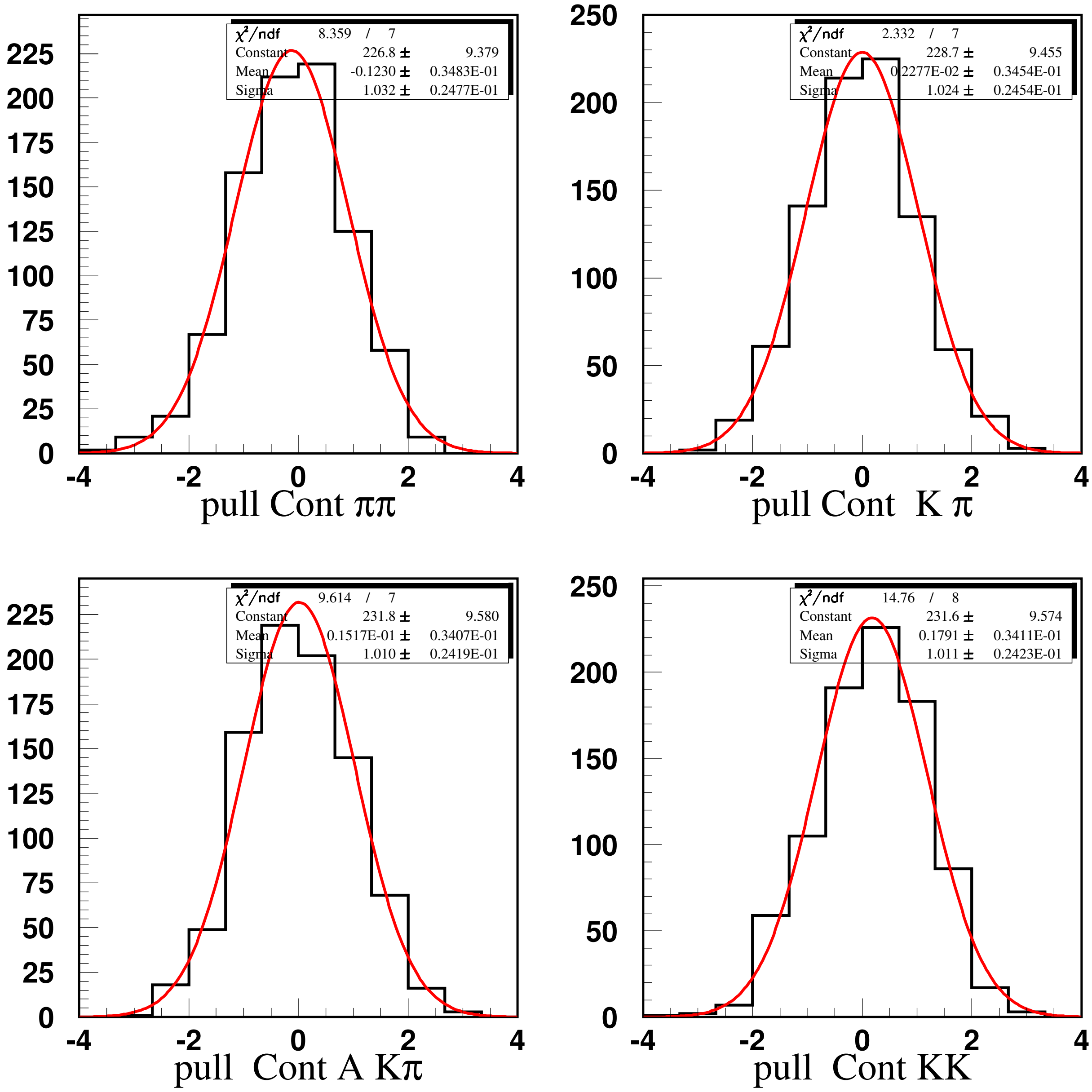

Figure 3.22: The distributions of pulls for background fit parameters $(N_{b\pi\pi}, N_{bK\pi}, \mathcal{A}_{bK\pi}, N_{bKK})$, obtained from 1000 ”toy” Monte Carlo experiments. This test reveals the presence of no significant bias or bad error estimates for the fitted parameters.

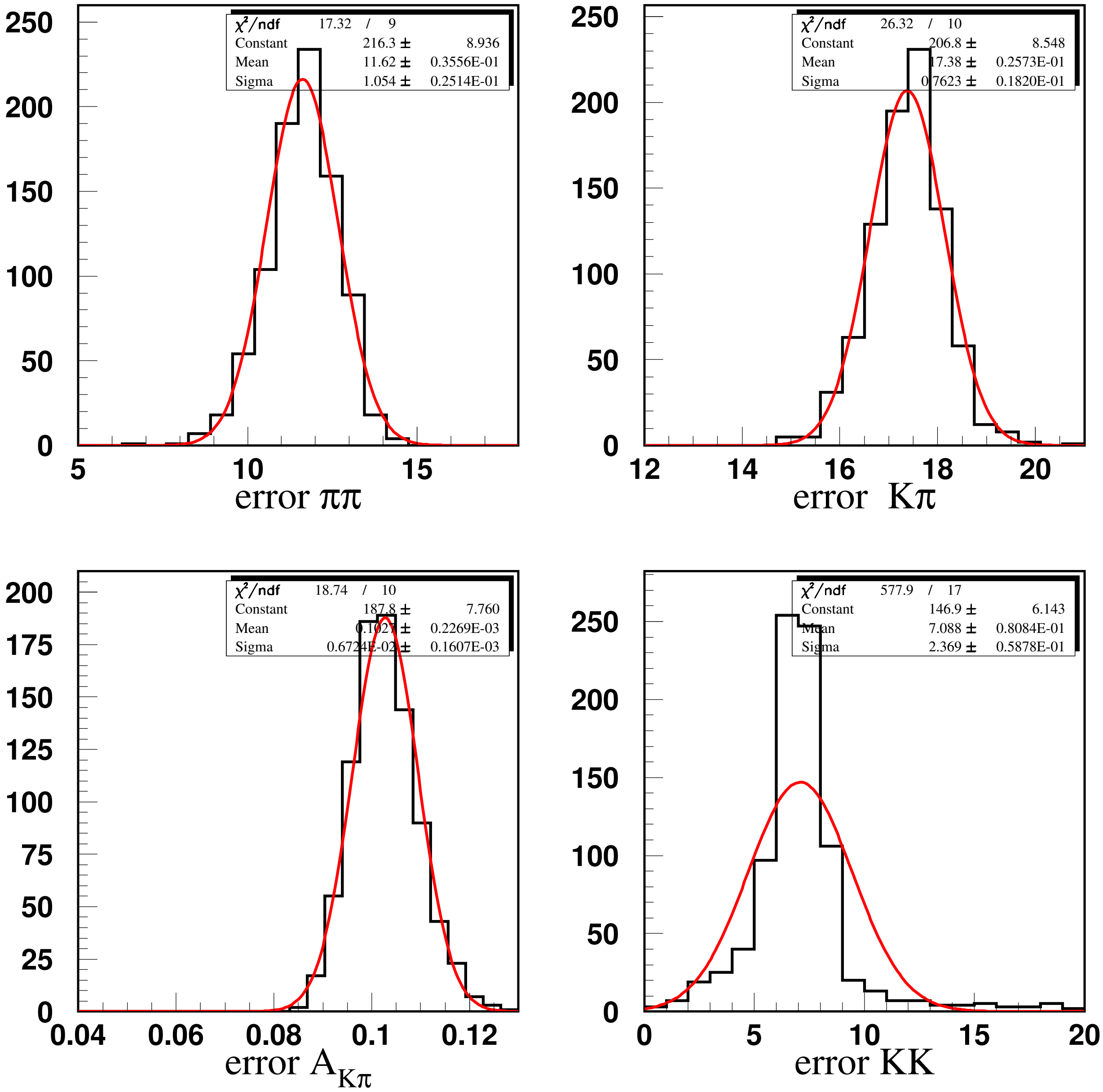

Figure 3.23: The distributions of errors of signal fit parameters ($N_{\pi\pi}$, $N_{K\pi}$, $\mathcal{A}_{K\pi}$, N_{KK}), obtained from 1000 "toy" Monte Carlo experiments.

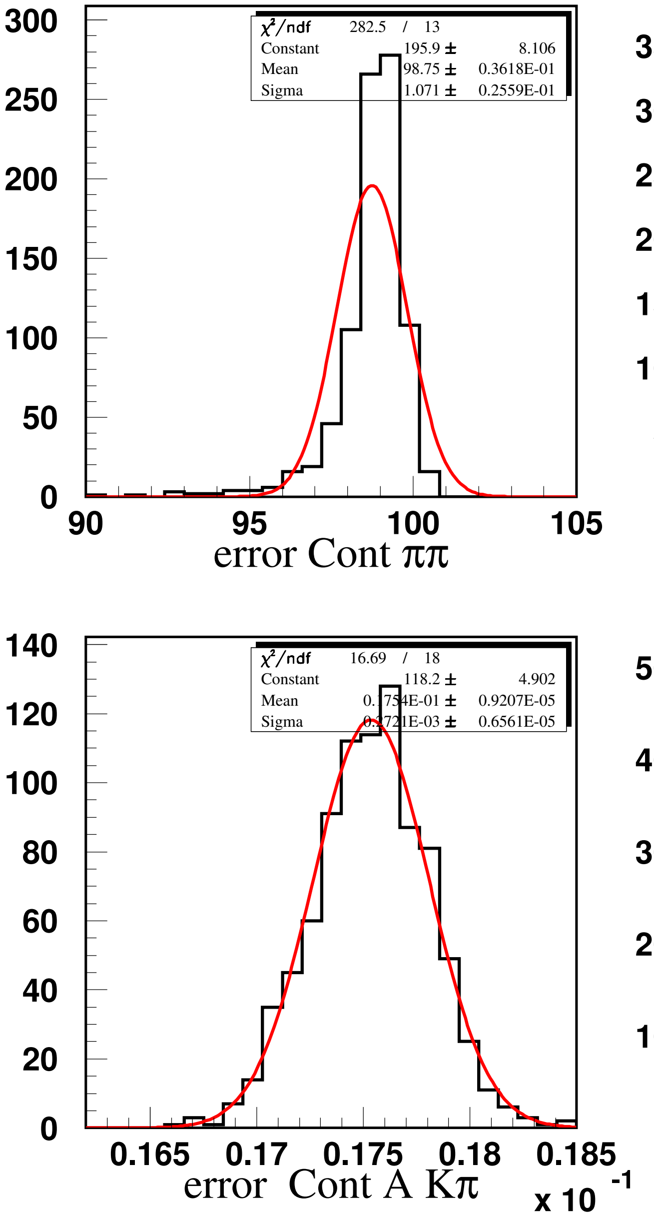

Figure 3.24: The distributions of errors of background fit parameters ($N_{b\pi\pi}$, $N_{bK\pi}$, $\mathcal{A}_{bK\pi}$, N_{bKK}), obtained from 1000 toy Monte Carlo experiments. The skewness of the N_{KK} error distribution is due to the constraint $N_{KK} > 0$ used in the likelihood fit.

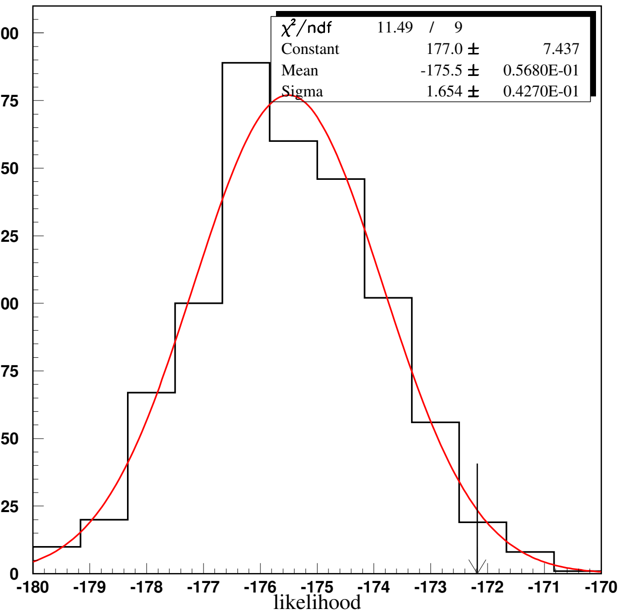

Figure 3.25: The distributions of $-2\log L$ minima obtained from 1000 toy Monte Carlo experiments. The arrow indicates the value obtained from the fit to the data.

differences between Monte Carlo events (or control samples) and data. The fit is to be repeated with each change of a PDF parameter, and the variations of the fit parameters from the central values of the nominal fit are taken as the estimated systematic uncertainties.

- The fit can be repeated using an alternative parameterization of a given PDF, derived from a sample that is independent from the sample used to determine the nominal parameterization. An example is to use control samples from the actual data in place of Monte Carlo simulated data, or vice versa.

Described below are the methods used to estimate the systematic uncertainty associated to each of the PDFs.

- **ΔE:** For the background ΔE shape, alternative parameterizations from Monte Carlo simulated background and off-resonance data (see Fig. 3.12) are used in assigning a systematic error. At this stage of the experiment, there is a relatively large uncertainty in the correct widths of the ΔE distributions for signal events. The comparison between ΔE resolutions for fully reconstructed $B^- \to D^0\pi^-$ events in data and Monte Carlo is used to estimate the amount of "smearing" to apply to the ΔE resolution in Monte Carlo $B \to h'^+h^-$ decays. We use a nominal ΔE resolution of 26 MeV and vary this value within a conservative range, $\sim$ 23.5-31 MeV, when estimating the associated systematic uncertainty. For the nominal fit, we assume the mean ΔE for each signal mode is shifted by $-5\,\mathrm{MeV}$ with respect to its expected mean, as is observed in $B^- \to D^0\pi^-$ decays. The amount of this shift is varied in the range -10 to $0\,\mathrm{MeV}$.

- **m_{ES}:** The mean value and resolution of m_{ES} for signal decays are varied by amounts determined from the uncertainties on the measured values from $B^- \to D^0\pi^-$ decays: $\pm 0.5\,\mathrm{MeV}/c^2$ and $\pm 0.2\,\mathrm{MeV}/c^2$ for the mean and the resolution, respectively. The background shape is varied within the range of the ARGUS parameter ξ, $\xi = 20$ and $\xi = 24$, derived from both off-resonance data and on-resonance ΔE sideband data fits.

- **PID:** The D^{*+} control sample sets strict constraints on the parameterization of the DIRC θ_c response. The θ_c offsets and resolutions that are used in the PDFs are varied within the error on those parameters obtained on the control sample data: $\pm 0.2\,\mathrm{mrad}$ for both the offsets and the resolutions. The relative size of the satellite peaks are also varied within a wide range. Values of $(1\%, 1\%)$, $(5\%, 5\%)$, $(4\%, 1\%)$ and $(1\%, 4\%)$ were used for the relative sizes of the (K, π) satellite peaks.

- **Fisher Output:** Because of the large correlation between parameters in the double Gaussian fits to the Fisher discriminant shapes, no attempt is made to vary those parameters in order to estimate systematic uncertainties. Alternative parameterizations from other data samples are used instead. The uncertainty due to the shape of the signal $\mathcal{F}$ is determined by using a parameterization obtained from $B^- \to D^0\pi^-$ decays in data (the nominal parameterization is derived from Monte Carlo simulated signal decays). Alternative parameterizations of the background $\mathcal{F}$ distribution are also used (Monte Carlo simulated background events and off-resonance data).

The systematic uncertainties in the fit results due to modelling of the PDFs are summarized in Tab.3.7 and Tab.3.8 for the branching ratio and the $\mathcal{A}_{K\pi}$ measurements, respectively.

Systematics due to charge asymmetries

In addition to the systematic uncertainties arising from imprecise knowledge of the PDFs, there are contributions to $\mathcal{A}_{K\pi}$ due to possible charge biases. The asymmetry $\mathcal{A}_{K\pi}$ is only

Param	bkg m_{ES}	bkg ΔE	bkg $\mathcal{F}$	$\langle m_{\text{ES}} \rangle$	$\sigma(m_{\text{ES}})$	$\langle \Delta E \rangle$	$\sigma(\Delta E)$	$\mathcal{F}\,(D^0\pi)$	θ_c	Total
$N_{\pi\pi}$	± 5.3	± 0.2	± 13	${}^{+0.0}_{-2.2}$	${}^{+0.7}_{-1.2}$	± 4.2	${}^{+5.9}_{-3.2}$	± 3.7	${}^{+5.0}_{-5.5}$	± 17
$N_{K\pi}$	± 1.6	± 0.2	± 3.0	${}^{+0.3}_{-1.4}$	± 0.5	${}^{+0.5}_{-1.4}$	${}^{+6.3}_{-4.3}$	0	± 1.3	${}^{+7.3}_{-6.0}$
N_{KK}	± 11	± 1.3	± 34	${}^{+10}_{-8.9}$	${}^{+5.1}_{-3.8}$	${}^{+7.6}_{-8.9}$	${}^{+4.6}_{-8.9}$	± 3.8	± 17	± 43

Table 3.7: Systematic errors (%) on the branching ratio results from the maximum likelihood fit.

Param	bkg m_{ES}	bkg ΔE	bkg $\mathcal{F}$	$\langle m_{\text{ES}} \rangle$	$\sigma(m_{\text{ES}})$	$\langle \Delta E \rangle$	$\sigma(\Delta E)$	$\mathcal{F}\,(D^0\pi)$	θ_c	Total
$\mathcal{A}_{K\pi}$	${}^{+0.003}_{-0.0}$	± 0.002	± 0.002	± 0.007	${}^{+0.003}_{-0.002}$	${}^{+0.022}_{-0.018}$	± 0.02	± 0.003	${}^{+0.007}_{-0.008}$	± 0.03

Table 3.8: Systematic errors on the $\mathcal{A}_{K\pi}$ result from the maximum likelihood fit.

sensitive to charge biases which are correlated with particle identification. From Monte Carlo we assume, in fact, that tracking efficiency at relatively high momenta do not distinguish between K and π. The effects considered are therefore possible differences in efficiencies for selection of $K^+\pi^-$ and $K^-\pi^+$ candidates, and biases in the maximum likelihood fit.

The systematic uncertainty on $\mathcal{A}_{K\pi}$ due to the PID cuts summarized in Tab.3.2 is estimated by measuring the asymmetry in neutral D decays, using the D^*-tagged control sample described in Section 2.4:

$$\mathcal{A}_D = \frac{N_{D^0} - N_{\overline{D}^0}}{N_{D^0} + N_{\overline{D}^0}}\,. \tag{3.28}$$

Both daugher tracks in the D decays are required to be in the momentum range of interest, 1.75-4.25 GeV/c, in order to mimic as closely as possible the kinematics of $B \to h'^+h^-$ decays. The raw asymmetry is measured to be $-(1.0 \pm 1.1)\%$. After application of all PID cuts, the asymmetry is $-(1.6 \pm 1.1)\%$. The difference is $-(0.60 \pm 0.41)\%$, where the statistical uncertainty takes into account the 93% correlation between the two measured asymmetries. A conservative procedure is to use the quadrature sum of the central value and its statistical uncertainty in estimating the systematic uncertainty on $\mathcal{A}_{K\pi}$. This yields a value of ± 0.0073.

The systematic uncertainty due to possible biases in the fit procedure itself is estimated by fitting the D control sample using the same θ_c PDFs that are used in the $B \to h'^+h^-$ fit. Since the θ_c PDFs are derived from this D sample in the first place, one would expect to obtain results for N_{D^0}, $N_{\overline{D}^0}$ and N_{bkgd} that are consistent with results obtained from simple χ^2 fits to the D^0 and $\overline{D}^0$ invariant mass distributions.

The selection of D^0 and $\overline{D}^0$ candidates for this test is as described in Section 2.4, with the additional requirement that *both* the daughter tracks of the $D^0/\overline{D}^0$ candidates fall into the DIRC acceptance, pass the standard PID cuts given in Tab.3.2 and are within the momentum range of interest to be compatible with $B \to h'^+h^-$ decays. The invariant mass distributions of the selected D^0 and $\overline{D}^0$ candidates are given in Fig. 3.26. The distributions are fitted to the sum of two Gaussians, whose means are both constrained to the value obtained from the fit to the sum of the D^0 and $\overline{D}^0$ distributions ($1.8647\,\mathrm{GeV}/c^2$), and a linear background term. The χ^2/ndof for the fits are reasonable, 1.13 and 1.61 for D^0 and $\overline{D}^0$, respectively, and the yields are $N_{D^0} = 3974 \pm 70$ and $N_{\overline{D}^0} = 4106 \pm 70$. This corresponds to an asymmetry of:

$$\mathcal{A}_D = \frac{N_{D^0} - N_{\overline{D}^0}}{N_{D^0} + N_{\overline{D}^0}} = -(1.6 \pm 1.1)\%\,. \tag{3.29}$$

The entire sample is then fit using an unbinned maximum likelihood fit. As a first test, only the invariant mass of the two tracks, $M(K\pi)$, is used in the fit. The signal PDF is given by a sum of two Gaussians, with means, widths and relative areas fixed to the results obtained from the χ^2 fit to the sum of the D^0 and $\overline{D}^0$ distributions. The background $M(K\pi)$ PDF is a linear function, with slope and intercept given by the same χ^2 fit. The fit parameters are the overall signal and background normalizations, $N_D \equiv N_{D^0} + N_{\overline{D}^0}$ and N_{bkgd}, respectively. The likelihood is defined exactly as in Eq. (3.20). The result of this fit is $N_D = 8067 \pm 91$, which is in excellent agreement with the simple χ^2 fit result of 8080 ± 99.

Next, the θ_c PDFs are introduced. They are identical to the ones used in the $B \to h'^+h^-$ fit. The fit parameters are now given as: $N_{\pi\pi}$, N_D, $\mathcal{A}_D$, N_{KK}, $N_{b\pi\pi}$, $N_{bK\pi}$, $\mathcal{A}_{bK\pi}$ and N_{bKK}, which are analogous to the 8 parameters in the $B \to h'^+h^-$ fit. The results of this fit are:

$$
\begin{aligned}
N_{\pi\pi} &= 45 \pm 17 \\
N_D &= 7913 \pm 92 \\
\mathcal{A}_D &= -0.017 \pm 0.012 \\
N_{KK} &= 123 \pm 17 \\
N_{b\pi\pi} &= 208 \pm 17 \\
N_{bK\pi} &= 330 \pm 25 \\
\mathcal{A}_{bK\pi} &= -0.150 \pm 0.073 \\
N_{bKK} &= 50.9 \pm 9.2\,.
\end{aligned}
$$

About 98% of the D signal is properly identified as being composed of $K^{\pm}\pi^{\mp}$ candidates, and the fitted D^0-$\overline{D}^0$ asymmetry, $(-1.7\pm1.2)\%$, is in good agreement with the asymmetry obtained from the χ^2 fits to the mass distributions, $(-1.6 \pm 1.1)\%$. The normalized θ_c distributions for $K^{\pm}$ and $\pi^{\pm}$ tracks from the D control sample are shown in Fig. 3.27. In making the plots, the measured offsets were first subtracted from the θ_c measurements. Both the offsets and the θ_c resolutions are functions of the polar angle of the track, as described in Section 2.4.1. The points with error bars represent the distributions for negatively charged tracks and the histograms represent the distributions for positively charged tracks. There are no significant differences observed between the the two charge species. We conclude that the systematic uncertainty on the asymmetry measurement due to the PDF description and fit procedure is negligible.

If the same fit is performed, but with the θ_c satellite peaks removed from the PDFs, the fitted $D \to K\pi$ yield goes down to $N_D = 7661 \pm 69$ and $N_{\pi\pi}$ and N_{KK} increase to 212 ± 18 and 208 ± 17, respectively. This is further evidence that the satellite peaks are indeed real features of the θ_c reconstruction.

In conclusion, the systematic uncertainty on $\mathcal{A}_{K\pi}$ due to intrinsic PID-related charge asymmetries is estimated to be ±0.0073. This is negligible in comparison with the uncertainties estimated from PDF variations, summarized in Tab.3.8.

3.4.4 Cross-checks

In this Section we describe a variety of checks which were performed in order to validate the performance of the fit method and ensure self-consistency within the data sample.

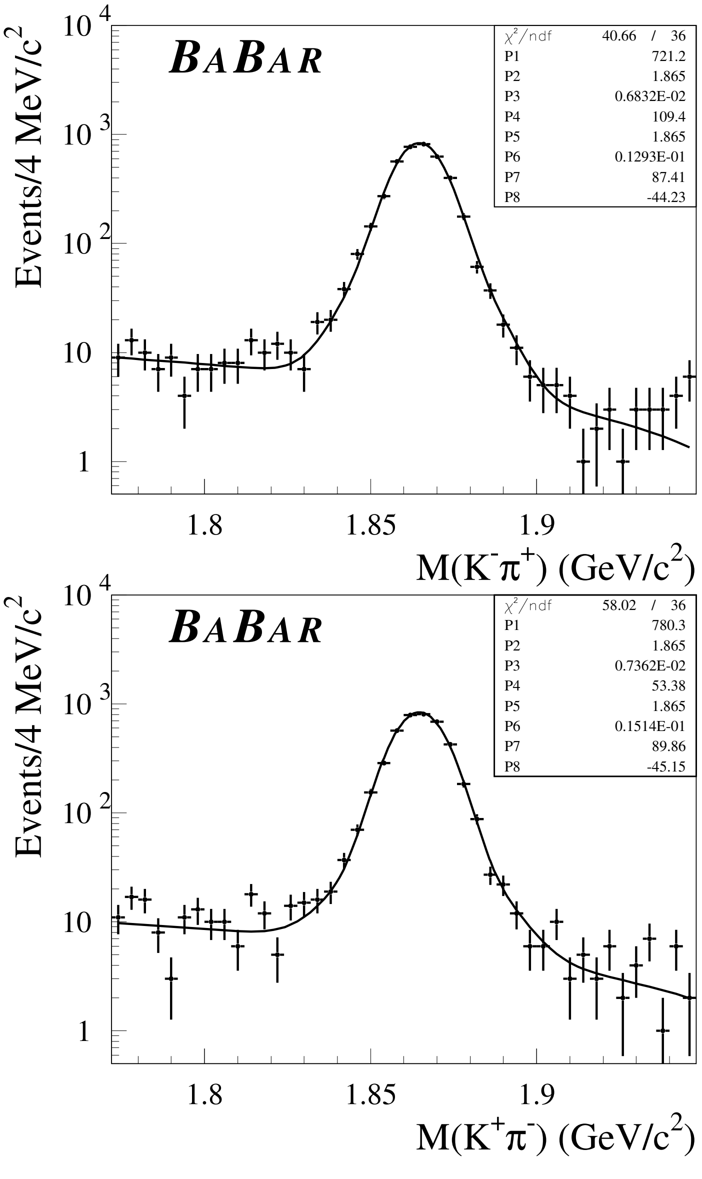

Figure 3.26: The invariant mass distributions for (top) $D^0 \to K^-\pi^+$ and (bottom) $\overline{D}^0 \to K^+\pi^-$ candidates from the D^{*+} control sample. The cuts and fit functions are described in the text.

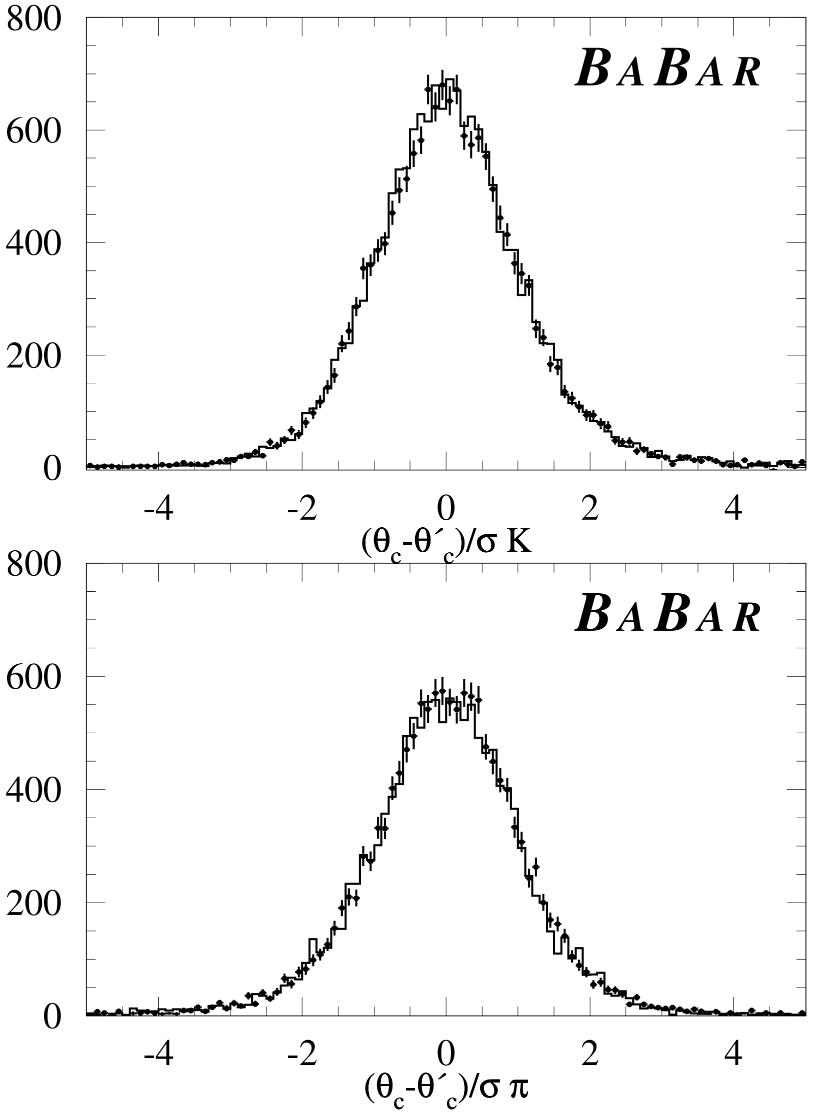

Figure 3.27: The distributions of $(\theta_c - \theta_c')/\sigma_{\theta_c}$ for kaon tracks (top) and pion tracks (bottom), selected from the D^{*+} control sample. The points with error bars represent negatively charged tracks and the histograms represent positively charged tracks.

This is achieved by fitting samples of Monte Carlo simulated events for which the true input signal and background yields are known and by performing fits to the data sample using a few alternative techniques. The latter tests have focused on the treatment of particle ID since this is perhaps the most important aspect of the analysis.

Fits to Monte Carlo samples

The reliability of the fit was extensively tested on high statistics pure signal Monte Carlo samples (to investigate any cross-feed between signal modes) as well as a mixture of Monte Carlo simulated signal and background decays. No significant biases are observed and the fit is found to always return the correct signal yields. Some of these tests are described in Tab.3.9 and Tab.3.10.

For the test summarized in Tab.3.10, the background consists of Monte Carlo continuum and τ events. MC-truth [4] was used to determine the number of background events of each species. Out of 3547 background events, 213 are found to not be of the type $\pi^{\pm}\pi^{\mp}$, $K^{\pm}\pi^{\mp}$ or $K^{\pm}K^{\mp}$, and are labelled as “other” in the table. About 70% of these other types of background are μh and the remainder are eh or ph. Given the definitions of the θ_c PDFs, the fit will primarily regard leptons as pions and protons as kaons. In any case, they will always be regarded as background, based on their m_{ES}, ΔE and Fisher values.

From these tests, we conclude that the fit returns reliable, unbiased results. “Toy” Monte Carlo studies (described in Section 3.4.2) were used to ensure that the statistical uncertainties determined by the fit are consistent with what is expected .

No-PID fit

Another cross check consists of selecting $B \to h'^{+}h^{-}$ candidates using all cuts *except* the PID cuts (given in Tab.3.2) and performing a maximum likelihood fit to obtain the overall $B \to h'^{+}h^{-}$ yield. For this fit, all variables except θ_c are used in the likelihood definition. Since the PID cuts are not applied for this test, the selection efficiencies are higher by a factor of 1.329 ± 0.008. The result of this fit is: $N_{\pi\pi} = 106 \pm 25$, $N_{K\pi} = 152 \pm 31$ and $N_{KK} = 59 \pm 21$. In this fit, the three signal modes are distinguished from each other very poorly since only ΔE provides any discriminating power. This is reflected in the fact that the correlation coefficients are large (of the order of -0.5). The only reliable result from

---

[4] Information on the nature of the generated particles obtained from the Monte Carlo generator is usually referred to as *MC-truth* .

Fit Variable	Input Value	Fitted Value
Test 1		
$N_{\pi\pi}$	4233	4179 ± 67
$N_{K\pi}$	4224	4237 ± 70
$\mathcal{A}_{K\pi}$	0.001	-0.009 ± 0.017
N_{KK}	4057	4025 ± 66
$N_{b\pi\pi}$	0	31.3 ± 6.7
$N_{bK\pi}$	0	30.6 ± 7.2
$\mathcal{A}_{bK\pi}$	0	-0.06 ± 0.23
N_{bKK}	0	11.1 ± 4.0
Test 2		
$N_{\pi\pi}$	4233	4186 ± 65
$N_{K\pi}$	0	13.3 ± 6.0
$\mathcal{A}_{K\pi}$	0	0.62 ± 0.43
N_{KK}	0	0.0 ± 1.2
$N_{b\pi\pi}$	0	31.1 ± 6.3
$N_{bK\pi}$	0	2.8 ± 2.7
$\mathcal{A}_{bK\pi}$	0	-0.7 ± 1.1
N_{bKK}	0	0.0 ± 0.96
Test 3		
$N_{\pi\pi}$	0	6.2 ± 4.6
$N_{K\pi}$	4224	4166 ± 65
$\mathcal{A}_{K\pi}$	0.001	-0.0058 ± 0.016
N_{KK}	0	22.1 ± 7.5
$N_{b\pi\pi}$	0	1.4 ± 1.8
$N_{bK\pi}$	0	27.3 ± 6.0
$\mathcal{A}_{bK\pi}$	0	0.26 ± 0.21
N_{bKK}	0	0.86 ± 1.2
Test 4		
$N_{\pi\pi}$	0	0.0 ± 0.53
$N_{K\pi}$	0	20.2 ± 6.6
$\mathcal{A}_{K\pi}$	0	-0.60 ± 0.28
N_{KK}	4057	4007 ± 63
$N_{b\pi\pi}$	0	0.0 ± 0.63
$N_{bK\pi}$	0	15.8 ± 4.7
$\mathcal{A}_{bK\pi}$	0	-0.20 ± 0.29
N_{bKK}	0	13.8 ± 4.5

Table 3.9: Summary of tests performed with Monte Carlo simulated $B \to h'^{+}h^{-}$ decays.

Fit Variable	Input Value	Fitted Value
Test 5		
$N_{\pi\pi}$	100	91 ± 12
$N_{K\pi}$	100	108 ± 12
$\mathcal{A}_{K\pi}$	-0.08	-0.09 ± 0.11
N_{KK}	10	10.5 ± 4.9
$N_{b\pi\pi}$	1811	1904 ± 48
$N_{bK\pi}$	916	967 ± 39
$\mathcal{A}_{bK\pi}$	0.05	0.073 ± 0.039
N_{bKK}	607	677 ± 29
Other	213	na

Table 3.10: Summary of test fit performed with Monte Carlo simulated events.

this fit is the total number of signal events, N_{hh}. Taking into account the correlations between the fit parameters, the result for N_{hh} is 317 ± 27. This is in good agreement with the nominal fit result scaled by the efficiency ratio: 290 ± 28.

Fit to off-resonance and ΔE sideband data

The fit was performed on the off-resonance and *upper* ΔE sideband samples, using the same PDFs as in the nominal fit (except that ΔE is not used in the fit). The lower ΔE sideband was not used since it contains feed-down from B decays. The fit to the off-resonance sample returns:

$$\begin{aligned}
N_{\pi\pi} &= 0.5^{+3.7}_{-0.5} \\
N_{K\pi} &= 1.0^{+2.0}_{-1.0} \\
\mathcal{A}_{K\pi} &= -0.99 \pm 1.7 \\
N_{KK} &= 0.0^{+1.0}_{-0.0} \\
N_{b\pi\pi} &= 1214 \pm 38 \\
N_{bK\pi} &= 710 \pm 32 \\
\mathcal{A}_{bK\pi} &= -0.002 \pm 0.044 \\
N_{bKK} &= 463 \pm 24
\end{aligned}$$

The upper sideband sample was fit without using ΔE in the fit, and the results are:

$$\begin{aligned}
N_{\pi\pi} &= 0.0^{+7.7}_{-0.0} \\
N_{K\pi} &= 0.0^{+5.2}_{-0.0} \\
\mathcal{A}_{K\pi} &= -0.13 \pm 0.23 \\
N_{KK} &= 0.0^{+6.4}_{-0.0} \\
N_{b\pi\pi} &= 5476 \pm 81 \\
N_{bK\pi} &= 3204 \pm 72 \\
\mathcal{A}_{bK\pi} &= -0.006 \pm 0.021 \\
N_{bKK} &= 1932 \pm 51
\end{aligned}$$

Both sets of results are consistent with no observed signal.

3.5 Determination of branching fractions

We determine branching fractions for $B \to \pi^+\pi^-$ and $B \to K^+\pi^-$ decays and an upper limit for the $B \to K^+K^-$ decay. The individual efficiencies have been reported in Section 2.3.

Branching fractions are calculated as

$$\mathcal{B} = \frac{N_S}{\epsilon \cdot N_{B\overline{B}}}, \tag{3.30}$$

where N_S is the central value from the fit, ϵ is the total efficiency and $N_{B\overline{B}} = (22.57 \pm 0.36) \times 10^6$ is the total number of $B\overline{B}$ pairs in our dataset. Implicit in Eq. 3.30 is the assumption of equal branching fractions for $\Upsilon(4S) \to B^0\overline{B}^0$ and $\Upsilon(4S) \to B^+B^-$.

In addition to the systematic errors given in Tab. 3.7, there are uncertainties in the selection efficiency (see Eq.3.16) and in $N_{B\overline{B}}$. The systematic uncertainties on the efficiencies come from tracking efficiency (1.2% per track), the cut on $\cos\theta_{\mathrm{S}}$ (2%) and the PID cuts (1.5%). The systematic error on $\cos\theta_{\mathrm{S}}$ is extracted by considering the deviation of the Monte Carlo signal distribution from a flat distribution. The systematic error on the PID cut efficiencies is estimated by comparing the efficiencies obtained from the D^{*+} control sample and from Monte Carlo simulated signal decays. These are summarized in Tab.3.11, along with the overall systematic uncertainties for the branching ratio measurements.

Mode	$N_{B\bar{B}}$	MC Stats.	Tracking Syst.	PID Cuts	$\cos\theta_{\mathrm{S}}$ Cut	PDFs	Total
$\pi^+\pi^-$	±1.6	±0.8	±2.4	±1.5	±2.0	±17	±17
$K^+\pi^-$	±1.6	±0.8	±2.4	±1.5	±2.0	$^{+7.3}_{-6.0}$	$^{+8.3}_{-7.1}$
K^+K^-	±1.6	±0.8	±2.4	±1.5	±2.0	±43	±43

Table 3.11: Systematic errors (%) on the branching ratio measurements.

For the K^+K^- mode we determine the 90% confidence level upper limit (N^0_{KK}) for the signal yield and for branching fraction, using the following procedure. N^0_{KK} is calculated by determining the value for which $\int_0^{N^0_{KK}} L_{max}\,\mathrm{d}N_{KK}/\int_0^{\infty} L_{max}\,\mathrm{d}N_{KK} = 0.90$, where L_{max} is the likelihood maximum value (as a function of N_{KK}), obtained by maximizing the likelihood with respect to all free fit parameters except N_{KK}. The result is then increased by the total systematic error on the yield. The efficiency is reduced by the value of its systematic uncertainty in computing the upper limit on the branching fraction.

The results are summarized in Tab.3.12. The statistical significance of a given signal yield is determined by setting the yield to zero and maximizing the likelihood with respect to all other variables.

Table 3.12: Summary of branching fraction results. Shown are the central fit values N_S and measured branching fractions $\mathcal{B}$. For the K^+K^- mode we show the 90% confidence level upper limit for the signal yield and branching fraction. For N_S and $\mathcal{B}$ the first error is statistical and the second is systematic.

Mode	N_S	Stat. Sig. (σ)	$\mathcal{B}\,(10^{-6})$
$\pi^+\pi^-$	$41 \pm 10 \pm 7$	4.7	$4.1 \pm 1.0 \pm 0.7$
$K^+\pi^-$	$169 \pm 17^{+14}_{-12}$	15.8	$16.7 \pm 1.6^{+1.4}_{-1.2}$
K^+K^-	$8.2^{+7.8}_{-6.4} \pm 3.5$ (< 24)	1.3	< 2.5

Chapter 4

Measurement of CP violating asymmetries

4.1 Introduction

This Chapter describes an analysis of the time evolution in $B^0 \to h'^+ h^-$ decays. In Section 4.2 we describe how finite experimental resolution affects Eq.1.38. The two main ingredients leading to time dependent *CP* asymmetry measurement are described, namely the role of flavor tagging algorithms and the knowledge of Δt resolution function. Definitions of tagging efficiency and dilution in different tagging categories are given in Section 4.2.1. In Section 4.2.2 a brief introduction to the resolution model for Δt is given: both tagging dilution and resolution model are extracted directly from data. In Section 4.3 the data sample used for this analysis is introduced. A selection is imposed to Run 1 and Run 2 data (for a total of about 30 fb^{-1}) similar to the Branching Ratios analysis described in Chapter 3. Due to the small decay rate ($\mathcal{B} \sim 4 \times 10^{-6}$) and large continuum $q\bar{q}$ background, a detailed study of background properties specific to the time dependent analysis is performed (Section 4.5). A global fit techinque is adopted to extract from the final data sample the *CP* violating parameters along with the raw yields for the various channels (Section 4.6): validation studies and cross checks are described and results are given in Section 4.8. Finally systematics uncertainties are evaluated. It is worth to mention here that when we fit the data set we use to extract the final results, a *blinding* of the fit output is used. This means that the true output of the fit is kept hidden to the physicists by adding a random offset to the asymmetries and randomly flipping its sign[50].

4.2 *CP* violation in interference between mixing and decay

The physical asymmetries which need to be measured in order to establish the presence of *CP* violation depend on the time difference $\Delta t = t_{CP} - t_{\text{tag}}$ between the decay of the *CP* mode B meson, B_{CP}, and the decay of the recoiling meson B_{tag}, and on the flavor of the b-quark (b or $\bar{b}$) of this tagging-B. It is therefore necessary to use a tagging algorithm to identify this flavor.

The b-quark flavor is derived from the correlation between the sign of the charge of the quark and the charges of the decay products of the B meson. The presence of a lepton in the final state, for instance, provides the most simple example of such a correlation. If the lepton originates from a semi-leptonic decay of the B meson, as in Fig. 4.1 a), the sign of the charge of the lepton is identical to q_b, the sign of the b quark. However, the lepton may come from the decay of a *charmed* meson (we refer to it as *cascade* production), in which case the sign of its charge may be opposite to that of q_b, as in Fig. 4.1 b), or the same as q_b, as in Fig. 4.1 c). On the other hand, the Cabibbo allowed decay chain $b \to c \to s$ provides another type of charge correlation useful for q_b determination: in this case it is the charge of the charged kaon emerging from s quark hadronization to carry the tagging infromation. The tagging algorithm divides up the events in *categories* according to the presence of a given type of particle (Electron category, Kaon category, etc.). More details on this are given in the next Section.

Leptons from the direct semi-leptonic decays ($b \to cl\nu$) may be distinguished from those coming from cascade production by using the momentum of the lepton in the $\Upsilon(4S)$ rest frame, since the spectrum of direct leptons is known to be harder than the spectrum of the cascade decays (Fig. 4.2)[1].

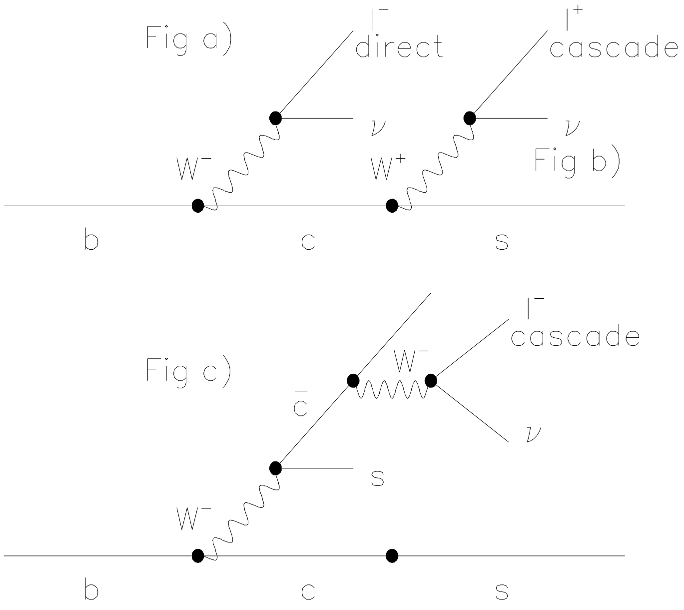

Figure 4.1: a) Direct production of a lepton. b) Cascade production of a lepton with reverse-sign. c) Cascade production of a lepton with direct-sign.

---

[1] This is due both to the kinematic difference in the B meson's decay with respect to the *charmed* meson's secondary decay originated from a B decay *and* to the opposite helicity of c quark with respect to b quark

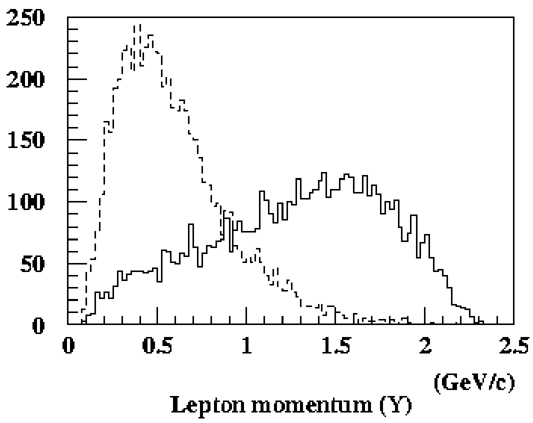

Figure 4.2: CMS momentum spectrum for lepton from B decays (solid histo) and from *charm* decays (dashed histo)

More generally, events can be sorted into two classes: one in which the sign attributed to the decay products is the same as the sign of the q_b, and the other, in which the sign attributed to the decay products is the opposite of the sign of q_b. It is the purpose of the tagging algorithm to perform the most efficient discrimination between these two classes, through the use of kinematical and topological information: this finally allows separation of events in B^0 and $\overline{B}^0$ tagged events.

Of course, any possible flavor tagging algorithm is intrinsically imperfect since it is affected by experimental resolution and by the features of the underlying physics process. For instance, in the case of tagging with leptons it is impossible to perfectly separate between direct-sign and reverse-sign leptons using a cut on the lepton's CMS momentum (Fig. 4.2). Eq.1.38 must be therefore substituted by new functions to include the *mistag probability* w ($\bar{w}$)

$$\begin{aligned} f_{B^0\,\mathrm{tag}} &= (1-w)f_+ + \bar{w}f_-, \\ f_{\overline{B}^0\,\mathrm{tag}} &= (1-\bar{w})f_- + wf_+, \end{aligned} \tag{4.1}$$

where w ($\bar{w}$) is the probability that a true B^0 ($\overline{B}^0$) meson is tagged as a $\overline{B}^0$ (B^0). Defining the *dilutions*, $D = (1-2w)$ and $\bar{D} = (1-2\bar{w})$, the average dilution $\langle D \rangle$, and the dilution difference ΔD,

$$\begin{aligned}\langle D\rangle &= \frac{D+\bar{D}}{2},\\ \Delta D &= D-\bar{D},\end{aligned}\tag{4.2}$$

the mistag probabilities can be written as

$$\begin{aligned}w &= \frac{1-\langle D\rangle-\frac{\Delta D}{2}}{2},\\ \bar{w} &= \frac{1-\langle D\rangle+\frac{\Delta D}{2}}{2}.\end{aligned}\tag{4.3}$$

The decay rate distributions, assuming perfect vertex resolution, are then

$$\begin{aligned}f_{B^0\,\mathrm{tag}} &= \frac{e^{-|\Delta t_{\mathrm{true}}|/\tau}}{4\tau}\left[1+\frac{\Delta D}{2}+\langle D\rangle\left(S_f\sin(\Delta m_d\Delta t_{\mathrm{true}})-C_f\cos(\Delta m_d\Delta t_{\mathrm{true}})\right)\right],\\ f_{\bar{B}^0\,\mathrm{tag}} &= \frac{e^{-|\Delta t_{\mathrm{true}}|/\tau}}{4\tau}\left[1-\frac{\Delta D}{2}-\langle D\rangle\left(S_f\sin(\Delta m_d\Delta t_{\mathrm{true}})+C_f\cos(\Delta m_d\Delta t_{\mathrm{true}})\right)\right]\end{aligned}\tag{4.4}$$

Moreover, because of the different underlying physics process, the dilutions depend on the tagging category ($w \to w_c$). These mistag probabilities can be determined by studying the time-dependent rate of $B^0\overline{B}^0$ oscillations in $\Upsilon(4S)$ decays when one of the two neutral B is fully reconstructed in a flavor eigenstate. This is the case of final states like[2] $D^{(*)}\pi$,$D^{(*)}\rho$, $D^{(*)}a_1$ or $J/\psi K^*$. They can be identified with good purity (see m_{ES} distribution for Run 1 data in Fig.4.3) and they are referred to as *flavor B sample* (B_{flav}). As soon as a B is fully reconstructed, the flavor tagging algorithm can be applied to the second not-recontructed B in the event (referred to as B_{tag}) after subtracting from the event all the particles belonging to the B_{flav}. In this case the mistag probabilities arises solely from this B_{tag} side.

On the other hand, the probability for B^0-$\overline{B}^0$ mixing is a function of Δm_d, the difference between the mass eigenstates B^0_H and B^0_L, and the true time difference Δt_{true} between the two B decays:

$$Prob(B^0\overline{B}^0 \to B^0B^0 \ or\ \overline{B}^0\overline{B}^0, B^0\overline{B}^0) \propto \mathrm{e}^{-\Gamma|\Delta t_{\mathrm{true}}|}(1\pm\cos\Delta m_d\Delta t_{\mathrm{true}}).\tag{4.5}$$

The observed $B^0\overline{B}^0$ system produced in an $\Upsilon(4S)$ decay can be classified as *mixed* or *unmixed* depending on whether the reconstructed B_{flav} has the same or the opposite flavor

---

[2] For instance $B^0(\bar{B}^0)$ decays to $D^-\pi^+(D^+\pi^-)$ while the decay to the charge conjugated final states $D^+\pi^-(D^-\pi^+)$ is strongly suppressed.

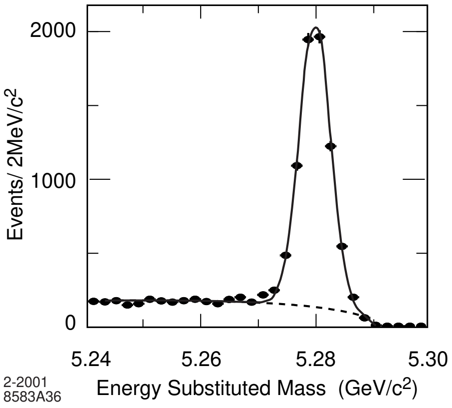

Figure 4.3: m_{ES} distribution for a sample of 6,700 neutral B mesons reconstructed in the final states $D^{(*)-}\pi^+, D^{(*)-}\rho^+, D^{(*)-}a_1^+$, and $J/\psi K^{*0}$ (Run 1 data).

as the B_{tag}. If Δz resolution and flavor tagging were perfect, the asymmetry

$$A_{\mathrm{mixing}}(\Delta t_{\mathrm{true}}) = \frac{N_{\mathrm{unmix}}(\Delta t_{\mathrm{true}}) - N_{\mathrm{mix}}(\Delta t_{\mathrm{true}})}{N_{\mathrm{unmix}}(\Delta t_{\mathrm{true}}) + N_{\mathrm{mix}}(\Delta t_{\mathrm{true}})} \tag{4.6}$$

as a function of Δt_{true} would be described by a cosine function with unit amplitude. However, the tagging algorithm incorrectly identifies the flavor of B_{tag} with a probability w. This mistag probability reduces the amplitude of the oscillation by a dilution factor $D = (1 - 2w)$. A simultaneous fit to the mixing frequency and its amplitude allows the determination of both Δm_d and the mistag probabilities.

The probability density functions (PDF's) for the mixed ($-$) and unmixed ($+$) events can be expressed as the convolution of the oscillatory component $h_\pm$, with a Δt resolution function $\mathcal{R}(\delta_{\mathrm{t}} = \Delta t - \Delta t_{\mathrm{true}}; \hat{a})$

$$\mathcal{H}_\pm(\Delta t; \Gamma, \Delta m_d, w, \hat{a}) = h_\pm(\Delta t_{\mathrm{true}}; \Gamma, \Delta m_d, w) \otimes \mathcal{R}(\delta_{\mathrm{t}}; \hat{a}), \tag{4.7}$$

where $\hat{a}$ are the parameters of the resolution function and

$$h_\pm(\Delta t_{\mathrm{true}}; \Gamma, \Delta m_d, w) = \frac{1}{4}\Gamma\, \mathrm{e}^{-\Gamma|\Delta t_{\mathrm{true}}|}\left[1 \pm (1-2w)\cos \Delta m_d \Delta t_{\mathrm{true}}\right]. \tag{4.8}$$

A likelihood function is then constructed from the sum of $\mathcal{H}_\pm$ over all mixed and unmixed events, and over the different tag types, c, each with its own characteristic mistag probabilities w_c

$$\ln \mathcal{L}_{\mathrm{mix}} = \sum_i^{\mathrm{tagging}} \left[\sum_{\mathrm{unmixed}} \ln \mathcal{H}_+(\Delta t; \Gamma, \Delta m_d, w_c, \hat{a}_c) + \sum_{\mathrm{mixed}} \ln \mathcal{H}_-(\Delta t; \Gamma, \Delta m_d, w_c, \hat{a}_c) \right]. \tag{4.9}$$

This likelihood can be maximized to extract the mistag probabilities w_c and resolution parameters $\hat{a}_c$ and, simultaneously, the mixing rate Δm_d. The correlation between these parameters is small, because the rate of mixed events at low values of Δt, where the $B^0\overline{B}^0$ mixing probability is small, is mainly governed by the mistag probability. Conversely, the sensitivity to Δm_d increases at larger values of Δt; when Δt is approximately twice the B lifetime, half of the neutral Bs will have oscillated.

Similarly, in neutral B meson decays to the $K^{\pm}\pi^{\mp}$ final state the flavor of the parent meson is tagged by the charge of the kaon. For a $B^0 \rightarrow K^+\pi^-$ ($\overline{B}^0 \rightarrow K^-\pi^+$) decay the event is therefore known to be a mixed event if the tag side is a B^0 ($\overline{B}^0$). The *CP* asymmetry analysis for $B^0 \rightarrow \pi^+\pi^-$ must include the effect of mixing in the $K\pi$ term, analogous to the B_{flav} sample. The decay rate distributions for mixed and unmixed $K\pi$ events when the tag side is a B^0 or $\overline{B}^0$ are:

$$\begin{aligned}
F_{\text{mix},\,B^0\,\text{tag}} &= \frac{e^{-|\Delta t_{\text{true}}|/\tau}}{4\tau}\left[\left(1+\frac{\Delta D}{2}\right)-\langle D\rangle\cos(\Delta m_d \Delta t_{\text{true}})\right]\otimes\mathcal{R}(\delta_{\text{t}};\hat{a}),\\
F_{\text{unmix},\,B^0\,\text{tag}} &= \frac{e^{-|\Delta t_{\text{true}}|/\tau}}{4\tau}\left[\left(1+\frac{\Delta D}{2}\right)+\langle D\rangle\cos(\Delta m_d \Delta t_{\text{true}})\right]\otimes\mathcal{R}(\delta_{\text{t}};\hat{a}),\\
F_{\text{mix},\,\overline{B}^0\,\text{tag}} &= \frac{e^{-|\Delta t_{\text{true}}|/\tau}}{4\tau}\left[\left(1-\frac{\Delta D}{2}\right)-\langle D\rangle\cos(\Delta m_d \Delta t_{\text{true}})\right]\otimes\mathcal{R}(\delta_{\text{t}};\hat{a}),\\
F_{\text{unmix},\,\overline{B}^0\,\text{tag}} &= \frac{e^{-|\Delta t_{\text{true}}|/\tau}}{4\tau}\left[\left(1-\frac{\Delta D}{2}\right)+\langle D\rangle\cos(\Delta m_d \Delta t_{\text{true}})\right]\otimes\mathcal{R}(\delta_{\text{t}};\hat{a}). \qquad (4.10)
\end{aligned}$$

Finally, the *observed* distribution $F(\Delta t)$ for the decay $B^0 \rightarrow \pi^+\pi^-$ relevant to *CP* asymmetry extraction, is the convolution of $f(\Delta t)$ (Eq.4.4)with the signal vertex resolution function $\mathcal{R}(\delta_{\text{t}};\hat{a})$

$$\begin{aligned}
F_{B^0\,\text{tag}} &= f_{B^0\,\text{tag}}\otimes\mathcal{R}(\delta_{\text{t}};\hat{a}),\\
F_{\overline{B}^0\,\text{tag}} &= f_{\overline{B}^0\,\text{tag}}\otimes\mathcal{R}(\delta_{\text{t}};\hat{a}). \qquad (4.11)
\end{aligned}$$

4.2.1 Definition of tagging categories

A fit able to extract $S_f(C_f)$ is only sensitive to the effective coefficient in front of the sine(cosine) function in Eq. 4.4. It actually measures a *raw* *CP* violating asymmetry A (let's suppose $C_f = 0$):

$$(1-2w)S_f = A \quad , \qquad (4.12)$$

This means that in the limit of $w = 0.5$ (a *random* tagging algorithm) the observed raw asymmetry is zero even if S_f is non-null.

The statistical uncertainty on the measurement of A, $\sigma[A]$, is inversely proportional to the square-root of the number of events entering the analysis. These events must be tagged, hence $\sigma^2[A]$ is inversely proportional to the *tagging efficiciency*, ϵ, which represents the fraction of events which are tagged by the tagging algorithm. ϵ is the fraction of true B^0 which are assigned a tag (either a correct or incorrect one), and $\bar{\epsilon}$ is the fraction of true $\overline{B}^0$ which are assigned a tag. Further we define:

$$\Delta\epsilon = \epsilon - \bar{\epsilon} \tag{4.13}$$

$$\Delta w = w - \bar{w} \tag{4.14}$$

$$r = \frac{\bar{\epsilon}}{\epsilon} \tag{4.15}$$

The statistical uncertainty on the measurement of S_f takes the form [51] :

$$\sigma[S_f] = \frac{const}{\sqrt{Q}} \quad , \tag{4.16}$$

where Q, called the (tagging) quality factor or *absolute separation*, summarizes the tagging performances as far as the statistical uncertainty on the determination of S_f is concerned. In the simplest case of a cut-based method applied on a single category, the quality factor is defined by:

$$Q = \epsilon(1-2w)^2 \quad . \tag{4.17}$$

When the tagging algorithm uses several categories labelled by c (e.g. Electron category, Kaon category etc.), each with its own tagging efficiency ϵ_c and mistag probability w_c, the quality factor is the sum of the quality factors:

$$Q = \sum_i Q_c \quad , \tag{4.18}$$

$$Q_c = \epsilon_c(1-2w_c)^2 \quad , \tag{4.19}$$

When, for a given category c, the tagging algorithm provides an event-dependent evaluation of the mistag rate, the contribution to the quality factor of this category is:

$$Q_c = \epsilon_c \, s^2{}_c \quad , \tag{4.20}$$

$$s^2{}_c = \langle(1-2w_c)^2\rangle \quad , \tag{4.21}$$

where the quantity s^2, termed the separation, is obtained from an average performed within the category under consideration.

	Electron	Muon	Kaon
Track quality	$d_0 < 4\,\mathrm{mm}$, $z_0 < 4\,\mathrm{cm}$		
Momentum cut	$p^* > 1.0\,\mathrm{GeV}$	$p^* > 1.1\,\mathrm{GeV}$	none
Tag determination	q of max. p^*	q of max. p^*	sum of q

Table 4.1: Summary of cuts used by the cut-based part of the tagging algorithm.

The flavor tagging algorithm used in this analysis is a hybrid tagging algorithm that classifies events with clearly identified tagging electrons, muons or kaons with a cut-based algorithm and uses two categories defined by the bins of the output of a neural network (*NetTagger*) to tag the remaining events (see Fig.4.4).

The motivation for using a hybrid tagging algorithm comes mainly from the fact that about 45% of events can be tagged by the cut-based algorithm (Electron, Muon, Kaon, Electron-and-Kaon and Muon-and-Kaon categories) and not much tagging performance can be gained with the probability based tagging algorithms for these event. Moreover systematics are easier to assess in a cut-based approach.

In the remaining events potential tagging separation comes from non-identified leptons, softer leptons from charm semileptonic decays (reverse sign leptons), soft pions from D^* decays and more generally from the momentum spectrum of charged particles from the B meson. On these events a multivariate (neural network) tagging algorithm can do better than a cut-based algorithm by combining the (correlated) information from different discriminating variables in an optimal way. For this analysis the mistag probability for each category of events is measured in data with an analysis of the B_{flav} sample as described in 4.2

The selection criteria used by the tagging algorithm are summarized in table 4.1 for the cut-based algorithm and in table 4.2 for the NetTagger part.

After removing from the event all tracks coming from the reconstructed B_{CP}, cuts on d_0 and z_0, and, except for kaons, on p^* are applied. The tracks passing these cuts are used to derive separate tags for electrons, muons and kaons by taking the charge of the electron or muon with the highest p^*, or by summing the charges of all kaons and taking the sign of the sum. Variables used for lepton and kaon PID selection are described in Chapter 2: an optimization of the tagging algorithm suggests very tight requirements for leptons, while for kaons loose requirements must be preferred.

Depending on the presence of such electron, muon or kaon tags, and on the output of

Category	Bins for *NetTagger* p(B^0)	
	for B^0 tag	for $\overline{B}^0$ tag
NetTagger category 1 (NT1)	0.75 — 1.0	0.0 — 0.25
NetTagger category 2 (NT2)	0.6 — 0.75	0.25 — 0.4

Table 4.2: Definition of categories for the tagging algorithm.

NetTagger (p(B^0), probability of a B_{tag} to be a B^0) for this event, the tagging category and tag for the B_{tag} is determined as follows. All categories are mutually exclusive and tagging categories listed first have higher priority.

1. **Electron-and-Kaon** category: If there are both an electron and a kaon tag, they are used to tag B_{tag} if they agree. If they disagree, the event is left for *NetTagger* .
2. **Muon-and-Kaon** category: If there is both an muon and a kaon tag, they are used to tag B_{tag} if they agree. If they disagree, the event is left for *NetTagger* .
3. **Electron** category: If there is an electron tag (and no kaon tag), it is used to tag B_{tag}.
4. **Muon** category: If there is a muon tag (and no kaon tag), it is used to tag B_{tag}.
5. **Kaon** category: If there is a kaon tag (and no electron or muon tag), it is used to tag B_{tag}.
6. **NT1** category If the *NetTagger* output p(B^0) falls into the bins defined for the NT1 category, the corresponding tag is used (see table 4.2).
7. **NT2** category: If the *NetTagger* output p(B^0) falls into the bins defined for the NT2 category, the corresponding tag is used (see table 4.2).
8. If none of the above criteria is satisfied, the event is not tagged.

Given the limited statistics available, categories with a small tagging efficiency like the **Electron-and-Kaon** and **Muon-and-Kaon** categories cannot be used directly and are merged together with the **Electron** and **Muon** categories into a single *Lepton* category (the tags for the corresponding events remain exactly the same, only the category assignement is changed).

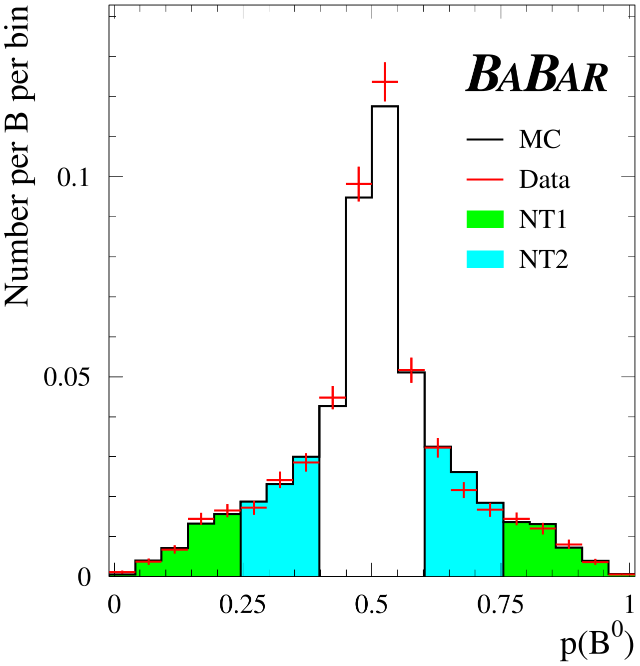

Figure 4.4: *NetTagger* output for events not tagged by the cut-based categories. The definition of the **NT1** and **NT2** categories is indicated graphically.

The output of *NetTagger* for events not tagged by the cut-based categories is shown in figure 4.4, where the definition of the **NT1** and **NT2** categories is indicated graphically.

Category	$\epsilon(\%)$	$w(\%)$	$\Delta w(\%)$	$Q(\%)$
Lepton	10.9 ± 0.3	8.9 ± 1.3	0.9 ± 2.2	7.4 ± 0.5
Kaon	35.8 ± 0.5	17.6 ± 1.0	-1.9 ± 1.5	15.0 ± 0.9
NT1	7.8 ± 0.3	22.0 ± 2.1	5.6 ± 3.2	2.5 ± 0.4
NT2	13.8 ± 0.3	35.1 ± 1.9	-5.9 ± 2.7	1.2 ± 0.3
Total	68.4 ± 0.7			26.1 ± 1.2

Table 4.3: Tagging performance for combined Run 1 and Run 2 B_{flav}+B_{CP} samples as published in [9].

4.2.2 Δt resolution model

Measurements of *CP*-violating asymmetries at the $\Upsilon(4S)$ require the determination of the distance, Δz, between the two B decay vertices. The decay length of each B is not observable because of the absence of charged stable particles emerging from the $\Upsilon(4S)$

decay point and so the decay length difference Δz has to be reconstructed[3]. One B meson, B_{CP}, is fully reconstructed and the decay vertex position can be measured using all the particles of the decay chain. The other B vertex ($B_{\rm tag}$ vertex) is reconstructed with the remaining charged tracks in the event. To retain high efficiency this has to be done using inclusive techniques, implemented in an algorithm ([52]) described in some details in Appendix A.

This algorithm reconstructs Δz and provides a per-event estimate $\sigma_{\Delta z}$ of the uncertainty on Δz itself. A time-dependent analysis must estimate Δt for each event,

$$\Delta t = t_{CP} - t_{TAG} = M_B \left[\frac{z_{CP}}{p_{z,CP}} - \frac{z_{TAG}}{p_{z,TAG}} \right] \tag{4.22}$$

t_{CP} and t_{TAG} are, however, defined in different frames, therefore the transformation from Δz to Δt is not straightforward. The standard approach in *BABAR* consists in assuming that both B's have the same average boost, $p_{z,CP} = p_{z,TAG} \approx \langle p_z \rangle$, and take it to be the same as for the $\Upsilon(4S)$ frame. This is equivalent to neglect the momentum of the B mesons in the $\Upsilon(4S)$ decay frame ($\langle p_B^{cms} \rangle = \sqrt{E_{e^+}E_{e^-} - M_B^2} \approx 340$ MeV/c). With these assumptions,

$$\Delta t = \Delta z / \gamma \beta_z c \tag{4.23}$$

where γ is the boost factor of the $\Upsilon(4S)$ in the laboratory frame and β_z its velocity projected on the z axis. At PEP-II $\beta_z \gamma$ is about 0.56. Using β_z instead of β we account for the rotation in the (x, z) plane of the beam axis with respect to the z axis (tilt angle about 20 mrad), reducing the full boost by about 1.2 MeV/c (0.02%). As a result, there is a small boost along the x axis (about 188 MeV/c) which generates azimuthal dependencies. This has, however, no direct effect when estimating Δz. This approximation, for which the B momentum does not need to be measured, is commonly called *boost approximation*. Compared with the experimental resolution on Δz, the effects on Δt produced by this approximation are small.

The resolution function $\mathcal{R}(\delta_{\rm t}; \hat{a})$ is determined along with dilutions in the $B_{\rm flav}$ sample. The adopted model (see appendix A) is a triple Gaussian, where two Gaussians (*core* and *tail*) have a width proportional to the event by event error $\sigma_{\Delta t}$ via scale factors (S_{core} and S_{tail}) and the third (*outlier*) has a width ($\sigma_{\rm outlier}$) fixed to 8 ps. The bias of the outlier

---

[3] This is different in Z^0 peak or hadronic collider experiment where the production point can be reconstrued from fragmentation particles

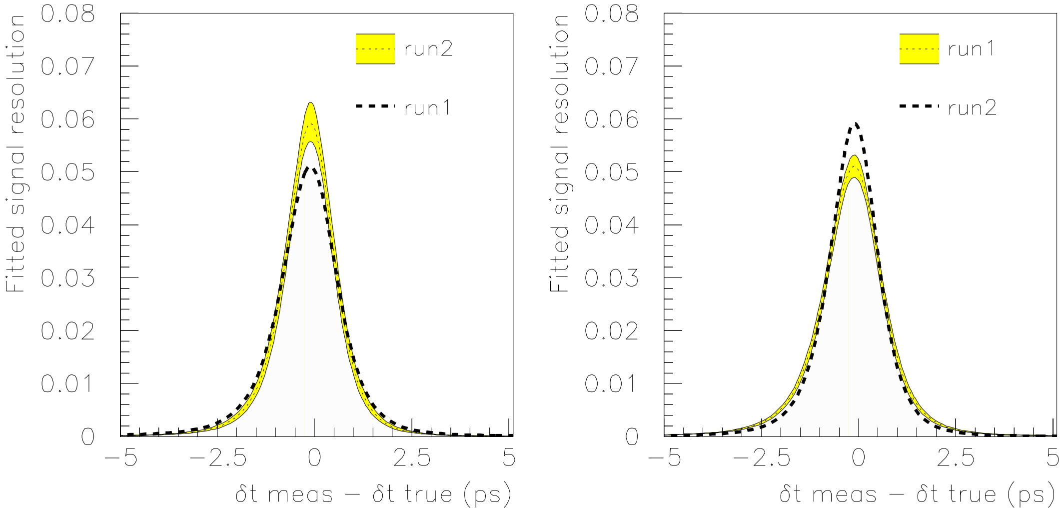

Figure 4.5: Resolution function determined from the Run 1 and Run 2 $B_{\rm flav}$ data samples. The plot on the left (right) show the run2 (run1) sample with the error envelope from the fit. From these curves, it appears that the Run 1 and Run 2 samples are roughly two "sigma" apart from each other, so different resolution functions are adopted for Run 1 and Run 2

Gaussian is fixed to 0, while the core and tail biases scale (α_{core} and α_{tail}) with the event by event error:

$$\begin{aligned}\mathcal{R}(\delta_{\rm t};\hat{a}) &= \sum_{k=1}^{2}\frac{f_{\rm core,tail}}{S_{\rm core,tail}\sigma_{\Delta t}\sqrt{2\pi}}\exp\left(-\frac{(\delta_{\rm t}-\alpha_{\rm core,tail}\sigma_{\Delta t})^2}{2S_{\rm core,tail}\sigma_{\Delta t}}\right) + \\ & \frac{f_{\rm outlier}}{\sigma_{\rm outlier}\sqrt{2\pi}}\exp\left(-\frac{\delta_{\rm t}^2}{2{\sigma_{\rm outlier}}^2}\right) . \qquad (4.24)\end{aligned}$$

The data show significant differences between these data samples, presumably due to the better SVT alignement in 2001 data taking and improved reconstruction code used to process the Run 2 data. This is shown for the $B_{\rm flav}$ sample in Fig. 4.5. These differences are accounted for by including a different resolution function for the Run 1 and Run 2 data samples.

4.3 Data samples and event selection

For this analysis data from 2000 and 2001 run are considered, 20.4 fb^{-1}, (22.57 million $B\overline{B}$ pairs) and 9.95 fb^{-1} ($\sim$ 11 million $B\overline{B}$ pairs) respectively. Full Monte Carlo events are also considered and thousands of "toy" Monte Carlo pseudo-experiments are generated.

Except for a tighter background suppression cut and the addition of Δt quality cuts, the selection criteria used in this analysis are identical to those in Chapter 3. These are the additional requirements

- tighter topological cuts

  $|\cos\theta_S| < 0.8$,

  where θ_S is the angle between the sphericity axis of the B candidate and the rest of the event.

- Δt selection

  $|\Delta t| < 17\,\mathrm{ps}$,

  $0.3 < \sigma_{\Delta t} < 3.0\,\mathrm{ps}$.

As usual, we define a "fit region" where we extract yields and *CP* parameters with an unbinned maximum likelihood fit and a "sideband" region are to extract various background parameters, according to the following definitions

- "fit region": $|\Delta E| < 0.150\,\mathrm{GeV}$ and $5.2 < m_{\mathrm{ES}} < 5.2895\,\mathrm{GeV}/c^2$,

- "m_{ES} sideband": $|\Delta E| < 0.420\,\mathrm{GeV}$, $5.2 < m_{\mathrm{ES}} < 5.26\,\mathrm{GeV}/c^2$,

This ΔE window of the fit region is wide enough to include the possibility of K^+K^- decays which are accounted for in the fit.

Tab. 4.4 summarizes the efficiency of the selection criteria as determined in signal Monte Carlo samples. The efficiency of each cut is relative to the ones above it and the separate efficiencies for the standard , PID, and Δt criteria are also shown.

Tab. 4.5 summarizes the tagging composition of the Run 1 and Run 2 data passing the selection criteria. Fig. 4.6 shows the corresponding distributions of m_{ES} in the combined Run 1 and Run 2 dataset for all events, and for the subset of untagged events[4]. Fig. 4.7 shows the m_{ES} distributions in each tagging category. We use the same ARGUS shape parameter ξ for all tag categories. The observed differences between the average ξ and the values obtained in the Lepton and NT1 have no significant effect on the results (Sec. 4.8).

---

[4] *Untagged* events are those events with no b flavor information according to the flavor tagging algorithm.

Table 4.4: Summary of detection efficiencies for $\pi^+\pi^-$, $K^+\pi^-$, and K^+K^- as determined in signal Monte Carlo samples. The efficiency of each cut is relative to the previous one and the errors are statistical only.

	$\epsilon(\pi^+\pi^-)$	$\epsilon(K^+\pi^-)$	$\epsilon(K^+K^-)$
Standard Selection			
reco + tag bits + R_2 + Sph	0.8372 ± 0.0027	0.8366 ± 0.0027	0.8318 ± 0.0027
GoodTracksAccLoose	0.8618 ± 0.0027	0.8386 ± 0.0029	0.8283 ± 0.0030
ΔE–$m_{\rm ES}$	0.9864 ± 0.0010	0.9833 ± 0.0011	0.9778 ± 0.0013
$\cos\theta_S$	0.7678 ± 0.0036	0.7726 ± 0.0037	0.7703 ± 0.0037
standard efficiency	0.5464 ± 0.0036	0.5331 ± 0.0036	0.5189 ± 0.0036
PID Selection			
θ_c	0.8223 ± 0.0038	0.8332 ± 0.0037	0.8298 ± 0.0038
N_γ	0.9351 ± 0.0027	0.9380 ± 0.0026	0.9318 ± 0.0028
proton veto	0.9792 ± 0.0016	0.9781 ± 0.0016	0.9764 ± 0.0017
electron veto	0.9997 ± 0.0002	0.9999 ± 0.0001	0.9997 ± 0.0002
PID efficiency	0.7527 ± 0.0042	0.7644 ± 0.0042	0.7549 ± 0.0043
Δt Selection			
Δt	0.9853 ± 0.0014	0.9861 ± 0.0013	0.9887 ± 0.0012
$\sigma_{\Delta t}$	0.9562 ± 0.0023	0.9585 ± 0.0023	0.9598 ± 0.0023
Δt efficiency	0.9422 ± 0.0026	0.9451 ± 0.0026	0.9489 ± 0.0026
nominal efficiency	0.3875 ± 0.0035	0.3851 ± 0.0035	0.3717 ± 0.0035
tracking correction	0.975	0.975	0.975
Total Efficiency	0.3778 ± 0.0034	0.3755 ± 0.0034	0.3624 ± 0.0034

Table 4.5: Event yields in Run 1 and Run 2 separated by tag flavor and category.

	Run 1			Run 2			Total		
Category	B^0	$\overline{B}^0$	Tot	B^0	$\overline{B}^0$	Tot	B^0	$\overline{B}^0$	Tot
Lepton	50	59	109	25	21	46	75	80	155
Kaon	920	877	1797	455	468	923	1375	1345	2720
NT1	215	195	410	107	92	199	322	287	609
NT2	621	560	1181	312	236	548	933	796	1729
untagged	–	–	3103	–	–	1425	–	–	4528
Total	1806	1691	6600	899	817	3141	2705	2508	9741

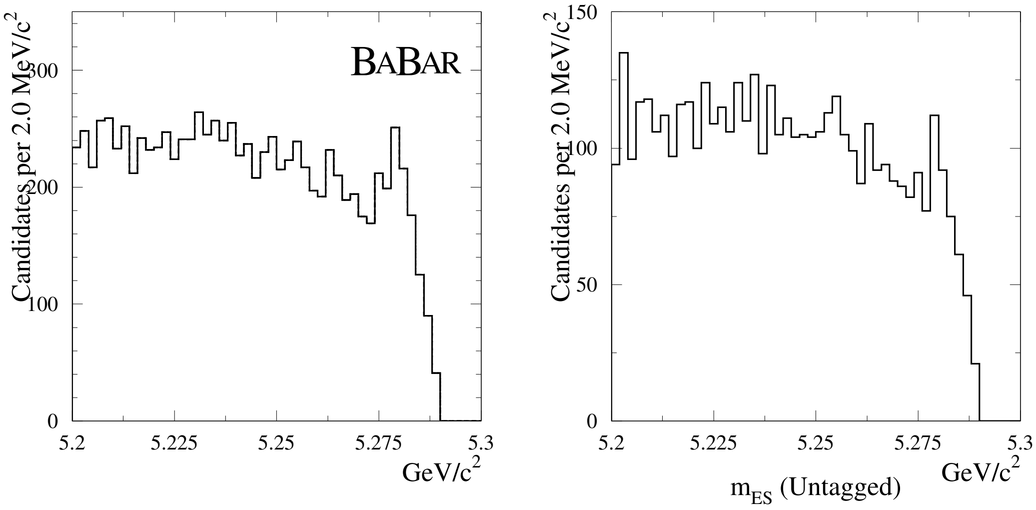

Figure 4.6: Distributions of m_{ES} in the Run 1 and Run 2 dataset for all events (left), and for the subset of untagged events (right).

Table 4.6: Results of a fit to the Run 1 data with the new analysis cuts. The Chapter 3 results, scaled by the relative efficiency, are shown for comparison.

Parameter	New Fit Result	Scaled Chap.3
$N_{\pi\pi}$	37 ± 10	34
$N_{K\pi}$	142 ± 15	139
$\mathcal{A}_{K\pi}$	-0.21 ± 0.11	-0.19
N_{KK}	6.2 ± 6.9	6.8
$N_{b\pi\pi}$	3087 ± 65	3268
$N_{bK\pi}$	2012 ± 58	1938
$\mathcal{A}_{bK\pi}$	0.004 ± 0.026	0.0
N_{bKK}	1322 ± 44	1127

Tab. 4.6 shows the fit results for the Run 1 dataset with the tighter topological cut and the Δt selection described above. For comparison, the expected values, based on the Chapter 3 analysis and the relative efficiency of the new cuts, are also shown. The relative efficiency is 82% for signal events and 40% for background events. Compatible results are obtained with this new analysis.

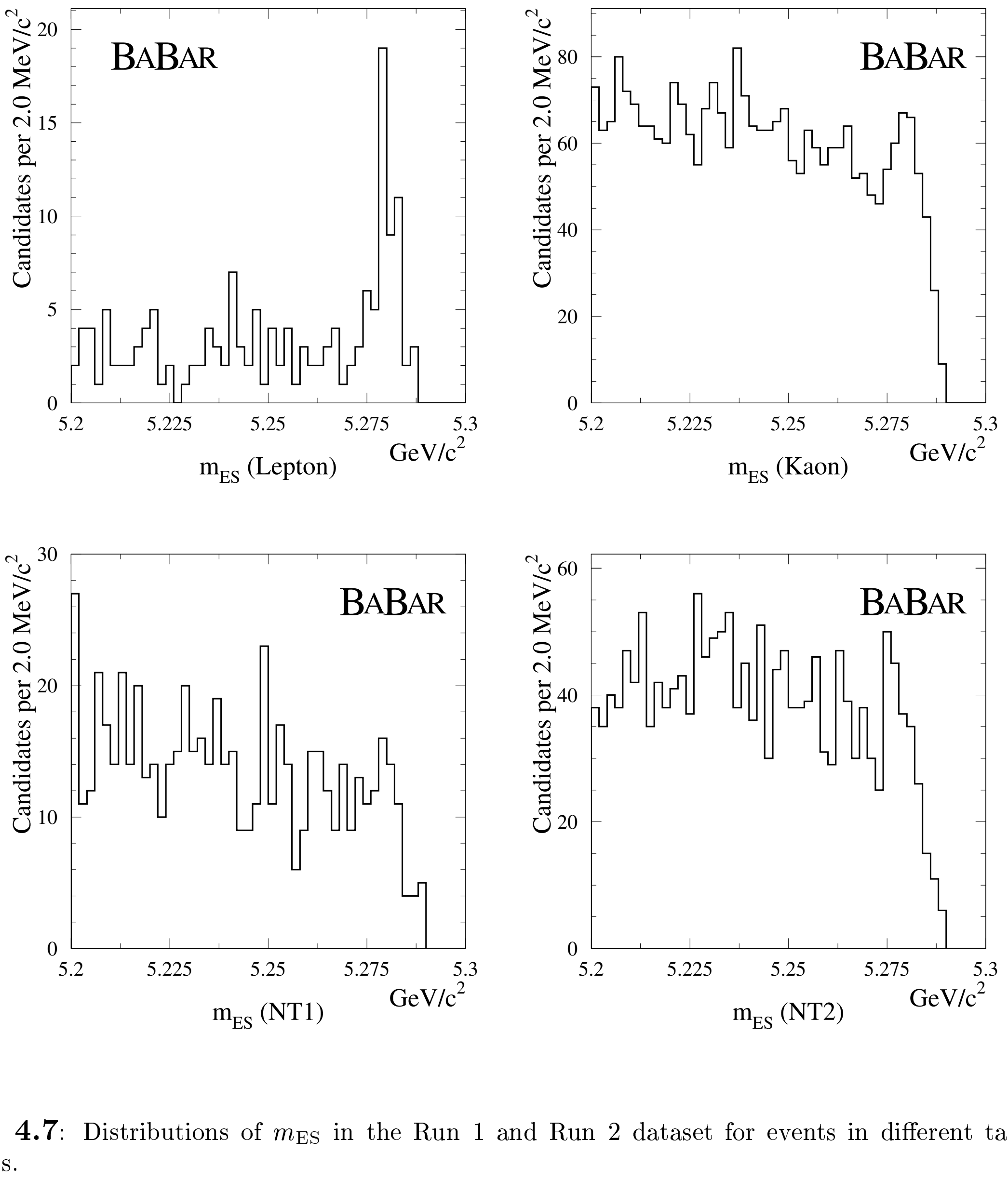

Figure 4.7: Distributions of m_{ES} in the Run 1 and Run 2 dataset for events in different tagging categories.

Table 4.7: Efficiency (%) for each tag category in signal $h'^{+}h^{-}$ Monte Carlo, the Run 1 and Run 2 $h'^{+}h^{-}$ fit region, and the Run 1 and Run 2 $B_{\rm flav}$ sample. The latter (highlighted) is used in the fit.

Sample	Lepton	Kaon	NT1	NT2	Untagged
$\pi^{+}\pi^{-}$ MC	13.0 ± 0.4	34.0 ± 1.6	7.8 ± 0.3	15.3 ± 0.4	30.0 ± 0.5
$K^{+}\pi^{-}$ MC	12.4 ± 0.4	33.7 ± 0.6	8.4 ± 0.3	14.7 ± 0.4	31.0 ± 0.5
$K^{+}K^{-}$ MC	11.6 ± 0.4	35.3 ± 0.6	7.9 ± 0.3	15.7 ± 0.4	29.5 ± 0.5
Run 1 $h'^{+}h^{-}$	13.7 ± 2.7	31.5 ± 4.1	4.4 ± 1.9	12.3 ± 3.0	38.1 ± 6.1
Run 2 $h'^{+}h^{-}$	13.2 ± 3.7	32.7 ± 5.6	6.7 ± 3.0	12.6 ± 4.2	34.8 ± 8.5
Run 1 and Run 2 $B_{\rm flav}$	**11.0 ± 0.3**	**35.8 ± 0.5**	**8.0 ± 0.3**	**13.9 ± 0.4**	**31.3 ± 0.5**

4.4 Signal tagging efficiency, dilutions, and Δt resolution

It is a fundamental assumption that the tagging performance and vertex resolution of the tag side in a $B\overline{B}$ event do not depend on the particular decay channel of the fully reconstructed B meson. With this assumption, the tagging efficiencies, dilutions, and Δt resolution function ($\mathcal{R}(\delta_{\rm t}; \hat{a})$) for $\pi\pi$, $K\pi$, and KK decays are obtained from the high statistics $B_{\rm flav}$ sample.

Tab. 4.7 compares the tagging efficiency in signal Monte Carlo, the Run 1 and Run 2 $B_{\rm flav}$ sample, and the $h'^{+}h^{-}$ fit region. The latter is obtained by floating the signal tag fractions in the final fit. No significant difference is observed between different species in signal Monte Carlo, and the on-resonance signal region gives consistent tagging efficiencies. Tab. 4.8 summarizes the average dilution and difference for each category as determined in the Run 1 and Run 2 $B_{\rm flav}$ sample. These are the numbers used in the final fit.

The signal Δt resolution function is parameterized as described in Section 4.2.2: the core bias does depend on the tag category. Tab. 4.9 lists the resolution function parameters obtained from a fit to the Run 1 and Run 2 $B_{\rm flav}$ sample (using both tagged and untagged events).

4.5 Background characterization

The decay $B^{0} \to \pi^{+}\pi^{-}$ is accompanied by significant background dominated by continuum $q\bar{q}$ production. Issues related to tagging and vertexing for background events are specific to this channel and need to be studied in the $h'^{+}h^{-}$ sideband and Monte Carlo samples. This Section describes the background composition and the parameterization of Δt used

Table 4.8: Average dilution and difference determined from the Run 1 and Run 2 $B_{\rm flav}$ sample. For comparison we show the parameters determined from $B_{\rm flav}$ Monte Carlo and $\pi\pi$ Monte Carlo.

	$B_{\rm flav}$ Run 1 and Run 2		$B_{\rm flav}$ MC		$\pi\pi$ MC	
Category	$\langle D\rangle$	ΔD	$\langle D\rangle$	ΔD	$\langle D\rangle$	ΔD
Lepton	0.823 ± 0.027	-0.021 ± 0.045	0.853	0.005	0.878	-0.004
Kaon	0.648 ± 0.020	0.035 ± 0.031	0.692	0.039	0.672	0.006
NT1	0.556 ± 0.042	-0.121 ± 0.067	0.621	-0.047	0.618	-0.036
NT2	0.302 ± 0.038	0.09 ± 0.057	0.301	0.062	0.308	0.056

Table 4.9: Parameters for $\mathcal{R}(\delta_{\rm t};\hat{a})$ obtained from the Run 1 and Run 2 $B_{\rm flav}$ tagged + untagged samples. The $B_{\rm flav}$ MC results are shown for comparison.

Parameter	Run 1 $B_{\rm flav}$	Run 2 $B_{\rm flav}$	MC $B_{\rm flav}$
S_{core}	1.411 ± 0.057	1.043 ± 0.104	1.151 ± 0.020
α_{core} lepton	-0.011 ± 0.119	-0.074 ± 0.163	-0.072 ± 0.021
α_{core} kaon	-0.323 ± 0.068	-0.196 ± 0.095	-0.181 ± 0.014
α_{core} NT1	-0.186 ± 0.144	-0.357 ± 0.207	-0.109 ± 0.027
α_{core} NT2	-0.388 ± 0.104	-0.184 ± 0.153	-0.171 ± 0.022
α_{core} notag	-0.361 ± 0.067	-0.155 ± 0.093	-0.212 ± 0.016
S_{tail}	3.0 ± 0.0	3.0 ± 0.0	4.358 ± 0.317
α_{tail}	-9.354 ± 2.844	-3.464 ± 3.341	-0.969 ± 0.143
f(tail)	0.006 ± 0.005	0.029 ± 0.039	0.061 ± 0.008
f(outlier)	0.002 ± 0.003	0.000 ± 0.003	0.005 ± 0.001

in the maximum likelihood fit.

4.5.1 Composition

The sample selected with the cuts described in the previous Section contains 97% continuum background. The $\pi^+\pi^-$ purity can be estimated from the fit result in Tab. 4.6 as $N_{\pi\pi}/\sigma^2_{\pi\pi} \sim 40\%$. The continuum background is dominated by high-momentum, back-to-back tracks with an invariant mass near the B mass. Tab. 4.10 summarizes the flavor and species content in uds, $c\bar{c}$, and $\tau^+\tau^-$ Monte Carlo samples. The background is 72% uds, 25% charm, and 3% tau events. The species content is determined from MC-truth information on the two daughter tracks, where the "other" category includes events where at least one of the tracks are associated to something other than a pion or kaon. These events typically contain leptons (mostly muons which are not explicitly rejected as the electrons) and/or protons.

The relative amount of $\pi\pi$, $K\pi$, and KK events varies significantly over the different background samples. The charm sample has a much larger fraction of $K\pi$ and KK decays than uds events due to the dominance of $c \to s$ decays. The tau sample contains no kaons and is dominated by events where one or both of the tracks come from a $\tau \to \mu$ decay. These differences affect the relative fraction of $\pi\pi$, $K\pi$, and KK background in each tagging category, which we take into account in the maximum likelihood fit.

Tab. 4.11 summarizes the percentage of events tagged in each category for continuum Monte Carlo and on-resonance sideband data. Tab. 4.12 shows a further breakdown into the different species from fits using the Čerenkov angle to separate $\pi\pi$, $K\pi$, and KK events. For Monte Carlo the results are cross-checked using MC-truth. The same trends are observed in data and Monte Carlo, with similar absolute tagging efficiencies. As a cross-check on the data, we include the parameterization obtained from the fit region by floating the tag efficiencies. The fit region and sideband regions are in excellent agreement, giving confidence that the higher statistics sideband sample can be used to determine the background tagging efficiencies. We therefore use the results from the combined Run 1 and Run 2 data in the maximum likelihood fit.

Table 4.10: Flavor and species content in 9.5 fb^{-1} samples of uds, $c\bar{c}$, and $\tau^+\tau^-$ generic Monte Carlo. Events in the "other" category have one or both tracks not associated to a true pion or kaon. These events typically include tracks associated with leptons (mostly muons) and protons.

Sample	$N_{\pi\pi}$	$N_{K\pi}$	N_{KK}	N_{other}	N	N/N_{tot}
uds	1145	570	242	45	2002	0.72 ± 0.01
$c\bar{c}$	228	173	255	53	709	0.25 ± 0.01
$\tau^+\tau^-$	26	1	0	48	75	0.027 ± 0.003

Table 4.11: Percentage of events tagged in each category for background Monte Carlo and on-resonance data samples. Results for data are obtained from the sideband region, and the combined Run 1 and Run 2 numbers (highlighted) are used in the final fit.

Sample	Lepton	Kaon	NT1	NT2	Untagged
uds MC	0.7 ± 0.2	24.9 ± 1.0	4.8 ± 0.5	15.7 ± 0.8	54.0 ± 1.1
$c\bar{c}$ MC	2.5 ± 0.6	29.3 ± 1.7	5.2 ± 0.8	17.9 ± 1.4	45.0 ± 1.9
$\tau^+\tau^-$ MC	0.0 ± 0.0	1.3 ± 1.3	16.0 ± 4.2	13.3 ± 4.0	69.3 ± 5.3
all bkg MC	1.2 ± 0.2	25.4 ± 0.8	5.2 ± 0.4	16.2 ± 0.7	52.1 ± 1.0
Run 1 h'^+h^-	1.1 ± 0.1	27.1 ± 0.4	6.2 ± 0.2	17.3 ± 0.3	48.3 ± 0.4
Run 2 h'^+h^-	1.1 ± 0.1	29.3 ± 0.6	6.6 ± 0.3	17.1 ± 0.5	45.9 ± 0.6
Run 1 and Run 2 h'^+h^-	$\mathbf{1.1 \pm 0.1}$	$\mathbf{27.7 \pm 0.3}$	$\mathbf{6.3 \pm 0.2}$	$\mathbf{17.3 \pm 0.3}$	$\mathbf{47.6 \pm 0.4}$

Table 4.12: Tagging efficiencies (%) within each species for the combined *uds* + charm + tau Monte Carlo, on-resonance sideband (SB), and on-resonance fit region (FR) samples. The "MC truth" results come from a direct count of events in each category/species using information at generation level. Events in the "other" category contain tracks not associated with either a pion or kaon. The Run 1 and Run 2 sideband results (highlighted) are used in the final fit.

Sample	Lepton	Kaon	NT1	NT2	Untagged
$\pi\pi$					
MC truth	0.8 ± 0.2	23.4 ± 1.1	5.2 ± 0.6	16.1 ± 1.0	54.5 ± 1.3
MC fit	0.7 ± 0.2	23.0 ± 1.1	5.2 ± 0.6	16.2 ± 1.0	54.8 ± 1.3
Run 1 $h'^{+}h^{-}$ (FR)	1.2 ± 0.2	24.8 ± 0.9	6.7 ± 0.5	19.1 ± 0.8	48.2 ± 1.3
Run 1 $h'^{+}h^{-}$ (SB)	1.0 ± 0.1	25.3 ± 0.5	6.5 ± 0.3	18.1 ± 0.5	49.2 ± 0.6
Run 1 and Run 2 $h'^{+}h^{-}$ (FR)	1.0 ± 0.2	25.7 ± 0.7	6.7 ± 0.4	18.7 ± 0.6	47.9 ± 1.0
Run 1 and Run 2 $h'^{+}h^{-}$ (SB)	**1.0 ± 0.1**	**26.0 ± 0.4**	**6.6 ± 0.2**	**17.6 ± 0.4**	**48.9 ± 0.7**
$K\pi$					
MC truth	1.2 ± 0.4	34.4 ± 1.7	3.5 ± 0.7	14.7 ± 1.3	46.2 ± 1.8
MC fit	1.1 ± 0.4	34.2 ± 1.7	4.1 ± 0.7	13.5 ± 1.2	47.0 ± 1.8
Run 1 $h'^{+}h^{-}$ (FR)	1.1 ± 0.3	32.3 ± 1.3	5.7 ± 0.6	15.4 ± 1.0	45.5 ± 1.8
Run 1 $h'^{+}h^{-}$ (SB)	1.0 ± 0.2	32.3 ± 0.7	5.6 ± 0.4	15.2 ± 0.6	45.8 ± 0.8
Run 1 and Run 2 $h'^{+}h^{-}$ (FR)	1.1 ± 0.2	33.4 ± 1.0	5.8 ± 0.5	15.5 ± 0.8	44.3 ± 1.4
Run 1 and Run 2 $h'^{+}h^{-}$ (SB)	**1.0 ± 0.1**	**33.1 ± 0.6**	**5.4 ± 0.3**	**15.3 ± 0.5**	**45.2 ± 0.6**
KK					
MC truth	2.2 ± 0.7	18.7 ± 1.8	6.8 ± 1.1	19.7 ± 1.8	52.5 ± 2.2
MC fit	2.5 ± 0.7	19.2 ± 1.7	6.5 ± 1.1	20.1 ± 1.8	51.8 ± 2.2
Run 1 $h'^{+}h^{-}$ (FR)	1.9 ± 0.4	24.3 ± 1.3	5.9 ± 0.7	19.2 ± 1.2	48.7 ± 2.0
Run 1 $h'^{+}h^{-}$ (SB)	1.5 ± 0.2	23.3 ± 0.8	6.6 ± 0.5	18.8 ± 0.7	49.8 ± 0.9
Run 1 and Run 2 $h'^{+}h^{-}$ (FR)	2.0 ± 0.3	24.1 ± 1.1	6.0 ± 0.6	19.8 ± 1.0	48.2 ± 1.6
Run 1 and Run 2 $h'^{+}h^{-}$ (SB)	**1.5 ± 0.2**	**23.5 ± 0.7**	**6.9 ± 0.4**	**19.7 ± 0.6**	**48.3 ± 0.8**
"Other"					
MC truth	0.7 ± 0.7	21.9 ± 3.4	7.5 ± 2.2	13.0 ± 2.8	60.3 ± 4.1

4.5.2 Parameterization of Δt

Continuum $q\bar{q}$ events typically produce $B \to h'^{+}h^{-}$ candidates by combining one high momentum track from each jet. The resulting background Δt distribution $\mathcal{R}_{\rm bkg}$ is not expected to have a significant lifetime component, even for $c\bar{c}$ events. We therefore choose to parameterize the distribution as the sum of three Gaussians: core, tail, and outlier, with the same parameters for $\pi\pi$, $K\pi$, and KK background.

$$\begin{aligned}\mathcal{R}_{\rm bkg} &= \sum_{k=1}^{2} \frac{f_{\rm core,tail}}{\sigma_{\rm core,tail}\sqrt{2\pi}} \exp\left(-\frac{(\Delta t - \mu_{\rm core,tail})^2}{2\sigma_{\rm core,tail}}\right) + \\ & \frac{f_{\rm outlier}}{\sigma_{\rm outlier}\sqrt{2\pi}} \exp\left(-\frac{(\Delta t)^2}{2{\sigma_{\rm outlier}}^2}\right) . \end{aligned} \tag{4.25}$$

Other functional forms have been studied, including double Gaussian with a lifetime component, but the triple Gaussian parameterization has been adopted being simple and sufficient.

The Gaussian parameters are obtained from an unbinned maximum likelihood fit to the on-resonance sideband sample, with the outlier mean fixed to 0 ps. Fig. 4.8 shows the fit result for Run 1 and Run 2 data. Tab. 4.13 lists the fitted parameters. The $\chi^2/ndof$ for the triple-Gaussian fit is 1.9 in Run 1 and 1.4 in Run 2. The Kolmogorov test returns a probability of 0.93 for both Run 1 and Run 2. There is a significant negative bias in $\mu_{\rm tail}$ in Run 1 and a positive bias in Run 2. The origin of the shifts is not understood yet, but it is accounted for in the systematic error (Section 4.9).

Several cross-checks have been performed to validate the Δt parameterization. Fig. 4.9 shows the on-resonance sideband data compared to a parameterization obtained in the fit region. In this fit the signal and background yields are determined from $m_{\rm ES}$, ΔE, $\mathcal{F}$, and θ_c simultaneously with the background Δt parameters. For the signal, we use the same resolution function described above. Good agreement is found between the parameters obtained from the fit region and sideband data.

In order to justify using an average of all species, we fit the sideband data with separate parameters for each species. Tab. 4.14 summarizes the results. We find no difference between the $\pi\pi$ and $K\pi$ parameters, and only small differences in the KK sample. These differences are probably due to the significant correlation between Gaussian parameters and the fewer number of KK events in the sample (Tab. 4.6). The average fit results (Tab. 4.13) are used in the CP fit.

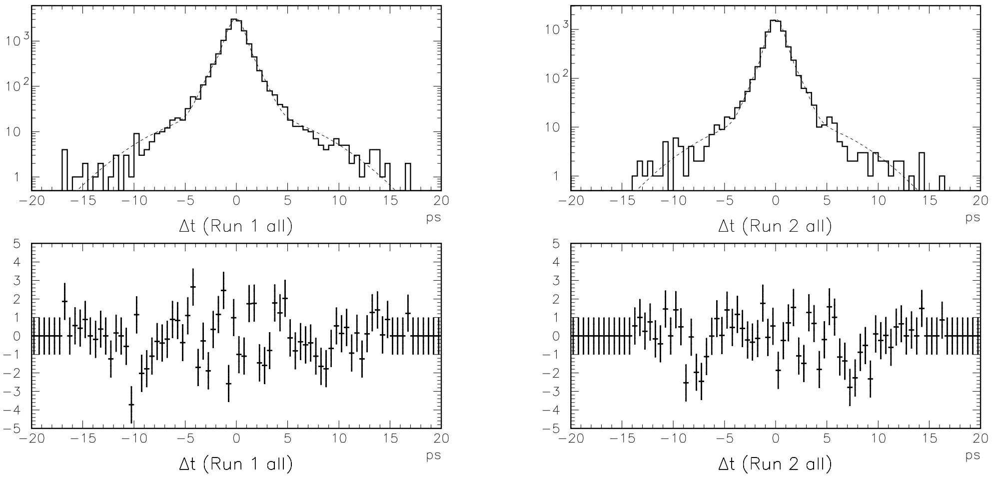

Figure 4.8: Top: Distributions of Δt in Run 1 (left) and Run 2 (right) on-resonance sideband samples. The result of a triple-Gaussian fit is overlayed. Bottom: The quantity $(N_i - F_i)/\sqrt{N_i}$ for each Δt bin, where F_i is the value of the function at the center of bin i.

Table 4.13: Parameters for the triple-Gaussian background Δt resolution function $\mathcal{R}_{\rm bkg}$ in on-resonance and continuum Monte Carlo samples. Separate parameterizations are used for Run 1 and Run 2. Means and resolutions are in ps.

Parameter	Run 1	Run 2	MC
$\mu_{\rm core}$	-0.037 ± 0.012	-0.005 ± 0.016	-0.014 ± 0.015
$\sigma_{\rm core}$	0.637 ± 0.022	0.611 ± 0.027	0.673 ± 0.022
$f_{\rm tail}$	0.399 ± 0.029	0.356 ± 0.042	0.273 ± 0.030
$\mu_{\rm tail}$	-0.119 ± 0.027	0.122 ± 0.040	0.116 ± 0.056
$\sigma_{\rm tail}$	1.531 ± 0.062	1.416 ± 0.087	1.745 ± 0.118
$f_{\rm out}$	0.054 ± 0.005	0.058 ± 0.007	0.030 ± 0.006
$\mu_{\rm out}$	0 (fixed)	0.0 (fixed)	0.0 (fixed)
$\sigma_{\rm out}$	5.486 ± 0.231	5.272 ± 0.288	6.294 ± 0.564

Finally, we check the dependence on tagging by fitting the sub-samples corresponding to each category (Tab. 4.15), as well as the untagged and all-tagged events (Tab. 4.16). We find reasonable consistency across tagging categories, and between tagged and untagged events. The average background parameterization is used for all categories, and systematic errors are evaluated using the other parameterizations.

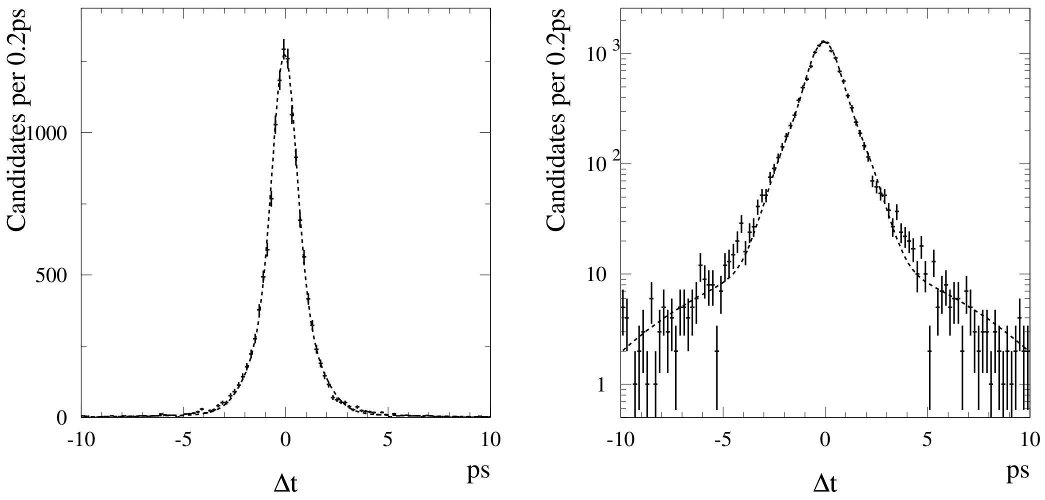

Figure 4.9: The Run 1 h'^+h^- on-resonance sideband sample compared to a parameterization obtained in the fit region. The parameterization is normalized to the number of events in the sideband sample.

Table 4.14: Comparison of background Δt parameters for each species as determined in the h'^+h^- sideband data. Means and resolutions are in ps.

Parameter	$\pi\pi$	$K\pi$	KK
μ_{core}	-0.054 ± 0.019	-0.056 ± 0.023	0.047 ± 0.033
σ_{core}	0.634 ± 0.048	0.665 ± 0.040	0.529 ± 0.046
f_{tail}	0.421 ± 0.061	0.327 ± 0.055	0.507 ± 0.056
μ_{tail}	-0.095 ± 0.040	-0.096 ± 0.070	-0.153 ± 0.054
σ_{tail}	1.514 ± 0.120	1.635 ± 0.153	1.261 ± 0.081
f_{out}	0.059 ± 0.009	0.046 ± 0.009	0.099 ± 0.021
μ_{out}	0.0 (fixed)	0.0 (fixed)	0.0 (fixed)
σ_{out}	5.551 ± 0.385	6.299 ± 0.564	3.432 ± 0.293

Table 4.15: Comparison of background Δt parameters for each tagging category as determined in the $h'^{+}h^{-}$ sideband data (means and resolutions are in ps). Due to low statistics, additional parameters were fixed in fits to the lepton and NT1 categories.

Parameter	Lepton	Kaon	NT1	NT2
μ_{core}	0.025 ± 0.148	-0.026 ± 0.023	-0.055 ± 0.040	-0.076 ± 0.031
σ_{core}	0.629 (fixed)	0.662 ± 0.044	0.588 ± 0.045	0.563 ± 0.060
f_{tail}	0.506 ± 0.094	0.365 ± 0.062	0.369 ± 0.059	0.484 ± 0.090
μ_{tail}	0.069 ± 0.218	-0.113 ± 0.060	-0.160 ± 0.118	-0.116 ± 0.050
σ_{tail}	1.508 (fixed)	1.490 ± 0.157	1.58 ± 0.143	1.218 ± 0.120
f_{out}	0.036 ± 0.023	0.064 ± 0.018	0.081 ± 0.017	0.065 ± 0.019
μ_{out}	0 (fixed)	0.0 (fixed)	0.0 (fixed)	0.0 (fixed)
σ_{out}	5.446 (fixed)	4.498 ± 0.686	5.45 (fixed)	3.770 ± 0.499

Table 4.16: Comparison of background Δt parameters between tagged and untagged events as determined in Run 1 and Run 2 sideband data (means and resolutions in ps).

	Run 1		Run 2	
Parameter	Tagged	Untagged	Tagged	Untagged
μ_{core}	-0.046 ± 0.015	-0.017 ± 0.019	-0.016 ± 0.020	0.013 ± 0.025
σ_{core}	0.661 ± 0.027	0.576 ± 0.040	0.648 ± 0.029	0.511 ± 0.048
f_{tail}	0.351 ± 0.038	0.482 ± 0.045	0.256 ± 0.044	0.528 ± 0.058
μ_{tail}	-0.114 ± 0.042	-0.126 ± 0.033	0.168 ± 0.073	0.083 ± 0.039
σ_{tail}	1.563 ± 0.093	1.449 ± 0.081	1.560 ± 0.169	1.267 ± 0.075
f_{out}	0.048 ± 0.007	0.063 ± 0.009	0.061 ± 0.011	0.056 ± 0.009
μ_{out}	0.0 (fixed)	0.0 (fixed)	0.0 (fixed)	0.0 (fixed)
σ_{out}	5.671 ± 0.360	5.246 ± 0.304	5.414 ± 0.425	5.055 ± 0.406

4.6 Fit technique

Assuming the same cuts used in the Branching Fraction analysis (Chapter 3), the expected number of tagged $\pi\pi$ events is $1.5/\,\mathrm{fb}^{-1}$, or ≈ 45 in $30\,\mathrm{fb}^{-1}$. This measurement is therefore expected to be dominated by statistical uncertainty and, assuming smaller systematic uncertainties and zero asymmetry in the background, the analysis that optimizes the effective $S/\sqrt{S+B}$ will also minimize the error on the *CP* asymmetry. It is therefore not necessary to obtain a pure sample of $\pi\pi$ candidates in order to minimize possible systematic effects from the continuum and cross-feed background. Instead, the *CP* asymmetries, as well as the signal and background yields, are determined simultaneously from a global maximum likelihood fit using both tagged and untagged $h'^{+}h^{-}$ sample. This procedure leads to a lower error on the Branching Fractions and *CP* asymmetries.

There are two *CP* observables in the time-dependent analysis: $|\lambda_{f_{CP}}|$ and $\mathcal{I}m\lambda_{f_{CP}}$. As described in Chapter 1, it would be most convenient to fit for $|\lambda_{f_{CP}}|$ and $\mathcal{I}m\lambda_{f_{CP}}/\,|\lambda_{f_{CP}}|$, since the latter provides a direct measurement of $\sin 2\alpha_{\mathrm{eff}}$. However, by means of a "toy" Monte Carlo study, it was found that this fit produces non-Gaussian pull distributions. Similar technical problems exist in a fit of $|\lambda_{f_{CP}}|$ and $\mathcal{I}m\lambda_{f_{CP}}$. Moreover, let us remind that from Eq. 1.39 it is evident that using $|\lambda_{f_{CP}}|$ as a fit parameter implicitly constrains $C_{\pi\pi}$ to be in the physical region $(-1,1)$, while there is no such constraint in the data, especially for small data sample.

In contrast, fitting for $S_{\pi\pi}$ and $C_{\pi\pi}$ is found to be very robust and does not bias the fit. The current analysis therefore uses $S_{\pi\pi}$ and $C_{\pi\pi}$ as fit parameters.

An unbinned maximum likelihood fit is used to simultaneously extract yields and *CP* asymmetry parameters from both tagged and untagged $h'^{+}h^{-}$ events. The only new feature of the fitting technique relative to the Branching Fraction analysis is the addition of a PDF describing the time dependence of each component and tagging category. The remainder of this Section describes the likelihood function and PDFs.

4.6.1 Likelihood function

The construction of the overall likelihood function L is similar to the branching fraction analysis. The sample is assumed to consist of signal and background components for the three species ($\pi\pi$, $K\pi$, and KK), separated by the flavor and category of the tag side. The variables m_{ES}, ΔE, and the Fisher discriminant $\mathcal{F}$ separate signal and background, while the Čerenkov angles for the positive and negative tracks (θ_c^+, θ_c^-) and, to a lesser extent, ΔE determine the relative amount of each species. The Δt measurement allows the *CP* asymmetry measurement and provides additional background rejection. The probability $\mathcal{P}_{i,c}$ for a single event i in tag category c is the sum of probabilities over all components,

$$\begin{aligned}
\mathcal{P}_{i,c} &= \frac{N_{\pi\pi}}{N_c'} f_c^{\pi\pi} \mathcal{P}_{i,c}^{\pi\pi} + \frac{N_{b\pi\pi}}{N_c'} f_c^{b\pi\pi} \mathcal{P}_{i,c}^{b\pi\pi} \\
&+ \frac{N_{KK}}{N_c'} f_c^{KK} \mathcal{P}_{i,c}^{KK} + \frac{N_{bKK}}{N_c'} f_c^{bKK} \mathcal{P}_{i,c}^{bKK} \\
&+ \frac{N_{K\pi}}{2N_c'} f_c^{K\pi} \left(1 + \mathcal{A}_{K\pi}\right) \mathcal{P}_{i,c}^{K^-\pi^+} + \frac{N_{bK\pi}}{2N_c'} f_c^{bK\pi} \left(1 + \mathcal{A}_{bK\pi}\right) \mathcal{P}_{i,c}^{bK^-\pi^+} \\
&+ \frac{N_{K\pi}}{2N_c'} f_c^{K\pi} \left(1 - \mathcal{A}_{K\pi}\right) \mathcal{P}_{i,c}^{K^+\pi^-} + \frac{N_{bK\pi}}{2N_c'} f_c^{bK\pi} \left(1 - \mathcal{A}_{bK\pi}\right) \mathcal{P}_{i,c}^{bK^+\pi^-} ,
\end{aligned} \tag{4.26}$$

where:

- N_k = fitted number of events of type k in the entire sample.
- f_c^k = fraction of events of type k that are tagged in category c.
- $N_c' = \sum N_k f_c^k$.
- $\mathcal{A}_k = (N_{K^-\pi^+} - N_{K^+\pi^-})/(N_{K^-\pi^+} + N_{K^+\pi^-})$, the direct *CP*-violating asymmetry.
- $\mathcal{P}_c^k = \mathcal{P}^k(m_{\mathrm{ES}}) \cdot \mathcal{P}^k(\Delta E) \cdot \mathcal{P}^k(\mathcal{F}) \cdot \mathcal{P}^k(\theta_c^+) \cdot \mathcal{P}^k(\theta_c^-) \cdot \mathcal{P}_c^k(\Delta t)$.

Untagged events are treated as a fifth category with $D = \Delta D = 0$. Due to the small number of signal events, we make the transformation of variables $N_c'^k \to N_k f_c^k$ and fit for the total yields N_k rather than the yield in each tagging category. Background tag fractions f_c come from Tab. 4.12. For signal we assume $f_c^{\pi\pi} = f_c^{K\pi} = f_c^{KK}$ and use the result from the B_{flav} data sample (Tab. 4.7).

The extended likelihood L_c for a single category is given by

$$L_c = e^{-N_c'} (N_c')^{N_c} \prod_i^{N_c} \mathcal{P}_{i,c}, \tag{4.27}$$

where the Poisson term is the probability of observing N_c events in category c when N_c' are expected. Including this term allows for the direct fitting of yields rather than fractions. Finally, the total likelihood function is the product over all categories:

$$L = \prod_{c=1}^{5} L_c. \tag{4.28}$$

The quantity $-2\ln(L) = -2\sum\ln(L_c)$ is minimized using *MINUIT* ([53]), equivalent to maximizing L.

4.6.2 Probability Density Functions

The PDF parameterizations for $m_{\rm ES}$, ΔE, $\mathcal{F}$, and θ_c are described in detail in Chapter 3. For signal we use a sample of $B^- \to D^0\pi^-$ decays to determine the mean and resolution of $m_{\rm ES}$ and ΔE. Fig. 4.10 shows the $m_{\rm ES}$ distributions for Run 1 and Run 2. We use $\mu m_{\rm ES} = 5280.0 \pm 0.2\,{\rm MeV}/c^2$ and $\sigma m_{\rm ES} = 2.6 \pm 0.2\,{\rm MeV}/c^2$ for both Run 1 and Run 2. The errors on these parameters come from a conservative estimate based on other fully reconstructed B samples. Fig. 4.11 shows the ΔE distribution in Run 2 and the combined Run 1 and Run 2 data. The Run 2 parameters are similar to the Run 1 results so we use a common mean, $\mu_{\Delta E} = -5 \pm 5\,{\rm MeV}$, and resolution, $\sigma_{\Delta E} = 26^{+5}_{-2.5}\,{\rm MeV}$, for the entire dataset. The lower limit on $\sigma_{\Delta E}$ comes from the statistical error on the scaling we apply to Monte Carlo and the upper limit is a conservative estimate based on fitting the Run 1 $K\pi$-selected sample.

The signal Fisher discriminant distribution is obtained from signal $\pi^+\pi^-$ Monte Carlo and cross-checked with the $D^0\pi^-$ control sample. After tightening the cut on $\cos\theta_S$, we find that the signal Fisher shape is a single Gaussian. This is quite natural, since there is generally correlation between topological variables: a tighter cut on $\cos\theta_S$ results in a less separating Fisher discriminant.

Fig. 4.12 shows the $D^0\pi^-$ samples in Run 1 and Run 2, while Fig. 4.13 shows the combined Run 1 and Run 2 sample and the signal Monte Carlo. We use the latter distribution for both Run 1 and Run 2, with the $D^0\pi^-$ sample used to estimate the systematic error.

Differently from the Branching Ratio fit in Chapter 3, the background $m_{\rm ES}$ and ΔE and Fisher shapes are left floating in the fit. Fig. 4.14 shows the distribution of $m_{\rm ES}$ in the region $0.2 < |\Delta E| < 0.42\,{\rm GeV}$, and Fig. 4.15 shows the Fisher distribution in the sideband region. We find similar shapes in Run 1 and Run 2, so we float common parameters for the entire dataset.

The θ_C pulls for pions and kaons are determined in a high-statistics data sample of $D^* \to D^0\pi$, $D^0 \to K\pi$ decays, where the same PDFs are used for signal and background, as described in Section 2.4.

Tab. 4.17 summarizes the parameterization of the various variables used in the fit.

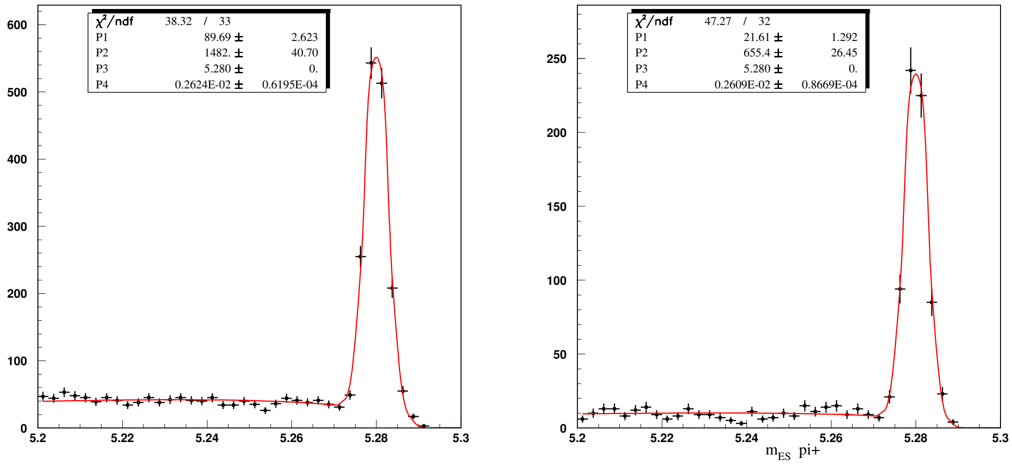

Figure 4.10: Distributions of m_{ES} for $B^- \to D^0\pi^-$ decays in Run 1 (left) and Run 2 (right).

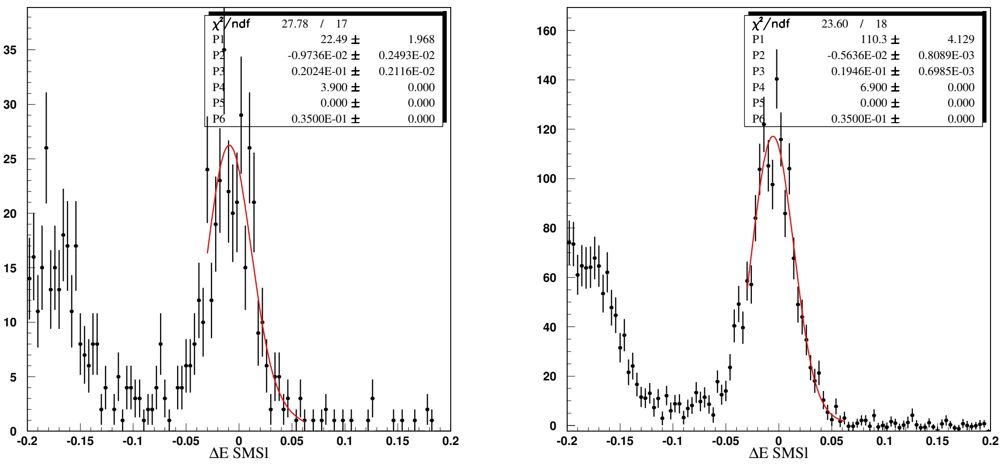

Figure 4.11: Distributions of ΔE for $B^- \to D^0\pi^-$ decays in Run 2 (left) and Run 1 and Run 2 (right).

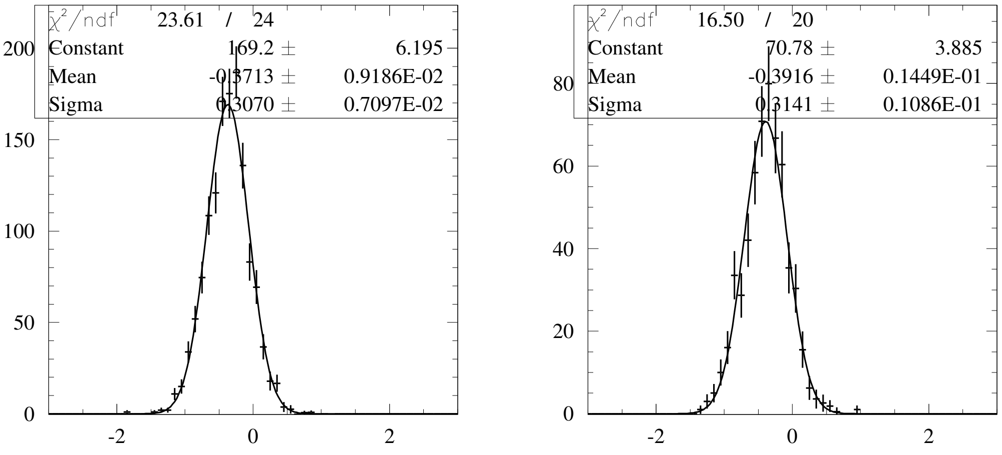

Figure 4.12: Distributions of $\mathcal{F}$ for $B^- \to D^0\pi^-$ decays in Run 1 (left) and Run 2 (right).

Table 4.17: Summary of PDFs for m_{ES}, ΔE, $\mathcal{F}$, and θ_c. The Čerenkov angle offsets and resolutions are functions of track polar angle θ.

Variable	Sig Func	Sig Params	Bkg Func	Bkg Params
m_{ES}	Gaussian	$\mu = 5.280\,\text{GeV}/c^2$ $\sigma = 2.6\,\text{MeV}/c^2$	ARGUS	ξ; free
ΔE	Gaussian	$\mu = -5\,\text{MeV}$ $\sigma = 26\,\text{MeV}$	quadratic	ΔE_{p1}, ΔE_{p2}; free
$\mathcal{F}$	Gaussian	$\mu = -0.3547$ $\sigma = 0.3098$	double Gaussian	$\mathcal{F}_{\mu_1}$, $\mathcal{F}_{\sigma_1}$, $\mathcal{F}_{\mu_2}$, $\mathcal{F}_{\sigma_2}$,$\mathcal{F}_{f_1}$; free
θ_c pulls	Gaussian	$\mu(\theta_c, \theta, p)$ $\sigma(\theta)$	same as Sig	same as Sig

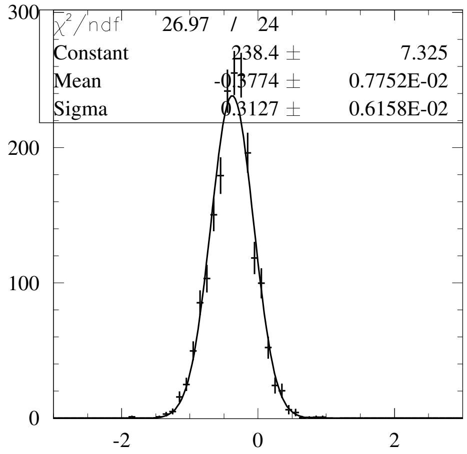

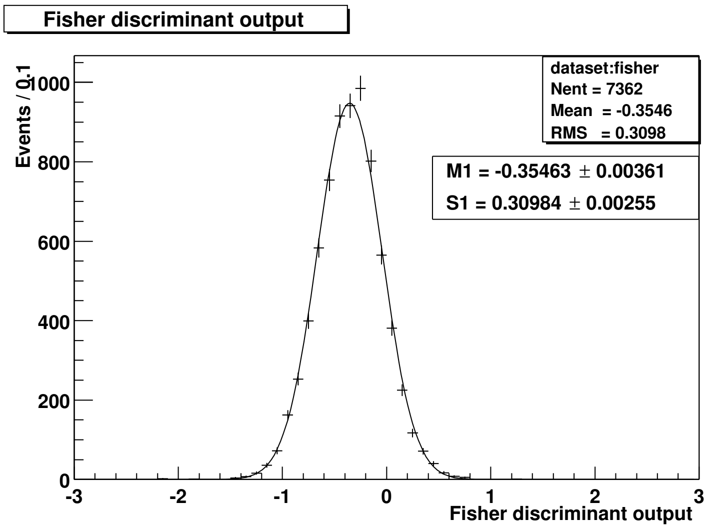

Figure 4.13: Distributions of $\mathcal{F}$ for $B^- \to D^0\pi^-$ decays in the combined Run 1 and Run 2 dataset (left) and signal $\pi^+\pi^-$ Monte Carlo (right).

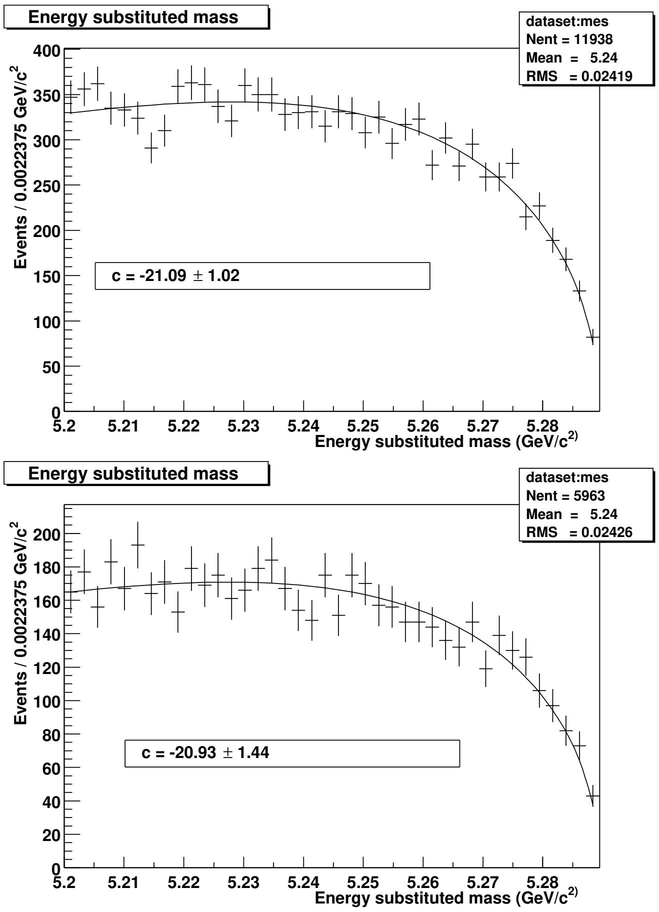

Figure 4.14: Distributions of m_{ES} for Run 1 (left) and Run 2 (right) on-resonance data in the region $0.2 < |\Delta E| < 0.42\,\mathrm{GeV}$.

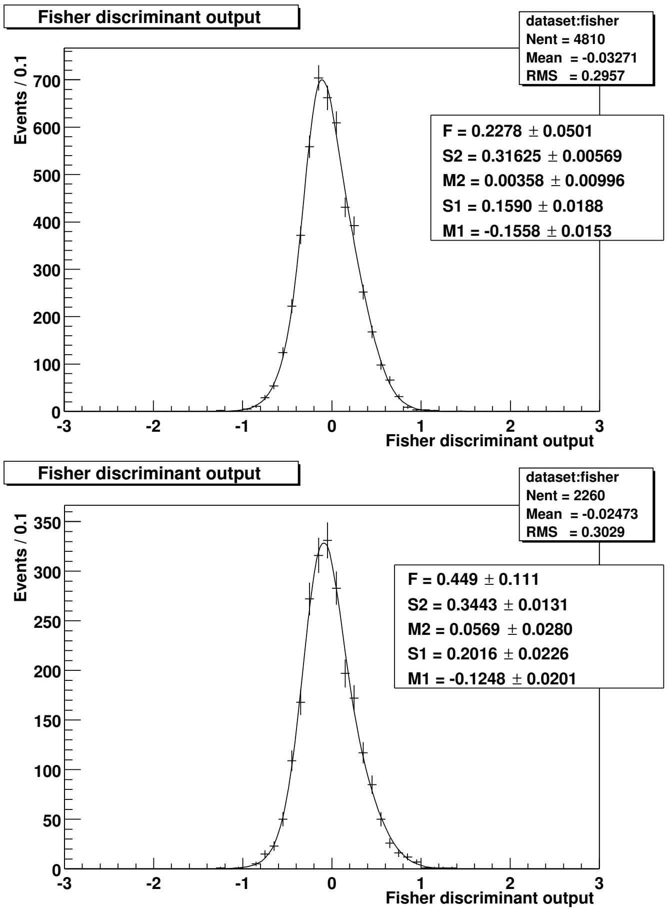

Figure 4.15: Distributions of $\mathcal{F}$ in Run 1 (left) and Run 2 (right) m_{ES} sideband data.

Table 4.18: Summary of PDFs for Δt.

Component	Function	Parameters
Signal $\pi\pi$	$F_{B^0\,\mathrm{tag}}$ or $F_{\overline{B}^0\,\mathrm{tag}}$	$S_{\pi\pi}$, $C_{\pi\pi}$; free $\mathcal{R}_{\mathrm{sig}}$; Tab. 4.9 $\langle D\rangle$, ΔD; Tab. 4.8 $\tau = 1.548\,\mathrm{ps}$ $\Delta m_d = 0.472\hbar\,\mathrm{ps}^{-1}$
Signal $K^+\pi^-$	$F_{\mathrm{mix},\,B^0\,\mathrm{tag}}$ or $F_{\mathrm{unmix},\,\overline{B}^0\,\mathrm{tag}}$	$\mathcal{R}_{\mathrm{sig}}$, $\langle D\rangle$, ΔD, τ, Δm_d
Signal $K^-\pi^+$	$F_{\mathrm{mix},\,\overline{B}^0\,\mathrm{tag}}$ or $F_{\mathrm{unmix},\,B^0\,\mathrm{tag}}$	$\mathcal{R}_{\mathrm{sig}}$, $\langle D\rangle$, ΔD, τ, Δm_d
Signal KK	exp $\otimes$ res	$\mathcal{R}_{\mathrm{sig}}$; τ
Background	triple Gaussian	$\mathcal{R}_{\mathrm{bkg}}$; Tab. 4.13

The signal Δt PDF depends on the flavor and category of the tag side. The functional form for the $\pi\pi$ component is given by Eqs. 4.4 and 4.11, where the resolution function $\mathcal{R}$ is defined in Tab. 4.9. We fit for the coefficients $S_{\pi\pi}$ and $C_{\pi\pi}$ of the sine and cosine terms, respectively. Although the K^+K^- final state is a *CP* eigenstate, we treat this component as a pure lifetime. The functional form for the $K\pi$ component is given by Eq. 4.10. We fix the parameters τ and Δm_d to their PDG values [14] and take the error into account as a systematic uncertainty. The background Δt PDF is given by the triple-Gaussian resolution function $\mathcal{R}_{\mathrm{bkg}}$, with the parameters defined in Tab. 4.13. The Δt parameterization is summarized in Tab. 4.18, and the final set of free parameters in the maximum likelihood fit are listed in Tab. 4.19.

Correlations between PDF variables

An implicit assumption in the construction of the likelihood function is that the variables entering the fit are uncorrelated. Tab. 4.20 summarizes the linear correlation coefficients (see definition Eq.3.25) for all pairs of m_{ES}, ΔE, $\mathcal{F}$, θ_c^+, θ_c^-, Δt, and $\sigma_{\Delta t}$ as found in Monte Carlo. Correlations greater than 10% are highlighted.

The correlation between m_{ES} and ΔE is thought to have no significant impact on the fit (mostly because the Monte Carlo correlation is inflated by the better ΔE resolution compared with data). The correlations between the Čerenkov angles, and between θ_c and ΔE, in $K\pi$ and KK events is due to the underlying momentum dependence. This is properly taken into account in the definition of θ_c and ΔE PDFs with their own momentum dependence. The correlation is incorporated into the "toy" Monte Carlo generator and

Table 4.19: Summary of free parameters in the *CP* fit.

$N_{\pi\pi}$	Number of signal $\pi\pi$ events
$N_{K\pi}$	Number of signal $K\pi$ events
$\mathcal{A}_{K\pi}$	charge asymmetry in signal $K^{\pm}\pi^{\mp}$ events
N_{KK}	Number of signal KK events
$N_{b\pi\pi}$	Number of background $\pi\pi$ events
$N_{bK\pi}$	Number of background $K\pi$ events
$\mathcal{A}_{bK\pi}$	charge asymmetry in background $K^{\pm}\pi^{\mp}$ events
N_{bKK}	Number of background KK events
ξ	background m_{ES} ARGUS shape parameter
ΔE_{p1}	background ΔE linear term
ΔE_{p2}	background ΔE quadratic term
$\mathcal{F}_{\mu_1}$	background Fisher mean of first Gaussian
$\mathcal{F}_{\sigma_1}$	background Fisher width of first Gaussian
$\mathcal{F}_{\mu_2}$	background Fisher mean of second Gaussian
$\mathcal{F}_{\sigma_2}$	background Fisher width of second Gaussian
$\mathcal{F}_{f_1}$	background Fisher fraction of first Gaussian
$S_{\pi\pi}$	coefficient of the sine oscillation in signal $\pi\pi$ events
$C_{\pi\pi}$	coefficient of the cosine oscillation in signal $\pi\pi$ events

we have confirmed that there is no bias in the fit yields. The 14% correlation between the Fisher discriminant and the error on Δt in the background samples is not yet understood. However, signal yields change only slightly between fits with and without Δt, which gives some confidence that the correlation does not significantly affect the yield estimate.

4.6.3 Alternative *CP* parameterizations

The most interesting (experimentally accessible) asymmetry parameter in this analysis is $\sin 2\alpha_{\text{eff}}$, or $\mathcal{I}m\lambda_{f_{CP}}/\left|\lambda_{f_{CP}}\right|$. We have therefore also investigated the possibility of fitting directly for $(\left|\lambda_{f_{CP}}\right|, \mathcal{I}m\lambda_{f_{CP}}/\left|\lambda_{f_{CP}}\right|)$ or $(\left|\lambda_{f_{CP}}\right|, \mathcal{I}m\lambda_{f_{CP}})$. To test the stability of these fits, 1179 ”toy” experiments were generated with random values of $S_{\pi\pi}$ and $C_{\pi\pi}$ in the physical range. Each experiment was fit three times with each of the three possible *CP* parameterizations. This procedure allows the direct comparison of different fits on an experiment-by-experiment basis.

Fig. 4.16 shows the pull distributions for $\mathcal{I}m\lambda_{f_{CP}}/\left|\lambda_{f_{CP}}\right|$ and $\left|\lambda_{f_{CP}}\right|$. The width of the $\mathcal{I}m\lambda_{f_{CP}}/\left|\lambda_{f_{CP}}\right|$ distribution is significantly overestimated by the fit error (pull $\sigma \sim 0.8$), and a strong bias is observed in $\left|\lambda_{f_{CP}}\right|$. Looking at the scatter plot of fitted values

Table 4.20: Linear correlation coefficients for the variable set $\{m_{\rm ES}, \Delta E, \mathcal{F}, \theta_c^+, \theta_c^-, \Delta t, \sigma_{\Delta t}\}$. The grand sideband (GSB) region is defined as ($5.2 < m_{\rm ES} < 5.3$, $|\Delta E| < 0.45\,{\rm GeV}$), and "SB" refers to the normal sideband region.

Variables	$\pi\pi$ MC	$K\pi$ MC	KK MC	bkg MC (GSB)	Run 1 (SB)
$(m_{\rm ES}, \Delta E)$	$\boxed{-0.121}$	$\boxed{-0.150}$	$\boxed{-0.131}$	0.016	0.014
$(m_{\rm ES}, \mathcal{F})$	−0.010	0.020	0.006	0.024	0.006
$(m_{\rm ES}, \theta_{c1})$	0.001	0.013	0.015	0.011	−0.001
$(m_{\rm ES}, \theta_{c2})$	−0.015	−0.002	−0.020	0.011	0.006
$(m_{\rm ES}, \Delta t)$	0.003	−0.006	−0.003	−0.000	0.005
$(m_{\rm ES}, \sigma_{\Delta t})$	−0.009	0.004	−0.002	−0.036	−0.040
$(\Delta E, \mathcal{F})$	0.005	0.010	0.019	−0.071	−0.063
$(\Delta E, \theta_{c1})$	−0.005	$\boxed{0.144}$	0.033	0.062	0.068
$(\Delta E, \theta_{c2})$	−0.028	$\boxed{0.141}$	0.090	0.069	0.037
$(\Delta E, \Delta t)$	0.021	0.013	0.021	0.055	0.043
$(\Delta E, \sigma_{\Delta t})$	−0.013	−0.014	−0.010	0.029	0.026
$(\mathcal{F}, \theta_{c1})$	0.003	0.011	0.031	−0.012	0.013
$(\mathcal{F}, \theta_{c2})$	−0.019	0.017	0.038	0.001	0.012
$(\mathcal{F}, \Delta t)$	0.004	0.008	−0.003	−0.008	0.000
$(\mathcal{F}, \sigma_{\Delta t})$	0.035	0.038	0.039	$\boxed{-0.143}$	$\boxed{-0.133}$
$(\theta_{c1}, \theta_{c2})$	−0.005	$\boxed{-0.553}$	$\boxed{-0.600}$	0.052	0.012
$(\theta_{c1}, \Delta t)$	0.021	−0.006	0.007	0.012	0.001
$(\theta_{c1}, \sigma_{\Delta t})$	−0.005	−0.006	−0.006	−0.003	0.024
$(\theta_{c2}, \Delta t)$	−0.005	0.009	−0.006	−0.009	−0.013
$(\theta_{c2}, \sigma_{\Delta t})$	−0.003	−0.011	−0.025	0.005	−0.001
$(\Delta t, \sigma_{\Delta t})$	−0.028	−0.027	−0.036	0.020	0.013

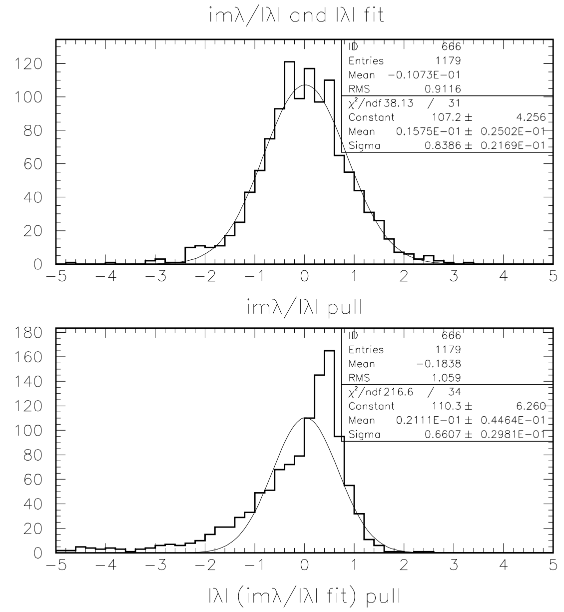

Figure 4.16: Pull plots for $\mathcal{I}m\lambda_{f_{CP}}/\,|\lambda_{f_{CP}}|$ and $|\lambda_{f_{CP}}|$ in "toy" Monte Carlo experiments.

for $|\lambda_{f_{CP}}|$ and $C_{\pi\pi}$ a clear trend emerges, Fig. 4.17. If the fitted value of $C_{\pi\pi}$ is in the physical region $(-1, 1)$ then the value of $|\lambda_{f_{CP}}|$ returned from the fit follows the exact functional relationship $|\lambda_{f_{CP}}| = \sqrt{(1 - C_{\pi\pi})/(1 + C_{\pi\pi})}$. However, if $C_{\pi\pi}$ is in the unphysical region, a fit for $|\lambda_{f_{CP}}|$ is unable to converge. A similar behavior is observed for fits using $(|\lambda_{f_{CP}}|, \mathcal{I}m\lambda_{f_{CP}})$ as *CP* parameters.

Fig. 4.18 shows distributions of the fraction of "toy" experiments that return physical values for $S_{\pi\pi}$ and $C_{\pi\pi}$. Depending on the generated values, the probability to obtain a fit in the physical region ranges between 50% and 90%, so there is a strong possibility that one or both coefficients will be in the unphysical region. In this case, it may only be possible to make a statement about the confidence at which we exclude zero asymmetry.

4.7 Validation studies

Numerous studies using "toy" Monte Carlo simulation and data have been performed to optimize and validate the analysis strategy. Fig.s 4.19 through 4.23 show pull plots for all free parameters in 695 "toy" experiments corresponding to the nominal *CP* fit. Signal and background yields are generated according to a Poisson distribution with means equal to the result given in Chapter 3 scaled to $30\,\mathrm{fb}^{-1}$. The yield for signal KK is generated with

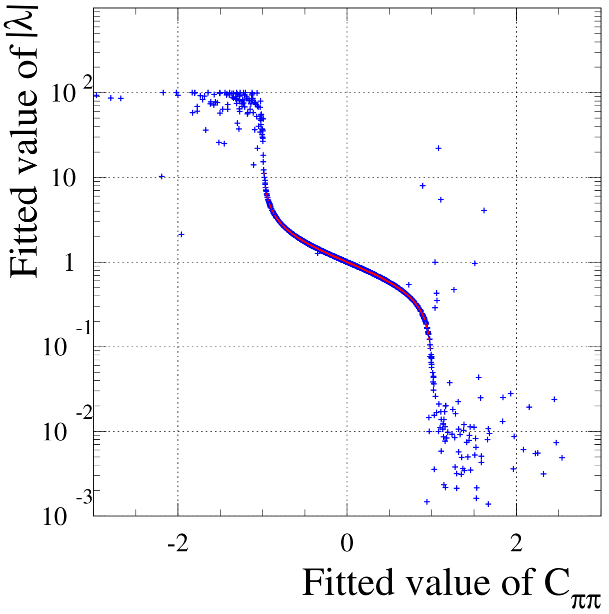

Figure 4.17: Scatter plot of the fitted value of $|\lambda_{f_{CP}}|$ vs. the fitted value of $C_{\pi\pi}$ in "toy" Monte Carlo experiments. The data points follow the functional relationship $|\lambda_{f_{CP}}| = \sqrt{(1 - C_{\pi\pi})/(1 + C_{\pi\pi})}$ when the fitted value of $C_{\pi\pi}$ is in the physical region.

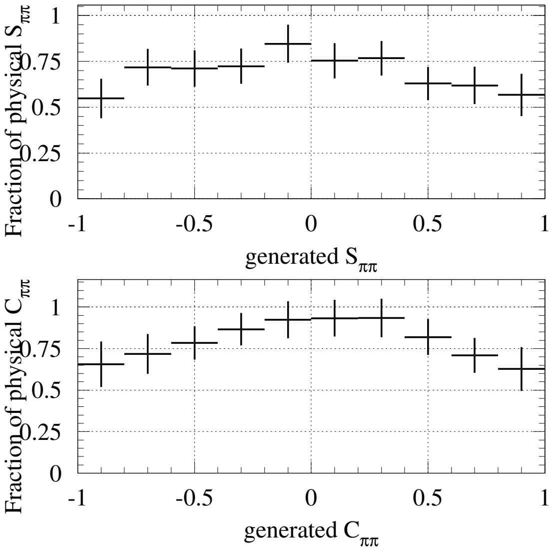

Figure 4.18: Fraction of "toy" experiments with fitted values of $S_{\pi\pi}$ or $C_{\pi\pi}$ in the physical region.

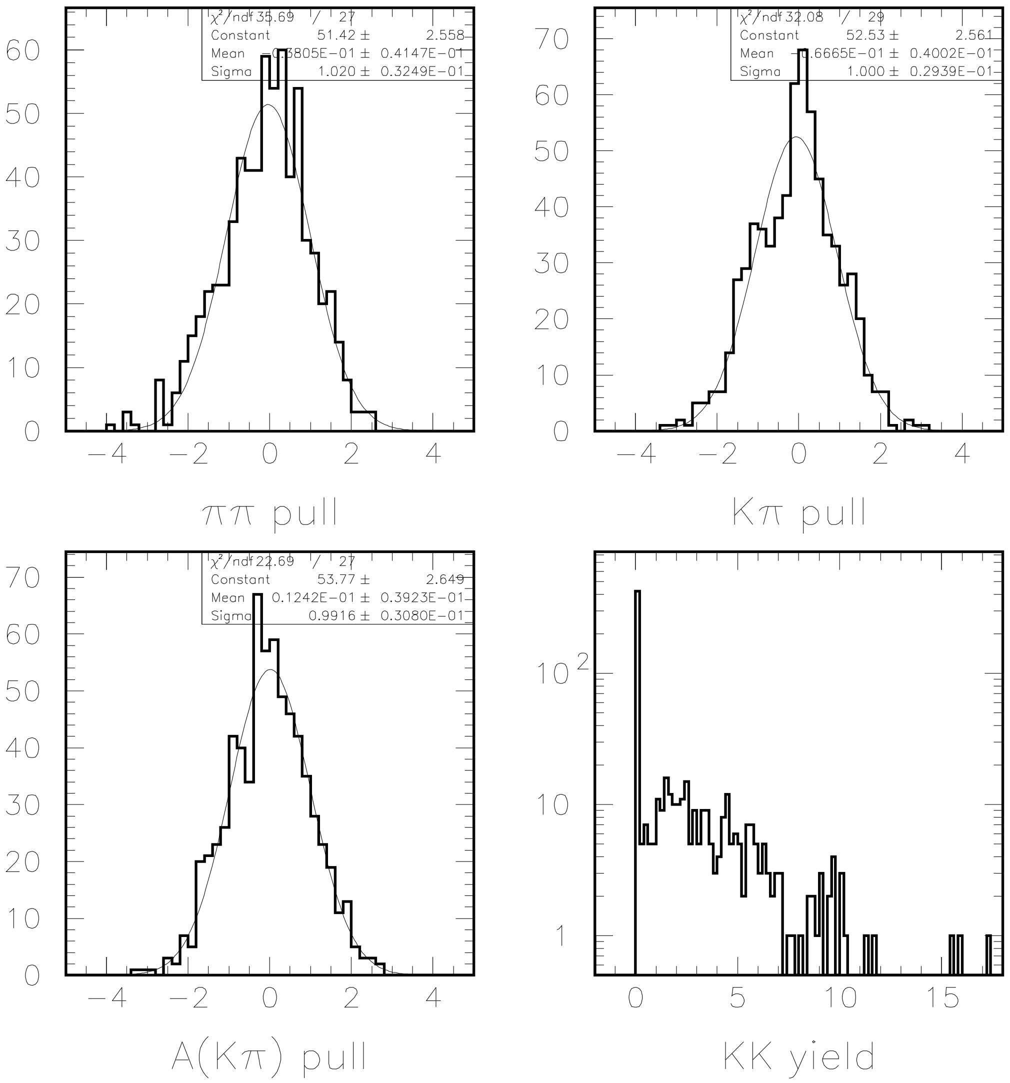

Figure 4.19: Pull plots for signal yields and the $K\pi$ charge asymmetry in 695 "toy" experiments generated with $30\,\mathrm{fb}^{-1}$ equivalent luminosity. The lower right plot shows the KK yield (not the pull). The likelihood fit does not introduce any bias and correctly estimates errors on yields.

zero Branching Fraction and fit with the constraint $N_{KK} > 0$. Random values of $C_{\pi\pi}$ are generated between ± 1 and random values of $S_{\pi\pi}$ are generated within the bounds allowed by $C_{\pi\pi}$. The numbers of B^0 and $\overline{B}^0$ tags are consistent with the generated value of $C_{\pi\pi}$.

Fig. 4.24 shows the CP asymmetry fit errors distributions for these "toy" experiments. Distribution are rather wide with a significant tail and the most probable values are $\sigma_{S_{\pi\pi}} \sim 0.6$ and $\sigma_{C_{\pi\pi}} \sim 0.45$.

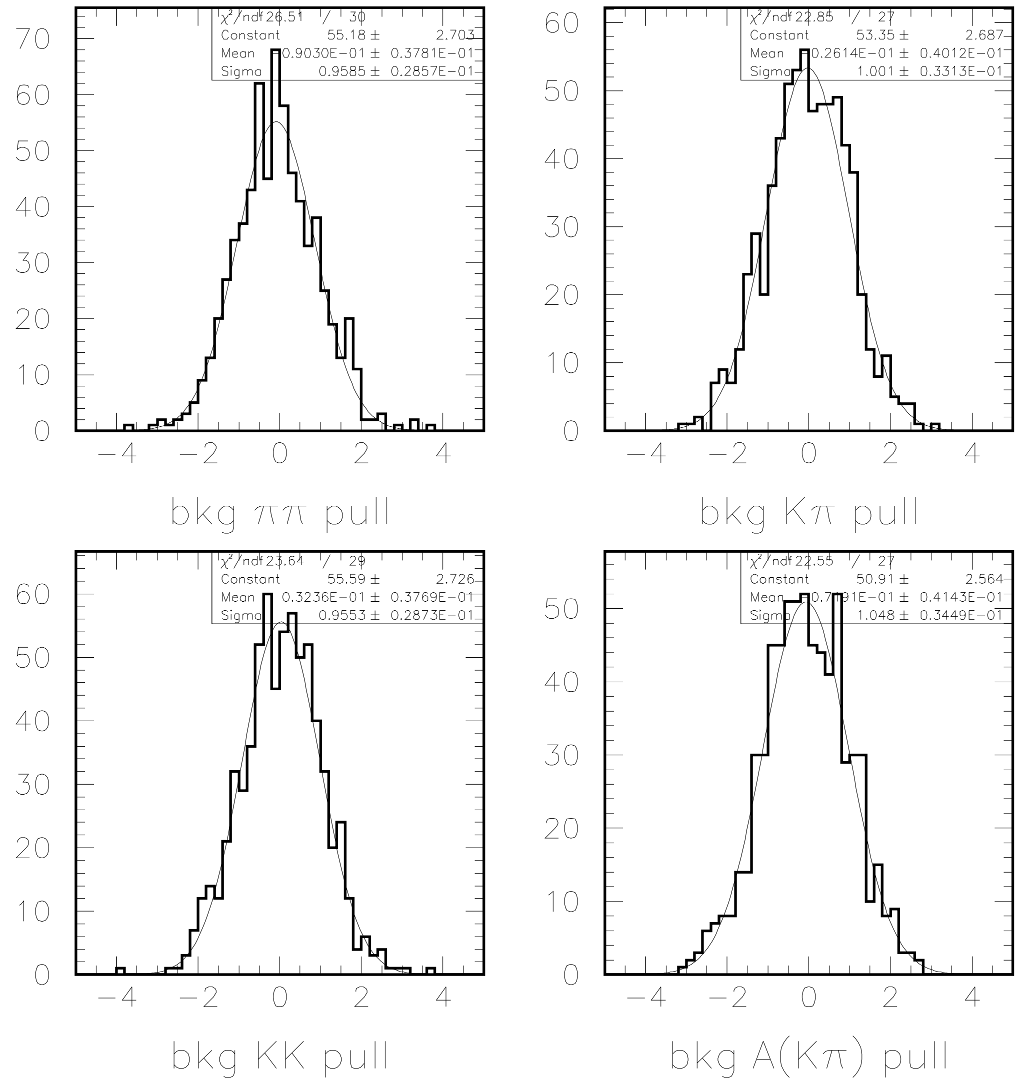

Figure 4.20: Pull plots for background yields and the $K\pi$ charge asymmetry in 695 "toy" experiments generated with $30\,\mathrm{fb}^{-1}$ equivalent luminosity.

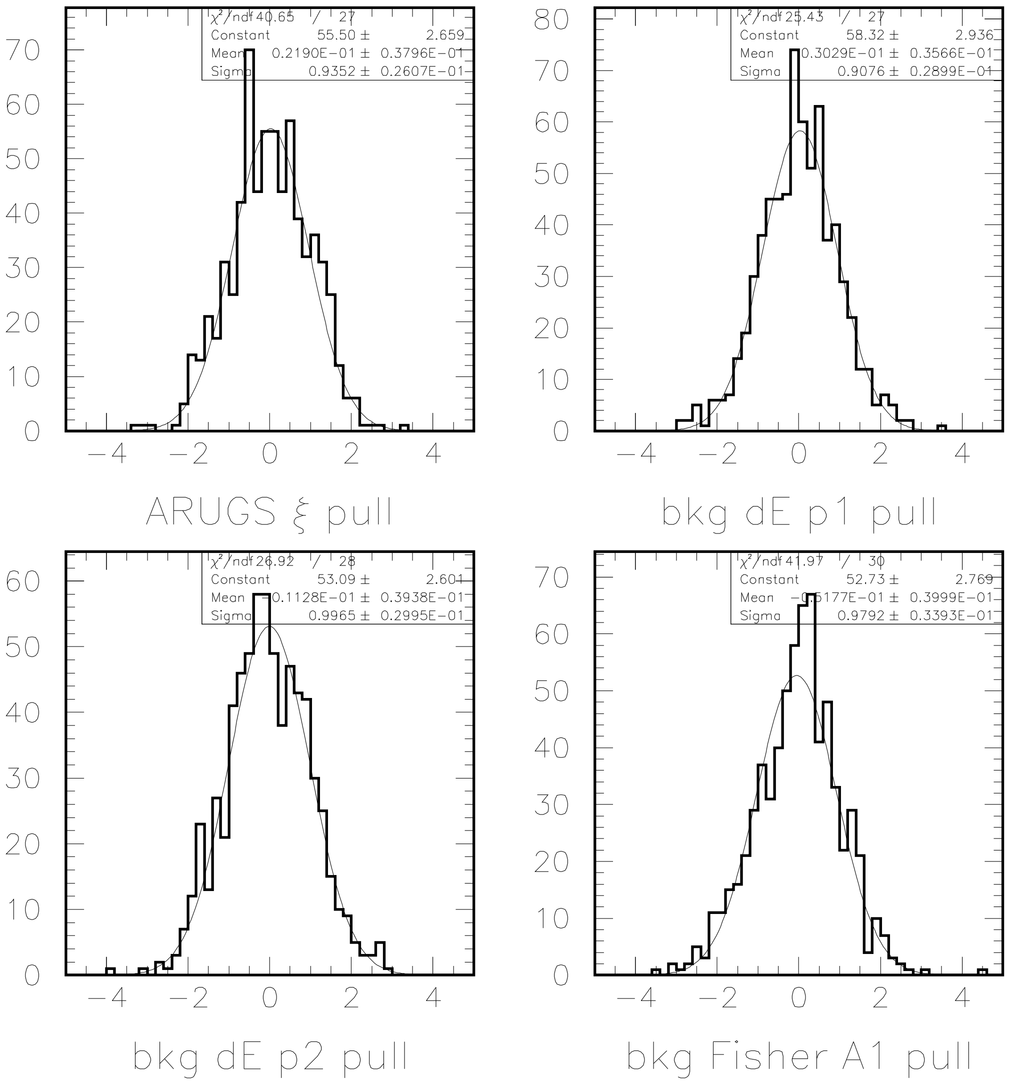

Figure 4.21: Pull plots for background m_{ES}, ΔE, and Fisher parameters in 695 "toy" experiments generated with $30\,\mathrm{fb}^{-1}$ equivalent luminosity.

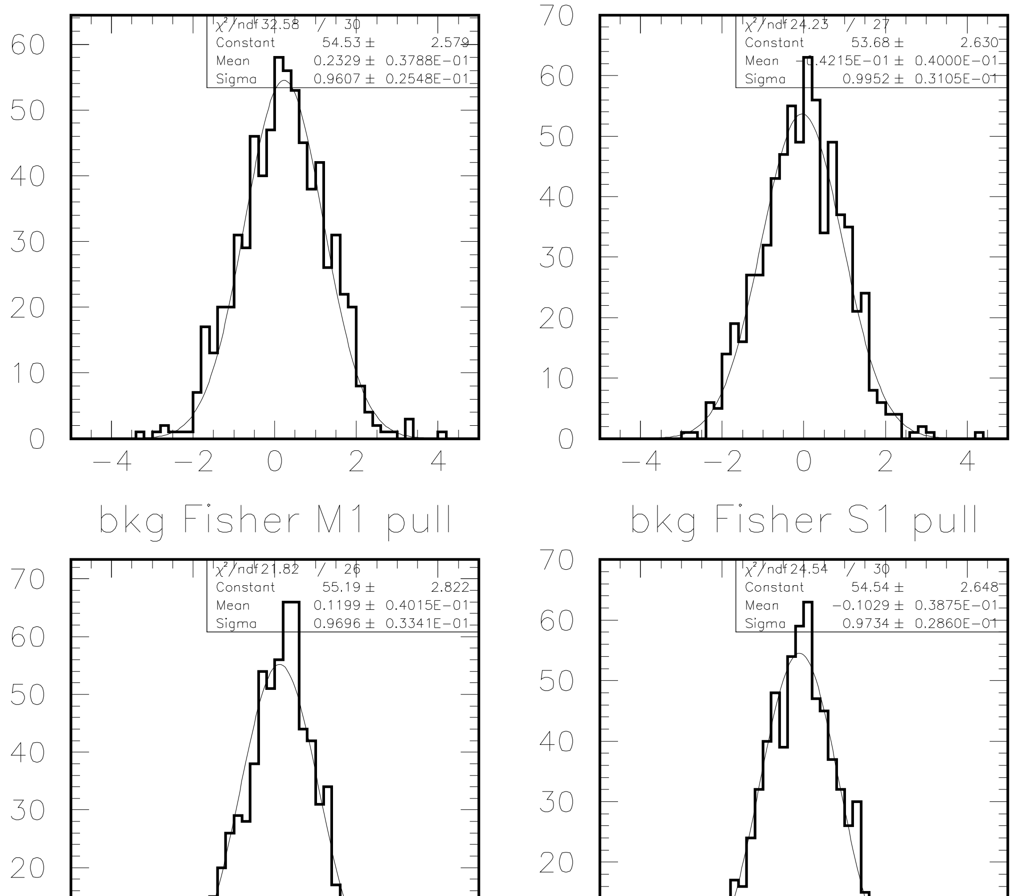

Figure 4.22: Pull plots for the background Fisher means and widths in 695 "toy" experiments generated with 30 fb^{-1} equivalent luminosity.

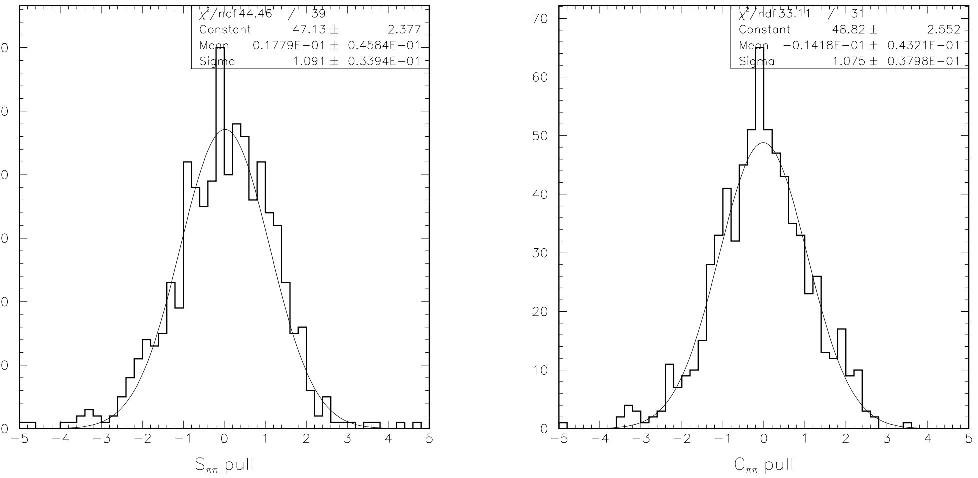

Figure 4.23: Pull plots for $S_{\pi\pi}$ (left) and $C_{\pi\pi}$ in 695 "toy" experiments generated with $30\,\mathrm{fb}^{-1}$ equivalent luminosity. No bias is induced by the likelihood fit and errors are correctly reproduced.

4.7.1 Effect of floating yields in the *CP* fit

The r.m.s. of the Δt distribution for $B\overline{B}$ events is greater than the corresponding r.m.s. for continuum $q\bar{q}$ events. It is therefore expected that adding this variable in the likelihood function will improve the statistical separation between signal and background. To see how much we gain in the branching fraction analysis by floating yields in the *CP* fit, we generated 685 "toy" experiments and fit each one with and without the Δt PDF in the likelihood. Fig. 4.25 shows the difference in the fitted error on $N_{\pi\pi}$. The error on $N_{\pi\pi}$ improves by 8%. The conclusion is that fitting simultaneously for yields and asymmetries optimizes the branching fraction measurement. Moreover, the uncertainty on the yield is included directly in the *CP* asymmetry fit error. In Fig 4.26 we show that the asymmetry errors increase only slightly when floating yields in the *CP* fit.

4.7.2 Monte Carlo fits

In $30\,\mathrm{fb}^{-1}$ we expect ~ 250 signal $\pi\pi$ and $K\pi$ events. The size of this sample allows to fit for the B^0 lifetime and mixing frequency, which is an important consistency check on the Δt resolution function and on the fit mechanism itself. Tab. 4.21 shows the results of several test fits on Monte Carlo samples. Fitting for the lifetime and Δm_d in pure signal, or in a mix of $\pi\pi$ and $K\pi$ events in the proper ratio, returns correct values for both parameters. We have also tried mixing into the $9.5\,\mathrm{fb}^{-1}$ continuum Monte Carlo

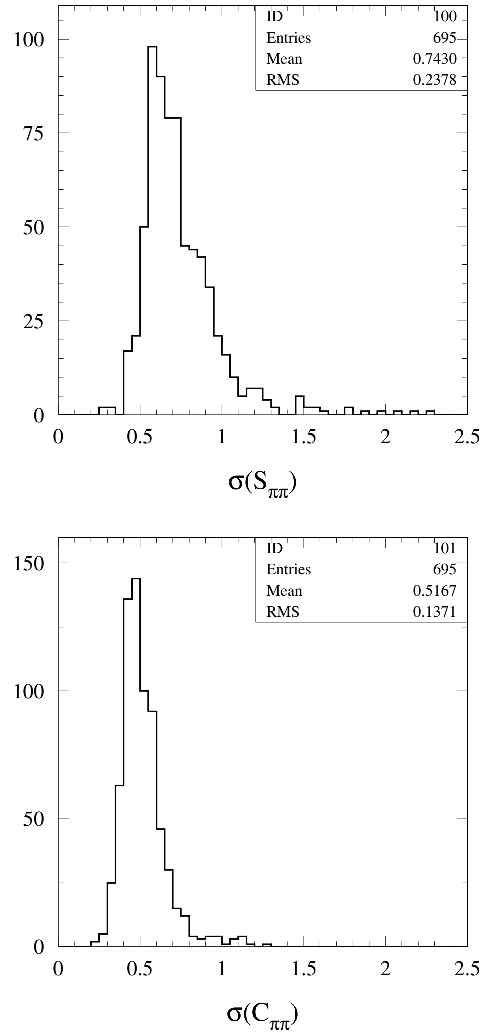

Figure 4.24: Error distributions for $S_{\pi\pi}$ (left) and $C_{\pi\pi}$ (right) in 695 "toy" experiments generated with $30\,\mathrm{fb}^{-1}$ equivalent luminosity.

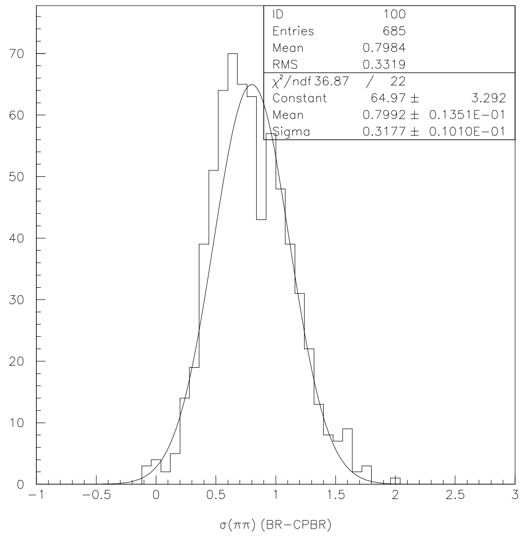

Figure 4.25: Distribution of the difference between $\sigma_{N_{\pi\pi}}$ in a likelihood fit *without* Δt and $\sigma_{N_{\pi\pi}}$ in a likelihood fit *with* Δt. The average $\sigma_{N_{\pi\pi}}$ is ~ 10, so the improvement in statistical error is about 8%.

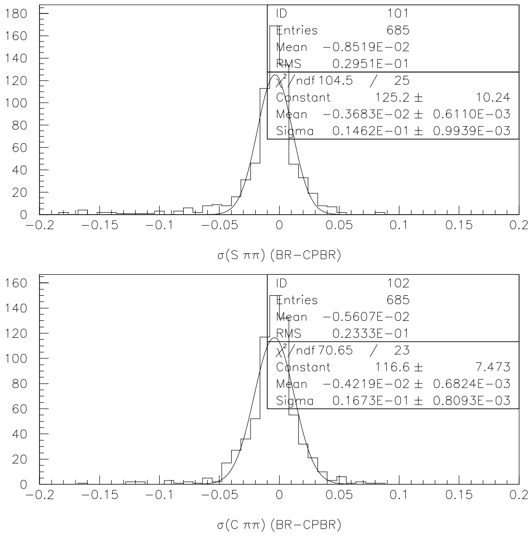

Figure 4.26: Top(Bottom): distribution of the difference between $\sigma_{S_{\pi\pi}}(\sigma_{C_{\pi\pi}})$ in a likelihood fit *without* floating yields and $\sigma_{S_{\pi\pi}}(\sigma_{C_{\pi\pi}})$ *with* floating yields. A slight increase in the errors is present.

Table 4.21: Lifetime, Δm_d, and *CP* fits to various signal and background Monte Carlo samples. The generated values are: $\tau = 1.548\,\mathrm{ps}$, $\Delta m_d = 0.472\hbar\,\mathrm{ps}^{-1}$, $S_{\pi\pi} = -0.4$, and $C_{\pi\pi} = 0$. When fixed, the fit parameters are set to: $\tau = 1.548\,\mathrm{ps}$, $\Delta m_d = 0.472\hbar\,\mathrm{ps}^{-1}$, $S_{\pi\pi} = C_{\pi\pi} = 0$.

Sample	τ (ps)	Δm_d ($\hbar\,\mathrm{ps}^{-1}$)	$S_{\pi\pi}$	$C_{\pi\pi}$
7388 $\pi\pi$	1.589 ± 0.021	fixed	fixed	fixed
7388 $\pi\pi$	fixed	fixed	-0.374 ± 0.040	0.013 ± 0.027
7342 $K\pi$	fixed	0.472 ± 0.013	fixed	fixed
7342 $K\pi$	1.536 ± 0.021	fixed	fixed	fixed
1835 $\pi\pi$ + 7342 $K\pi$	1.513 ± 0.019	fixed	fixed	fixed
1835 $\pi\pi$ + 7342 $K\pi$	fixed	fixed	-0.369 ± 0.085	0.002 ± 0.058
$9.5\,\mathrm{fb}^{-1}$ equiv.	1.84 ± 0.22	fixed	fixed	fixed
$9.5\,\mathrm{fb}^{-1}$ equiv.	fixed	fixed	-0.41 ± 0.78	-0.82 ± 0.80
$9.5\,\mathrm{fb}^{-1}$ equiv.	fixed	0.460 ± 0.087	fixed	fixed
$9.5\,\mathrm{fb}^{-1}$ equiv.	fixed	0.438 ± 0.084	-0.48 ± 0.83	-0.86 ± 0.78

sample the correct amount of signal yields according to the measured Branching Ratios. We find consistent values of τ and Δm_d. Finally, fitting for $S_{\pi\pi}$ and $C_{\pi\pi}$ returns the correct values in high statistics signal Monte Carlo and consistent values in the sample with background.

To check that the fit errors on the *CP* asymmetries in full Monte Carlo sample are consistent with what we estimate in "toy" Monte Carlo, we take the same sample of $9.5\,\mathrm{fb}^{-1}$ continuum Monte Carlo and add to it ten different sets of $(N_{\pi\pi}, N_{K\pi})$ signal Monte Carlo events, with $N_{\pi\pi}$ and $N_{K\pi}$ determined by Poisson statistics. Tab. 4.22 sumarizes the results of this test. The average error on $S_{\pi\pi}$ and $C_{\pi\pi}$ are 1.33 and 0.85, respectively. Scaled to $30\,\mathrm{fb}^{-1}$ we would predict an expected error of 0.75 on $S_{\pi\pi}$ and 0.48, in excellent agreement with the "toy" Monte Carlo prediction (Fig. 4.24).

4.7.3 Branching fraction fits

Having validated the analysis on "toy" and full Monte Carlo events, we fit without Δt to validate the branching fraction sector of the likelihood. Tab. 4.23 summarizes fits to the Run 1, Run 2, and combined samples. The yields for both Run 1 and Run 2 are consistent and the background parameters for m_{ES}, ΔE, and $\mathcal{F}$ are consistent between the two datasets. To evaluate the effect of floating the background PDF parameters we also show in Tab. 4.23 a fit where the parameters are fixed to the values obtained from the fit with these same parameters floating. The contribution to the error on the $\pi\pi$ yield can

Table 4.22: A set of ten *CP* fits on $9.5\,\mathrm{fb}^{-1}$ equivalent continuum Monte Carlo with the correct proportion of $\pi\pi$ and $K\pi$ signal. The asymmetry input values are $S_{\pi^+\pi^-} = -0.4$ and $C_{\pi\pi} = 0$.

Fit #	$N_{\pi\pi}$	$N_{K\pi}$	$S_{\pi\pi}$	$C_{\pi\pi}$
1	22	75	-0.72 ± 1.27	-1.74 ± 0.85
2	24	81	0.50 ± 0.94	-0.27 ± 0.59
3	21	92	-0.15 ± 0.84	0.02 ± 0.59
4	26	71	0.29 ± 0.72	0.84 ± 0.60
5	17	99	-1.43 ± 1.97	-0.26 ± 0.73
6	13	98	1.06 ± 1.32	0.37 ± 0.78
7	11	75	-3.70 ± 3.06	-3.12 ± 1.77
8	21	77	-1.74 ± 1.09	-0.64 ± 0.88
9	17	89	-1.75 ± 1.29	0.28 ± 0.97
10	25	88	-0.42 ± 0.75	-0.86 ± 0.78
Average	19.7	84.5	$\langle\sigma_{S_{\pi\pi}}\rangle = 1.33$	$\langle\sigma_{C_{\pi\pi}}\rangle = 0.85$

Table 4.23: Summary of fits using only the branching fraction part of the likelihood function (no Δt). To estimate the effect of floating background parameters for m_{ES}, ΔE, and $\mathcal{F}$, we also show a fit with fixed background parameters.

Parameter	Run 1	Run 2	Run 1 and Run 2	Run 1 and Run 2
$N_{\pi\pi}$	38.4 ± 9.9	26.6 ± 7.0	66.2 ± 12.4	66.2 ± 12.3
$N_{K\pi}$	144.4 ± 15.4	67.5 ± 10.3	211.8 ± 18.5	211.8 ± 18.4
$\mathcal{A}_{K\pi}$	-0.191 ± 0.104	0.107 ± 0.150	-0.090 ± 0.087	-0.090 ± 0.087
N_{KK}	5.9 ± 6.2	0.0 ± 1.5	2.0 ± 6.4	2.0 ± 6.4
$N_{b\pi\pi}$	3081.9 ± 63.0	1453.8 ± 40.0	4533.2 ± 72.6	4533.2 ± 72.6
$N_{bK\pi}$	2010.5 ± 55.4	979.7 ± 35.2	2994.3 ± 65.4	2994.3 ± 65.3
$\mathcal{A}_{bK\pi}$	-0.001 ± 0.027	-0.025 ± 0.036	-0.009 ± 0.021	-0.009 ± 0.021
N_{bKK}	1318.9 ± 42.8	613.5 ± 26.3	1933.5 ± 48.9	1933.5 ± 48.8
ξ	20.6 ± 1.4	22.7 ± 2.1	21.3 ± 1.2	21.3 (fixed)
ΔE_{p1}	-1.146 ± 0.147	-0.900 ± 0.212	-1.071 ± 0.121	-1.071 (fixed)
ΔE_{p2}	0.649 ± 1.886	0.695 ± 2.697	0.691 ± 1.559	0.691 (fixed)
$\mathcal{F}_{\mu_1}$	0.323 ± 0.067	0.516 ± 0.120	0.385 ± 0.061	0.385 (fixed)
$\mathcal{F}_{\sigma_1}$	-0.134 ± 0.015	-0.099 ± 0.020	-0.122 ± 0.012	-0.122 (fixed)
$\mathcal{F}_{\mu_2}$	0.187 ± 0.016	0.217 ± 0.020	0.198 ± 0.013	0.198 (fixed)
$\mathcal{F}_{\sigma_2}$	0.018 ± 0.012	0.054 ± 0.025	0.029 ± 0.011	0.029 (fixed)
$\mathcal{F}_{f_1}$	0.326 ± 0.007	0.356 ± 0.017	0.335 ± 0.007	0.335 (fixed)

be estimated as $\sqrt{\sigma^2_{\mathrm{float}} - \sigma^2_{\mathrm{fix}}} = 1.6$ events, which is significantly less than the systematic error derived with the conservative procedure described in Chapter 3.

Table 4.24: Summary of data fits floating τ only, Δm_d only, or both. These fits are performed with $S_{\pi\pi} = C_{\pi\pi} = 0$. Units are ps for τ and $\hbar\,\text{ps}^{-1}$ for Δm_d.

			floating both	
Sample	τ only	Δm_d only	τ	Δm
Run 1	1.54 ± 0.15	0.553 ± 0.091	1.54 ± 0.16	0.553 ± 0.091
Run 2	1.49 ± 0.20	0.454 ± 0.221	1.49 ± 0.20	0.457 ± 0.220
Run 1 and Run 2	1.52 ± 0.12	0.539 ± 0.087	1.52 ± 0.12	0.540 ± 0.088

Table 4.25: Summary of fits floating τ, Δm_d, and the blinded *CP* asymmetries $S_{\pi\pi}$ and $C_{\pi\pi}$. Units are ps for τ and $\hbar\,\text{ps}^{-1}$ for Δm_d.

Sample	τ	Δm_d	$S_{\pi\pi}$ (blind)	$C_{\pi\pi}$ (blind)
Run 1	1.53 ± 0.16	0.540 ± 0.096	2.73 ± 0.84	4.42 ± 0.56
Run 2	1.49 ± 0.20	0.634 ± 0.114	-0.65 ± 1.14	3.50 ± 0.63
Run 1 and Run 2	1.52 ± 0.12	0.542 ± 0.087	1.45 ± 0.56	4.21 ± 0.49

4.7.4 Lifetime and mixing fits

As a cross-check on the signal and background Δt parameterizations we perform *CP* fits to the lifetime τ, mixing frequency Δm_d, and *CP* asymmetries in Run 1 and Run 2 data. When fitting only τ and Δm_d we "blind" ourselves to the *CP* asymmetry by explicitly setting $S_{\pi\pi} = C_{\pi\pi} = 0$. For the *CP* fit we blind by adding a random offset between ± 5 and randomly flipping the sign of the asymmetries. The large offset is motivated by the significant probability of obtaining an fit with unphysical values and the desire to remain blind to that information.

Tab. 4.24 summarizes the fit results. We obtain values of τ and Δm_d consistent with the PDG and fitting for these parameters does not significantly change the yields. Tab. 4.25 summarizes fits floating τ, Δm_d, and the blinded *CP* asymmetries $S_{\pi\pi}$ and $C_{\pi\pi}$. Again, all results for τ and Δm_d are consistent with the PDG.

4.8 Results and cross-checks

Tab. 4.26 summarizes the unblinded fit results on the full dataset. Fig. 4.27 shows scans of the likelihood function with respect to the *CP* parameters. To estimate how likely the error obtained on the full dataset is, we generated 1279 "toy" experiments with yields given by the data fit (with no Poisson fluctuations on the number of events). Fig. 4.28 shows the pull distributions for $S_{\pi\pi}$ and $C_{\pi\pi}$. Fig. 4.29 shows the error distribution from the ensemble of "toy" experiments, with the data results indicated by the arrows. The fit errors are observed to be largely independent of the generated values (Fig. 4.30).

Fig. 4.31 shows distributions of $m_{\rm ES}$ and ΔE for events enhanced in signal $\pi\pi$ and $K\pi$ decays using likelihood ratio cuts. The curves represent projections of the fit result scaled by the efficiency of the additional cuts.

Fig. 4.32 shows the Δt distributions and the asymmetry

$$A(\Delta t) = \frac{N_{B^0}(\Delta t) - N_{\overline{B}^0}(\Delta t)}{N_{B^0}(\Delta t) + N_{\overline{B}^0}(\Delta t)} \tag{4.29}$$

for tagged events enhanced in signal $\pi\pi$ decays. The selection procedure is the same as Fig. 4.31, with the likelihoods defined including the PDFs for θ_c, $\mathcal{F}$, $m_{\rm ES}$, and ΔE. Approximately 24 $\pi\pi$, 22 $q\bar{q}$, and 5 $K\pi$ events satisfy the selection. We find that the background resolution function describes the core of the Δt distribution well and the tail is consistent with B decay.

Given that we measure a value of Δm_d consistent with the PDG value, we have searched for visual evidence of mixing in $B \to K^{\pm}\pi^{\mp}$ decays. Fig. 4.33 shows the distribution of $|\Delta t|$ for mixed, unmixed, and the ratio of mixed events to the sum of mixed and unmixed. The data sample is enhanced in signal $K\pi$ decays by cutting on likelihood ratios, with an estimated $K\pi$ yield of 67 events. Although not conclusive, the data is not inconsistent with mixing, and with more statistics in future this would be a nice validation of the analysis technique.

4.8.1 Cross-checks

Tab. 4.27 summarizes several tests made to cross-check the stability of the result. We fit separately the Run 1 and Run 2 datasets and find that the weighted averages are consistent with the results for the entire dataset. Errors are not supposed to naively scale as $\frac{1}{\sqrt{N_{\pi\pi}}}$ given the smallness of the signal sample. We also fit the B^0 and $\overline{B}^0$ tag samples separately, again with consistent results. To test the stability of the fit against tag category, we fit only the Lepton and Kaon categories and find consistent results, with slightly larger errors for $S_{\pi\pi}$ and $C_{\pi\pi}$ (as expected since $NT1$ and $NT2$ cateogories have a small Q).

Fig. 4.7 indicates some discrepancy in ARGUS shape between different tag categories.

Table 4.26: Summary of the unblinded fit results on the Run 1 and Run 2 dataset. The last row gives the correlation between the time-dependent *CP* asymmetry parameters.

Parameter	Fit Result
$N_{\pi\pi}$	$65.0^{+12.0}_{-11.1}$
$N_{K\pi}$	$216.7^{+18.4}_{-17.6}$
$\mathcal{A}_{K\pi}$	-0.07 ± 0.08
N_{KK}	$4.3^{+6.3}_{-4.3}$
$N_{b\pi\pi}$	4532^{+73}_{-72}
$N_{bK\pi}$	2990 ± 65
$\mathcal{A}_{bK\pi}$	-0.01 ± 0.02
N_{bKK}	1933^{+49}_{-48}
ξ	$21.2^{+1.2}_{-1.2}$
ΔE_{p1}	$-1.07^{+0.12}_{-0.12}$
ΔE_{p2}	$0.67^{+1.58}_{-1.54}$
$\mathcal{F}_{\mu_1}$	$0.388^{+0.066}_{-0.057}$
$\mathcal{F}_{\sigma_1}$	-0.121 ± 0.012
$\mathcal{F}_{\mu_2}$	0.198 ± 0.013
$\mathcal{F}_{\sigma_2}$	$0.030^{+0.012}_{-0.010}$
$\mathcal{F}_{f_1}$	$0.335^{+0.008}_{-0.006}$
$S_{\pi\pi}$	$0.03^{+0.53}_{-0.56}$
$C_{\pi\pi}$	$-0.25^{+0.45}_{-0.47}$
Corr($S_{\pi\pi}$,$C_{\pi\pi}$)	-21%

Table 4.27: Separate fits to Run 1 and Run 2, B^0 and $\overline{B}^0$ tags, and the subsample of Lepton and Kaon tagged events.

Sample	$\mathcal{A}_{K\pi}$	$S_{\pi\pi}$	$C_{\pi\pi}$
Run 1	-0.16 ± 0.10	$+1.34 \pm 0.82$	-0.03 ± 0.52
Run 2	$+0.11 \pm 0.14$	-1.19 ± 0.76	-1.09 ± 0.65
B^0 tags	$+0.24 \pm 0.15$	-0.44 ± 0.77	-0.1 ± 1.3
$\overline{B}^0$ tags	-0.36 ± 0.14	$+0.42 \pm 0.65$	-0.1 ± 1.4
no NT tags	-0.07 ± 0.08	$+0.09 \pm 0.58$	-0.54 ± 0.53

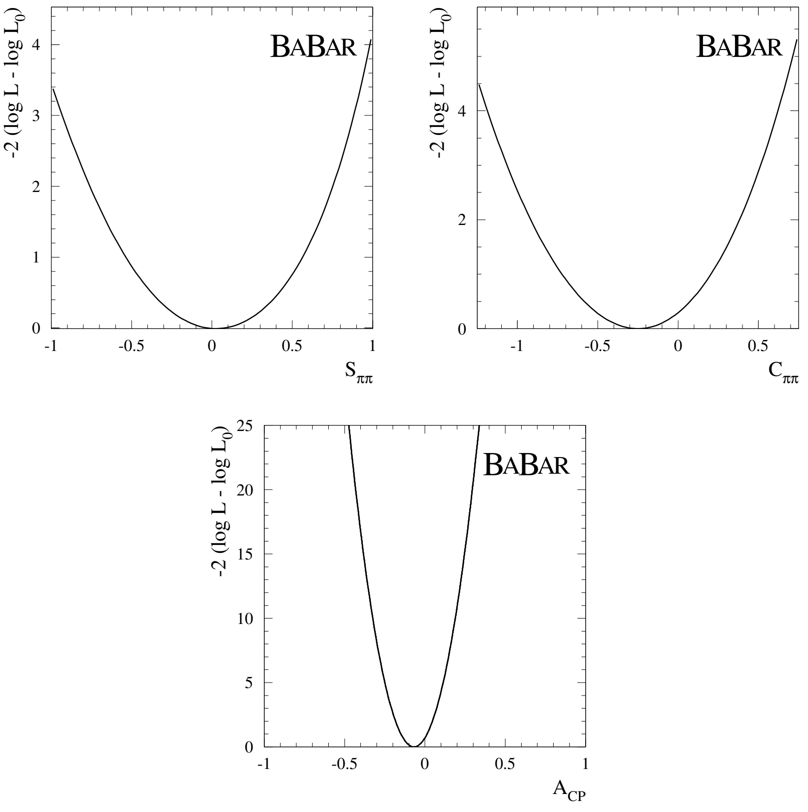

Figure 4.27: Scans of the likelihood function vs. $S_{\pi\pi}$, $C_{\pi\pi}$, and $\mathcal{A}_{K\pi}$.

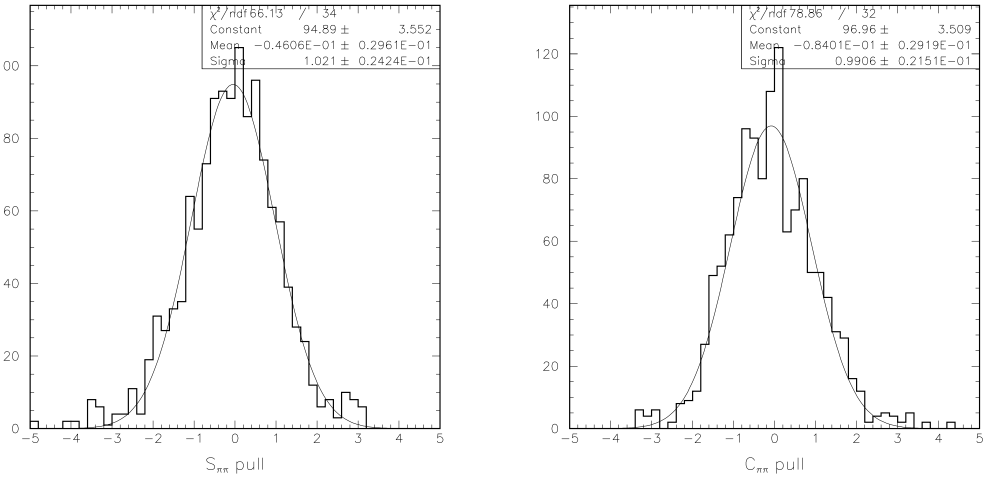

Figure 4.28: Pull distributions for $S_{\pi\pi}$ and $C_{\pi\pi}$ from 1279 "toy" experiments with fixed yields generated according to the Run 1 and Run 2 result.

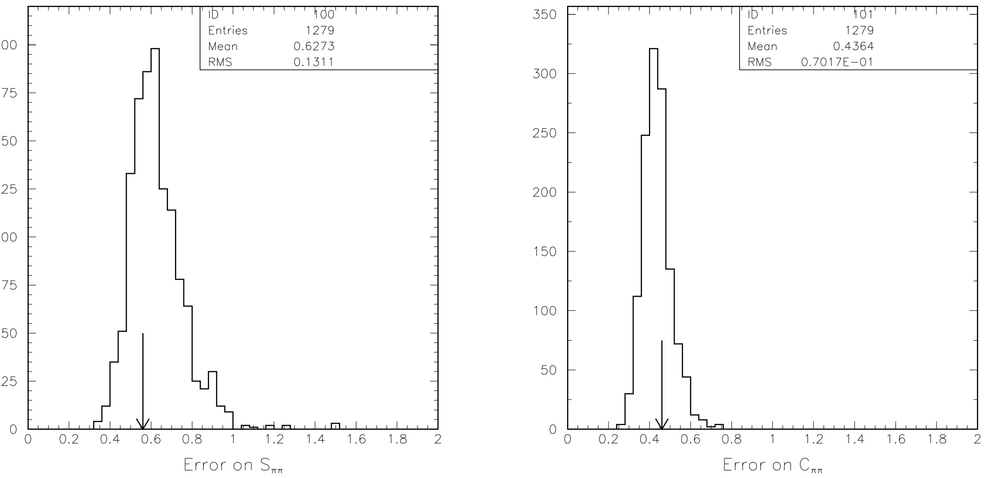

Figure 4.29: Error distributions for $S_{\pi\pi}$ and $C_{\pi\pi}$ from 1279 "toy" experiments with fixed yields generated according to the Run 1 and Run 2 result. The data result is indicated by the arrows.

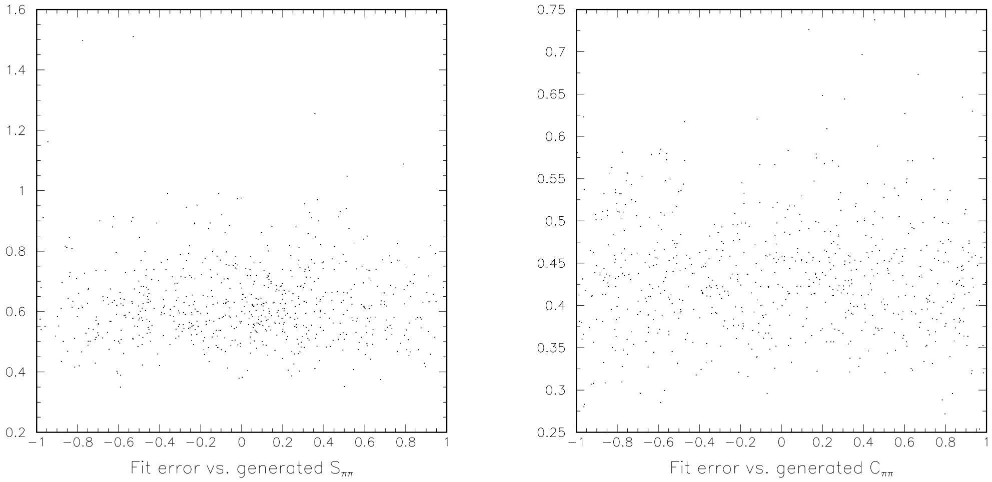

Figure 4.30: Scatter plots of fit error vs. generated $S_{\pi\pi}$ and $C_{\pi\pi}$ from 1279 "toy" experiments with fixed yields generated according to the Run 1 and Run 2 result.

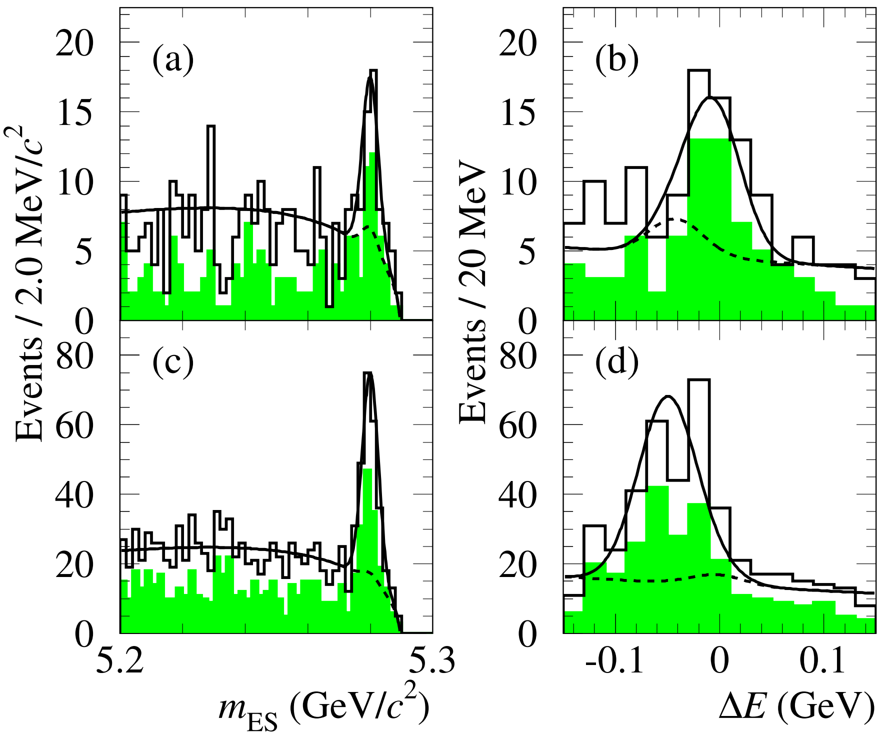

Figure 4.31: Distributions of m_{ES} and ΔE (points with errors) for events enhanced in signal (a), (b) $\pi\pi$ and (c), (d) $K\pi$ decays based on the likelihood ratio selection described in the text. Solid curves represent projections of the maximum likelihood fit result after accounting for the efficiency of the additional selection, while dashed curves represent $q\bar{q}$ and $\pi\pi \leftrightarrow K\pi$ cross-feed background. Shaded histograms show the subset of events that are tagged.

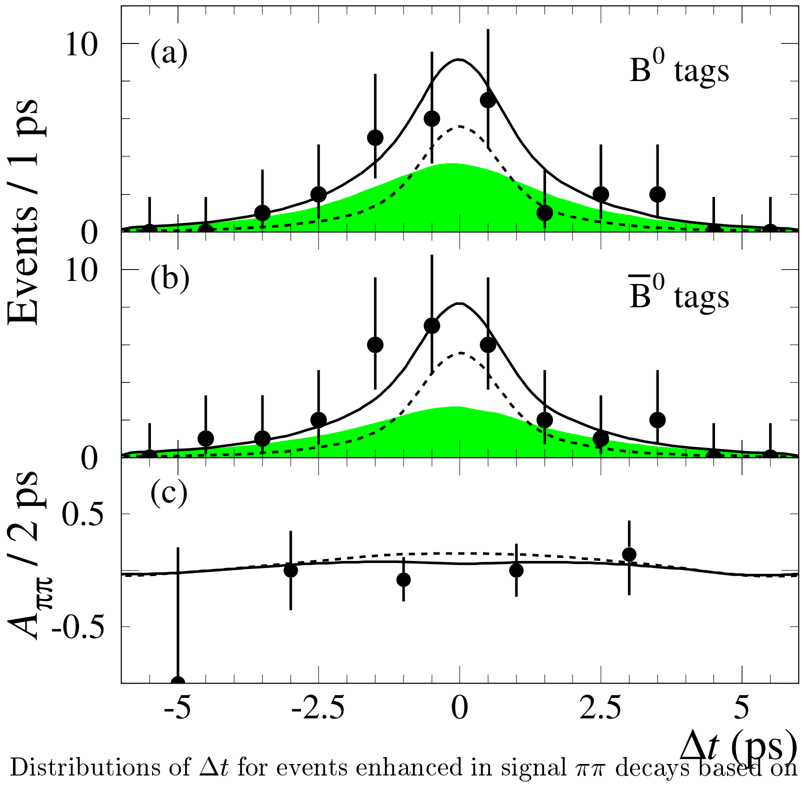

Figure 4.32: Distributions of Δt for events enhanced in signal $\pi\pi$ decays based on the likelihood ratio selection described in the text. Fig.(a) and Fig.(b) show events (points with errors) with $B_{tag} = B^0$ or $\bar{B}^0$. Solid curves represent projections of the maximum fit, dashed curves represent the sum of $q\bar{q}$ and $K\pi$ background events, and the shaded region represents the contribution from signal $\pi\pi$ events. Fig.(c) shows $A(\Delta t)$ for data (points with errors), as well as fit projections for signal and background events (solid curve), and signal events only (dashed curve).

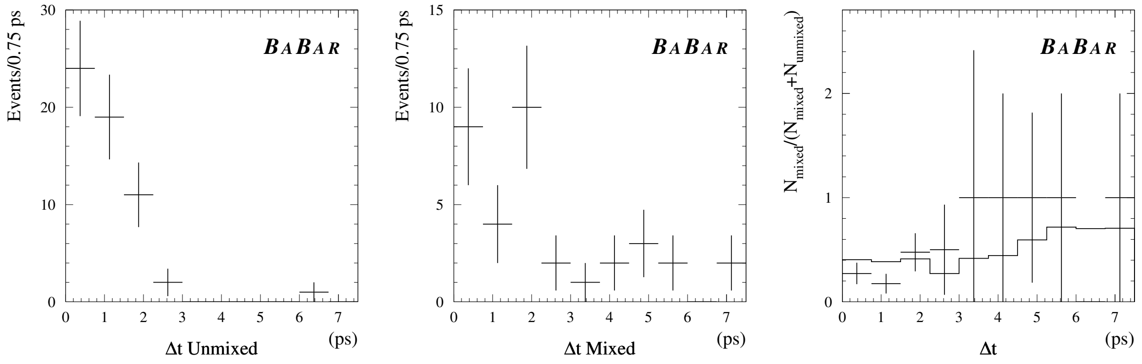

Figure 4.33: Distributions of $|\Delta t|$ for unmixed (left), mixed (middle), and mixed/(mixed + unmixed) (right) for events enhanced in signal $K\pi$ decays using likelihood ratio cuts.

Table 4.28: Results of a fit floating separate values of ξ for each tagging category. The average ξ from the nominal fit is 21.2 ± 1.2.

Category	Fitted ξ
Lepton	34.6 ± 10.6
Kaon	20.2 ± 2.2
NT1	13.7 ± 4.7
NT2	22.0 ± 2.7
Untagged	22.1 ± 1.7

Table 4.29: Results of a fit floating signal tagging efficiencies in Run 1 and Run 2, along with yields, background parameters, and *CP* parameters.

Category	Floating	Nominal
f_{Lepton}(Run1)	0.137 ± 0.027	0.110 (fixed)
f_{Kaon}(Run1)	0.315 ± 0.041	0.358 (fixed)
f_{NT1}(Run1)	0.044 ± 0.019	0.080 (fixed)
f_{NT2}(Run1)	0.123 ± 0.030	0.139 (fixed)
f_{Lepton}(Run2)	0.132 ± 0.037	0.110 (fixed)
f_{Kaon}(Run2)	0.327 ± 0.056	0.358 (fixed)
f_{NT1}(Run2)	0.067 ± 0.030	0.080 (fixed)
f_{NT2}(Run2)	0.126 ± 0.042	0.139 (fixed)

Since we assume one common shape in the nominal fit, we have investigating the possible systematic effect on the *CP* parameters. We refit the data allowing a different ξ for each category and we fit for them. Tab. 4.28 summarizes the results. The Lepton and NT1 categories have a different ξ than the nominal value, but the $\pi\pi$ yield changes by only 0.2 events, and the values of $S_{\pi\pi}$ and $C_{\pi\pi}$ change by only -0.005 and $+0.012$, respectively. There appears to be no bias in using an average value of ξ.

As a check on the consistency of the tagging efficiencies in signal events with the B_{flav} sample nominal values(Tab. 4.7), we performed a fit floating the efficiencies for each category separately for Run 1 and Run 2. Tab. 4.29 summarizes the result. The values are consistent between Run 1 and Run 2, and they agree with the nominal values.

We have some indication that the Fisher discriminant shape varies across tag categories. To study the effect, we generated "toy" Monte Carlo experiments with different

Fisher shapes for each category, based on fits to on-resonance sideband data, and fit each pseudo-experiment with the average Fisher shape. All parameters show no bias.

4.9 Systematic uncertainties

We evaluate the variations in $\mathcal{A}_{K\pi}$, $S_{\pi\pi}$, and $C_{\pi\pi}$ arising from uncertainties in various parameters, determined by changing each parameter by $\pm 1\sigma$. This basically covers the uncertainty originating from the imperfect knowledge of PDF parameters due to limited control sample statistics. In the case of Δt signal resolution function and Δt background distribution fluctuating each parameter up and down independently is a rather conservative approach, since PDF parameters are known to be correlated in this case. The detailed tables relative to this systematics evaluation are reported in Appendix B.

Moreover, Tab. 4.30 summarizes systematic uncertainties due to other effects not accounted by previous tests. We list them here below:

- we use for the signal Fisher PDF the parameters we get from $D^0\pi^-$ control sample; this estimates any systematic discrepancy between data and Monte Carlo for this topological variables;
- we use for background Fisher PDF a bifurcated Gaussian[5] in alternative to a double Gaussian; this tests systematic uncertainty due to the use of a specific functional form for this variable;
- we swap Run 1 and Run 2 Δt signal resolution function $\mathcal{R}$ and Δt background distribution $\mathcal{R}_{\text{bkg}}$ separately; since SVT alignement quality is rather different in Run 1 and Run 2 data (causing Run 1 and Run 2 resolution function being different) this conservatively tests the effect SVT alignement on these measurements;
- we fit to the $\mathcal{R}_{\text{bkg}}$ parameters in the fit region rather than the sideband region: this tests the systematic uncertainty coming from differences between fit region and sideband region (this is done separately for Run 1 and Run 2);

---

[5] A bifurcated Gaussian is defined as

$$BifG(x\,;\mu,\sigma_L,\sigma_R) = \begin{cases} \frac{1}{2\sqrt{2\pi}\sigma_R}\exp\left(-(x-\mu)^2/(2\sigma_R^2)\right) & ,\ x>\mu \\ \frac{1}{2\sqrt{2\pi}\sigma_L}\exp\left(-(x-\mu)^2/(2\sigma_L^2)\right) & ,\ x<\mu \end{cases}$$

where μ is the most probable value of x and $\sigma_L(\sigma_R)$ the square root of the *left*(*right*) Gaussian

- in order to test systematic differences in $\mathcal{R}_{\text{bkg}}$ between tagged and untagged events, we use parameters extracted respectively from tagged or from untagged events only;
- we also use a same $\mathcal{R}_{\text{bkg}}$ distribution determined on the whole data set for both Run 1 and Run 2 data;
- in order to asses the effect of systematically different dilutions in the B_{flav} events with respect to $B^0 \to \pi^+\pi^-$ events, we fit data alternatively with dilution and tagging efficiencies determined in $B^0 \to \pi^+\pi^-$ Monte Carlo and B_{flav} Monte Carlo. This is a rather crude estimate of the effect since we know that Monte Carlo does not reproduce tagging performances in data;
- we determine background tagging efficiencies (ϵ_{bkg}) from the fit region instead of m_{ES} sideband (Tab.4.12).

Finally, Tab. 4.31 summarizes the systematic errors coming from all sources, and the total systematic error calculated as the quadrature sum of the individual uncertainties. We have also calculated the total systematic error on $N_{\pi\pi}$. We find an uncertainty of ±4.6 events, which is a fractional error of 7%.

Systematic errors on $\mathcal{A}_{K\pi}$, $S_{\pi\pi}$ and $C_{\pi\pi}$ are generally of the order of 0.01 or less. Uncertainties on the knowledge of the ΔE absolute scale are affecting $\mathcal{A}_{K\pi}$ and $C_{\pi\pi}$. Improvements on detector performance study with new Monte Carlo simulation helps in reducing this systematics that is presently covered with a conservative variation of the PDF parameters.

Table 4.30: Systematic errors evaluated from variation of signal and background Δt parameterizations, and from using the background tagging efficiencies determined from background events in the fit region. These errors are symmetrized when calculating the total systematic errors.

Variation	$\mathcal{A}_{K\pi}$	$S_{\pi\pi}$	$C_{\pi\pi}$
Signal Fisher $D^0\pi^-$	-0.003	-0.019	0.007
Dbl Gauss ↔ Bif Gauss $\mathcal{F}$	-0.007	-0.014	0.045
$\mathcal{R}_{\text{sig}}$ Run 1 ↔ Run 2	-0.001	0.053	0.012
$\mathcal{R}_{\text{bkg}}$ Run 1 ↔ Run 2	-0.001	0.047	0.016
$\mathcal{R}_{\text{bkg}}$ params from fit region (Run 1)	0.001	0.006	0.007
$\mathcal{R}_{\text{bkg}}$ params from fit region (Run 2)	-0.000	0.004	-0.001
$\mathcal{R}_{\text{bkg}}$ params from tagged events	-0.001	0.010	0.005
$\mathcal{R}_{\text{bkg}}$ params from untagged events	-0.001	-0.014	-0.005
Average $\mathcal{R}_{\text{bkg}}$ for Run 1 and Run 2	-0.001	0.025	0.004
Signal $\pi\pi$ ↔ B_{flav} MC Tagging	0.000	0.040	0.008
ϵ_{tag}(bkg) from fit region	-0.000	0.002	-0.007

Table 4.31: Summary of systematic errors from all sources. The total systematic error is calculated as the quadrature sum of the individual uncertainties.

	$\mathcal{A}_{K\pi}$		$S_{\pi\pi}$		$C_{\pi\pi}$	
Parameter	+	−	+	−	+	−
m_{ES}	0.003	0.002	0.007	0.005	0.019	0.021
ΔE	0.014	0.013	0.009	0.035	0.096	0.110
$\mathcal{F}$	0.007	0.007	0.024	0.024	0.046	0.046
θ_c	0.004	0.004	0.021	0.022	0.038	0.041
Sig Tagging	0.001	0.001	0.048	0.048	0.034	0.034
Bkg Tagging	0.001	0.001	0.007	0.006	0.009	0.009
Sig Δt	0.001	0.001	0.068	0.069	0.032	0.027
Bkg Δt	0.002	0.002	0.052	0.053	0.020	0.020
τ and Δm_d	0.000	0.000	0.011	0.011	0.007	0.007
Total	0.017	0.016	0.105	0.110	0.126	0.137

4.10 Preliminary Results

In this Chapter a preliminary measurement on time-dependent *CP* violating asymmetry in $B^0 \to \pi^+\pi^-$ decays, and a measurement of the charge asymmetry in $B^0 \to K^+\pi^-$ decays in $30.4\,\mathrm{fb}^{-1}$ have been presented. In this sample we find 65 $\pi^+\pi^-$ and 217 $K^\pm\pi^\mp$ candidates and measure:

$$\begin{aligned} S_{\pi\pi} &= 0.03^{+0.53}_{-0.56} \pm 0.11, \\ C_{\pi\pi} &= -0.25^{+0.45}_{-0.47} \pm 0.14, \\ \mathcal{A}_{K\pi} &= -0.07 \pm 0.08 \pm 0.02, \end{aligned}$$

where the first error is statistical and the second is systematic. The systematic error on $\mathcal{A}_{K\pi}$ is the quadrature sum of the total from Tab. 4.31 and an uncertainty of ± 0.01 from possible charge bias in track reconstruction and particle identification as explained in Chapter 3. We calculate the 90% confidence limit on $\mathcal{A}_{K\pi}$, $[-0.21, 0.07]$, including the statistical and systematic errors and assuming Gaussian errors.

Chapter 5

Interpretation of the results

In this Chapter, *QCD factorization* predictions for Branching Ratios of twobody charmless hadronic B decays are compared with the most recent experimental values. In principle, once validated, this would serve as a theoretical framework to extract a value for $\sin 2\alpha$ from time dependent CP asymmetries and thus put constraints in the (ρ, η) plane to Unitarity Triangle: this issue, however, is strongly debated at the moment, so no conclusion is attempted here. Finally, evolution of this analysis is discussed in prevision of more data being accumulated by B-factories.

5.1 Comparison with theoretical model

In Tab.5.1 we summarize the results of the measurements of Branching Ratios and time-dependent *CP* analysis of charmless hadronic twobody B decays to $h'^{+}h^{-}$ with $h = \pi, K$ presented in this thesis. Branching Ratios results are based on Run 1 dataset ($20.7\,\mathrm{fb}^{-1}$), while *CP* asymmetry results are given for an enlarged dataset ($30\,\mathrm{fb}^{-1}$). We do not extract any new Branching Ratio from the enlarged dataset since tracking efficiency and B counting for the year 2001 data are not available at the moment.

Table 5.1: Summary of signal yield N_S and branching fraction $\mathcal{B}$ results for B decays to $h'^{+}h^{-}$ with $h = \pi, K$. Statistical significance of the signal is also given. In the second part of the table *CP* asymmetry parameters results are given (they are obtained on an enlarged dataset). The first error is statistical and the second is systematic.

Mode	N_S	Stat. Sig. (σ)	$\mathcal{B}\,(10^{-6})$
$\pi^{+}\pi^{-}$	$41 \pm 10 \pm 7$	4.7	$4.1 \pm 1.0 \pm 0.7$
$K^{+}\pi^{-}$	$169 \pm 17^{+14}_{-12}$	15.8	$16.7 \pm 1.6^{+1.4}_{-1.2}$
$K^{+}K^{-}$	$8.2^{+7.8}_{-6.4} \pm 3.5$ (< 24)	1.3	< 2.5

		N_S
$S_{\pi\pi}$	$0.03^{+0.53}_{-0.56} \pm 0.11$	$65.0^{+12.0}_{-11.1}$
$C_{\pi\pi}$	$-0.25^{+0.45}_{-0.47} \pm 0.14$	$65.0^{+12.0}_{-11.1}$
$\mathcal{A}_{K\pi}$	$-0.07 \pm 0.08 \pm 0.02$	$216.7^{+18.4}_{-17.6}$

In addition to $h'^{+}h^{-}$ final states, other charmless twobody B decays Branching Ratios and $\mathcal{A}_{\mathcal{CP}}$ have been measured and published in [1] by the *BABAR* Collaboration. In Tab.5.2 we review those results.

Beneke *et al.* in [35] give theoretical predictions for these Branching Ratios. From

Mode	ε (%)	N_S	S (σ)	$\mathcal{B}(10^{-6})$	$\mathcal{A}$
$\pi^+\pi^0$	32	$37 \pm 14 \pm 6$	3.4	< 9.6 (90% C.L.)	
$K^+\pi^0$	31	$75 \pm 14 \pm 7$	8.0	$10.8^{+2.1}_{-1.9} \pm 1.0$	$0.00 \pm 0.18 \pm 0.04$
$K^0\pi^+$	14	$59^{+11}_{-10} \pm 6$	9.8	$18.2^{+3.3}_{-3.0} \pm 2.0$	$-0.21 \pm 0.18 \pm 0.03$
$\overline{K}^0K^+$	14	$-4.1^{+4.5}_{-3.8} \pm 2.3$	–	< 2.4 (90% C.L.)	
$K^0\pi^0$	10	$17.9^{+6.8}_{-5.8} \pm 1.9$	4.5	$8.2^{+3.1}_{-2.7} \pm 1.2$	

Table 5.2: Summary of results for detection efficiencies (ε), fitted signal yields (N_S), statistical significances (S), measured branching fractions ($\mathcal{B}$), and charge asymmetries for other charmless twobody B decays in Run 1 dataset. The efficiencies include the branching fractions for $K^0 \to K^0_S \to \pi^+\pi^-$ and $\pi^0 \to \gamma\gamma$. Equal branching fractions for $\Upsilon(4S) \to B^0\overline{B}^0$ and B^+B^- are assumed. The 90% confidence level (C.L.) intervals for the charge asymmetries include the systematic uncertainties, which have been added in quadrature with the statistical errors.

Eq.1.102 and Eq.1.103 it is clear how the theoretical prediction is affected by the input values used for the CKM matrix elements (V_{ub},V_{cb}) and for the semileptonic form factors $F_0^{B\to\pi}(0)$. Moreover, penguin amplitudes suffer from uncertainties present in the model itself, generally identified as contributions of order $\frac{\Lambda}{m_b}$ (weak annihilation diagrams, chirally enhanced terms) that in *QCD factorization* should be neglected. These uncertainties are believed to be largely cancelled by taking ratios of Branching Ratios.

In Fig.5.1 (from [35]), Beneke *et al.* show *QCD factorization* predictions for different Ratios as bands of allowed values as a function of the CKM angle γ. If γ is determined from the combination of indirect measurements , known as Unitarity Triangle analysis ($(54.8 \pm 6.2)^o$, Section 1.4), a true theoretical prediction can be made and compared with the experiments (Tab.5.3). For instance, the experimental value for the ratio $\frac{\mathcal{B}(\pi^+\pi^-)}{\mathcal{B}(\pi^\mp K^\pm)}$ seems to be hardly compatible even at the present level of statistics. From Fig.5.1, however, it is clear that predictions are largely affected by the (relatively) poor knowledge of $|\frac{V_{ub}}{V_{cb}}|$. New more precise measurement of $|V_{ub}|$ that can be done with *BABAR* can change the predictions and help in reducing those bands.

channels	B Factory
$B^0 \to \pi^+\pi^-$	$(4.4 \pm 0.9) \cdot 10^{-6}$
$B^+ \to \pi^+\pi^0$	$(5.6 \pm 1.5) \cdot 10^{-6}$
$B^0 \to K^+\pi^-$	$(17.2 \pm 1.5) \cdot 10^{-6}$
$B^+ \to K^+\pi^0$	$(17.2 \pm 2.5) \cdot 10^{-6}$
$B^+ \to K^0\pi^0$	$(10.3 \pm 2.5) \cdot 10^{-6}$

Table 5.3: World average value for twobody charmless Branching Ratio determined and used in [35] as input values.

An alternative interpretation of these results can be given if the information from all the charmless twobody Branching Ratios is combined in a single global fit that produces allowed regions in the $(\bar{\rho}, \bar{\eta})$ plane. If the Standard Model holds, compatibility of these "direct" measurements with the "indirect" Unitarity Triangle analysis would serve as a validation of the *QCD factorization* . In [35] a global fit is performed with a χ^2 minimization, where a scale factor S is extracted to account for the overall uncertainty due to $(F_0^{B\to\pi}(0)|V_{cb}|)^2$,

$$\chi^2 = \sum_i^m \frac{(E_i - ST_i)^2}{\sigma_i^2} \tag{5.1}$$

where E_i is the i^{th} measured Branching Ratio (among the m published), σ_i is its experimental error, and T_i is the theoretical prediction. The contours of constant $\Delta\chi^2 = \chi^2 - \chi^2_{min}$ in Fig.5.2 are obtained by *scanning* ([25],[26]) all the theory parameters in their allowed ranges. For each set of theory parameters a χ^2 minimization is performed. The absolute minimum of χ^2 (among all the χ^2 minimizations) corresponds to a *best-fit* value in the $(\bar{\rho}, \bar{\eta})$ plane (shown in Fig.5.2 as a dark dot). At this level, there is compatibility between the *QCD factorization* analysis of charmless twobody B decays and the Unitarity Triangle analysis. However, the best fit with Branching Ratios prefers a larger value of γ, about 90^o.

Consensus on the application of *QCD factorization* to charmless twobody B decays is not universal. Other groups have discussed in recent papers possible flaws of the *QCD factorization* approach ([4],[54]). Ciuchini *et al.* stress the fact that leading $\frac{\Lambda}{m_b}$ terms cannot be neglected and are therefore phenomenologically relevant. They, in fact, propose to include further corrections to the *QCD factorization* amplitudes to account for them.

In particular Ciuchini *et al.* claim that the disagreement between data and pure *QCD factorization* predictions is more general and that a better agreement is obtained when suitable complex parameters are added to the amplitudes. These extra parameters account for *charming* and *GIM penguins* according to the definition given in [55]. They are extracted directly from the experimental Branching Ratios values *and* from the value of γ determined from the Unitarity Triangle analysis. The error Ciuchini *et al.* obtain from the fit for the absolute values and the phases ϕ of those parameters is rather large (30 % - 50 %) and they do not claim to be able to control all the $\frac{\Lambda}{m_b}$ effects at the moment. So, while they do not attempt to give a reliable prediction for Branching Ratios, they observe that the phases of those additional parameters are rather large (about 180^o) and

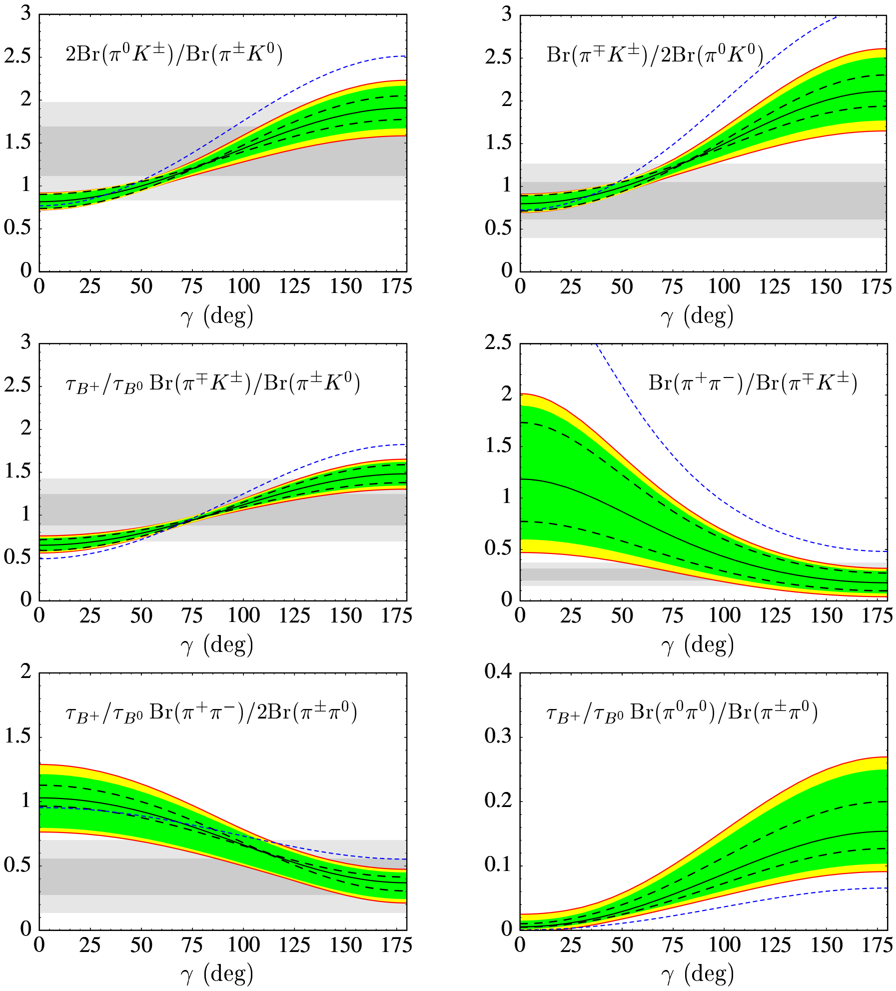

Figure 5.1: Ratios of Branching Ratios as a function of γ. The central values of *QCD factorization* ([35]) predictions are show as a solid line. The dark band represents the uncertainty due to the variation of input paramenters (theoretical *and* $|\frac{V_{ub}}{V_{cb}}|$) while the light outer band include further theoretical uncertainties (weak annihilation contributions). The long-dashed lines indicates the sensitivity to $|\frac{V_{ub}}{V_{cb}}|$. The horizontal bands show the 1σ and 2σ error bands for the averaged experimental results.

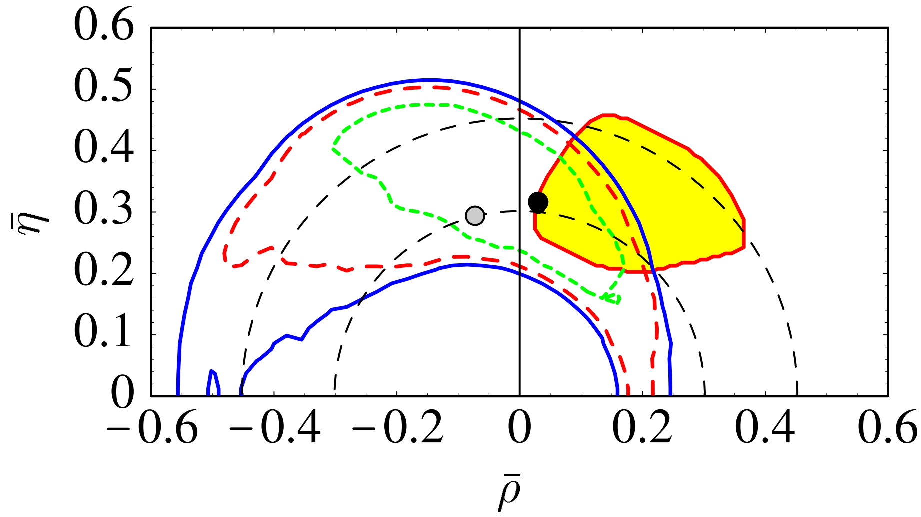

Figure 5.2: 95% (solid), 90 % (dashed) and 68% (short-dashed) confidence level contours in the $(\bar{\rho}, \bar{\eta})$ plane obtained from a global fit to the charmless twobody Branching Ratios, using the method detailed in [25]. The dark dot represents the overall best fit, while the shaded region is the allowed region from Unitarity Triangle analysis from [25]. The light dot indicates the best fit for the central values of the theory parameters used in [35].

$\lvert\mathcal{A}_{\mathcal{CP}}\rvert$	Charming + GIM	$\lvert\mathcal{A}_{\mathcal{CP}}\rvert$	Charming + GIM
$K^0\pi^0$	0.05 ± 0.03	$K^+\pi^0$	0.16 ± 0.08
$K^0\pi^+$	0.02 ± 0.02	$K^+\pi^-$	0.15 ± 0.07
$\pi^+\pi^-$	0.44 ± 0.21	$\pi^0\pi^0$	0.61 ± 0.29

Table 5.4: Absolute values of the CP asymmetries for $B \to K\pi$ and $B \to \pi\pi$ decays (from [54]).

could therefore induce a rather large direct CP asymmetry $\mathcal{A}_{\mathcal{CP}}$. In Tab.5.4 (from [54]) some predictions for the absolute values of $\mathcal{A}_{\mathcal{CP}}$ are given.

While those predictions suffer from very large uncertainties, they open new perspectives. Within pure factorization, in fact, all the direct asymmetries would be so small to be basically unobservable, since any strong phase is a perturbative effect of order α_s ([35]). No discrepancy is found between those predictions and experimental results so far. A non-zero value for $C_{\pi\pi}$ (that is a direct *CP* violation effect in $\pi^+\pi^-$ decays) seems to be suggested by data. But given the limited statistics available, no definitive conclusion can be drawn. The measured $\mathcal{A}_{\mathcal{CP}}$ value for $K^\pm\pi^\mp$, however, does not suggest any direct *CP* violation effect.

The theoretical interpretation of experimental data of charmless twobody decays is still controversial. So we must remember that at this stage the extraction of sin2α is a *model dependent* procedure. It is therefore relevant to identify how the model assumptions enter this procedure and how important they are.

5.2 Limits on CKM α angle.

J.Charles clarifies in [33] how the theoretical uncertainties on the knowledge of the strong interaction effects can affect sin2α extraction. As already explained in Section 1.5 (Eq.1.94), just from the weak phase structure of the Standard Model, we can rewrite the $B^0 \to \pi^+\pi^-$ physical amplitude as

$$\begin{aligned} A_{\pi\pi} &= V_{ud}V_{ub}^* M^{(u)} + V_{td}V_{tb}^* M^{(t)} \\ &\equiv e^{+i\gamma} T_{\pi^+\pi^-} + e^{-i\beta} P_{\pi^+\pi^-} \end{aligned} \tag{5.2}$$

This definition is unambigous and general since any contribution proportional to $V_{cd}V_{cb}^*$ (for instance *charming penguins*,[55]) can be rewritten in terms of the two other combinations, $V_{ud}V_{ub}^*$ and $V_{td}V_{tb}^*$, by CKM unitarity ($V_{cd}V_{cb}^* = -V_{ud}V_{ub}^* - V_{td}V_{tb}^*$).

The CP-conjugate channels are obtained by reversing the sign of the weak phases:

$$\bar{A}_{\pi\pi} = e^{-i\gamma} T_{\pi\pi} + e^{+i\beta} P_{\pi\pi} \, . \tag{5.3}$$

and from Eq.5.2 and Eq.5.3 and assuming $\alpha = \pi - \beta - \gamma$,

$$\begin{aligned} -(2i\text{sin}\alpha)P &= e^{-i\gamma} A_{\pi\pi} - e^{i\gamma} \bar{A}_{\pi\pi} \, , && (5.4) \\ (2i\text{sin}\alpha)T &= e^{i\beta} A_{\pi\pi} - e^{-i\beta} \bar{A}_{\pi\pi} \, , && (5.5) \end{aligned}$$

Calculating the ratio $|\frac{P}{T}|^2$ from Eq.5.4 and using the definitions

$$\begin{aligned} C_{\pi\pi} &= \frac{|A_{\pi\pi}|^2 - |\bar{A}_{\pi\pi}|^2}{|A_{\pi\pi}|^2 + |\bar{A}_{\pi\pi}|^2} && (5.6) \\ 2\alpha_{eff} &= Arg(\frac{q}{p}\bar{A}_{\pi\pi}A_{\pi\pi}^*) \, , && (5.7) \end{aligned}$$

we obtain the equation:

$$\cos(2\alpha - 2\alpha_{\text{eff}}) = \frac{1}{\sqrt{1 - C_{\pi\pi}^2}} \left[1 - \left(1 - \sqrt{1 - C_{\pi\pi}^2} \cos 2\alpha_{\text{eff}} \right) \left| \frac{P}{T} \right|^2 \right] \, . \tag{5.8}$$

Thus Eq.5.8 defines 2α as a four-valued function of $|\frac{P}{T}|$: indeed, $2\alpha_{\text{eff}}$ is known up to a twofold discrete ambiguity ($2\alpha - 2\alpha_{\text{eff}} \to -(2\alpha - 2\alpha_{\text{eff}})$), while Eq.5.8 also contains a twofold discrete ambiguity as long as 2α is concerned, because of the cosine function ($2\alpha_{\text{eff}} \to \pi - 2\alpha_{\text{eff}}$).

The solutions of this equation can be represented in a $(|\frac{P}{T}|, 2\alpha)$ plane (See Fig.5.2). There are in general two branches corresponding to the $\cos 2\alpha_{eff} < 0$ solution and to $\cos 2\alpha_{eff} > 0$ solution. The range of variation of $|\frac{P}{T}|$ is limited by the requirement that $|\cos 2\alpha - 2\alpha_{eff}| < 1$. The ambiguity can be solved by

$$\tan\alpha = \frac{1-\sqrt{1-C_{\pi\pi}^2}\cos 2\alpha_{eff}}{\frac{C_{\pi\pi}}{\tan\delta}+\sqrt{1-C_{\pi\pi}^2}\sin 2\alpha_{eff}} \tag{5.9}$$

where δ is the strong phase of $\frac{P}{T}$. Therefore if $|\frac{P}{T}|$ and δ are known from a given model with sufficient precision, only one value of 2α satisfies Eq.5.8 and Eq.5.9. It is interesting to notice that by eliminating α between Eq.5.8 and Eq.5.9, δ can be obtained as a function of $|\frac{P}{T}|$. Any estimation of $(\frac{P}{T},\delta)$ from a given model must satisfy this relationship.

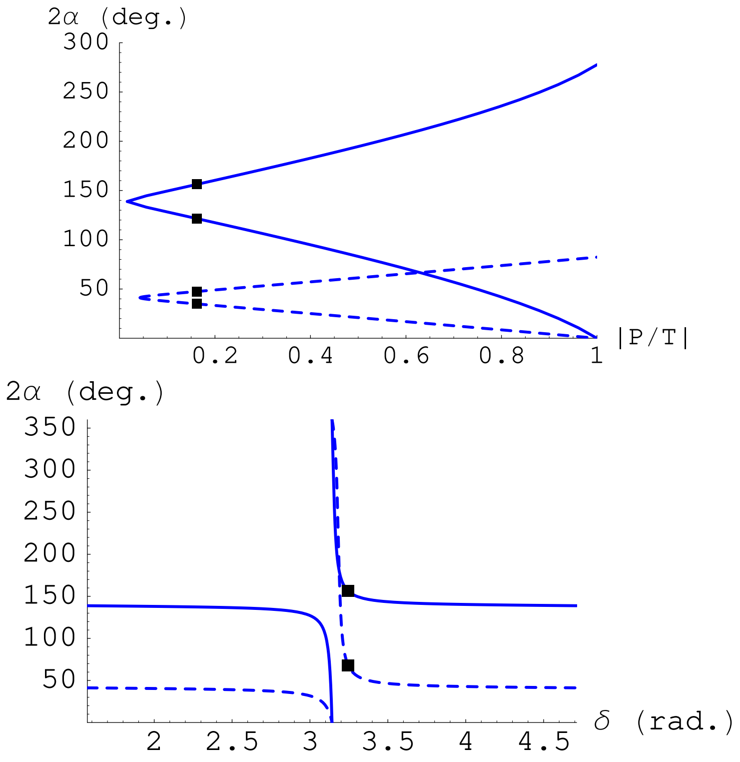

Figure 5.3: Upper plot ([57]): CKM angle 2α (degree) as a function of $|\frac{P}{T}|$ obtained from Eq.5.8 with $\sin 2\alpha_{eff} = 0.66$ and $C_{\pi\pi} = 0.03$. Lower plot: CKM angle 2α (degree) as a function of δ (radiants) from Eq.5.9. Dots corresponds to a possible theoretical estimate. In each plot upper curves corresponds to $\cos 2\alpha_{eff} < 0$ solution and the lower curves to $\cos 2\alpha_{eff} > 0$. The range of variation of $|\frac{P}{T}|$ is limited by the requirement that $|\cos 2\alpha - 2\alpha_{eff}| < 1$.

The relevance of this approach is that all the experimental information coming from $S_{\pi\pi}$ and $C_{\pi\pi}$ is contained in the curves themselves: given a theoretical prediction with its uncertainties it is possible to determine 2α. It is worth noting that $S_{\pi\pi}$ can be re-expressed as

$$S_{\pi\pi} = \sqrt{1 - C_{\pi\pi}^2}\sin 2\alpha_{eff} \tag{5.10}$$

Reparemetrizing the PDF Eq.4.4 in this way, we get

$$\begin{aligned} C_{\pi\pi} &= -0.25 \pm 0.46 \\ \sin 2\alpha_{eff} &= 0.03 \pm 0.56 \end{aligned} \tag{5.11}$$

where the error is statistical only. The correlation factor between these two fitted parameters is 17%. These values are the central values in Fig.5.5. For this particular experiment, the two branches are well separated in $|\frac{P}{T}|$, and values of $|\frac{P}{T}| < 1$ can accidentaly lift the fourfold ambiguity. Given the present statistics, solving Eq.5.8 does not give any interesting insight to the value of $\sin 2\alpha$, since the derived allowed range for valid 2α solutions is almost trivial.

On the other hand, *QCD factorization* is in principle able to connect a $S_{\pi\pi}$ measurement to 2α. Again we must notice that *QCD factorization* generally predicts small values for the strong phases. In [35] strong phases estimates are usually around 10^o. This means that the strong phase of $\frac{P}{T}$ is almost negligible in factorization. This leads, again, to the prediction that direct CP asymmetries ($C_{\pi\pi}$) should be about zero. In this sense measuring a null $C_{\pi\pi}$ would be another validation of *QCD factorization* . Given the measured value of $S_{\pi\pi}$ and the theoretical value for $|\frac{P}{T}|$ it is therefore possible to put a constraint in the $(\bar{\rho}, \bar{\eta})$ plane equivalent to the measurement of 2α. This is shown in Fig.5.2 (obtained with [25], [56]) where confidence level regions are displayed. When the world average of $\sin 2\beta$ are included the fit, narrower allowed regions are obtained as shown in Fig.5.2 too.

5.3 Perspectives

In this thesis I have shown a measurement of charmless twobody B decays Braching Ratios with the *BABAR* experiment. Moreover, a project of measuring CP asymmetries in these channels has been successfully initiated.

Branching Ratios and direct CP asymmetries have been recently published in [1]. A time dependent CP analysis has been presented this summer at the XX International Symposium on Lepton and Photon Interactions at High Energies [2].

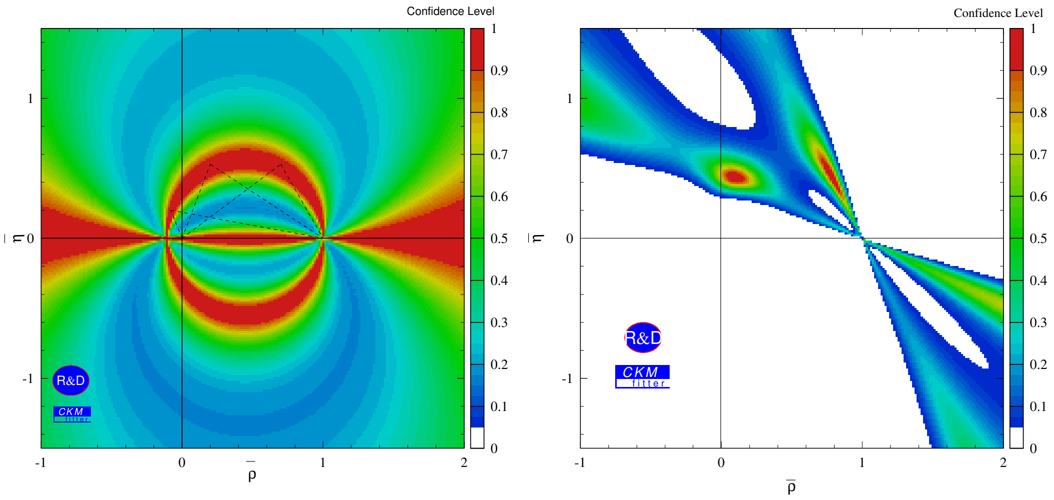

Figure 5.4: Left: constraints in the $(\bar{\rho}, \bar{\eta})$ plane from the parameter $S_{\pi\pi}$, measured by *BABAR* , and using the calculation in [35] of the $\frac{P}{T}$ ratio. Theoretical errors as quoted in [35] have been neglected. Three examples of possible CKM triangles are shown. Right: the world average of sin2β has been additionally used in the fit.

The comparison between experiment and theory is still controversial, since it is difficult to understand and describe strong interaction effects in a non-perturbative regime. However, theoretical efforts are still actively going on and it is reasonable to expect new useful insights to those topics in the next years.

BABAR is going to collect more data in the coming years, with a project to reach 0.5 ab^{-1} by 2005 thanks to luminosity upgrades of PEP-II well beyond its design.

In Fig.5.5 we show the curves representing the present measurements of $C_{\pi\pi}$ and $S_{\pi\pi}$, given the functional relation between the theoretical values for $\frac{P}{T}$ and 2α. Scaling the statistical error to 0.5 ab^{-1} collected luminosity, the curves corresponding to $\pm 1\sigma$ variation of $C_{\pi\pi}$ and $S_{\pi\pi}$ are shown. A reasonably controlled theoretical prediction for $|\frac{P}{T}|$ and δ can therefore limitedly affect the extraction of 2α.

On the other hand, at 0.5 ab^{-1}, measurement of $B^0 \to \pi^0\pi^0$ Branching Ratios and direct CP asymmetry will probably be available, allowing the completion of the isospin analysis that, in fact, represents an experimental estimate of $(2\alpha_{eff} - 2\alpha)$ deviation. In conclusion it is realistic to assume that *BABAR* will measure $C_{\pi\pi}$ and $S_{\pi\pi}$ with a statistical error of about 0.15 by 2005. This will probably set an important milestone in our understanding of *CP* violation in the Standard Model and of the physics of the flavor sector.

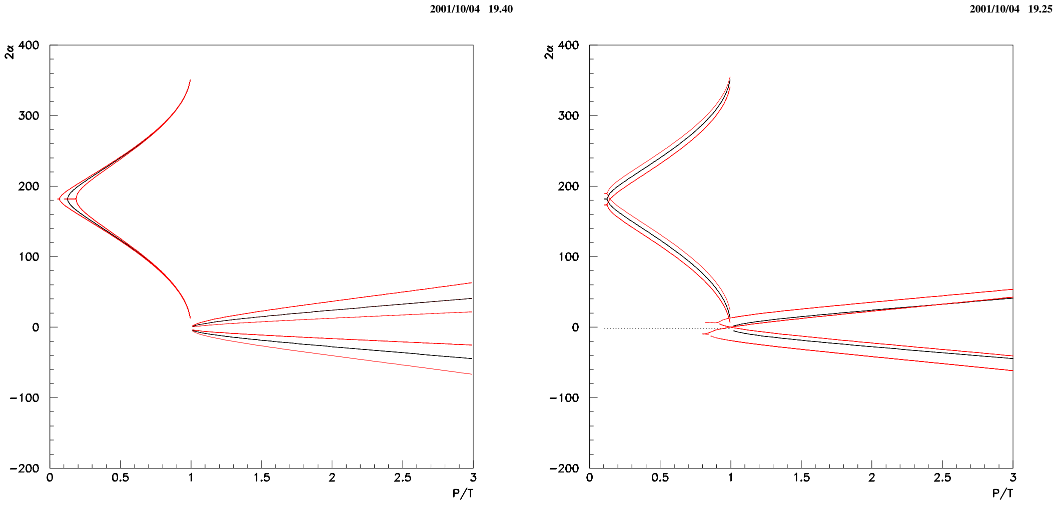

Figure 5.5: CKM angle 2α (degree) as a function of $|\frac{P}{T}|$ obtained from Eq.5.8 for the measured $C_{\pi\pi}$ and $S_{\pi\pi}$ values obtained in this analysis. The upper curves corresponds to $\cos 2\alpha_{eff} < 0$ solution and the lower curves to $\cos 2\alpha_{eff} > 0$. The range of variation of $|\frac{P}{T}|$ is limited by the requirement that $|\cos 2\alpha - 2\alpha_{eff}| < 1$. Dark curves represents solutions corresponding to central values for $C_{\pi\pi}$ and $S_{\pi\pi}$. Left plot shows solutions (as lighter lines) corresponding to variation of $\pm 1\sigma$ of $C_{\pi\pi}$; right plot shows solutions (as lighter lines) corresponding to variation of $\pm 1\sigma$ of $S_{\pi\pi}$. σ used in these plots are simply the statistical σ from the fit of Chapter 4 scaled to an integrated luminosity of $500\,\mathrm{fb}^{-1}$ (assuming it scales as $\frac{1}{\sqrt{N_S}}$)

Appendix A

Δz vertexing algorithm

The tagging B vertex reconstruction is difficult because secondary tracks from short and long lived particles will bias the vertex position. Algorithms try to deal with these problems and minimize their impact using slightly different approaches. Reconstructed V^0 candidates and veto from gamma conversions are used in an attempt to minimize tails and outliers in the resolution.

The general strategy to find the tagging B vertex is the following:

- fully reconstruct the signal B (B_{CP});
- start with a list of all charged tracks in the event, except those from the B_{CP} decay;
- remove charged tracks from reconstructed V^0's (K^0_S and Λ), and add the corresponding composite particle. Useful V^0's will be those which decay close to the IP and have still SVT information. The remaining ones will be removed to reduce the bias in the vertex position and outliers in the resolution.
- fit the tracks from the tagging side to a common vertex.
- if the fit is bad (i.e. $\chi^2 > \chi^2_{cut}$), remove the candidate with the largest contribution to χ^2 and then refit (previous step). Stopping criteria are optimized.

The algorithm used by *BABAR* (`VtxTagBtaSelFit`) tries to make use of all the position and kinematic constraints available in the $\Upsilon(4S) \to B\overline{B}$ decay. The $B\overline{B}$ pair creation point is reconstructed by intersecting the reconstructed signal B_{CP} with the beam spot elipsoid. The line of flight of the $B_{\,TAG}$ is given by the (reverse) momentum vector of the reconstructed B_{CP} and its vertex. The interaction point is estimated from the intersection of this line with the beam spot position in y. Due to the very small size of the beam-spot in y, the information from the beam spot can be reduced to just the y coordinate (Fig. A.1).

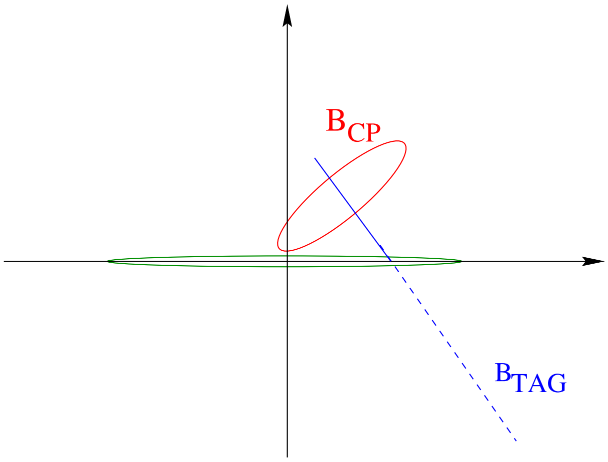

Figure A.1: Geometry of $\Upsilon(4S) \to B\overline{B}$ decay in transverse plane. The line of flight of the $B_{\ TAG}$ is given by the (reverse) momentum vector of the reconstructed B_{CP} and its vertex. The interaction point is the intersection of this line with the beam spot position in y.

For the same reason, the decay path $L_z^{CP} = z_{CP} - z_{\Upsilon(4S)}$ of the B_{CP} can be extracted ensuring that the direction of the line connecting the $\Upsilon(4S)$ and the vertex of the B_{CP} is given by the fitted momentum of the reconstructed $B_{\ CP}$. In the limit where $\sigma_y(\Upsilon(4S)) \approx 0$,

$$L_z^{CP} \approx \frac{y_{CP} - y_{\Upsilon}}{p_{y,CP}/p_{z,CP}} \tag{A.1}$$

The dominant factor in the precision on L_z^{CP} is the accuracy on y_{CP}: the error on L_z^{CP} is, however, about one order of magnitude larger than the error on y_{CP}. Since typically $\sigma(y_{CP}) \approx 45\ \mu$m, the final precision on L_z^{CP} is very poor.

However, from momentum conservation, the momentum of the tag B meson, $B_{\ TAG}$, is known:

$$\vec{p}_{TAG} = \vec{p}_{\Upsilon(4S)} - \vec{p}_{CP} \tag{A.2}$$

From this momentum and the $B\overline{B}$ pair creation point we can form a “pseudo-track” which can be used to fit a common vertex as any other tagging side candidate. Requiring the compatibility of the tracks which make the tagging side with this pseudo-track helps in getting rid of the tracks that do not come directly from the B candidate, hence reducing the "charm" bias[1]. From the knowledge of $\vec{p}_{TAG}$ from Eq.A.2 and the $B_{\ TAG}$ vertex position from the vertex fit, one can get an estimate of the decay path for the tagging side, L_z^{TAG}. In the $\sigma_y(\Upsilon(4S)) \approx 0$ limit,

$$L_z^{TAG} \approx \frac{y_{TAG} - y_{\Upsilon}}{p_{y,TAG}/p_{z,TAG}} \tag{A.3}$$

Unfortunately, as for the case of the B_{CP} case, the precision on L_z^{TAG} is extremelly poor.

Owing to the pinched geometry, L_z^{CP} and L_z^{TAG} have a positive correlation close to 1, therefore when we compute the difference $\Delta z{=}L_z^{CP} - L_z^{TAG}$ the effect of the correlation is basically removed, and this observable becomes much more precise than the separate decay lengths.

Δz resolution and Δz scale are basically rather insentivite to resolution and scale in B_{CP}, and only the reconstructed vertex of the tagging side tracks and the beam spot determine the improvement in error on the reconstructed Δz. This mechanism allows to improve Δz track selection and resolution, without spoiling the very basic assumption in all the analyses that the resolution function is independent of the specific B_{CP} mode.

The convergence criteria in the minimization process requires a change in χ^2 between two successive iterations less than 0.001, with a maximum of 10 iterations. The iterative procedure for track selection removes the candidate with the largest contribution to the total χ^2. The procedure is iterated until there are no tracks contributing more than 6 units to the χ^2. If any track contributes more than 6 to the vertex χ^2, the largest contributor is dropped from the fit and the fit is redone: this would reduce contributions from charm decay, which could bias the vertex estimation.

Fig. A.2 shows the distribution of the per-event error $\sigma_{\Delta z}$ as well as the mean and width of the Δz residual distribution as a function of $\sigma_{\Delta z}$ for simulated B^+B^- events from the charged B signal Monte Carlo. The same qualitative behaviour is observed using fully reconstructed $B^{\pm}$ decays to charmonium final states and $B^0\overline{B}^0$ events where one of the B mesons is fully reconstructed in a decay to open charm or charmonium. Events with high $\sigma_{\Delta z}$ tend to have high Δz residuals. A resolution model in which the width of the Δt residual distribution is proportional to $\sigma_{\Delta t}$ is therefore assumed. The last plot in Fig. A.2 shows the existence of correlations between the bias on Δz and $\sigma_{\Delta z}$.

---

[1] This kind of constraint is also referred to as *beam constraint* In absence of the beam constraint, the B's can be required to be consistent with the beam-spot within errors which take into account the lifetime of the B mesons themselves. A *beam spot* constraint is said to be applied in this case.

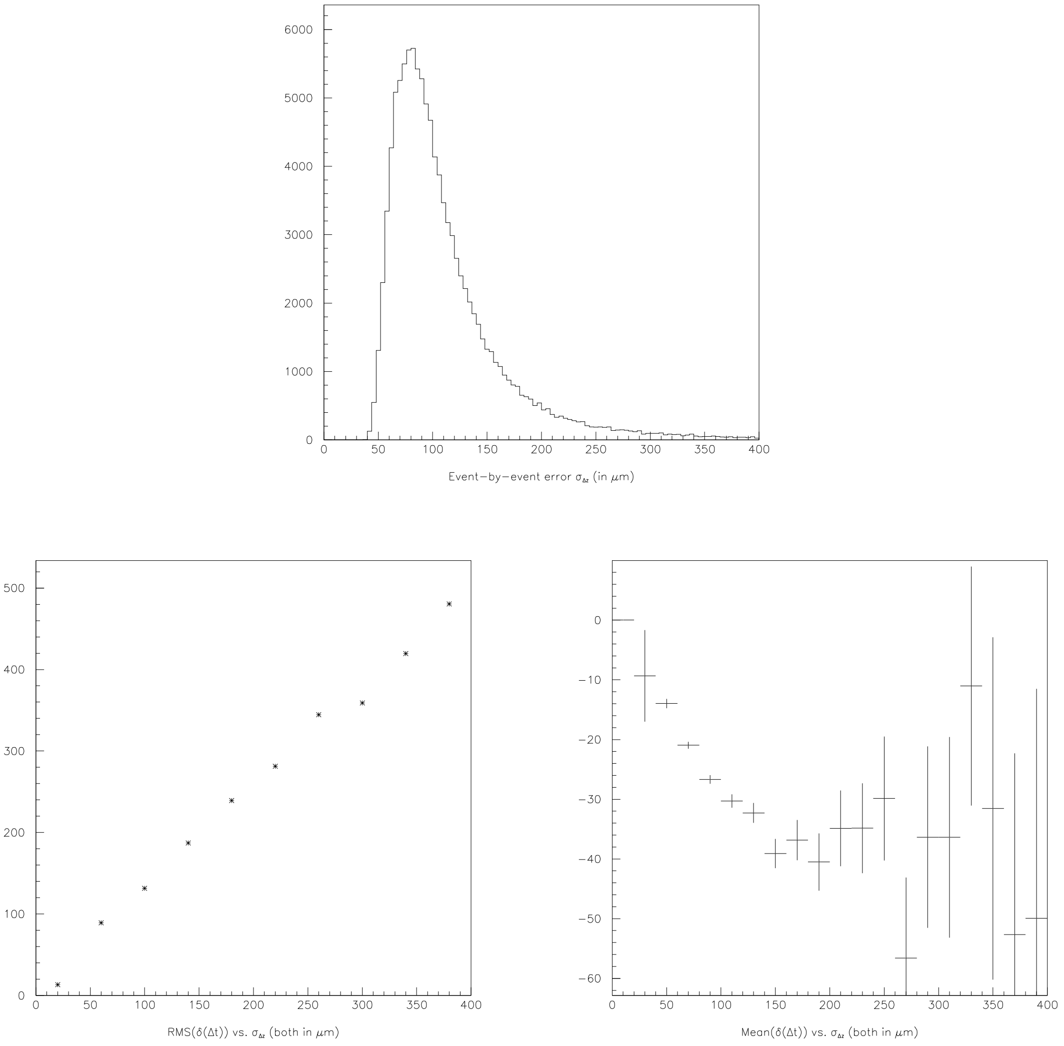

Figure A.2: **Top plot**: distribution of per-event error $\sigma_{\Delta z}$. **Bottom left**: Width (RMS) of the Δz residual (reconstructed - truth) distribution in bins of $\sigma_{\Delta z}$. **Bottom right**: Mean of the Δz residual residual distribution in bins of $\sigma_{\Delta z}$. Approximately one million generated events of the charged BReco signal Monte Carlo cocktail have been used to make these plots.

A possible reason for this effect is the following. When `VtxTagBtaSelFit` reconstructs the tagging side vertex, it tries to select tracks that come from a common vertex. A beam spot constraint [52] favours, on average, convergence on the vertex of the B rather than the vertex of a long-lived particle produced in the B decay. In most cases, the tracking resolution is not good enough to separate the two or more vertices of the B decay products, and the list of selected tracks used to fit the opposite vertex contains both primary tracks that originate directly from the decay vertex of the B_{tag}, and secondary tracks that originate from the decay vertex of a long-lived particle produced in the decay of the B_{tag}. If there is one long-lived particle (for example a D meson) among the decay products of the B_{tag}, we have two determinations of the B_{tag} vertex. The first one, using the primary tracks, is unbiased, and the second one, using the secondary tracks, is biased in the forward z direction. The result of the vertex fit is the weighted mean of the two determinations, where the tracking errors on primary and secondary tracks determine the weight of the primary and secondary vertex, respectively. The bias on the z position of the fitted vertex depends on the separation in z of the two vertices. For a given species of long-lived particle, this separation depends on the angle θ (see Fig. A.3) of the flight direction of the long-lived particle with respect to the z axis. As illustrated in Fig. A.3 and discussed in the captio, the weight of the secondary tracks also depends on the angle θ. This is a source of correlation between the bias on Δz and the per-event error $\sigma_{\Delta z}$.

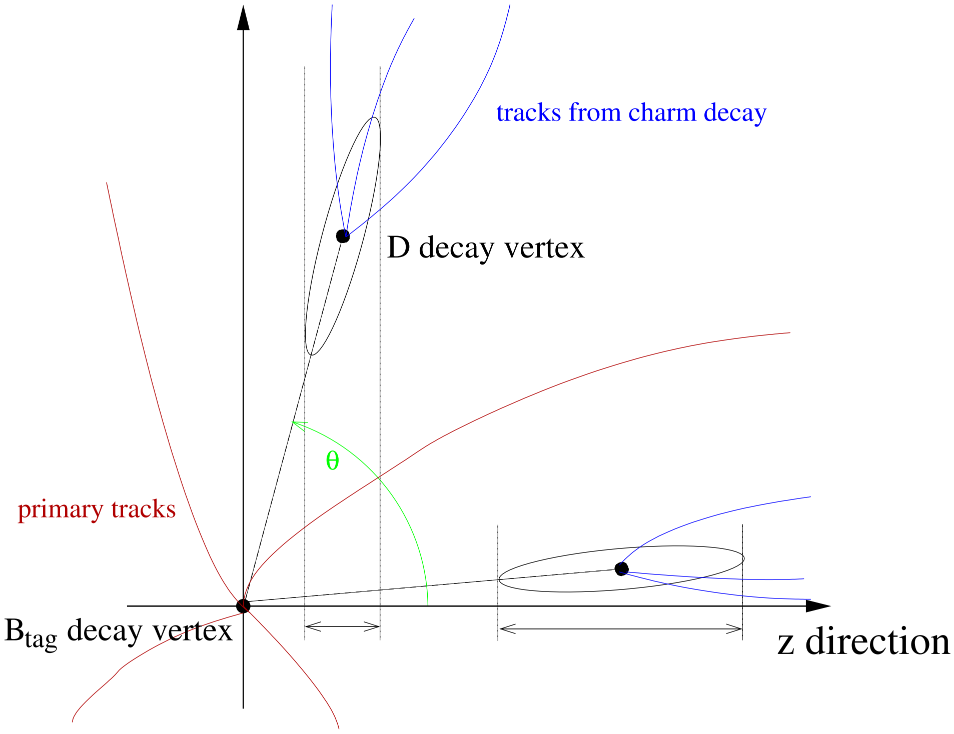

Figure A.3: Illustration of the effect that results in the leading contribution to the correlations between the per-event error $\sigma_{\Delta z}$ and the bias on Δz. The figure shows the decay vertex of a tagging B (B_{tag}) in the rest frame of the detector. The primary tracks that come directly from the B_{tag} decay vertex do not have a preferred direction in the centre-of-mass frame, and are slightly boosted in the forward direction in the detector frame. The figure also contains a D meson that originates from the B_{tag} vertex and decays after having flown in the forward direction. The secondary tracks from the D decay vertex are distributed uniformly in a cone around the D flight direction. The ellipse around the D decay vertex illustrates the error ellipse on the decay vertex that can be reconstructed from the secondary tracks, provided that these tracks have been reconstructed and identified as secondary tracks. The figure shows two possible flight directions of the D: in one case, the D travels essentially in the forward direction, and in the other case it travels essentially in the transverse plane. In the former case, the flight length in z tends to be larger than in the latter case. If the error ellipse has the same size in both cases, then its projection on the z axis is larger for the D meson that travels in the forward direction. The figure is not drawn to scale.

Appendix B

PDF parameters systematics

In this Appendix we gather all the evaluation of the absolute variations in $\mathcal{A}_{K\pi}$, $S_{\pi\pi}$, and $C_{\pi\pi}$ arising from uncertainties in various parameters, determined by fluctuating each parameter up and down by 1σ. Most of the entries of these tables contain values smaller than 0.01. One of the most important systematics on $C_{\pi\pi}$ is the effect of changing $\mu_{\Delta E}$. This effect is still under investigation.

Table B.1: Systematic errors due to uncertainties in the signal m_{ES}, ΔE, and θ_c parameterizations.

	$\mathcal{A}_{K\pi}$		$S_{\pi\pi}$		$C_{\pi\pi}$	
Parameter	$+\sigma$	$-\sigma$	$+\sigma$	$-\sigma$	$+\sigma$	$-\sigma$
μm_{ES}	-0.00065	0.00076	0.00275	-0.00246	-0.01209	0.01171
σm_{ES}	0.00248	-0.00214	-0.00443	0.00679	0.01341	-0.01778
$\mu_{\Delta E}$	-0.01295	0.01343	-0.01100	0.00291	-0.10899	0.09543
$\sigma_{\Delta E}$	-0.00368	0.00481	-0.03284	0.00884	-0.01309	0.01306
θ_c offsets (Run 1)	-0.00191	0.00211	-0.01578	0.01367	-0.03438	0.03273
θ_c offsets (Run 2)	-0.00223	0.00214	0.00484	-0.00602	-0.00665	0.00667
σ_{θ_c} (Run 1)	0.00247	-0.00266	-0.00285	0.00417	0.01593	-0.02030
σ_{θ_c} (Run 2)	-0.00057	0.00024	-0.01333	0.01436	0.00620	-0.00517

Table B.2: Systematic errors due to signal tagging efficiencies.

	$\mathcal{A}_{K\pi}$		$S_{\pi\pi}$		$C_{\pi\pi}$	
Parameter	$+\sigma$	$-\sigma$	$+\sigma$	$-\sigma$	$+\sigma$	$-\sigma$
Lepton	-0.00023	0.00025	0.00033	-0.00026	-0.00160	0.00169
Kaon	-0.00028	0.00029	-0.00068	0.00066	0.00082	-0.00079
NT1	0.00002	-0.00001	-0.00084	0.00084	-0.00040	0.00042
NT2	-0.00016	0.00017	0.00001	-0.00010	-0.00036	0.00033

Table B.3: Systematic errors due to uncertainties on background tagging efficiencies.

	$\mathcal{A}_{K\pi}$		$S_{\pi\pi}$		$C_{\pi\pi}$	
Parameter	$+\sigma$	$-\sigma$	$+\sigma$	$-\sigma$	$+\sigma$	$-\sigma$
Run 1						
Lepton $(\pi\pi)$	-0.00002	0.00001	-0.00428	0.00464	-0.00309	0.00381
Lepton $(K\pi)$	-0.00043	0.00045	0.00060	-0.00090	-0.00393	0.00470
Lepton (KK)	0.00003	-0.00003	-0.00006	0.00002	-0.00028	0.00024
Kaon $(\pi\pi)$	-0.00003	0.00002	-0.00078	0.00086	-0.00022	0.00025
Kaon $(K\pi)$	-0.00043	0.00042	0.00004	0.00005	-0.00004	0.00008
Kaon (KK)	-0.00011	0.00010	0.00001	0.00008	0.00002	0.00003
NT1 $(\pi\pi)$	0.00005	-0.00006	-0.00062	0.00069	0.00018	-0.00014
NT1 $(K\pi)$	0.00020	-0.00024	0.00013	-0.00006	-0.00023	0.00029
NT1 (KK)	-0.00002	0.00001	0.00004	0.00003	0.00004	0.00000
NT2 $(\pi\pi)$	0.00001	-0.00002	-0.00023	0.00032	-0.00044	0.00052
NT2 $(K\pi)$	-0.00009	0.00009	0.00002	0.00007	0.00000	0.00005
NT2 (KK)	-0.00004	0.00004	0.00000	0.00003	0.00002	0.00001
Run 2						
Lepton $(\pi\pi)$	-0.00010	0.00009	0.00385	-0.00380	-0.00042	0.00046
Lepton $(K\pi)$	-0.00052	0.00054	0.00042	-0.00036	-0.00036	0.00041
Lepton (KK)	0.00001	-0.00003	-0.00005	0.00001	-0.00002	0.00000
Kaon $(\pi\pi)$	0.00003	-0.00004	-0.00016	0.00025	0.00093	-0.00084
Kaon $(K\pi)$	0.00005	-0.00005	0.00002	0.00003	0.00002	0.00001
Kaon (KK)	0.00005	-0.00006	0.00002	0.00003	0.00003	-0.00001
NT1 $(\pi\pi)$	-0.00008	0.00006	-0.00027	0.00028	-0.00052	0.00047
NT1 $(K\pi)$	-0.00011	0.00011	-0.00008	0.00017	-0.00001	0.00006
NT1 (KK)	0.00000	-0.00001	0.00002	0.00003	0.00001	0.00002
NT2 $(\pi\pi)$	0.00001	-0.00001	0.00028	-0.00025	0.00016	-0.00014
NT2 $(K\pi)$	-0.00005	0.00005	0.00005	0.00002	0.00013	-0.00010
NT2 (KK)	-0.00001	0.00001	0.00000	0.00001	0.00001	0.00000

Table B.4: Systematic errors due to uncertainties on tagging dilution and dilution differences.

	$\mathcal{A}_{K\pi}$		$S_{\pi\pi}$		$C_{\pi\pi}$	
Parameter	$+\sigma$	$-\sigma$	$+\sigma$	$-\sigma$	$+\sigma$	$-\sigma$
Lepton $\langle D\rangle$	0.00050	−0.00042	0.01837	−0.01885	0.00043	−0.00167
Lepton ΔD	0.00062	−0.00057	−0.00366	0.00445	−0.01653	0.01621
Kaon $\langle D\rangle$	−0.00014	0.00016	−0.01417	0.01513	−0.00088	0.00058
Kaon ΔD	−0.00010	0.00010	0.00308	−0.00294	−0.01633	0.01637
NT1 $\langle D\rangle$	0.00007	−0.00005	−0.00572	0.00566	−0.01005	0.01039
NT1 ΔD	0.00006	−0.00004	0.00426	−0.00444	−0.01087	0.01073
NT2 $\langle D\rangle$	0.00062	−0.00057	−0.00366	0.00445	−0.01653	0.01621
NT2 ΔD	0.00046	−0.00045	0.00028	−0.00034	−0.00730	0.00720

Table B.5: Systematic errors due to uncertainties on the signal Δt parameterization.

	$\mathcal{A}_{K\pi}$		$S_{\pi\pi}$		$C_{\pi\pi}$	
Parameter	$+\sigma$	$-\sigma$	$+\sigma$	$-\sigma$	$+\sigma$	$-\sigma$
Run 1						
f Outlier	0.00020	−0.00023	−0.00101	0.00091	−0.00322	0.00316
f Tail	−0.00004	0.00005	−0.00312	0.00319	0.00045	−0.00044
μ Kaon	0.00002	−0.00004	0.01156	−0.01155	−0.00668	0.00632
μ Lepton	0.00004	−0.00005	−0.00338	0.00330	−0.00226	0.00225
μ NoTag	0.00006	−0.00006	0.00011	−0.00004	0.00013	−0.00010
μ NT1	−0.00005	0.00007	0.00005	−0.00075	−0.00420	0.00435
μ NT2	0.00017	−0.00016	0.00415	−0.00403	0.00075	−0.00096
μ Tail	0.00009	0.00003	−0.00004	0.00079	0.00071	−0.00087
σ Core	0.00036	−0.00036	0.00152	−0.00175	−0.00491	0.00412
σ Tail	0.00000	0.00000	0.00000	0.00000	0.00000	0.00000
Run 2						
f Outlier	−0.00005	0.00003	0.00079	−0.00067	0.00124	−0.00116
f Tail	−0.00029	−0.00028	0.02767	−0.02597	−0.00215	−0.00110
μ Kaon	−0.00007	0.00007	−0.00890	0.00857	−0.00006	0.00008
μ Lepton	0.00002	−0.00005	−0.02081	0.02225	0.02130	−0.02075
μ NoTag	0.00017	−0.00019	0.00029	−0.00018	0.00042	−0.00033
μ NT1	0.00013	−0.00015	0.00768	−0.00764	−0.00254	0.00236
μ NT2	−0.00003	0.00000	0.00031	0.00019	0.00330	−0.00336
μ Tail	0.00030	−0.00050	−0.01058	−0.00912	0.00166	0.01692
σ Core	−0.00003	0.00003	0.01705	−0.01655	−0.00460	0.00535
σ Tail	0.00000	0.00000	0.00000	0.00000	0.00000	0.00000

Table B.6: Systematics errors due to uncertainty on the background Δt parameterization.

	$\mathcal{A}_{K\pi}$		$S_{\pi\pi}$		$C_{\pi\pi}$	
Parameter	$+\sigma$	$-\sigma$	$+\sigma$	$-\sigma$	$+\sigma$	$-\sigma$
Run 1						
Core μ	-0.00017	0.00016	-0.00015	0.00022	0.00083	-0.00079
Core σ	-0.00004	0.00003	-0.00122	0.00117	-0.00005	0.00025
Tail f	-0.00019	0.00020	-0.00551	0.00547	-0.00174	0.00175
Tail μ	-0.00017	0.00017	0.00096	-0.00099	0.00083	-0.00088
Tail σ	-0.00048	0.00050	-0.00496	0.00469	-0.00315	0.00335
Outlier f	-0.00029	0.00033	-0.00250	0.00255	-0.00151	0.00160
Outlier σ	-0.00020	0.00024	0.00035	-0.00026	-0.00019	0.00033
Run 2						
Core μ	-0.00014	0.00013	-0.00050	0.00056	0.00004	0.00001
Core σ	0.00010	-0.00011	-0.00056	0.00075	0.00195	-0.00218
Tail f	-0.00030	0.00035	0.00266	-0.00293	-0.00063	0.00081
Tail μ	-0.00007	0.00007	-0.00138	0.00151	-0.00020	0.00022
Tail σ	-0.00064	0.00068	0.00799	-0.00798	-0.00156	0.00163
Outlier f	-0.00014	0.00014	0.00126	-0.00124	0.00014	-0.00018
Outlier σ	0.00003	-0.00004	-0.00066	0.00084	-0.00024	0.00034

Table B.7: Systematic errors due to uncertainty on τ and Δm_d.

	$\mathcal{A}_{K\pi}$		$S_{\pi\pi}$		$C_{\pi\pi}$	
Parameter	$+\sigma$	$-\sigma$	$+\sigma$	$-\sigma$	$+\sigma$	$-\sigma$
τ	0.00019	-0.00020	-0.00193	0.00194	-0.00091	0.00085
Δm_d	0.00017	-0.00017	-0.01092	0.01122	-0.00658	0.00657

Acknowledgements

I am indebted to my supervisor, prof. Fernando Ferroni, and to the *BABAR Charmless TwoBody Working Group*. Or, better, the *gang*. This analysis has been possible thanks to them. I am very grateful to prof. Carlo Dallapiccola, prof.A.Jawahery, and prof. Jim Olsen. Many suggestions came from the *BABAR* $sin2\beta$ *working group*. Special thanks to Riccardo Faccini, Shahram Rahatlou and Gerhard Raven. My deepest gratitude to the whole *BABAR* Roma group, it is just fun working with all of them. My gratitude to prof. Guido Martinelli and his coworkers for discussions on the theoretical aspects of this work. And to all the *BABAR* people around the world I met during these years, thanks again.

Ringraziamenti

Meriti e colpe di questa tesi non sono solo miei.
In ordine alfabetico, un grazie a:

ale, per chi crede nel *quid* e intanto produce endorfine come puó
amir, please, next August leave for the Caribeean Sea...
antonella, per la determinazione e la tenacia
asarti, e tutti quelli che si possono permettere di essere *buoni*
baudo, consulente *strategico* della mia vita
beppe fenoglio, per *Il Partigiano Johnny*
carlo, don't you need a passport to travel abroad ?
cate, per aver sopportato tutto questo. Almeno per un po'
cecilia, per *Sally*, per l'uva, ...ma che giá te ne vai???
cristina, per i 400 Mbyte della quota AFS a Roma
daniele, per come sa cucinare le bistecche. E per la *signorina*
eddie vedder, *Alive*
fabbino, per aver occupato il cesso sempre al momento giusto
francesca, per i *profiterol* all'aeroporto
franz, la sua tagliente luciditá
giancarlo, la classe e l'eleganza. Servono anche quelle
guido martinelli, per non averci ancora detto quanto fa α
jim, for that same killer instict
joni mitchell, *Sire of Sorrow*
leggenda, per l'albero verde della sua serenitá
leo, perché è semplicemente questa la *nostra* rivoluzione
marcella, chi per avere tutto il mondo fra le braccia, ci si è trovato anche la morte
marcello, per non aver mai smesso di far schioccare le dita
marijuccia, sorellina che mi ha insegnato a stirare le camicie
maurizio, la *gaia scienza*, la societá ideale,...
nando, per tutto il coraggio e l'entusiasmo dimostrati
necci& federica, per il piccolo riccardo
paola, per essersi fatta *ammirare*

popolo, quanto è difficile trovare casa di questi tempi...
ric, perché siamo riuciti a non lavare il bagno per tre mesi
sandra, per aver quasi pagato le mie bollette del telefono
sandro, la *mailing* list degli incazzati
shahram, e tutti quelli che ci credono. Costi quel che costi
silvio, e i suoi quaranta moduli di kiu-si
soliman, per avermi fatto comprare un paio di pessimi mocassini
tutz, per l'elevato tasso alcoolico. Insieme, al tramonto a Sperlonga. E per sua cugina
willis, l'irrefrenabile spirale del cazzeggio. E tutta la sua buona musica
zakkia, per essere stata uno specchio. E per il *bene superiore*
E a tutti i vicini e i lontani, gli attenti e i distratti, ancora grazie per il loro esser-*ci*.

References

[1] B.Aubert *et al.*, [*BABAR* Collaboration], *Phys. Rev. Lett.* **87** (2001) 151802 .

[2] B.Aubert *et al.*, [*BABAR* Collaboration], SLAC-PUB-8929, BABAR-CONF-01-05, Jul 2001. Contributed to LP01, Rome, Italy, [`hep-ex/0107074`].
B.Aubert *et al.*, [*BABAR* Collaboration], SLAC-PUB-9012, BABAR-PUB-01-21, Oct 2001. Submitted to PRD [`hep-ex/0110062`].

[3] M. Beneke, G. Buchalla, M. Neubert and C.T. Sachrajda, *Nucl. Phys. B***591** (2000) 313 [`hep-ph/0006124`].

[4] M.Ciuchini, E.Franco, G.Martinelli, M.Pierini, L.Silvestrini, *Phys. Lett. B* **515** (2001) 33

[5] D. Cronin-Hennessy *et al.*, [CLEO Collaboration], *Phys. Rev. Lett.* **85** (2000) 515.

[6] J. H. Christenson *et al.*, *Phys. Rev. Lett.* **13** (1964) 138.

[7] A. Abashian *et al.* [BELLE Collaboration],*Phys. Rev. Lett.* **86** (2001) 2509

[8] B. Aubert *et al.* [*BABAR* Collaboration], *Phys. Rev. Lett.* **86** (2001) 2515

[9] B. Aubert *et al.* [*BABAR* Collaboration], *Phys. Rev. Lett.* **87** (2001) 091801

[10] A. Abashian *et al.* [BELLE Collaboration], *Phys. Rev. Lett.* **87** (2001) 091802

[11] P. Harrison and H.R. Quinn, *The BABAR Physics Book*, SLAC-R-504 (1998).

[12] See for example: J.J. Sakuray, *Modern Quantum Mechanics, Revised Edition*, Addison-Wesley (1985).

[13] I. I. Bigi *et al.*, in *CP Violation*, ed. C. Jarlskog, World Scientific, Singapore (1992).

[14] D.E. Groom *et al.*, the Particle Data Group, *Review of Particle Physics*, *Eur. Phys. Jour. C* **15**, 1 (2000).

[15] S.L. Glashow, *Nucl. Phys.* **22** , (1961) 579;
S. Weinberg, *Phys. Rev. Lett.* **19** , (1967) 1264 .

[16] N. Cabibbo, *Phys. Rev. Lett.* **10** , (1963) 531

[17] M. Kobayashi and T. Maskawa, *Prog. Th. Phys.* **49** (1973) 652.

[18] L. Wolfenstein, *Phys. Rev. Lett.* **51** (1983) 1945.

[19] A. J. Buras, M. E. Lautenbacher and G. Ostermaier, *Phys. Rev. D* **50** (1994) 3433.

[20] M.Ciuchini, G.D'Agostini, E.Franco, V.Lubicz, G.Martinelli, F.Parodi, P.Roudeau, A.Stocchi, *JHEP* **0107** (2001) 013 [`hep-ph/0012308`].

[21] T. Inami and C.S. Lim,*Prog. Theor. Phys.* **65** (1981) 297; *ibid.* **65** (1981) 1772.

[22] G. Buchalla, A. J. Buras e M. E. Lautenbacher, *Rev. Mod. Phys.* **68** (1996) 1125 [`hep-ph/9512380`].

[23] A.J. Buras, M. Jasmin and P.H. Weisz, *Nucl. Phys. B* **347** (1990) 491.

[24] S. Herrlich and U. Nierste, *Nucl. Phys. B* **419** (1994) 192.

[25] A. Höcker, H. Lacker, S. Laplace, and F. L. Diberder, *Eur.Phys.J.* **C21** (2001) 225-259 [`hep-ph/0104062`].

[26] S. Plaszczynski and M. Schune, Talk given at 8th International Symposium on Heavy Flavor Physics, Southampton, England, 1999 [`hep-ph/9911280`].

[27] Y. Grossman and H.R. Quinn, *Phys. Rev. D* **56** (1997) 7259.

[28] M. Gronau and D. London, *Phys. Rev. Lett.* **65** (1990) 3381.

[29] N.G. Deshpande and X.G. He, *Phys. Rev. Lett.* **74** (1995) 26 .

[30] S. Gardner, *Phys. Rev. D* **59** (1999) 077502.

[31] Y. Grossman and H.R. Quinn, *Phys. Rev. D* **58** (1998) 017504.

[32] A. Bevan *et al.*, *Measurement of branching fractions for charmless $B \to h^0 h'^0$ decays*, *BABAR* Analysis Document #148, May 2001.

[33] J.Charles, *Phys. Rev. D* **59** , 054007 (1999).

[34] M. Gronau, D. London, N. Sinha, and R. Sinha, *Phys. Lett. B* **514** (2001) 315 [`hep-ph/0105308`].

[35] M. Beneke, G. Buchalla, M. Neubert, and C.T. Sachrajda, *Nucl. Phys. B* **606** (2001) 245 [`hep-ph/0104110`].

[36] M. Beneke, G. Buchalla, M. Neubert and C.T. Sachrajda, *Phys. Rev. Lett.* **83** (1999) 1914 [`hep-ph/9905312`].

[37] S.Chen *et al.*, [CLEO Collaboration], *Phys. Rev. Lett.* **85** (2000) 525.

[38] B.Aubert *et al.*, [*BABAR* Collaboration], SLAC-PUB-8569, [`hep-ex/0105044`].

[39] GEANT 3.15: R.Brun *et al.*, Report No. CERN DD/EE/84-1.

[40] T.Sjöstrand, *Comput. Phys. Commun.* **82**, 74 (1994); T.Sjöstrand and M.Bengston *ibid.* **43**, 367 (1987); T.Sjöstrand, *ibid.* **39**, 347 (1986)

[41] P.Billoir, *Nucl.Instr.Methods* , A225 (1984) 225

[42] E. Varnes, N. Kuznetsova, C. Dallapiccola and G. Cavoto, *Measurement of the* `GoodTracksLoose` *Efficiency using SVT Tracks*, *BABAR* Analysis Document #157, 2001.

[43] B.N. Ratcliff, SLAC-PUB-5946 (1992); B. N. Ratcliff, SLAC-PUB-6067 (1993); P. Coyle *et al*, *Nucl.Instr.Methods* , A343 (1994) 292.

[44] W.T. Ford, *Choice of Kinematic Variables in B Meson Reconstruction– Take 3*, *BABAR* Analysis Document #53, 2000.

[45] S. Brandt *et al.*, *Phys. Lett.* **12** (1964) 57;
E. Fahri, *Phys. Rev. Lett.* **39** (1977) 1587.

[46] J. D. Bjorken and S. J. Brodsky, *Phys. Rev. D* **1** (1970) 1416.

[47] G. C. Fox and S. Wolfram, *Nucl. Phys.* **B149** (1979) 413.

[48] R. A. Fisher, *Annals of Eugenics* **7** (1936) 179.

[49] H. Albrecth *et al.*, The ARGUS Collaboration, *Z. Phys. C* **48** , 543 (1990).

[50] A. Roodman, *Proposal for a Blind Analysis of sin2β*, *BABAR* Analysis Document #43, 2000.

[51] J. Beringer *et al.*, *B* Tagging Tools Group, *B Tagging in BABAR: Status for the sin2β Journal Publication*, *BABAR* Analysis Document #119, January 2001.

[52] F. Martinez-Vidal *et al.*, Vertexing and Composition Tools Group, *The BABAR Vertexing*, *BABAR* Analysis Document #102, March 2001; *Vertexing performances and systematic checks with fully reconstructed B events*, *BABAR* Analysis Document #130, March 2001.

[53] CERN Program Library, "**MINUIT** - function minimization and error analysis.". D506

[54] M.Ciuchini, E.Franco, G.Martinelli, M.Pierini, L.Silvestrini, [`hep-ph/0110022`]

[55] M.Ciuchini, E.Franco, G.Martinelli, and L.Silvestrini, *Nucl. Phys. B* **501** (1997) 271, M.Ciuchini, R.Contino, E.Franco, G.Martinelli, and L.Silvestrini, *Nucl. Phys. B* **512** (1998) 3.

[56] A. Höcker, H. Lacker, S. Laplace, and F. L. Diberder, *CKM fitter* web page, http://www.slac.stanford.edu/ laplace/ckmfitter.html.

[57] J.Charles, *Nucl. Phys. Proc. Suppl.* 99A, 287-294 (2001).